UNIVERSITAT DE BARCELONA

# CMOS/GaN integration in micro/nanoLED arrays for biomedical applications

Víctor Moro Moreno

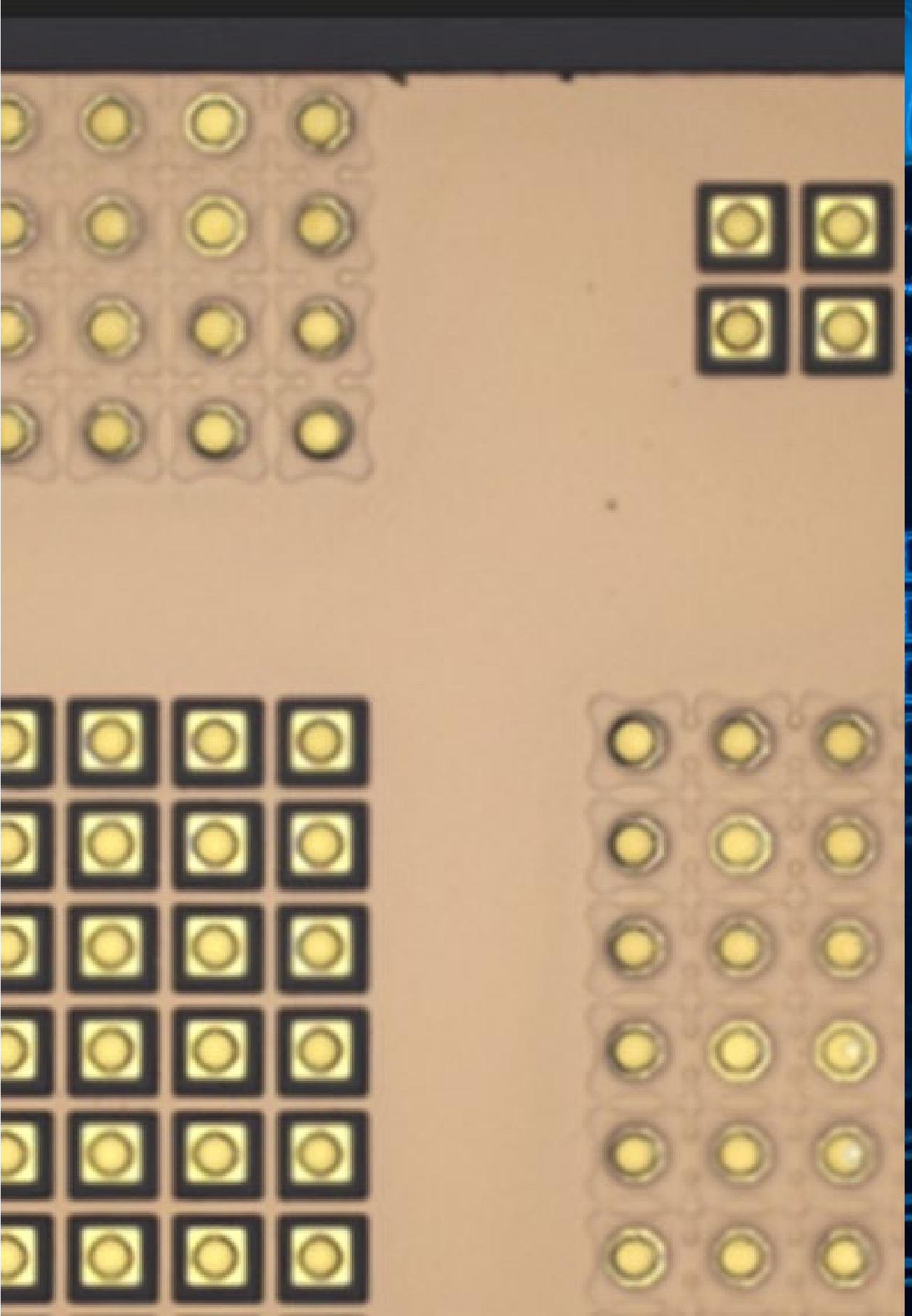

Victor Moro Moreno - CMOS/GaN integration in micro/nanoLED arrays for biomedical applications

PhD Thesis

# CMOS/GaN integration in micro/nanoLED arrays for biomedical applications


**Author: Victor Moro Moreno**

**Supervised by: Ángel Diéguez Barrientos**




UNIVERSITAT DE BARCELONA

# CMOS/GaN integration in micro/nanoLED arrays for biomedical applications

## Programa de doctorado en Ingeniería y Ciencias Aplicadas

Autor: Victor Moro Moreno

Director: Ángel Diéguez Barrientos

Tutor: Ángel Diéguez Barrientos

Departamento de Ingeniería Electrónica y Biomédica

Facultad de Física, Universitat de Barcelona


UNIVERSITAT DE BARCELONA

# Agradecimientos

Me gustaría comenzar expresando mi agradecimiento al Dr. Ángel Diéguez por su supervisión y apoyo durante mi etapa en el grupo de diseño microelectrónico. Su guía ha sido invaluable, no solo a lo largo de esta tesis doctoral, sino desde el momento en que me ofreció la oportunidad de realizar prácticas en su laboratorio. Gracias al ingreso en su grupo de investigación, he desarrollado un profundo aprecio por mi profesión, especialmente por el diseño de circuitos integrados, lo cual me brinda una gran satisfacción en mi labor.

También deseo agradecer la implicación y el esfuerzo del Dr. Joan Canals y del Dr. Nil Franch. Sin sus valiosas contribuciones y experiencia, así como su apoyo en los momentos difíciles cuando todo me parecía destinado al fracaso, esta tesis no habría sido posible.

Otra persona a quien quiero expresar mi agradecimiento es Sergio Moreno, quien ahora sigue los pasos que yo recorrí recientemente. Le deseo un camino tan gratificante como el que yo he tenido.

Además, me gustaría reconocer la implicación de todas las personas con quienes he compartido largas horas en el laboratorio. Al Dr. Óscar Alonso, que siempre ha estado presente para ofrecer su experiencia en diseño y a Juan Luís, junto a tantos otros por su compañía y su experiencia.

Quiero extender mi gratitud a los equipos de los proyectos europeos ChipScope y SMILE. Esta tesis ha sido posible gracias al esfuerzo conjunto de todos los participantes. En particular, quiero mencionar al Dr. Daniel Prades, quien ha desempeñado un papel clave en la cooperación entre los desarrolladores y fabricantes de las matrices de microLEDs (TUBs) y nuestro equipo.

Finalmente, aunque no menos importante, quiero expresar mi más profundo agradecimiento a mi pareja, Alina. El desarrollo de este trabajo, y mucho más, no habría sido posible sin su amor y total apoyo. Ella siempre ha estado a mi lado, brindándome su apoyo y ayudándome en los momentos de mayor tribulación. También quiero recordar a alguien que, lamentablemente, nunca estará aquí, pero cuyo recuerdo permanecerá siempre vivo en mi corazón. Espero que continúes brillando y guiándonos como una pequeña estrella.

# Agradecimientos

No puedo concluir sin expresar mi agradecimiento a mis padres por su apoyo incondicional a lo largo de los años. Les estoy profundamente agradecido por brindarme todo lo necesario para llegar hasta aquí, por sus sacrificios para ofrecerme la mejor educación posible y por haberme convertido en la persona que soy hoy. También quiero reconocer a toda mi familia, que ha estado a mi lado incondicionalmente en todo momento.

# Abstract

Since their inception, LEDs have replaced traditional incandescent and fluorescent lighting in numerous sectors, ranging from general illumination and display technologies to specialized applications, such as in the biomedical field. LEDs provide significant energy savings, reduced environmental impact, and greater design flexibility, marking a significant shift in how light is utilized across different domains, even being able to substitute lasers in a wide range of applications.

Building on the success of conventional LEDs, microLED technology has emerged as a groundbreaking advancement. MicroLEDs are significantly smaller than traditional LEDs, typically ranging from a few micrometers to a few hundred micrometers in size. This miniaturization opens new possibilities for high-resolution displays, where microLEDs offer superior brightness, contrast, and energy efficiency compared to OLED and LCD technologies. Additionally, the fast response times and robustness of microLEDs make them suitable for dynamic and demanding applications, such as augmented reality and virtual reality displays, as well as advanced biomedical devices.

The integration of CMOS technology with GaN microLEDs in the development of products based on micro or nanoLED arrays is a significant step forward for all the applications where microLEDs can be used. In this work, we will focus on their potential usage in the biomedical field. CMOS technology is known for its scalability, low power consumption and high integration density, which are essential characteristics for creating compact and efficient electronic systems. On the other hand, GaN is valued for its high electron mobility, thermal stability and direct wide bandgap properties, enabling efficient light emission and operation under high power conditions. Combining these technologies, it is possible to create lighting devices with micro or nanoLEDs that leverage the best attributes of both materials, resulting in a compact device with enhanced performance and functionality.

This PhD thesis explores the development of CMOS drivers to be integrated with GaN microLED arrays, addressing the inherent challenges posed by the material and processing incompatibilities between silicon-based CMOS and GaN. This research provides a detailed analysis of the optical, electrical, and thermal

performance of these devices, demonstrating their superior characteristics compared to conventional LED arrays and other light sources.

In the context of biomedical applications, the thesis focuses on microscopy and PoC diagnostics. In advanced microscopy, integrated micro/nano LED arrays can provide high-intensity, uniform illumination with precise control over wavelength and intensity. This capability enhances imaging resolution and contrast, allowing for more detailed and accurate observations at the cellular and molecular levels. The miniaturized form factor of these LEDs also facilitates the development of compact and portable microscopy devices, broadening their accessibility and utility in various medical and research settings. Furthermore, in this thesis we explore the use of micro and nanoLED devices combined with CMOS electronics to create a new type of microscopy technique, Nano-Illumination Microscopy (NIM).

For PoC diagnostics, the high speed and high optical power that microLEDs can deliver when driven by CMOS IC is crucial to develop fluorescence based PoC. These arrays can be used to develop portable diagnostic devices that offer real-time monitoring and rapid analysis of biological markers. This is crucial for early disease detection and personalized medicine, where timely and accurate diagnostics can significantly improve patient outcomes. The integration of these LEDs into PoC devices ensures that they are not only effective but also energy-efficient and cost-effective, making them suitable for widespread use, including in resource-limited settings. Furthermore, microLED arrays are a perfect fit to accomplish the ASSURED criteria provided by WHO for PoC devices.

In conclusion, this PhD thesis shows that the integration of CMOS and GaN technologies in micro/nano LED arrays offers a transformative approach for advancing biomedical applications, specifically in microscopy and PoC diagnostics. The enhanced performance, combined with the reliability and scalability of these integrated systems, holds significant promise for future innovations in medical diagnostics, treatment, and research. This work lays the groundwork for further exploration and development in the field, potentially leading to new breakthroughs in biomedical technology.

# Resumen

Desde su invención, los LEDs han reemplazado la iluminación tradicional incandescente y fluorescente en numerosos sectores, desde la iluminación general y las tecnologías de visualización hasta aplicaciones más especializadas, como por ejemplo en el campo biomédico. Los LEDs ofrecen un ahorro significativo de energía, un menor impacto ambiental y una mayor flexibilidad de diseño, marcando un cambio importante en la utilización de la luz en diferentes áreas, incluso llegando a sustituir a los láseres en un amplio espectro de aplicaciones.

A partir del éxito de los LEDs convencionales, el desarrollo de la tecnología microLED ha supuesto un avance revolucionario. Los microLEDs son significativamente más pequeños que los LEDs tradicionales, variando tipicamente desde unos pocos micrómetros hasta unos pocos centenares de micrómetros. Esta miniaturización abre nuevas posibilidades en el desarrollo de pantallas de alta resolución, donde los microLEDs ofrecen un brillo, contraste y eficiencia energética superiores en comparación con las tecnologías OLED y LCD. Además, su gran ancho de banda, su rápido tiempo de respuesta y su robustez los hacen adecuados para un gran número de aplicaciones, como pantallas de realidad aumentada y realidad virtual, así como dispositivos biomédicos avanzados.

La integración de la tecnología CMOS con microLEDs de GaN en la construcción de dispositivos basados en matrices de micro o nanoLEDs promete un avance significativo para todas las aplicaciones donde se pueden utilizar. En este trabajo, nos centraremos en su uso potencial en el campo biomédico. La tecnología CMOS es conocida por su escalabilidad, bajo consumo de energía y alta densidad de integración, características esenciales para crear sistemas electrónicos compactos y eficientes. Por otro lado, la tecnología de GaN es valorada por su alta movilidad de electrones y estabilidad térmica, lo que permite una emisión de luz eficiente y una operación bajo condiciones de alta potencia. Combinando estas tecnologías, es posible crear dispositivos de iluminación con micro o nanoLEDs que aprovechen los mejores atributos de ambos materiales, resultando en un dispositivo compacto con un rendimiento y funcionalidad mejorados.

Esta tesis doctoral explora el desarrollo de circuitos controladores CMOS diseñados para ser integrados con matrics de microLEDs de GaN, abordando los

desafíos planteados por las incompatibilidades de material y procesamiento entre las tecnologías CMOS y GaN. Esta investigación proporciona un análisis detallado del rendimiento óptico y eléctrico, demostrando sus características superiores en comparación con matrices LED convencionales y otras fuentes de luz.

En el contexto de las aplicaciones biomédicas, la tesis se centra en la microscopía y los diagnósticos en el punto de atención (PoC). En la microscopía avanzada, las matrices integradas de micro/nano LED pueden proporcionar una iluminación uniforme de alta intensidad con un control preciso sobre la longitud de onda y la intensidad. Esta capacidad mejora la resolución y el contraste de la imagen, permitiendo observaciones más detalladas y precisas a niveles celulares y moleculares. El factor de forma miniaturizado de estos LEDs también facilita el desarrollo de dispositivos de microscopía compactos y portátiles, ampliando su accesibilidad y utilidad en diversos entornos médicos y de investigación. Además, en esta tesis exploramos el uso de dispositivos de micro y nanoLED combinados con electrónica CMOS para crear una nueva técnica de microscopía, la Microscopía de Nano-Iluminación (NIM).

Para los diagnósticos PoC, la alta velocidad y potencia óptica que los microLEDs pueden proporcionar cuando son controlados por circuitos integrados CMOS son cruciales para desarrollar PoC basados en fluorescencia. Estas matrices pueden usarse para desarrollar dispositivos de diagnóstico portátiles que ofrecen monitoreo en tiempo real y análisis rápido de marcadores biológicos. Esto es esencial para la detección temprana de enfermedades y la medicina personalizada, donde diagnósticos oportunos y precisos pueden mejorar significativamente los resultados de los pacientes. La integración de estos LEDs en dispositivos PoC asegura que no solo sean efectivos, sino también eficientes en términos de energía y costos, haciéndolos adecuados para un uso generalizado, incluso en entornos con recursos limitados. Además, las matrices de microLED son una solución perfecta para cumplir con los criterios ASSURED proporcionados por la OMS para dispositivos PoC.

En conclusión, esta tesis doctoral muestra que la integración de las tecnologías CMOS y GaN en matrices de micro/nano LED ofrece un enfoque transformador para el avance de las aplicaciones biomédicas, específicamente en la microscopía y los diagnósticos en el punto de atención. El rendimiento mejorado, combinado

con la fiabilidad y escalabilidad de estos sistemas integrados, ofrece una promesa significativa para futuras innovaciones en diagnósticos médicos, tratamientos e investigación. Este trabajo sienta las bases para una mayor exploración y desarrollo en el campo, lo que podría llevar a nuevos avances en la tecnología biomédica.

# Content

# Content

# List of Figures

# List of Figures

# List of Figures

# List of Figures

# List of Tables

# Abbreviations

**2T1C** 2 Transistors 1 Capacitor

**AM** Active Matrix

**AMS** Austrian MicroSystems

**AR** Augmented Reality

**ASSURED** Affordable, Sensitive, Specific, User-friendly, Rapid and Robust, Equipment-free, and Deliverable

**AWG** Arbitrary Waveform Generator

**CMOS** Complementary Metal-Oxide-Semiconductor

**DA** Direct Addressed

**DAC** Digital-to-Analog Converter

**DC** Direct Current

**DRAM** Dynamic Random-Access Memory

**EBL** Electron-Beam Lithography

**ESF** Edge Spread Function

**FLIM** Fluorescence Lifetime Imaging Microscopy

**FoV** Field-of-View

**FPGA** Field-Programable Gate Array

**FWHM** Full Width at Half Maxmimum

**GaAs** Gallium Arsenide

**GaN** Gallium Nitride

**GaN-on-Si** Gallium Nitride on Silicon

**HBO** Mercury Arc Lamp

**HID** High-Intensity Discharge

# Abbreviations

| | |
|---|---|
| **IC** | Integrated Circuit |
| **IFFT** | Inverse Fast Fourier Transform |
| **IR** | Infrared |
| **LED** | Light-Emitting Diode |
| **LoD** | Limit of Detection |
| **LSF** | Line Spread Function |
| **MA** | Matrix Addressed |
| **MH** | Metal-Halide |
| **NIM** | Nano-Illumination Microscopy |
| **NMOS** | N-type Metal-Oxide-Semiconductor |
| **NTE** | Near to Eye |
| **OLED** | Organic Light-Emitting Diode |
| **PALM** | Photo-Activated Localization Microscopy |
| **PCB** | Printed Circuit Board |
| **PM** | Passive Matrix |
| **PMOS** | P-type Metal-Oxide-Semiconductor |
| **PoC** | Point-of-Care |
| **PPI** | Pixels Per Inch |
| **PWM** | Pulse Width Modulation |
| **QD** | Quantum Dot |
| **RF** | Radio Frequency |
| **SPAD** | Single-Photon Avalanche Diode |
| **SRAM** | Static Random-Access Memory |
| **STED** | Stimulated Emission Depletion Microscopy |

# Abbreviations

| | |
|---|---|
| **STORM** | Stochastic Optical Reconstruction Microscopy |
| **TCA** | Transconductance Amplifier |
| **TCSPC** | Time-Correlated Single Photon Counting |
| **TDC** | Time-to-Digital Converter |
| **UV** | Ultraviolet |
| **VLC** | Visual Light Communication |
| **VR** | Virtual Reality |
| **WHO** | World Health Organization |
| **XBO** | Xenon Arc Lamp |

# 1.

# Introduction

This thesis is presented as an article compendium, divided into five principal chapters. In this first chapter, Introduction, the thesis structure is shown, along with the motivation and interest of this investigation. Moreover, in this chapter the aimed objectives are described, from the development of microLED and CMOS platforms to microscopy and PoC applications, to the design of a full microdisplay backplane. The second chapter, Light sources for biomedical applications, is a travel from the most antique light sources used in biomedical imaging and sensing, arc lamps, to the last and most standard light sources in our time, lasers and LEDs, ending with a view of the promising future microLEDs arrays and microdisplay offers. The large possibilities that microLEDs offer, especially when driven by custom integrated circuits, motivates the work presented later in this thesis. The third chapter is formed by the results. The results are structured to show first the research produced during this thesis in matter of microLED driving circuits, and then to describe the use of these drivers in different applications implemented with different microLED arrays. These applications englobe raster microscopy, shown in Publications #1 and #2, where a series of microscopes are developed using microLEDs and custom driver ICs. Publication #3 explores methods on how to

decrease acquisition times in order to be used in the microscopes, but the method presented can be used elsewhere. Then, another application is the development of PoC devices. In Publication #4, a fluorescence PoC that uses Matrix Addressable microLED arrays along with custom drivers is described. The PoC described is capable of performing both intensity and time resolved fluorescence measurements. This chapter ends with a description of the design of a hybrid interconnected microdisplay. Publication #5 and #6 describe a microdisplay backplane designed for an array of 512 x 512 microLEDs. Finally, chapter four illustrates the conclusions extracted from the work developed, along with the next paths that need to be followed to continue this line of investigation, from our point of view. Chapter five contains the bibliography referenced in the writing and execution of this thesis.

The main objective that led the research performed in this work is the study of the use of CMOS/GaN integration of micro and nanoLED arrays and its applications in the biomedical field. Furthermore, this research is focused on the use of GaN microLED arrays with specific driving circuits developed in CMOS technology that can be used in microscopy or PoC devices. The research presented in each publication included in this doctoral thesis is of significant importance for the advances that it enhances in the field of biomedical imaging and sensing. As the use of microLEDs continues to expand, it is expected that the cost of these devices will decrease significantly in the future. In addition to being a strong candidate due to their high efficiency and long lifespan, microLEDs are likely to become even more attractive due to their reduced cost. Each study contributes uniquely to the broader research landscape.

- **Publication #1:** Franch, N.; Canals, J.; Moro, V.; Vilà, A.; Romano-Rodríguez, A.; Prades, J.D.; Guelink, J.; Bezshlyakh, D.; Waag, A.; Kluczyk, K.; Auf der Maur, M.; Di Carlo, A.; Diéguez, A. *Nano-Illumination Microscopy: A Technique Based on Scanning with an Array of Individually Addressable NanoLEDs.* Opt Express 2020, 28, 19044–19057 https://doi.org/10.1364/OE.391497

The research presented in this publication is of major importance, since it is the first time a microscope has been developed using microLED arrays, especially one where the resolution is provided by the microLEDs pitch and size. This publication paved the way for a wide range of applications and

research paths, from improving the microscope described, to the creation of newer microscopes that could work with fluorescence.

- **Publication #2:** Canals, J.; Franch, N.; Moro, V.; Moreno, S.; Prades, J.D.; Romano-Rodríguez, A.; Bornemann, S.; Bezshlyakh, D.D.; Waag, A.; Vogelbacher, F.; Schrittwieser, S.; Kluczyk, K; Auf der Maur, M., Di Carlo, A.; Diéguez, A. *A Novel Approach for a Chip-Sized Scanning Optical Microscope.* Micromachines (Basel) 2021, 12 https://doi.org/10.3390/mi12050527

In this publication the technique presented in Publication #1 is improved. This work is of major importance, since it explores the resolution gain when the microLED pitch and size is improved.

- **Publication #3:** Moro, V.; Moreno, S.; Alonso, O.; Vilà, A.; Prades, J.D.; Diéguez, A. *Using Time-Correlated Single-Photon Counting Technique on SPAD Sensors to Enhance Acquisition Time and Dynamic Range* Proceedings of SPIE 2022 https://doi.org/10.1117/12.2641176

What was observed until this point was that microscopy based on microLED arrays, or raster microscopy, had a major handicap. If a sample was to be scanned by an array of microLEDs turned on and off individually, the larger the FoV is, the larger the time for an acquisition. This could be a problem where biological samples that change in short periods of time are observed. Thus, the research presented in this publication is of high importance, since the study of several statistical methods applied to a histogram of a constant light source can decrease acquisition time.

- **Publication #4:** Moro, V.; Canals, J.; Moreno, S.; Bornemann, S.; Alonso, O.; Waag, A.; Prades, J.D.; Dieguez, A. *Fluorescence Multi-Detection Device Using a Lensless Matrix Addressable MicroLED Array* Biosensors (Basel) 2024, 14, 264 https://doi.org/10.3390/bios14060264

The line of research paved by Publication #1 showed that another area of interest was the development of fluorescence microscopes. In this publication, the use of a fluorescence microscope is studied, not for imaging, but for diagnosis. Thus, the study of a PoC built using microLEDs for both intensity and time-resolved fluorescence is studied. The possibility to develop cheap

diagnosis devices is crucial in the actual world, since there is a vast number of people that have limited access to healthcare.

- **Publication #5:** Moro, V.; Canals, J.; Schöttler, G.; Bornemann, S.; Waag, A.; Prades, J.D.; Diéguez, A. *SRAM-based LED CMOS Driver Circuit for a 512x512 GaN Microdisplay* SID Symposium Digest of Technical Papers 2023, 54, 135–139 https://doi.org/10.1002/sdtp.16244
- **Publication #6:** Canals, J.; Moro, V.; Schöttler, G.; Bornemann, S.; Waag, A.; Prades, J.D.; Diéguez, A. *A 9 Kfps 1411 PPI GaN-Based MLED Display CMOS Backplane*. SID Symposium Digest of Technical Papers 2023, 54, 125-128 https://doi.org/10.1002/sdtp.16504

The trend in microLEDs is to build microdisplays with use in visual applications. But microLEDs have properties that can be used in several scientific applications. Thus, it is important to develop a microdisplay platform to study the possibilities it offers. In these publications, there is the development of this platform.

Taking into account the goals proposed in this work, the primary objectives of this doctoral dissertation are focused on the design, development, and integration of microLED driving circuits, both with commercial ICs and designing and manufacturing full custom CMOS chips, with a particular emphasis on their application in microscopy and biomedical fields. The research presented in this dissertation addresses both the technical challenges associated with microLED technology and its potential for advancing scientific imaging and diagnostic tools.

The first major objective is to design a highly precise driving circuit for Direct Addressable microLED arrays. This circuit is required to control bias currents across a wide range, from microamperes (μA) to milliamperes (mA). Achieving such a broad range of current control is crucial for studying the behavior and capabilities of microLEDs in microscopic applications. The ability to finely tune the current enables the optimization of light output, which is essential for high-resolution imaging where even small variations in illumination can significantly impact the quality and accuracy of the observed data. This precise control is especially important in applications such as fluorescence microscopy, where consistent light delivery can enhance the detection of subtle biological processes. This driver was used to achieve the results presented in Publication #1.

In parallel with current control, another critical objective is the development of an integrated CMOS driving circuit capable of producing ultra-short optical pulses with a FWHM in the nanosecond range. Such short pulse duration, and especially a fast switch off of the microLED, is vital for time-resolved fluorescence and high-speed imaging applications. In time-resolved fluorescence, for example, the ability to generate nanosecond pulses allows for the differentiation of fluorophores based on their emission lifetimes, providing an additional dimension of data that can be used for more detailed and informative analyses. This is the driver that was used to build the microscope presented in Publication #2.

Additionally, the dissertation focuses on the design of a CMOS driving circuit tailored specifically for Matrix Addressable microLED arrays. Unlike Direct Addressable arrays, Matrix Addressable arrays require sophisticated driving circuits that can handle the complexities of addressing higher LEDs parasitic components simultaneously while maintaining high performance. The designed circuit must be capable of delivering high optical power and generating pulses with an FWHM in the nanosecond range, making it suitable for integration into advanced imaging systems. These capabilities are crucial for applications such as fluorescence lifetime imaging microscopy and PoC systems, where high optical power is needed to excite fluorophores effectively, and precise pulse control is essential for accurate time-resolved measurements. The integration of these systems with the microLED arrays opens new possibilities for portable, high-performance diagnostic tools that can be used in a variety of settings, from research laboratories to clinical environments. The same chip designed for the DA approach had another circuit in it so it could work for both DA and MA arrays. The MA driving circuits were used to develop the PoC reported in Publication #4.

One of the more advanced objectives is the integration of the Matrix Addressable microLED platform with a SPAD camera. SPAD cameras are known for their exceptional sensitivity and ability to detect single photons, making them ideal for applications that require the detection of extremely low light levels. By combining the microLED arrays with a SPAD camera, this research aims to develop and characterize a new type of PoC system that can use multiple fluorophores for multidetection. This capability is particularly useful in multiplexed assays, where the ability to detect different fluorophores simultaneously can greatly increase the throughput and efficiency of the analysis. The integration of these technologies

could lead to the development of new tools for biomedical research and diagnostics.

Finally, a substantial and technically challenging objective is the development of a CMOS backplane for a microLED array consisting of approximately 250,000 microLEDs, each with a size of 10 µm and a pitch of 18 µm. The design and fabrication of such a backplane requires advanced semiconductor processing techniques and careful consideration of the electrical requirements. The backplane must be capable of delivering high driving currents to the microLEDs to ensure sufficient brightness and performance for scientific applications. Furthermore, it must support high frame rate switching (~10 kfps) and rapid on/off switching speeds exceeding 1 MHz. These capabilities are essential for applications that require high-speed imaging and precise control of light output, such as in dynamic biological studies or real-time diagnostic systems. The successful development of this backplane will represent a significant advancement in the field of microLED technology, enabling new applications and expanding the potential uses of microLED arrays in scientific research and biomedical applications.

# 2.

# Light sources for biomedical applications

Throughout history, light has been a guiding force in the development of observation tools within the field of biomedicine. From the earliest rudimentary devices to the cutting-edge technologies of today, the harnessing of light has enabled remarkable advancements in our ability to explore and understand the human body and biological systems. During the Middle Ages and the Renaissance, the renewed interest in the study of anatomy and medicine in general forced several advances in observation methods to analyze biomedical samples. One of the most significant advances was the invention of lenses, allowing physicians to magnify their vision and provided detailed observation of the anatomical structures. Additionally, concave, and convex mirrors were used to direct and focus light on specific areas of the body during surgery, therefore improving visibility and precision of surgical proceedings. These advancements laid the groundwork for the development of the first microscopes, paving the way for the observation of biological tissues at the cellular level.

The invention of the first microscope is highly controversial, since in the same dates, several instrument makers made advances in the field. The oldest record

extant depicting a microscope is a rough sketch of a Drebbel microscope drawn by hand in 1631 in the diary of Isaac Beeckman [1]. Nevertheless, in the preface of *Extracts from Micrographia* [2], R. Hooke describe how to build his single-lens microscope, which was used by the Dutch scientist Anton van Leeuwenhoek. Van Leuwenhoek reported several microscopic observations on microorganisms in the latter 17$^{th}$ century using this microscope [3]. This was one of the most transformative developments in the history of medicine. The use of the different microscopes allowed for unprecedent magnification and resolution. These primitive microscopes relied typically on sunlight, but in *Extracts from Micrographia* [2] R. Hooke also explained the construction of a lamp that would provide sufficient light whenever needed for microscopic observations.

Further advances were made in the field of imaging technologies, but it was not until the 19$^{th}$ and 20$^{th}$ centuries when significant advances were made in imaging and diagnostics technologies were achieved. The use of electromagnetic waves to visualize internal structures and processes within the human body and to perform ex vivo diagnostics has been crucial in the last centuries. These techniques have revolutionized medical diagnosis, treatment, and research by providing detailed and non-invasive ways to examine biological tissue and functions. One of the first inventions that used a light source to aid the diagnosis of illness was the endoscope, which suffered a huge development at the latter 19$^{th}$ century due to the introduction of the light bulb by Thomas Edison in 1880 [4].

In 1845, F. W. Herschel made the first reported observation of fluorescence, when he noticed that a quinine solution, even being colorless and transparent, exhibited a “vivid and beautiful celestial blue color” when it was illuminated and observed at certain incidence of sunlight [5]. In 1852, G. Stokes described fluorescence with greater detail [6] . After E. Abbe demonstrate the limitations of transmitted light microscopy [7], the expectations of fluorescence in microscopy increased. There was the expectation that fluorescence could provide higher resolution [8]. Even Braum claimed that objects that could emit light were not subject to diffraction [9]. Later, in the early 20$^{th}$ century, fluorescence microscopes were developed. The development of a steady source of ultraviolet light was a prerequisite to the first reliable fluorescence microscope. In 1903, R. W. Wood demonstrated how to isolate a band of ultraviolet light from an arc lamp [10]. This allowed H. Lehmann to make a prototype bright-field fluorescence microscope in 1910. Arc lamps have

been a key component for biomedical imaging since the invention of the fluorescence microscope as light sources, since their emission bands match the absorption bands of a great number of organic fluorophores, which are typically used. These light sources emit light by making an electrical discharge passing through a bulb filled with an ionized gas. Arc lamps include those built with mercury (HBO, where H is short for the element mercury, Hg, B is the luminance symbol and O is the symbol for unforced cooling), xenon (XBO, where Xenon is shortened by X), and metal-halide (MH). In the last decades, since LED technology has evolved, they have become the preferred choice for the majority of applications, since LEDs overcome some of the limitations arc lamps have.

LEDs, or Light-Emitting Diodes, have revolutionized microscopy and PoC (PoC) diagnostics [11]. The advantages of LEDs over traditional arc lamps include their longer lifespan, lower heat generation, and more stable light output [12]. These features make LEDs ideal for continuous and high-resolution imaging, which is crucial in both research and clinical settings [13]. In fluorescence microscopy, LEDs provide specific wavelengths of light necessary to excite fluorophores, improving the clarity and detail of the images obtained.

Lasers have also played a pivotal role in advancing microscopy. They offer highly coherent and monochromatic light, which is essential for techniques such as confocal microscopy and two-photon microscopy [14]. These methods allow for deeper tissue penetration and higher spatial resolution, facilitating the detailed study of cellular and subcellular structures. Lasers' precision and ability to be modulated rapidly enhance dynamic studies of biological processes, making them indispensable in modern biomedical research.

The recent introduction of Gallium Nitride (GaN) microLED technology marks another significant milestone. GaN microLEDs offer superior brightness, efficiency, and durability compared to conventional LEDs [15]. Their small size allows for integration into high-density arrays, providing unprecedented resolution and uniformity in illumination. This is particularly beneficial for high-throughput screening and PoC diagnostics, where accurate and reliable light sources are critical [16]. Moreover, GaN microLEDs' ability to emit across a wide spectrum, including ultraviolet and visible light, expands their utility in various imaging and analytical techniques [17].

# 2. Light sources for biomedical applications

The integration of GaN microLEDs into biomedical devices is already showing promising results. For instance, microLED-based arrays can be used in optogenetics to control neuronal activity with high precision, opening new avenues for neuroscience research [18].

These advancements are part of a broader trend towards miniaturization and increased functionality in biomedical devices. The continued development of microLED technologies leads to further innovations in microscopy and PoC diagnostics, improving our ability to understand and treat various medical conditions [19]. In this work we present different advances in the use of micro and nanoLEDs and their driving circuits to be used in biomedical applications.

# 2. Light sources for biomedical applications

## 2.1. Light sources

### 2.1.1. Arc lamps

Arc lamps are lamps that emit light by an electric arc or a voltaic arc. The first arc lamp was invented in the first decade of the 1800s by H. Davy. This is the carbon arc light, that consists of an arc between carbon electrodes in air [20]. This arc lamp paved the invention of the lamps used in fluorescence, which does not work in air, but in special gases. As mentioned before, for fluorescence use there exist three types of arc lamps, the mercury arc lamp, or HBO, where H is for the chemical symbol of mercury, B for the luminance symbol and O for the unforced cooling symbol, the xenon lamp or XBO, where X is for Xenon, and the metal-halide lamp, or MH. All these lamps are described as high-intensity discharge (HID) lamps.

#### 2.1.1.1. Mercury arc lamp

Mercury arc lamps, invented by Peter Cooper Hewitt in 1901, were among the first electric light sources [21]. They gained popularity in the early 20th century for their efficiency and brightness, finding use in factories, street lighting, and public spaces. Throughout the century, improvements led to more stable and efficient designs, including high-pressure mercury lamps that produced a whiter light. By the mid-20th century, fluorescent and metal halide lamps began to replace mercury arc lamps due to better light quality and efficiency. Today, mercury arc lamps are less common but still used in specific scientific and industrial applications. Environmental concerns over mercury's toxicity have led to stricter regulations and a shift towards more eco-friendly lighting options. Despite this, mercury arc lamps played a crucial role in the evolution of modern lighting technology.

High pressure mercury vapor arc-discharge lamps are one of the light sources that can provide higher luminance of any continuously operating light sources, they are capable of providing a brightness in a range of 10 to 100 times higher compared with incandescent lamps. Moreover, these lamps are capable of produce intense illumination for specific wavelength bands as shown in Figure 1. These

lamps, combined with the appropriate filters, can be used to excite a wide range of fluorophores.

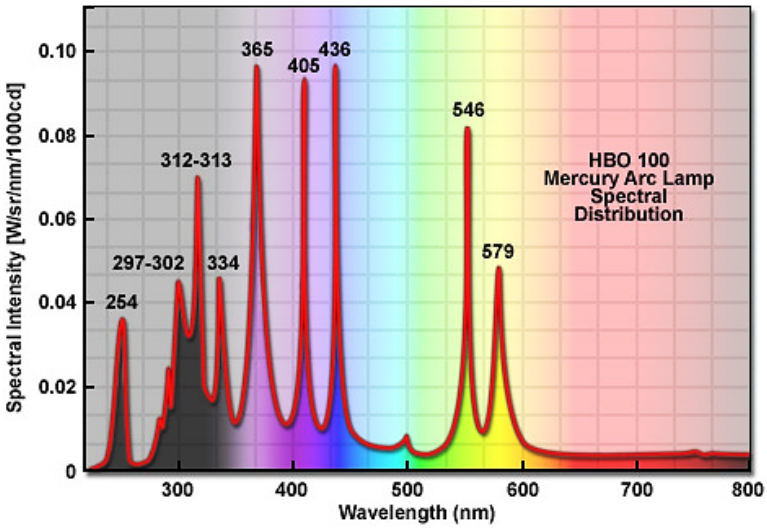


**Figure 1.** Emission profile of mercury arc lamp, with emission present in ultraviolet, blue, green, and yellow spectral regions. Extracted from [22].

A large amount of fluorescent probes were developed for HBOs emission wavelength peaks that are shown in Figure 1, such as Alexia 546 [23] for the 546 nm peak or Marina Blue [24] for the 365 nm peak. These light sources were introduced to the market in 1930s and have been used in many thousands of microscopes. HBO lamps produce among the highest luminance and radiance output levels compared to any other continuous light source used in optical microscopy. Nevertheless, mercury lamps have a significant fluctuation in intensity compared with other light sources, such as LEDs or laser sources. Despite these lamps being much brighter, they had major inconveniences, such as critical mechanical alignment, short lifetime, lack of light homogeneity, necessity of specialized lamphouses and power supplies, higher costs, or potential explosion hazards. But, even with these drawbacks, HBOs still are a golden standard for fluorescence microscopy and are considered one of the best illumination sources.

Mercury arc lamps have been used for fluorescence microscopy during almost all the existence time fluorescence detection and imaging has been used. There are examples in the literature of using mercury arc lamps for fluorescence microscopy back to the early 1900s. For example, in [25], that was published in 1933, a microscope for fluorescence analysis using a mercury arc lamp is described. The

microscope allows for rapid identification and differentiation of substances with different chemical compositions by their emission bandwidth. K. Saito *et al.* [26] developed a multi-point scanning confocal microscope. In this work, they use a mercury arc lamp to replace lasers, since they strongly restrict the choice of fluorescent dyes because only a limited amount of laser lines can be introduced into a confocal system.

#### 2.1.1.2. Xenon arc lamp

Xenon arc lamps were developed in the 1940s and quickly became popular due to their ability to produce a bright, white light similar to daylight. These lamps work by creating an arc between two electrodes in a xenon gas-filled bulb, producing a continuous spectrum of light. They found early use in movie projectors and searchlights because of their high intensity and excellent color rendering. Over the decades, xenon arc lamps have been improved for greater efficiency and longevity. Today, they are widely used in various applications, including automotive headlights, cinema projectors, and scientific instruments. Xenon arc lamps are valued for their stability and intense brightness, making them essential in fields that require precise and powerful illumination. Despite advances in LED and laser technologies, xenon arc lamps remain a crucial tool in high-intensity lighting applications.

As mercury arc lamps, XBO show a similar behavior when talking about luminance. XBO is one of the brightest light sources that can be found when operating continuously. Moreover, xenon arc lamps are a very similar approach to the ideal model of a punctual light source. The emission profile of xenon arc lamps, in contrast with mercury arc lamps, is a large uniform and continuous spectrum at the visual region. Its emission profile features a color temperature of around 6000 K, similar to sunlight, and has no prominent emission lines. This makes XBO more suitable for applications in quantitative fluorescence microscopy.

XBO lamps were introduced to the scientific community in the late 1940s. XBO lamps' lifetime is higher than those of similar HBO lamps, but they have a drawback. The majority of their emission (75%) falls into the infrared spectral region, and only 25% of the optical power is emitted in wavelengths above 700 nm. Moreover, only 5% of the emission spectrum is above 400 nm, which highly

restricts the fluorophores that can be excited by a XBO lamp. Due to this spectral emission distribution (Figure 2), XBO is more suitable for applications where multiple fluorophores in a wide range of wavelengths needs to be analyzed, rather than in applications where a specific fluorophore is being detected.

Xenon arc lamps have been standard in fluorescence microscopy, particularly in applications requiring a continuous emission pattern. These lamps are widely used due to their ability to provide a stable and consistent light source, crucial for detecting a wide range of fluorophores. In 1973, L. Enerbäck *et al.* [27] developed a device able to perform cytofluorometry. The device can detect several fluorophores during short (ms) and long (minutes) illumination periods. XBO) were chosen for this device due to their long lifespan and continuous emission spectrum, which are essential for such precise measurements. L.A. Thomson *et al.* [28] conducted a comparative study of various light sources for incident immunofluorescence microscopy, concluding that XBO lamps provide sufficient brightness to detect samples diluted up to 32 times more than with similar HBO lamps and other halogen sources. This enhanced detection capability is attributed to the higher emission power of XBO lamps across the continuous spectrum, as depicted in Figure 2. Moreover, xenon arc lamps offer significantly higher power emission in the infrared spectrum, with prominent peaks at 827, 885, 919, 980, and 992 nm, as shown in Figure 2. This characteristic was leveraged by H. Puchtler *et al*. [29] to develop an infrared fluorescence microscopy technique for stained tissues, demonstrating the broader application potential of these lamps in specialized microscopy setups. These examples were chosen to highlight the unique advantages of xenon arc lamps in fluorescence microscopy, showcasing their critical role in enhancing detection sensitivity and expanding the range of detectable wavelengths.

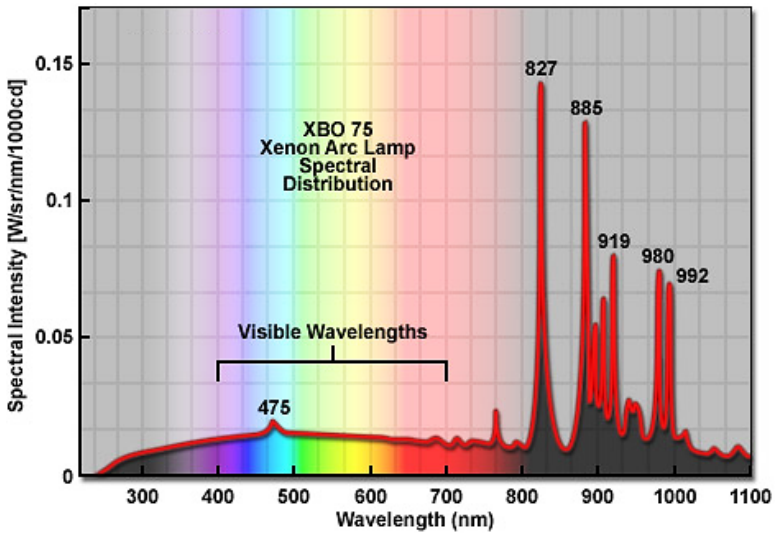


**Figure 2.** Emission profile of xenon arc lamp, where it can be found the continuous emission spectra from 300 to 700 nm and the near infrared emission lines. Extracted from [30].

Furthermore, nowadays in conventional fluorescence microscopy, even with the recent appearance of white light lasers and LEDs that are prone to substitute the arc lamps, they still have room for competition. Fluorescence microscopy needs high photon-flux densities in the sample plane that only can be provided by some light sources, such as lasers, LEDs and arc lamps. However, when using lasers and LEDs, the excitation wavelengths are limited to a narrow spectrum, while arc lamps have a continuous emission distribution, where the user can select the desired wavelength lines or wavelength regions depending on the application.

### 2.1.1.3. Metal Halide lamp

Metal halide arc lamps were developed in the 1960s as an advancement over mercury vapor lamps. These lamps produce light by passing an electric arc through a mixture of metal halides and mercury vapor, resulting in high efficiency and excellent color rendering. They quickly became popular for their bright, white light and were widely used in stadiums, street lighting, and industrial settings. Over time, improvements increased their efficiency and lifespan, making them suitable for a broader range of applications. Today, metal halide lamps are valued for their powerful illumination and are used in sports arenas, large indoor spaces, and horticulture. Despite competition from LED and other lighting technologies,

metal halide lamps remain important for applications requiring high-intensity, high-quality light.

Metal Halide light sources work similar to the other arc lamps. When an electrical arc passes from its electrodes and through a gaseous solution, it emits light. In the case of MH lamps, the electrical gas goes through a mix of gases, which normally include mercury, xenon or argon, and a variety of metal halides, which are obtained from combining halogen with a metal.

MH arc lamps that are of more use for fluorescence microscopy are the ones that use mercury among the metal halides. This makes the emission spectra to be like the HBO lamps including its spectral lines with additional higher emission levels in the continuous regions that fall between those lines. The emission spectrum has up to 50% greater intensity between peak illumination bands, allowing for the excitation of a wider range of fluorophores. The emission spectra compared to one of the HBO lamps is shown in Figure 3. Metal halide lamps offer significant advantages over mercury arc lamps. They have a much longer lifespan, often exceeding 1,500 hours, and come with pre-attached reflectors, eliminating the need for alignment [31].

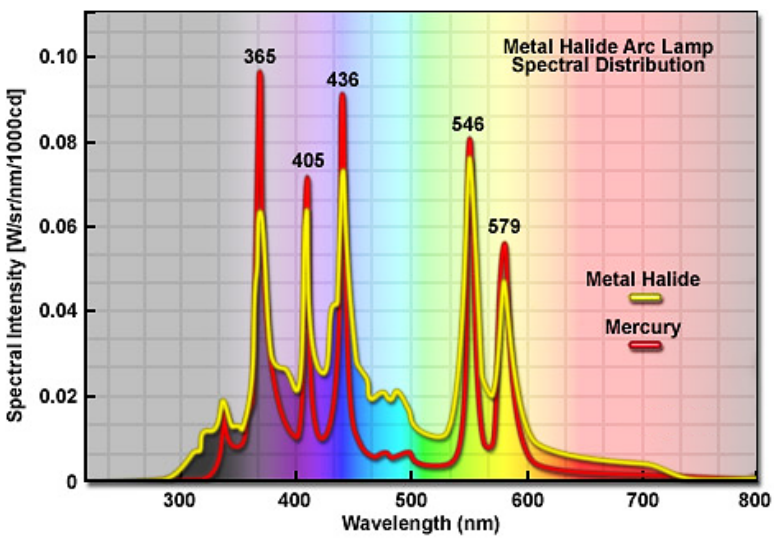


**Figure 3.** Emission profile of metal halide arc lamp compared to those of the HBO arc lamp where it is observed that MH lamps have the same emission lines with lower power but a more continuous emission between the lines. Extracted from [32].

As shown in Figure 3Figure 3, over half of the light emitted by the arc, approximately 55 percent, falls within the ultraviolet and visible wavelengths between 350 and 700 nanometers. The spectral lines in metal halide lamps, which result from elemental excited state transitions in mercury vapor, occur at 365, 405, 436, 546, and 579 nanometers (see emission peaks in Figure 3). This makes these light sources highly efficient for imaging fluorophores specifically designed for excitation by mercury arc lamps. The higher radiation levels in off-peak regions, combined with the superior temporal stability of metal halide lamps, make these sources more effective than mercury arc lamps for imaging fluorophores excited in the 480 to 500 nanometer range. It can be observed that the main differences between a MH lamp and an HBO lamp are that the MH lamp has lower power emission in the peaks in exchange for higher power emission in the continuous spectrum. This comparison can be observed in Figure 3, where the emission spectra for both lamps is shown. Additionally, metal halide lamps are better suited than mercury lamps for quantitative imaging of radiometric dyes.

MH lamps have been used in several microscopes. For instance, W. D. Brighton *et al.* [33] studied the usage of a 250 W C.S.I lamp, which is a mercury arc lamp with added metal halides, in their 1972 study. They found that metal halide arc lamps perform better than traditional mercury arc lamps, particularly at the 495 nm wavelength where mercury lamps have relatively low emission. Specifically, MH lamps provide six times more optical power than mercury lamps in this wavelength range. Additionally, due to their lower UV emission, MH lamps are safer for observing living cultures.

### 2.1.2. Lasers

Lasers, short for Light Amplification by Stimulated Emission of Radiation, are devices that emit coherent, intense beams of light. They rely on a gain medium, energy source (pump), and optical cavity with mirrors to amplify light through stimulated emission. Laser light is monochromatic, coherent, and highly directional, making it invaluable in numerous scientific and technological applications. Lasers are used in diverse fields including spectroscopy, microscopy, telecommunications, and materials processing, due to their precise control and unique properties. Gas and solid-state lasers are two common types, each offering specific advantages and applications. Despite their complex operation, lasers have

become indispensable tools in research, engineering, and everyday life, shaping advancements across various disciplines.

The first conceptual design of the laser was done by Albert Einstein in his 1916 proposal, where he defined that photons could stimulate emission of identical photos from excited atoms [34]. But it was not until 1928 when Rudolf Ladenburg reported indirect evidence of this theory [35]. However, it was considered of little practical importance by his contemporaries. It was not until May 16$^{th}$, 1960, that Theodore Maiman built the first laser. It was a ruby laser [36]. It was built with the coil of a photographic flashlamp and introduced a small rod of ruby inside, all of this enclosed in a reflective cylinder. After this discovery, several lasers appeared. Peter Soroking and Mirek Stevenson built a similar laser using a rod of calcium fluoride doped with uranium, making it the first four-level laser [37].

Another key discovery was semiconductor diode lasers. In early 1953, John von Neuman wrote about the possibility that semiconductors could produce stimulated emission, but it was not published until more than 30 years later [38]. After the invention of the first Light Emitting Diodes, GaAs LEDs cooled to liquid nitrogen [39], led to Robert N. Hall and his colleagues at the General Electric R&D laboratory in Schenectady, New York to develop the first GaAs diode laser [40]. Although diode lasers represented a significant advancement, the early models were wide area homojunction devices that required cooling to liquid nitrogen temperatures and powerful current pulses to function. It took several more years for these lasers to achieve continuous operation at room temperature, a crucial capability for most practical applications. It was not until 1969 when Zhores Alferov developed the first continuous room-temperature operating diode laser [41]. Alferov won the 2000 Nobel prize for the heterojunction discovery, which was shared with Herbert Kroemer, who developed a similar laser diode a few weeks later in the USA [41].

The high bandwidth lasers can achieve is another important characteristic. In 1964, Willis Lamb demonstrated that modelocking a laser could produce pulses whose duration was limited by the Fourier transform of the bandwidth [41]. Using passive modelocking on a continuous-wave laser, Erich Ippen and Charles Shank initially created 1.5-ps pulses [42], and subsequently achieved subpicosecond pulses with kilowatt-level peak power [43]. This sparked extensive research into producing even shorter pulses through a combination of pulse compression and

spectral broadening. This line of work reached a milestone in 1987 when Richard Fork's team at Bell Labs generated 6-fs pulses using pulse compression and phase compensation techniques [44]. The advent of ultrafast pulses paved the way for new types of spectroscopies. Winifred Denk, J. H. Strickler, and Watt Webb concentrated femtosecond red or IR pulses to such a high intensity that a sample could simultaneously absorb two or more photons to excite fluorescence, but only during the brief peak intensity of the pulse [14].

Laser devices emit light across the ultraviolet, visible, and infrared regions of the electromagnetic spectrum. Ultraviolet radiation, with wavelengths between 180 and 400 nm, is utilized in UV lasers. Visible light, spanning from 400 to 700 nm, encompasses the colors perceptible to the human eye. The infrared region, extending from 700 nm to 1 mm, is employed in IR lasers. The specific color or wavelength of light emitted by a laser depends on the laser material employed. For instance, a Neodymium:Yttrium Aluminum Garnet (Nd:YAG) crystal emits light at a wavelength of 1064 nm. Table 1 outlines various lasing materials and their associated wavelengths. It's noteworthy that certain materials and gases can emit multiple wavelengths, with emitted light wavelengths determined by the laser's optical setup.

**Table 1.** Commonly used lasers and their emission wavelengths.

| Laser type | Wavelength (nm) |
|---|---|
| **Argon Fluoride** | 193 |
| **Xenon Chloride** | 308 and 459 |
| **Xenon Fluoride** | 353 and 459 |
| **Helium Cadmium** | 325 – 442 |
| **Copper Vapor** | 511 and 578 |
| **Argon** | 457 – 528 |
| **Frequency doubled Nd:YAG** | 532 |
| **Helium Neon** | 543, 594, 612 and 632.8 |
| **Krypton** | 337.5 – 799.3 |
| **Ruby** | 694.3 |
| **Laser Diodes** | 630 – 950 |
| **Ti:Sapphire** | 690 – 960 |
| **Nd:YAG** | 1064 |
| **Hydrogen Fluoride** | 2600 – 3000 |
| **Carbon Monoxide** | 5000 – 6000 |

Lasers provide several compelling advantages over other light sources for fluorescence applications, such as microscopy. Additionally, for other applications such as PoC, where compactness is important, laser diodes are highly

useful because they offer high integration capabilities along with the benefits of lasers. These advantages primarily arise from the unique properties of laser light, including coherence, monochromaticity, high intensity, and directionality, which collectively enhance the performance and reliability of fluorescence-based techniques. One of the foremost advantages of lasers is their coherence, which allows for highly focused illumination. In fluorescence microscopy, this enables precise excitation of fluorophores within a small focal volume, reducing background noise from out-of-focus light [45–47]. This enhancement in the signal-to-noise ratio is crucial for achieving high-resolution images, especially in confocal and two-photon microscopy, where optical sectioning and deep tissue imaging are required. Lasers also emit light at a single wavelength, providing monochromatic illumination, which is particularly critical in fluorescence applications, where specific excitation wavelengths are necessary to selectively excite particular fluorophores. The use of a laser ensures that the excitation light matches the absorption spectrum of the fluorophore precisely, maximizing the efficiency of fluorescence emission and minimizing cross-talk between different fluorophores in multi-color experiments [48,49]. Additionally, the high intensity of laser light is a significant advantage. Lasers can deliver intense, concentrated light to excite fluorophores efficiently, resulting in strong fluorescence signals even from weakly fluorescing samples. This high intensity is particularly beneficial in applications such as single-molecule fluorescence and super-resolution microscopy (e.g., STED [50–52], PALM [53,54], STORM [55–57]), where a high photon flux is necessary to achieve the required resolution and sensitivity. The directionality and collimation of laser beams further enhance their utility in fluorescence applications. These properties ensure that light can be directed precisely to the area of interest without significant divergence, providing uniform illumination across the sample. This uniformity is essential for quantitative fluorescence measurements and ensures consistent excitation across the entire field of view in wide-field microscopy. Moreover, lasers offer precise temporal control over light emission, enabling the use of pulsed laser systems. This temporal precision is essential for time-resolved fluorescence techniques, such as FLIM [58,59] or Point of Care applications [60].

Moreover, for PoC diagnostics, the compact and efficient design of diode lasers allows for the development of portable and robust devices. These lasers can be integrated into compact fluorescence detection systems, offering the high

sensitivity and specificity required for rapid and accurate diagnostics at the point of care. Furthermore, lasers provide consistent and stable light output over extended periods, essential for reproducibility in fluorescence measurements. Unlike other light sources, such as mercury or xenon arc lamps, lasers do not suffer from significant intensity fluctuations or require frequent replacements, making them more reliable and cost-effective in the long run. Despite that, lasers are an expensive component and in recent years, applications using LEDs are emerging to replace the use of those with laser devices.

### 2.1.3. LEDs

The development of LED technology has come a long way. The phenomenon of electroluminescence was first observed in 1907 by H.J. Round of Marconi Labs. He noticed that silicon carbide crystals emitted a dim yellow light when a current was applied. This marked the beginning of the exploration into light emission from semiconductors [61]. However, it was Oleg Losev, a Russian scientist, who significantly expanded on this discovery in the 1920s. Losev observed light emission from zinc oxide and silicon carbide diodes and published several papers on the subject, laying the groundwork for future developments in LED technology [62]. Unfortunately, his research was ignored at that time. The real breakthrough in LED technology came in the early 1960s. In 1962, Nick Holonyak Jr., working at General Electric, developed the first practical visible-spectrum LED. Holonyak's LED emitted red light and was significantly more efficient than previous attempts, making it the first usable LED for practical applications[63]. This innovation marked a significant milestone, as LEDs began to find use as indicator lights in electronic devices due to their low power consumption and long operational life.

In the 1970s and 1980s is when we can find significant advancements in LED technology, particularly in the materials used to produce them. Researchers developed LEDs in various colors by using different semiconductor materials. Gallium arsenide phosphide (GaAsP) and gallium phosphide (GaP) were instrumental in producing red, orange, and green LEDs [64,65]. The ability to produce LEDs in multiple colors expanded their use beyond simple indicators to more complex displays and lighting applications. Furthermore, a major breakthrough occurred in the early 1990s with the development of high-brightness

blue LEDs by Shuji Nakamura at Nichia Corporation. Nakamura's use of Gallium Nitride allowed for the production of blue light, which was previously difficult to achieve with LEDs [66]. The creation of blue LEDs was pivotal because it enabled the production of white light LEDs by combining blue LEDs with yellow phosphor. This development expanded the application of LEDs to general lighting and displays, making them a viable alternative to traditional incandescent and fluorescent lighting.

The design of LEDs for different emission spectra culminated in the development of white LEDs. This marked a significant turning point for LED technology. White LEDs are created by coating a blue LED with yellow phosphor, resulting in light that appears white to the human eye. This innovation made LEDs suitable for a wide range of lighting applications, from residential and commercial lighting to automotive and street lighting [67–69]. White LEDs are known for their high energy efficiency and long lifespan, which have driven their adoption in various industries focused on sustainability and energy conservation. Throughout the late 1990s and early 2000s, continuous improvements in LED efficiency, brightness, and manufacturing processes reduced the cost of production and increased the accessibility of LED technology. Advances in semiconductor fabrication techniques and materials science have enabled the production of LEDs that are brighter, more efficient, and more durable than ever before [70,71]. These improvements have made LEDs the preferred choice for a wide range of applications, from consumer electronics to large-scale lighting installations.

Another key benefit of LEDs is their positive environmental impact. LEDs consume significantly less energy than traditional incandescent and fluorescent bulbs, resulting in lower greenhouse gas emissions and reduced energy costs. Additionally, LEDs have a much longer operational life, reducing the frequency of replacements and the associated waste. These factors make LEDs an environmentally friendly lighting option, contributing to global efforts to reduce energy consumption and combat climate change.

Today, LEDs are ubiquitous in modern technology. They are used in a wide range of applications, including display technology (such as televisions, smartphones, and computer monitors), automotive lighting, traffic signals, and architectural lighting. LEDs are also crucial in medical devices, scientific instrumentation, and horticultural lighting, where their efficiency and precision offer significant

advantages. The versatility and reliability of LEDs have cemented their role as a fundamental component of modern electronics and lighting. Especially, LEDs have revolutionized biological microscopy and fluorescence applications due to their numerous advantages over traditional light sources such as mercury and xenon arc lamps. These advantages span across various critical parameters, including spectral properties, energy efficiency, longevity, and control over illumination, making LEDs an indispensable tool in modern biological research.

One of the most significant benefits of LEDs is their precise and customizable spectral output. Unlike traditional light sources, which have broad emission spectra requiring complex filtering systems to isolate desired wavelengths, LEDs can be engineered to emit light at specific wavelengths tailored to the excitation of various fluorophores used in fluorescence microscopy [72]. This precise spectral control allows for efficient excitation and better separation of emission signals, reducing background noise and improving signal-to-noise ratios [73]. It can be seen some examples of emission spectra of LEDs in Figure 4. Moreover, in Table 2 are shown some LEDs that are used for fluorescence microscopy. There is shown the LED color and the fluorophores it excites among with the wavelengths of excitation and the Full Width at Half Maximum (FWHM) of the LEDs. The FWHM emission spectra of the LEDs is around 15-20nm, even not being as narrow as laser emission, it is narrow enough for a wide range of fluorescence applications.

Energy efficiency is another crucial advantage of LEDs. They convert a higher proportion of electrical energy into light rather than heat, significantly reducing energy consumption compared to traditional arc lamps [74]. This efficiency not only lowers operational costs but also minimizes heat production, which is vital for preserving the integrity of biological samples during microscopy. Excessive heat can cause sample degradation and photobleaching, compromising the quality and reproducibility of experimental results. Additionally, the operational lifespan of LEDs far exceeds that of traditional light sources. LEDs typically last for tens of thousands of hours, compared to a few hundred hours for mercury lamps and a few thousand hours for xenon lamps [75]. This extended lifespan reduces the frequency of replacements, thereby lowering maintenance costs and minimizing downtime in laboratory settings. Consistent and stable illumination over long periods is essential for reproducible and reliable experimental outcomes.

Moreover, LEDs offer superior stability and control over illumination parameters. They can be rapidly switched on and off, allowing for precise timing in fluorescence imaging and minimizing photobleaching of samples [76]. This rapid switching capability is particularly advantageous in time-lapse imaging and high-speed applications. Furthermore, LEDs provide adjustable intensity and spectral tuning, enabling researchers to optimize illumination for different fluorophores and experimental conditions, a level of control difficult to achieve with traditional light sources [77].

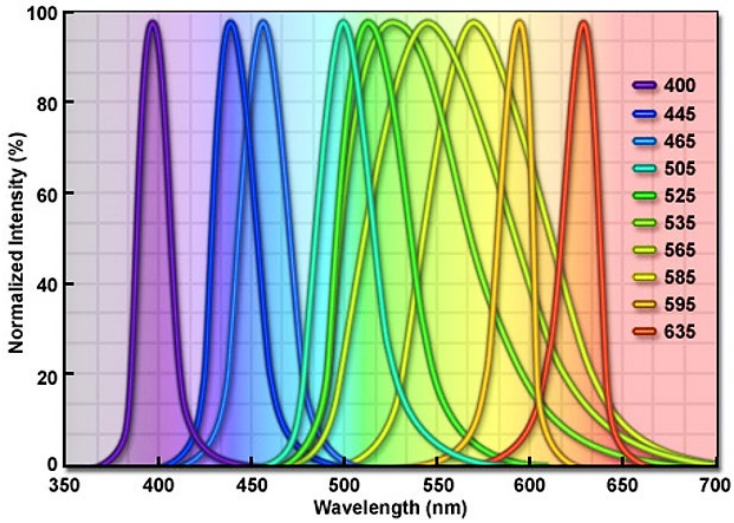


**Figure 4.** Spectral emission of LEDs. The spectra were recorded at the microscope objective focal plane using a broadband mirror positioned in a fluorescence optical block. Extracted from [78].

**Table 2.** LEDs organized by emission color and the fluorophores they excite, presented among their excitation wavelength and the FWHM bandwidth.

| Fluorophore excitation spectra | Wavelength of excitation (nm) | LED FWHM Bandwidth (nm) |
|---|---|---|
| **Ultraviolet (DAPI, BFP)** | 400 | 393-408 |
| **Cyan (ECFP)** | 445 | 433-453 |
| **Blue (EGFP, Cy2, AF488)** | 465 | 449-473 |
| **Blue-Green (EYFP)** | 505 | 491-520 |
| **Green (AF532)** | 525 | 503-539 |
| **Green (TRITC, Cy3, AF546)** | 535 | 503-573 |
| **Green-Yellow (TRITC, Cy3)** | 565 | 515-594 |
| **Green-Yellow (TRITC, Cy3)** | 565 | 515-594 |
| **Yellow (TR, MitoTracker)** | 585 | 547-613 |
| **Orange (TR, mCherry)** | 595 | 587-604 |
| **Red (Cy5, AF635)** | 635 | 620-637 |

# 2. Light sources for biomedical applications

LEDs are particularly beneficial for advanced imaging techniques such as super-resolution microscopy, optogenetics, and live-cell imaging. In super-resolution microscopy, precise control over LED illumination is essential for achieving the high spatial resolution required [79]. LEDs' ability to provide stable and uniform illumination across the field of view enhances the quality of super-resolution images. In optogenetics, where light is used to control genetically modified cells, the ability to deliver specific wavelengths with high precision is crucial. LEDs' rapid switching and wavelength specificity make them ideal for this application, allowing for precise temporal and spatial control of light stimulation [80,81].

For all of that, LEDs have established themselves as a superior light source for biological microscopy and fluorescence applications. Their precise spectral properties, energy efficiency, long operational lifespan, and enhanced control over illumination parameters make them a perfect fit to substitute all the other light sources.

LED technology has come a long way, and two main technologies have appeared derived from LEDs, inorganic LEDs, or GaN microLEDs, and OLEDs.

OLEDs emerged as a transformative technology in the field of display and lighting applications due to their unique properties, such as thinness and flexibility. Unlike traditional LEDs, which rely on inorganic semiconductors, OLEDs utilize organic molecules that emit light in response to an electric current. This distinction allows OLEDs to offer superior contrast ratios, wider viewing angles, and more vivid colors, making them highly desirable for next-generation displays and lighting solutions [82].

The structure of an OLED typically consists of multiple layers, including a substrate, an anode, organic layers (comprising the emissive layer, conductive layer, and others), and a cathode. The color of the emitted light is determined by the specific organic materials used in the emissive layer, which can be tuned to produce red, green, blue, or even white light [83]. The basic structure of an OLED cell [84] consists of a stack of thin organic layers placed between a conductive anode and a conductive cathode. The substrate, which serves as the foundation of the OLED, can be made from plastic, glass, or metal foil. The anode, which is positively charged, injects holes (or electron deficiencies) into the organic layers and may be transparent depending on the type of OLED. Directly above the anode

is the Hole Injection Layer (HIL), which receives the holes from the anode and pushes them deeper into the device. The next layer, the Hole Transport Layer (HTL), facilitates the movement of holes towards the emissive layer. The emissive layer, which is the core of the device, is where light is produced by converting electrical energy into light; it contains a color-emitting material (the emitter) doped into a host material. To improve the efficiency of OLEDs, a Blocking Layer (BL) is often included, which helps to confine electrons in the emissive layer. The Electron Transport Layer (ETL) helps move electrons toward the emissive layer. Finally, the cathode, which is negatively charged, injects electrons into the organic layers and, like the anode, may or may not be transparent depending on the OLED type. This arrangement of layers is critical for the functionality and performance of OLED devices. as illustrated in Figure 5.

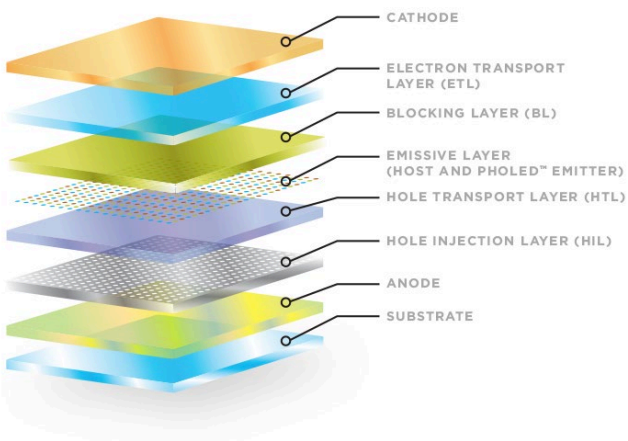


**Figure 5.** Schematic of a typical OLED construction [84].

One of the most significant advantages of OLED technology is its ability to be fabricated on flexible substrates, enabling the development of flexible and even rollable displays. This flexibility, combined with the potential for high energy efficiency and low power consumption, positions OLEDs as a key technology for a wide range of applications, from smartphones and televisions to wearable devices and solid-state lighting [85].

However, despite their advantages, OLEDs face challenges such as limited operational lifetimes, particularly for blue emitters, and sensitivity to moisture and oxygen, which can degrade performance over time. Ongoing research aims to

address these challenges by developing more stable materials and advanced encapsulation techniques to enhance the durability and longevity of OLED devices [86]. These are areas where microLEDs stand out.

In this work, we will focus on studying the biomedical applications that can be built using GaN microLEDs, a technology that appeared in the 2000s-2010s.

#### 2.1.3.1. GaN microLEDs

Since their inception in the early 1990s, Gallium Nitride based LEDs have undergone remarkable advancements, evolving from laboratory novelties to indispensable components in various lighting and display applications. This evolutionary journey has not only revolutionized the illumination industry but has also paved the way for innovative technologies such as microLED arrays and microdisplays. The outstanding work by Isamu Akasaki, Hiroshi Amano, and Shuji Nakamura in the early 1990s marked a significant milestone in semiconductor physics and optoelectronics. Their groundbreaking research on GaN-based materials led to the realization of efficient blue and green LEDs, overcoming longstanding challenges in materials growth and device fabrication [87]. This breakthrough not only completed the RGB color palette for LED lighting but also laid the foundation for the development of high-density data storage, optical communication, and solid-state lighting [88]. The discovery of p-type doping of GaN, a critical component for the development of efficient LEDs, was a pivotal achievement. This breakthrough enabled the fabrication of p-n junctions in GaN materials, laying the groundwork for the efficient conversion of electrical energy into light. Subsequent advancements in epitaxial growth techniques, such as metalorganic chemical vapor deposition and molecular beam epitaxy, further improved the material quality and device performance [89].

Following the initial breakthrough, decades of intensive research efforts focused on improving the performance, efficiency, and reliability of GaN LEDs. Key advancements include the development of novel epitaxial growth techniques such as metalorganic chemical vapor deposition and molecular beam epitaxy, which enabled precise control over material properties and device structures [90]. Additionally, the introduction of strain engineering, quantum well structures, and defect reduction strategies contributed to significant enhancements in device efficiency and brightness [91]. The evolution of GaN LED technology also

witnessed advancements in device packaging and thermal management techniques. Innovations such as flip-chip bonding, wafer-level packaging, and advanced heat sinks have helped mitigate thermal issues and improve the long-term reliability of GaN LEDs [92,93]. In parallel with the advancements in GaN LED technology, the concept of microLEDs began to gain traction in the early 2000s. MicroLEDs are characterized by their miniature size and high pixel density, which promised breakthroughs in display technology by offering superior brightness, contrast, and energy efficiency compared to conventional display technologies [94]. Initial challenges such as epitaxial transfer, pixel uniformity, and mass production scalability were gradually addressed through innovative fabrication techniques and materials engineering [91,95].

The development of microLED arrays requires precise control over epitaxial growth, device fabrication, and assembly processes. Techniques such as selective area growth, metal-assisted chemical etching, and transfer printing have been employed to achieve high-resolution microLED arrays with uniform pixel characteristics [96]. Furthermore, advancements in wafer bonding, interconnection technology, and color conversion layers have enabled the realization of full-color microLED displays with excellent color fidelity and brightness uniformity [97]. The microLED fabrication process involves several techniques, including photolithography, electron beam lithography, dry and wet etching, and dielectric and metal evaporation. As illustrated in Figure 6, the process can be broadly categorized into four main steps: (a) insulation layer deposition, (b) pixel opening, (c) wiring, and (d) etching to expose the n-buffer, which serves as the common n-contact [98].

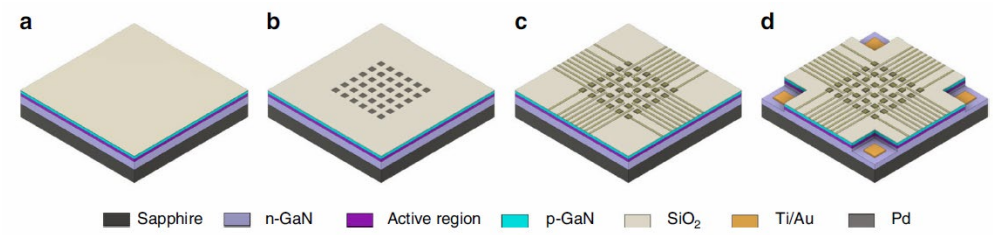


**Figure 6.** Steps in the fabrication process of the MOGaN nanoLED array include: (a) deposition of an SiO2 insulation layer on the p-GaN LED surface; (b) dry etching of the SiO2 layer to create pixel openings and subsequent filling of these openings with a thin palladium (Pd) film; (c) patterning of the p-contact lines using a Ti/Au deposition; and (d) deep etching and metallization for the n-contacts [98].

# 2. Light sources for biomedical applications

Recent years have witnessed significant progress in microLED array technology, fueled by advancements in epitaxial growth, transfer printing, and integration methodologies. State-of-the-art microLED displays boast pixel densities exceeding 1000 pixels per inch, enabling ultra-high-resolution applications in virtual reality, augmented reality, and wearable electronics [99–102].

Despite the tremendous progress achieved in MicroLED technology, several challenges remain to be addressed. These include improving the yield and throughput of microLED fabrication processes, enhancing the reliability and stability of microLED devices, and reducing the manufacturing cost of MicroLED displays [103].

The more basic structure that can be used for biomedical imaging and diagnosis are single microLEDs. For example, several microLEDs arranged in a line combined with electrodes are used for neuroimaging, where they are employed to study brain activity and neurological disorders. H. Yasunga *et al.* [104] have developed a neural probe (Figure 7) with six microLEDs and 15 neural electrodes for optogenetic applications. In this study a neural probe was fabricated and tested in cortical tissue of mice, indicating that these neural probes are useful tools for in vivo optogenetics diagnosis. E. Ko *et al.* [105] developed a flexible probe for long-term chronic deep-brain studies, formed by 12 individually operated microLEDs and 32 recording electrodes. In this study they demonstrate the reliability of the device by recording and modulating hippocampal neurons of a freely moving mice for over 8 months.

Another field where single microLEDs are used is in PoC technology. In [106], H. Robbins *et al.* designed a PoC solution (Figure 8) using a single GaN microLED with a a-Si:H fluorescence sensor to detect fluorescence from a streptavidin R-phycoerythrin conjugate bounded with biotinylated antibody-coated microbeads in a microfluidic channel.

# 2. Light sources for biomedical applications

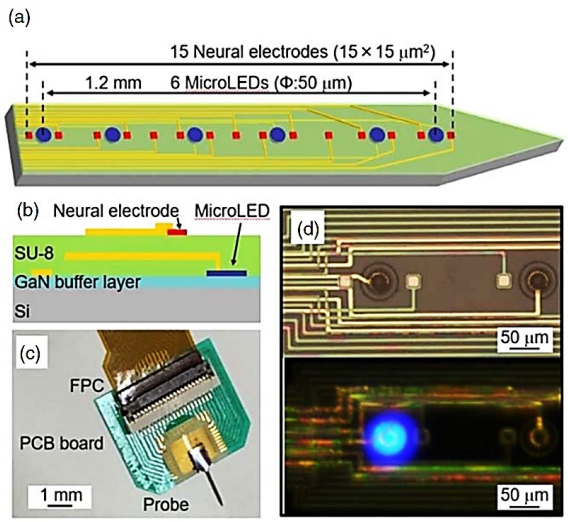


**Figure 7.** Probe developed by H. Yasunga *et al.* extracted from [104]. In (a) they show a 3D schematic. The cross-section of the probe containing the integrated microLEDs and neural electrode probe is shown in (b). A photograph of the neural probe mounted on a PCB (c) and an optical microscope image of a neural probe before and during LED operation (d).

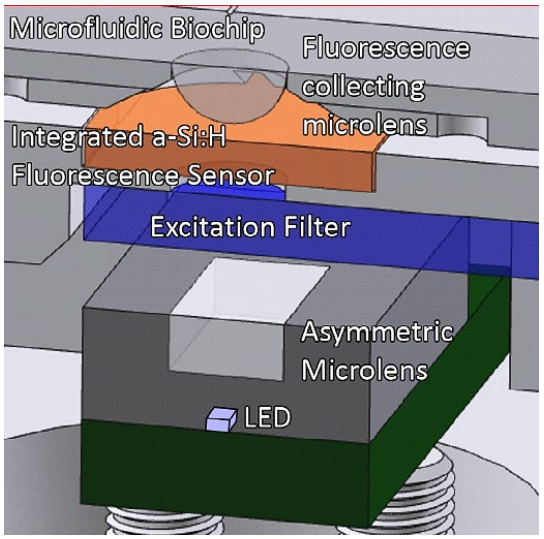


**Figure 8.** Cross-section view of the whole microLED integrated with the a-Si:H fluorescence detection sensor of the PoC designed by H. Robbins *et al.* [106].

But what had more impact for scientific applications and specifically for biomedical research was microLED arrays. These arrays can be categorized by the way they are driven or by the way they are designed and addressed. When

categorizing them based on the driving mechanisms, there are two types of arrays, each one offering unique advantages and challenges:

- **Active Matrix microLEDs:** Active Matrix (AM) microLEDs employ thin-film transistor (TFT) or Complementary Metal-Oxide-Semiconductor (CMOS) backplanes to individually address each microLED pixel [107]. This approach allows for precise control over each pixel's brightness and color, enabling high-resolution displays with excellent image quality and uniformity. Active matrix microLEDs are commonly used in high-end displays, including televisions, monitors, and virtual reality headsets.
- **Passive Matrix microLEDs:** Passive Matrix (PM) microLEDs utilize row and column lines to address and control the pixels [108] Unlike active matrix microLEDs, passive matrix arrays do not require thin-film transistors for pixel control, making them simpler and more cost-effective to manufacture. However, passive matrix displays may suffer from limited brightness, lower refresh rates, and potential cross-talk between adjacent pixels.

If we categorize the microLED arrays by how they are designed and addressed, we find two categories:

- **Direct Addressable microLEDs:** Direct Addressable (DA) microLEDs (Figure 9 a) feature individually addressable pixels, allowing for precise control over each pixel's state without the need for complex addressing schemes [98]. Direct addressable arrays offer flexibility and scalability, making them suitable for applications requiring high-resolution, real-time control, such as head-up displays (HUDs), smart mirrors, and digital signage.
- **Matrix Addressable microLEDs:** Matrix Addressable (MA) microLEDs (Figure 9 b) employ a grid-like structure to address and control groups of pixels simultaneously [109]. This approach reduces the complexity of the driving circuitry while still offering high-resolution display capabilities. Matrix addressable arrays are commonly used in large-scale displays, outdoor billboards, and stadium screens, where high brightness and scalability are essential.

# 2. Light sources for biomedical applications

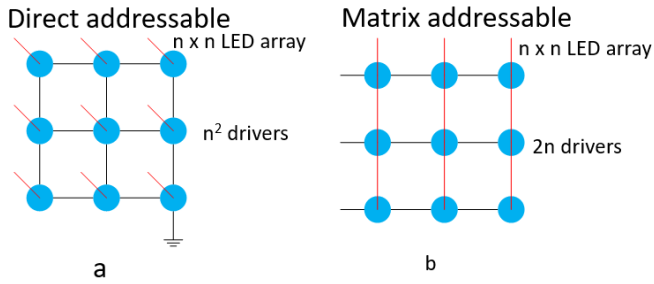


**Figure 9.** Direct addressed (a) and matrix addressed (b) microLED fabrication strategies.

Each type of array has advantages and disadvantages when used for biomedical imaging and diagnosis. One of the most used types of arrays in the state of the art is active matrix with directly addressable LEDs, since they offer high-resolution, high brightness and high bandwidth, which can translate in real-time imaging capabilities. For example, one field where AM DA microLEDs are used for endoscopy. In [110], N. Modir *et al.* describe an endoscopic system capable of the detection of several diseases, including cancer, by using an array of microLEDs capable of provide multiple wavelengths.

Where microLED arrays are gaining more and more attention is in microscopy. S. Li *et al,* [111] demonstrated the use of a microLED-based chromatic confocal microscope with a virtual confocal slit for three-dimensional profiling. In their work, they describe that thanks to the use of microLED arrays instead of a single punctual light source, no mechanical scanning or external light sources are needed. They accomplish to have a scanning area (or field of view) with the microscope of 186 x 167 $\mu m^2$ achieving a lateral resolution of 2.3 µm. Another example of microLED arrays used for microscopy is [112], where V. Kumar *et al.* describe the use of an array of microLEDs, specifically a directly addressable striped microLED display with 100 rows (Figure 10). With this array of 100 rows, they are capable of imaging within a 500 µm think fixed brain slice from a transgenic mouse. With this system they detect oligodendrocytes labeled with a green fluorescent protein (GFP), resulting in an improvement of contrast in reconstructed optically sectioned images.

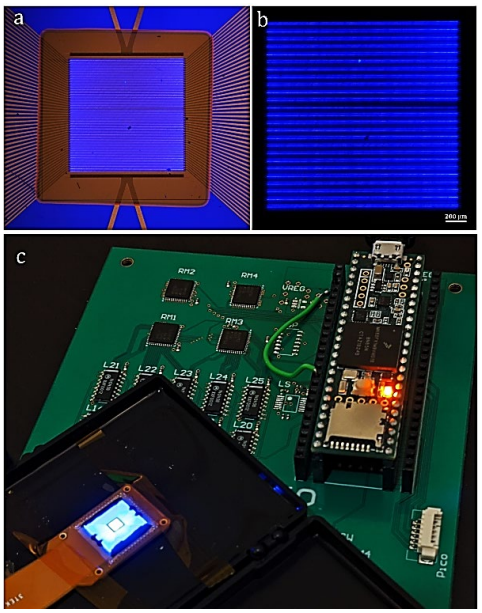


**Figure 10.** The microLED array used in [112] by V. Kumar *et al*. (a) shows the brightfield microstrip display, which consists of 100 lines exhibiting various illumination patterns for the SIM light source. In (b), the darkfield image of the display is shown. The lines measure 2000 µm by 15 µm. The overall size of the display is 2 mm by 2 mm. A photograph of the micro-display along with the rigid control PCB can be observed (c).

Up to this date, the smallest microLEDs achieved were developed by D. Bezshlyakh *et al.* [98], were they achieved to manufacture an array of 32x2 squared nano LEDs with 200 nm side size and 400 nm pitch (Figure 11 b). Also, in that work, they report the manufacture of a nano-LED array of 6x6 squared nano LEDs with 400 nm side size and 800 nm pitch (Figure 11 a).Some of the microscopes presented in this thesis (Section 3.2.5 [113] and Section 3.2.6 [114]) were developed using these microLED arrays, achieving resolutions up to 1.56 µm resolution. Although the resolution depends on the pitch of the LEDs, the articles in this thesis (Section 3.2.5 [113] and Section 3.2.6 [114])) describe the reasons for not achieving it.

# 2. Light sources for biomedical applications

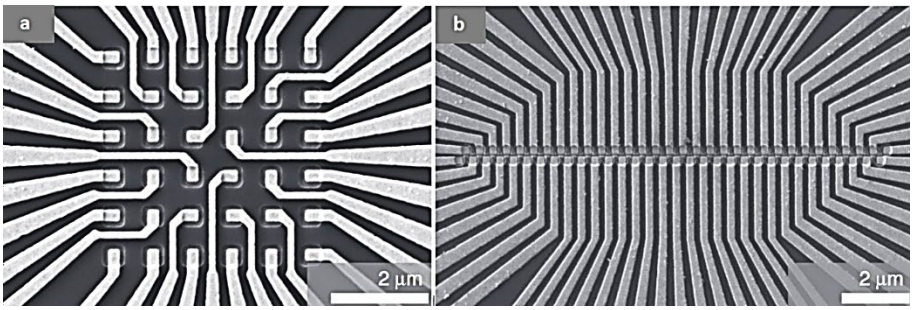


**Figure 11.** Final structures of the two geometries reported by D. Bezshlyakh *et al.*: a 6 × 6 array of 400 nm nanoLEDs and b 2 × 32 array of 200 nm nanoLEDs [98].

### 2.1.3.2. GaN microdisplays

Microdisplays based on GaN microLEDs have rapidly emerged as a transformative technology in the field of high-resolution displays, offering unparalleled performance characteristics that have the potential to revolutionize a wide range of applications. From virtual and augmented reality to wearable devices and advanced optical systems, these microdisplays are at the forefront of display innovation. The integration of GaN microLED technology into microdisplays has been particularly notable due to the inherent advantages of GaN materials, including high brightness, excellent efficiency, and superior durability.

A significant advancement in the development of GaN microdisplays is the use of GaN-on-Si substrates [115]. This approach leverages the cost-effectiveness and scalability of silicon wafers while maintaining the exceptional optoelectronic properties of GaN. The compatibility of GaN with silicon manufacturing processes also facilitates the integration of microLEDs with CMOS circuitry, enabling the development of advanced active matrix microdisplays.

One of the most significant achievements in this field is the development of high-density active matrix microLED displays, which utilize thin-film transistors or CMOS technology to individually control each microLED pixel. This precise control over pixel brightness and color makes active matrix microdisplays suitable for high-performance applications, including augmented reality headsets and head-up displays [116,117]. For instance, researchers have demonstrated active matrix microLED microdisplays with resolutions exceeding 1000 pixels per inch (PPI), showcasing their potential for ultra-high-definition applications [118].

GaN-on-Si microdisplays also offer significant advantages in terms of thermal management and device reliability. The superior thermal conductivity of silicon substrates helps dissipate heat more effectively, which is crucial for maintaining the performance and longevity of high-brightness microLEDs [119].

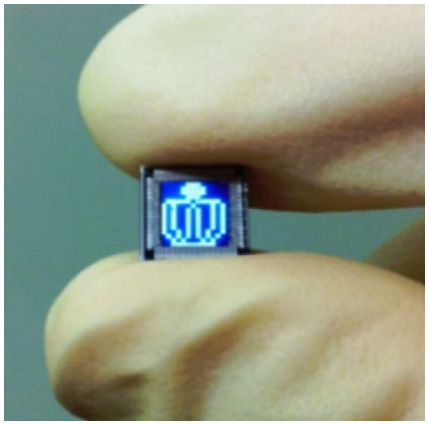

**Figure 12.** Example of a blue microdisplay for wereable applications [120].

Recent advancements have focused on overcoming the remaining challenges related to mass production, pixel uniformity, and integration of GaN-on-Si microdisplays with existing electronic systems. Novel pixel architectures and scalable transfer printing methods are being explored to enhance the manufacturability and performance of these microdisplays [121,122].

As the research and development of GaN-on-Si microdisplays continue to progress, they are poised to become a dominant technology in the display market, offering unparalleled performance for next-generation visual applications. The combination of high brightness, excellent efficiency, and compatibility with silicon manufacturing processes ensures that GaN-on-Si microdisplays will play a crucial role in the future of high-resolution, high-performance display technologies.

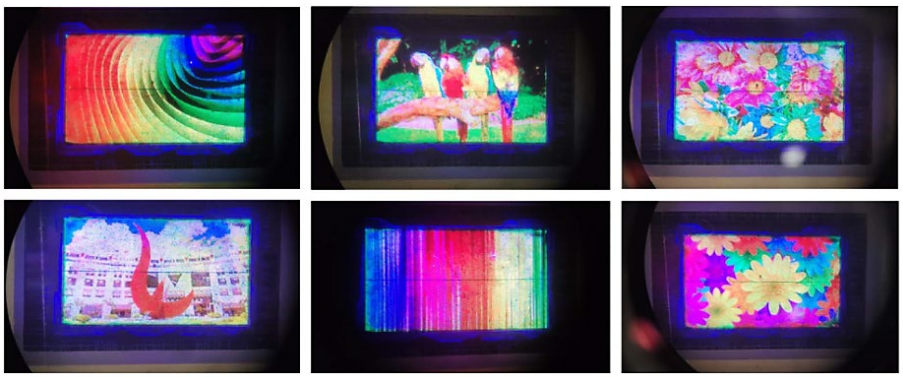

**Figure 13.** A 4-bit full-color GaN-on-Si monolithically integrated microdisplay developed by L. Qi *et al.* [123].

## 2.2. MicroLED drivers

During the last decades, along with the apparition of microLEDs, microLED drivers appeared in order to provide an adequate control for the light emission depending on the application they are used for. The bast majority of micro and nano LEDs are driven by CMOS circuits, and they can be found as a fully integrated circuit driving the LEDs, or as a system formed by different discrete components in a PCB. Historically, there have been two main ways to build a micro-LED array, direct addressing [124,125] and matrix addressing techniques [126–128], as described above. For the control of direct addressing arrays there is one independent driver for every LED, while in the case of matrix addressing arrays, there is only one driver per row and column of the array. So, for a NxN LED array, NxN and 2N drivers are required for direct and matrix addressing, respectively. In direct addressing, as the LED density increases it is more difficult to access the LEDs by wire bonding and then it is usual to have hybrid systems built by flip-chip [116,129] or wafer-to-wafer approaches [130,131]. This increases the integration density capabilities and to achieve lower pixel size, but at the same time, it limits the size of the driver and consequently the quality of the driving. In this respect, matrix addressing is much more flexible, allowing for much larger drivers that can be placed on adjacent chips interconnected by simple wire-bonding. At the end, there is a trade-off between pixel density and pixel size versus driving capabilities.

The functionality of control electronics is also specific to the application. For example, in Near to Eye (NTE) devices, microdisplays need quite low speed, having framerates of some hundreds of fps, and relatively low optical power, with driving currents around 1 μA. Despite this, NTE devices require high integration densities, above 1000 PPI. To achieve structures with high PPI, hybrid integration technology is needed with very small in-pixel drivers.

Although the use of microLEDs in the display field is one of the broadest and most important, there are several other applications where it is necessary to use drivers capable of providing different characteristics, in which the ability to integrate large number of pixels into a device is not as important as having high driving currents and high switching speeds.

For example, for VLC, high bandwidth and precise optical power modulation are crucial for achieving high-speed data transmission. For instance, D. Peng *et al.* [132] designed a driver capable of selecting rows and columns in a matrix-addressable microLED array using a row of current sinks to control the optical power, achieving currents of 20 mA and switching speeds of 1 MHz. Similarly, Z. Wek *et al.* [133] demonstrated a VLC system transmitting at 1.25 Gbps with a current of 4.19 mA, using an amplifier (ZX60-43+) and a bias-Tee (ZFBT-6GW+) with a 5V bias voltage.

In neural stimulation, the primary requirement is the ability to create stable optical power patterns. B. McGovern *et al.* [134] employed a PIC® microcontroller and 32 constant current sources (TB62710) driving the LEDs with 5 mA. Meanwhile, V. Poher *et al.* [135] used 8 programmable voltage sources (MIC5891) to set the patterns and constant current sources (MAX6971) to control the optical power, capable of driving up to 90 mA per LED.

Optogenetic applications necessitate full control over the LED array, including individual control for specific location stimulation and varying light intensities. M. Wang *et al.* [136] described a driver using a constant current source, providing up to 2 mA per LED via an op-amp measuring the current through a resistance, with switching speeds of 100 kHz. For single-point control, they used a shift register memory and a PWM dimming module for fast switching. F. Dehkhoda *et al.* [137] developed a driver using an H-bridge per LED, controlling the supply

voltage through a DAC and a transconductance amplifier (TCA), delivering up to 6 mA per LED.

In fluorescence applications, the light source must provide high optical power with a narrow wavelength directed at the fluorophores. MicroLEDs have demonstrated sufficient wavelength precision and optical power to excite fluorophores with driving currents up to 40 mA [106]. B. R. Rae *et al.* [138] introduced a driver based on an inverter, capable of fluorescence measurements with driving voltages up to 5V and switching speeds in the GHz range.

### 2.2.1. High power microLED drivers

High power microLED drivers are a critical component in the burgeoning field of microLED technology, facilitating the control and management of high-density microLED arrays in applications such as displays, lighting, and biomedical devices. As the demand for higher resolution and more efficient display technologies grows, the development of robust, high-performance microLED drivers has become increasingly important. For example, the capability to provide high power optical power is key for the majority of biomedical applications, furthermore for those requiring fluorescence, since the optical power emitted by the fluorophores is directly related to the one exciting them (Figure 14).

There are several driver designs that take advantage of the high optical power that microLEDs can provide when driven at high currents. For example, E. Xie *et al.* [139] developed a custom CMOS driver based on NMOS transistors for Visible Light Communications (VLC), featuring four independent current-steering digital-to-analog converter (DAC) driver channels with 8-bit resolution. Each channel is capable of sinking a full-scale current up to 70 mA and operates at an electrical-to-electrical modulation bandwidth of 250 MHz. The integration of the μLED array with the CMOS driver involves wire-bonding the array to a commercial ceramic package.

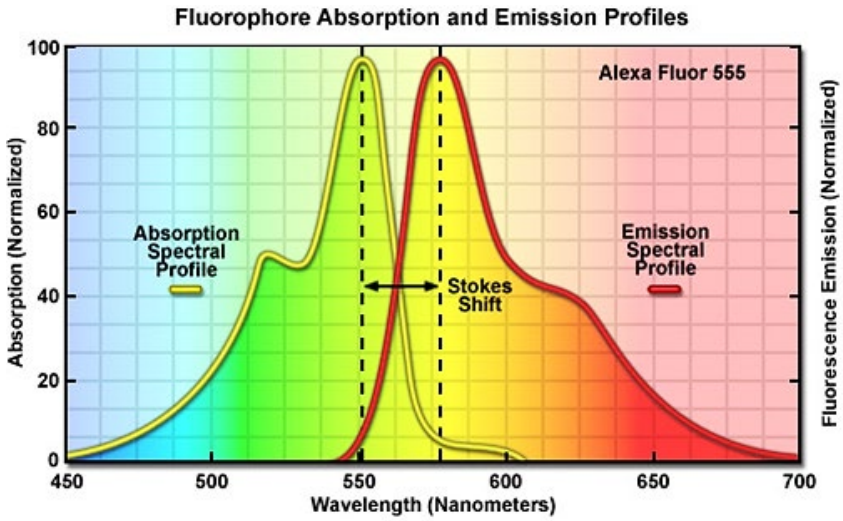


**Figure 14.** This figure illustrates the absorption (blue-green curve) and emission (yellow-red curve) spectra of the fluorophore Alexa Fluor 555. The peak absorption occurs around 555 nm, closely followed by the peak emission at a slightly longer wavelength. Extracted from [140].

M. Zuhdi *et al*. [141] developed a driver able to deliver current up to 360 mA per driver, which is traduced into 8 mW optical power. This circuit is also designed for VLC, where transmission speed is also a key factor. The bandwidth of this circuit is 147 MHz. The whole system consists of an array of 40x10 pixels implemented with a pixel pitch of 100 µm, with an active microLED area of 4 mm x 1 mm. The driver (Figure 15) was designed in Austrian MicroSystems (AMS) foundry in their 0.35 µm technology and consists of two blocks, the addressing and the driving block. The addressing block controls the LEDs that turn on and off and the working modes (continuous wave and pulsed mode). The driving circuit consists of a buffer chain which increases the W/L ratio in order to increase the current the driver can deliver, and a final modified buffer formed by M1, M2 and M3, which are the transistors with the larger W/L ratio.

# 2. Light sources for biomedical applications

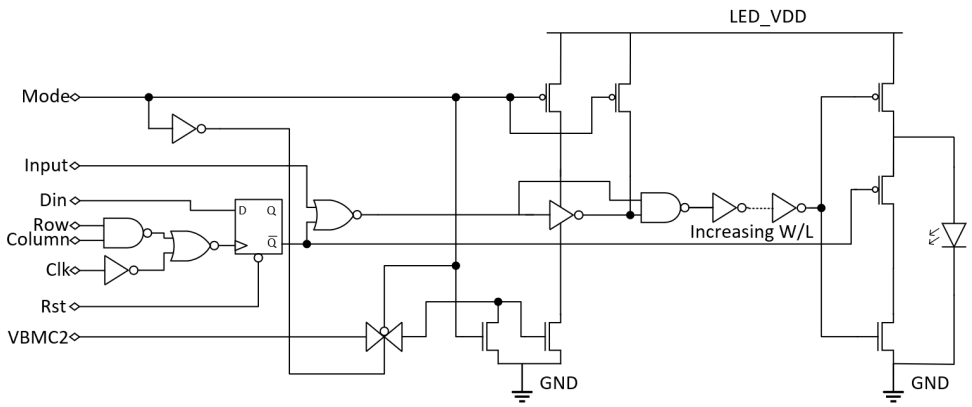


**Figure 15.** Schematic of the microLED driver presented in [141]. In the schematic can be found the addressing logic and the driving circuit.

Another driver able to provide up to 40 mA is the one described by Z. Wei *et al*. [142]. This driver is also designed for VLC and can achieve data transfer rates of 2.74 Gbps. This microLED is directly driven by an RF signal generated by an Arbitrary Waveform Generator (AWG), which is amplified and then combined with a DC bias. This configuration enables the micro-LED to achieve high modulation bandwidth and emit light for data transmission in the downlink of the optical wireless communication system.

P. Tian *et al.* [143] describe the driver used for a blue GaN-based micro-LED in a high-speed underwater optical wireless communication system. The micro-LED driver includes a bias-tee configuration that integrates an RF signal with a DC bias. The RF signal, generated by a pulse patter generator that generates pseudo-random binary sequences, is amplified and combined with the DC bias through the bias-tee to drive the micro-LED. This setup enables the micro-LED to achieve a maximum modulation bandwidth of approximately 160 MHz and currents up to 90 mA.

B. Rae *et al.* [144] describe a driver to be used for fluorescence measurements in which they achieve currents up to 100 mA with 5V bias voltage. The circuit consists of a buffer chain that increases W/L ratio in order to achieve such high current (Figure 16). Moreover, the microLED ground terminal (or cathode) is separated from the ground of the driver circuit, this allowing to drive the LED with more than 5V bias voltage, which is the limit of the CMOS process. The CMOS drivers were designed so they can pulse the micro-LEDs with a minimum pulse

duration of 300 ps, measured as the FWHM. To generate these short pulses, they included a square-wave input signal designated as INPUT_SIG, which is inverted using an inverter (I1), where the pulse width is determined by the delay through the inverter. This delay can be adjusted by the gate voltage, denoted as VBMC2, applied to a current-starving transistor (M1).

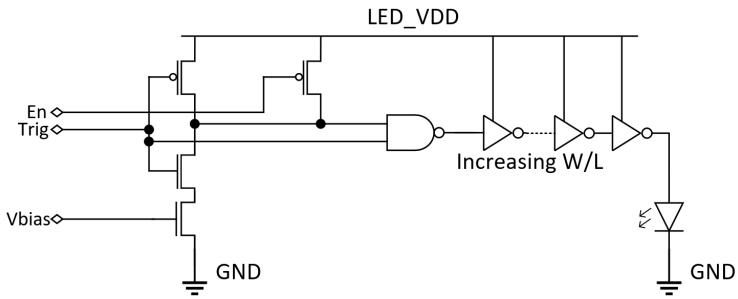


**Figure 16.** LED driver described by B. Rae *et al.* [144]. In the schematic it can be seen the circuit that enables the 300 ps pulses and the buffer chain with increased W/L ratio.

V. Poher *et al*. [135] developed a driver for a neuron stimulation system. This driver (Figure 17) consists of 8 MIC5891 programable voltage sources, that can work at a rate up to 38.000 columns per second, and four constant current sources MAX6971 as current sink drivers. The emitter driving current is adjustable through an external resistor from 4 to 50 mA per emitter, which is modulated by a 10-bit PWM control.

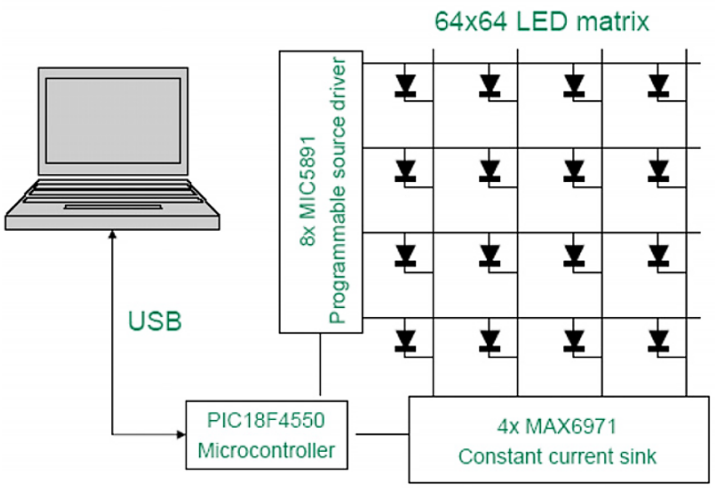


**Figure 17.** Schematic of the microLED driver presented by V. Poher *et al.* [135] where can be observed both the current sinks and the programable voltage driver.

As can be seen, the majority of high-power drivers are designed for VLC, since the strength of the signal impacts directly on the distance the communication can achieve. Nevertheless, driven techniques used for VLC can be used for biomedical measurements. For example, B. Rae *et al.* [144] describe a system with high similarity to the one described by M. Zuhdi *et al*. [141].

### 2.2.2. High speed microLED drivers

MicroLED have the capability of provide high speed optical pulses, achieving bandwidths of up to 800 MHz [90]. This allows the LEDs to be used for several applications such as VLC, or more on the area this work is centered, time-resolved fluorescence. Some of the drivers mentioned in the section above can be also categorized as high-speed drivers. E. Xie *et al.* [139] driver can achieve speeds up to 250 MHz. M. Zuhdi *et al*. [141], that can achieve switching speed up to 150 MHz. These drivers are allowed to high bandwidth speeds by modulating the LED current. But, in the case of B. Rae *et al.* [144], where the time-resolved fluorescence application only needs for a single fast pulse with high period, they achieved to perform a pulse of 300 ps FWHM, which is the narrowest pulse performed with a microLED reported in the literature. There exist more circuits that are able to modulate microLEDs at high speeds, that will be discussed.

H. Chun *et al*. [145] describe a system for VLC, where they encode the bit stream and turn it into a discrete time domain signal through an inverse fast Fourier transform (IFFT) operation and a cyclic prefix addition. Then, they use an AWG, specifically the Agilent N8241A to convert the discrete signal into an analog signal using. This signal is then amplified by a wide-band amplifier, the Mini-Circuits ZHL-6A. A DC bias from a laser driver (LDC205C) is applied through a bias-T, the Mini-Circuits ZFBT-6GW, resulting in the transmission of the modulated intensity. With this driver (Figure 18), they achieve a bandwidth of 531 MHz, with 1.68Gbit/s transmission rate.

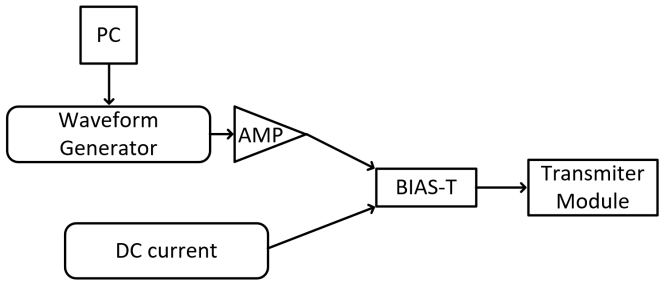


**Figure 18.** Driver used by H. Chun *et al.* [145]. The transmitter module is formed by the microLED and a collimating lens.

There are plenty of examples of high-speed drivers using a waveform generator, and amplificatory and a DC current or voltage bias in VLC drivers. In [146], L. Wang *et al*. achieve speeds of up to 4Gbps, and Z. Wei *et al*. [147] achieve a 2 Gbps data rate using this type of drivers, but further examples can be found in the literature with similar results.

Even most of the drivers for high speed are used in VLC, again B. Rae *et al.* [144] demonstrate that high-speed drivers are of use in biomedical imaging and sensing applications, which is the focus of this work. One of the drivers developed during this thesis was designed to be capable of providing high speed pulses. It was designed to be used for time-resolved fluorescence measurements, both for PoC and for imaging and was used in Section 3.2.6 [114], where its high speed capabilities are not taken advantage, and in Section 3.3.4 [148].

A comparison between the drivers described above is shown in Table 3. As can be observed, this work drives both DA and MA microLED arrays. It improves the

existing works by increasing the maximum driving voltage without decreasing significantly the

**Table 3.** Comparison of different CMOS driver circuits for microLED arrays.

| Reference | [139] | [141] | [142] | [143] | [144] | [145] | This work [148] |
|---|---|---|---|---|---|---|---|
| **Driver type** | DAC - NMOS | CMOS | Discrete | Discrete | CMOS | Discrete | CMOS |
| **Application** | VLC | VLC | VLC | VLC | Fluorescence | VLC | Fluorescence |
| **Max. LED current** | 70 mA | 360 mA | 40 mA | 90 mA | 100 mA | - | 20 mA |
| **LED bias voltage** | 9 V | - | 6.5 V | - | 5 V | - | 10 V |
| **Speed** | 250 MHz | 147 MHz | 2.74 Gbps | 160 MHz | 1 GHz | 531 MHz | 500 MHz |
| **CMOS Tech. Node** | - | 0.35 µm | - | - | 0.35 µm | - | 0.35 µm |
| **Nº of drivers** | 6x6 | 16x16 | 1 | 1 | 16x16 | 1 | 32x2 DA 32x32 MA |

### 2.2.3. Microdisplay drivers

Since the develop of more classic drivers, that are bonded to a PCB and then bonded to the microLED array, was not optimal in order to achieve high PPI arrays, which are needed for the vast range of applications where light sources can be applied, several efforts were made to innovate and enhance integration techniques. From these improvements, classic flip chip bonding was refined to the point that microLEDs in the range of the micrometer could be directly bonded to their drivers and also has been possible to grow directly GaN layers on the silicon substrates. The integration of GaN with Si substrates has unlocked new potential in high-resolution, high brightness displays suitable for applications in augmented reality (AR), virtual reality (VR), and wearable electronics. GaN-on-Si microdisplays combine the superior optoelectronic properties of GaN with the well-established, cost-effective, and scalable silicon platform. Central to the functionality and performance of these microdisplays are the drivers, which manage the operation of the micro-LED arrays.

The first technology developed to build GaN-on-Si microdisplays was constructed by growing GaN layers on Si substrates. Silicon substrates, available in larger diameters and at lower costs, are compatible with standard CMOS (complementary metal-oxide-semiconductor) processing techniques, facilitating the integration of driving electronics and micro-LEDs on a single chip. The typical

architecture involves depositing a GaN epitaxial layer on a silicon wafer using metal-organic chemical vapor deposition or molecular beam epitaxy. Micro-LED arrays are then fabricated through etching processes, creating individually addressable pixels arranged in a matrix configuration for precise control [149]. This matrix addressing is crucial for high-resolution displays, where each LED functions as an individual pixel controlled by the integrated driving electronics.

The other method developed was to flip-chip bond the microLEDs to the CMOS drivers. This is a method where the GaN micro-LED array and the CMOS driver circuitry are fabricated separately and then joined face-to-face through solder bumps or conductive adhesives [115]. This technique provides several advantages, including improved thermal management, reduced parasitic inductance, and enhanced electrical performance due to the short interconnects between the microLEDs and the driving electronics. This technology is still under constant development, but it has already positioned GaN-on-Si microdisplays as promising candidates for the emerging applications [90,116]. The use of GaN-on-Si provides microdisplays with huge density of pixels, accomplished due to the miniaturization of GaN microLEDs, including even microLEDs in the nanometric scales developed recently [18].

To achieve devices with such high pixels per inch (PPI), the area for the CMOS driver is limited to the LED pitch in direct addressing hybrid interconnected displays. Several in-pixel drivers have been developed in recent years. Most of them are based on a 2 transistor 1 capacitor (2T1C) circuit [102,150]. The major advantage of the use of the 2T1C circuit is its simplicity (Figure 19 a). This circuit forms a current sink with a DRAM memory. They allow a high PPI because of the small area of the circuit. However, this type of circuits lacks voltage stability over time, leading to a deterioration of the LED current in the microsecond scale [150]. This deterioration is produced in pixel due to the leakage current of the switch transistor.

Several modifications of the basic driver circuit were presented in the literature. In order to increase the grey levels of a display, a transistor is added to the typical 2T1C circuit (Figure 19 b) to allow PWM dimming [151]. Also, to achieve higher stability times, two extra transistors (4T1C) are added (Figure 19 c), leading to a current degradation in the LED current around 25% of the programmed current in 16 ms [150]. A modification of this circuit that includes the 4T1C structure where

the transistor that fixes the LED current is bulk-driven (Figure 19 d), extends the input data voltage range and improves the performance of the greyscale accuracy [152]. However, in spite of these efforts, the use of a capacitance as an analog storage unit always has leakage over time, making the microLED optical power to have poor stability over time. Thus, it has been always necessary to refresh each frame in the range of microseconds (≥10kHz). Nevertheless, this does not allow the frame to change.

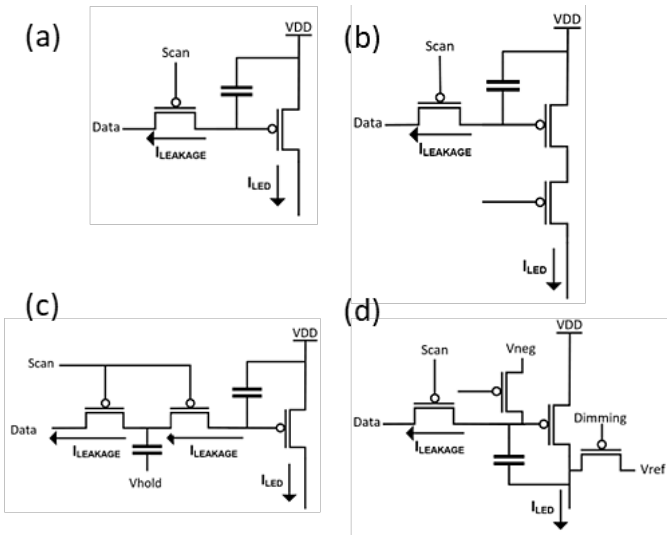


**Figure 19.** The different circuits described are shown. (a) shows the 2T1C standard circuit, (b) shows the circuit described in [151]. (c) is a 4T1C circuit to reduce the leakage current [150] and (d) is a 4T1C circuit with PHM capabilities [153].

Another modification of the circuit (Figure 20) can be found in the literature [154]. In this case the driver exhibits several distinctions compared to a typical 2T1C driver. The driving circuit is designed to ensure high brightness and uniform luminance. This driving circuit operates in two phases: current initialization and LED emission. During the current initialization phase the current is calibrated and stored. In this phase, transistors P5 and P6 are turned ON, while P1 and P2 are diode-connected, forming current mirrors. This configuration prevents errors due to voltage drops and threshold voltage variations in P1 and P2. A column foot DAC provides the appropriate current (IDAC) through P1 and P2, and the voltage $V_{g\,(P1,\,P2)}$ is stored in the parasitic capacitors $C_{GS1}$ and $C_{GS2}$. In the LED emission phase, the LED is turned ON or OFF based on the PWM data stored in the pixel's digital memory. For a logical '1', the LED is turned ON, emitting a luminance

value determined by $I_{DAC}$. The current sources P1 and P2 are cascoded to minimize current variations due to differences in drain-to-source voltages, ensuring uniform luminance, enhancing the performance of the single transistor found in the typical 2T1C circuits. The use of PWM with in-pixel digital memory allows for finer control over the LED brightness levels, enhancing the grayscale performance.

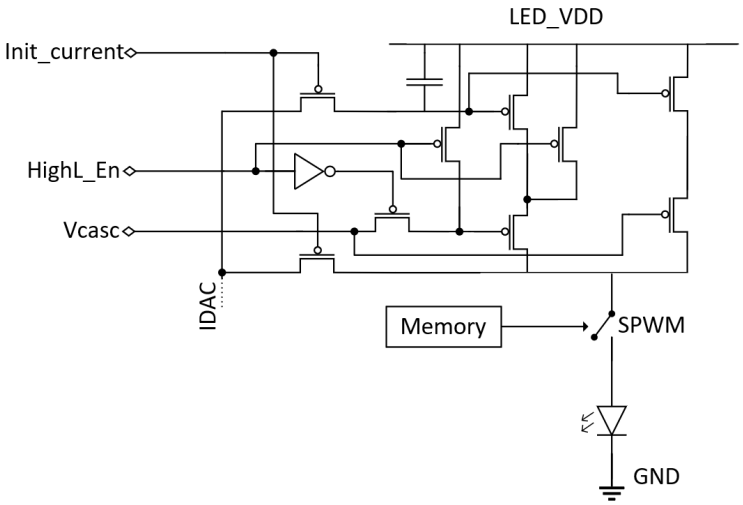


**Figure 20.** Circuit reported by M. Vigier *et al.* [154].

Furthermore, another problem appears with high area displays, especially if the display has a high pixel density. It occurs that there is a voltage drop for the supply lines, which increases as close the pixel is to the center of the array. J. Seong *et al.* [150] propose a pixel circuit with leakage and voltage drop compensation for an array with 5000 PPI or higher (Figure 21). They offer a solution using a 6T2C pixel circuit that combines a low leakage switch structure with an IR drop compensation circuit by configuring the MDRV_N and MDRV_P transistors in such a way that the current through the pixel (ILED) is determined by the gate-source voltages of these transistors. This setup ensures that the current remains stable despite variations in voltage, thereby mitigating the effects of IR drop.

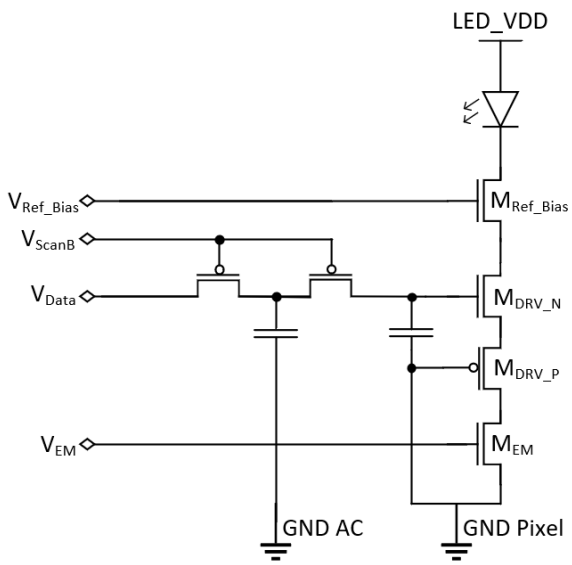


**Figure 21.** Pixel circuit reported by J. Seong *et al.* [150] with leakage and voltage drop compensation for an array with 5000 PPI or higher.

In the last years, some high speed and power microdisplays have been published. The microdisplay backplane developed in this thesis (Section 3.4 [155,156]) was one of them, achieving to drive a microdisplay of 512x512 10 µm LEDs. The backplane allows the microdisplay to switch on and off at a 1 MHz speed with a frame refreshment up to 10 kfps. Moreover, this backplane is, to date and to our knowledge, the one that achieves a higher driving current, up to 120 µA. In parallel, N. B. Hassan *et al.* [157] developed a microdisplay of 128x128 50 µm LEDs which driver allows 83 kfps and currents up to 87 µA. Nevertheless, since in microdisplays the area of the driver is limited to the LED pitch, it is difficult to achieve drivers that allow larger currents and higher framerates [157]. In that work, N. B. Hassan *et al.* introduce a driver with a more advanced architecture tailored for high-speed and high-resolution performance. Unlike the 2T1C driver and its modifications, which are relatively simple, the CMOS driving circuit described involves a more complex pixel architecture. Each pixel in the CMOS circuit is designed to handle higher currents and provide precise control over the micro-LEDs.

The driving circuit incorporates a 5-bit current steering DAC for each pixel. This DAC architecture allows for precise current control through the LEDs, enhancing brightness uniformity and enabling fine-tuned luminance adjustments. This is a

significant upgrade over the simpler charge storage and release mechanism in a 2T1C driver, which lacks such precision. This DAC is formed by 5 Static Random-Access Memories (SRAMs) and 5 transistors with different W/L ratios, which in this case, each transistor has a factor of 2 W/L ratio for each bit, i.e., the transistor controlled by bit 0 is W/L, the transistor controlled by bit 1 is $2^1$ W/L, the transistor controlled by bit 2 is $2^2$ W/L… Moreover, the pixel has a separated current source with 2 mA driving capabilities and a 2-bit in-pixel memory for high-speed pattern toggling.

Table 4 shows a comparison of some of the microdisplays that can be found in the literature. As can be observed, those with higher PPI, used for visual applications, have low current and are not focused on framerates. The table comparison shows how the microdisplay reported in this thesis is the one with higher max LED current bias. Furthermore, compared with the other work that uses SRAMs, this work reports a smaller pixel (from 50 µm pitch to 18 µm) with a minimum loss of properties (1 bit grayscale).

**Table 4.** Comparison of different CMOS driver backplanes for GaN-on-Si microdisplays. Microdisplays used for imaging use a lower frame rate than 100 fps.

| Reference | [154] | [158] | [159] | [99] | [160] | [157] | This work [155] |
|---|---|---|---|---|---|---|---|
| **Driver type** | by column | in-pixel | in-pixel | in-pixel | in-pixel | in-pixel | in-pixel |
| **Resolution** | 1640×1033 | 2560×1536 | 10×40 | 1920×1080 | 8×8 | 128×128 | 512×512 |
| **Pixel pitch** | 9.5 µm | 5 µm | 100 µm | 2.5 µm | 200 µm | 50 µm | 18 µm |
| **Pixel density** | 2677 PPI | 5080 PPI | n.a. | 10000 PPI | n.a. | 508 PPI | 1411 PPI |
| **Frame rate** | n.a. | n.a. | n.a. | 100 fps | n.a. | 83 kfps | 9.15 kfps |
| **Max. LED current** | 5 µA to 20 µA | up to 2 µA | up to 400 mA | 1.6 µA. | up to 100 mA | up to 87 µA | up to 120 µA |
| **LED bias voltage** | 5.5 V | 5 V | up to 8.3 V | n.a. | > 5 V | 5 V | up to 5 V |
| **Color** | Mono/RGB | RGB | Mono | Mono | Mono | Mono | Mono |
| **Grayscale** | 5-bit | 8-bit | n.a. | 8-bit | n.a. | 5-bit | 4-bit |
| **CMOS Tech. Node** | 0.18 µm | 0.18 µm | 0.35 µm | n.a. | 0.35 µm | 0.18 µm | 0.18 µm |

# 2. Light sources for biomedical applications

## 2.3. MicroLED Biomedical applications

MicroLEDs are proving to be a transformative technology in biomedicine, offering enhanced capabilities for imaging, diagnostics, and therapeutic applications. Their small size, high efficiency, and precise control make them suitable for a wide range of biomedical uses, from advanced microscopy to wearable health monitors. As research progresses, the integration of microLEDs into medical devices and systems is expected to expand, further advancing the field of biomedicine. The capability of microLEDs to provide a continuous light intensity for a long lifespan along with their good emission in the blue emission spectrum makes them a perfect candidate for optogenetics. Their high efficiency and scalability make them good candidates for both transmission and fluorescence microscopy. Furthermore, their high bandwidth, along with the scalability and high efficiency, makes them a perfect candidate for all kind of fluorescence measurements, including time-resolved fluorescence.

In the field of optogenetics, K. Kim *et al*. [161] developed an optoelectrode (Figure 22) using microLEDs where they can eliminate stimulation artifacts by using a multi-metal-layer structure with a shielding layer to suppress capacitive coupling. In their work they use transient stimulation pulse shaping to reduce the artifacts below 50 $\mu V_{PP}$ while having a high temporal resolution (< 1 ms) for in vivo experiments.

M. Grossman *et al*.[162] developed a novel two-dimensional photostimulation tool using a 64 × 64 high-power microLED array and demonstrated its proof-of-concept (Figure 23). They described experimental setups for both neural network stimulation and single-cell computation studies. Their results showed that even the lower irradiance spots generated enough power to precisely trigger action potentials and dendritic currents in ChR2-expressing neurons. This matrix photostimulation system is a straightforward yet powerful tool, capable of providing sophisticated spatiotemporal stimulation patterns for investigating neural network dynamics, neuronal disorders, and applications in neural prostheses.

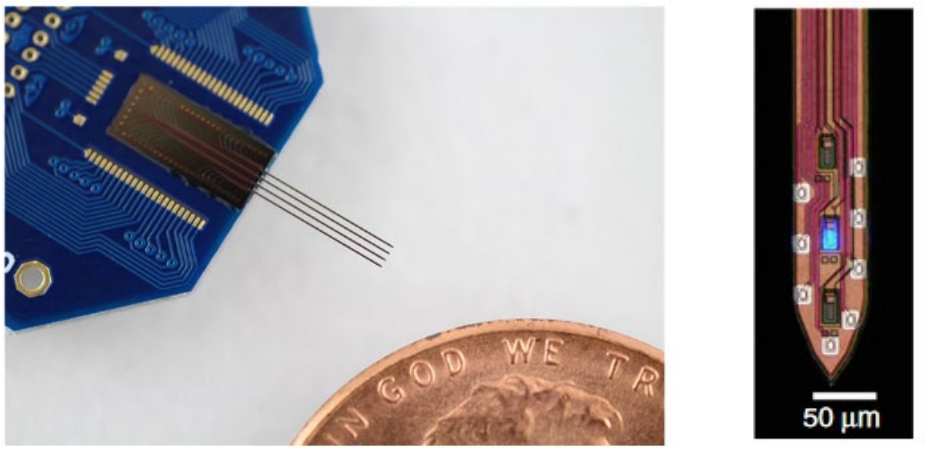


(a) (b)

**Figure 22.** Photograph of the optoelectrodes mounted on a PCB (a) and microphotograph of the tip of a microelectrode containing the microLED (b) reported in [161].

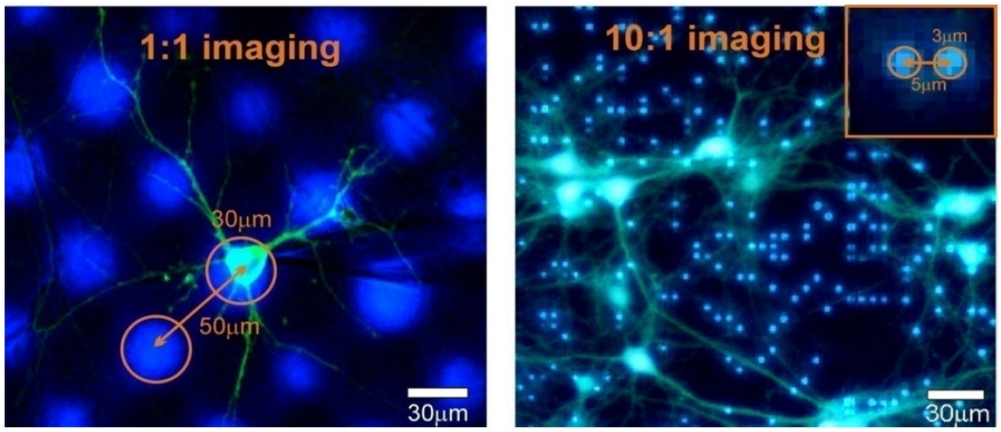


**Figure 23.** An example of brightfield image of microLEDs projected onto neural samples using 1:1 and 1:10 optic configurations obtained using the device reported by M. Grossman *et al.*[162]

Furthermore, J. H. Lee *et al*. [163] analyzes the use of microLEDs for optogenetic applications, in which they state that the work being performed now (which is performed mostly in mice) is pathing the way to the use of this technology in human applications.

Another field where microLEDs are used for biomedicine is phototherapy. M. Zhanghu *et al.* [164] have explored the advantages of microLED technology in this domain, emphasizing its wide spectral range, good monochromaticity, low

power consumption, and high brightness. Their research delves into various applications, such as the development of a phototherapy eye mask (Figure 24) designed to treat periocular fat granules and acne. The mask leverages blue light to stimulate collagen production and enhance blood circulation, thereby improving skin conditions and accelerating the elimination of fat granules. Additionally, they introduced the use of microLED arrays in the treatment of neonatal jaundice, highlighting the technology's ability to deliver targeted phototherapy.

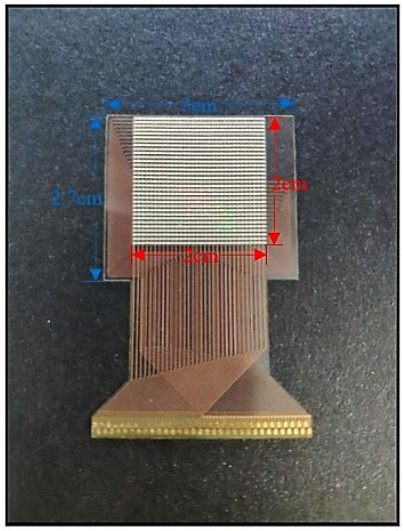


**Figure 24.** Picture of the microLED eye mask reported in [164].

But in this work, our scope is to focus on the use of microLED arrays for their usage in microscopy and PoC applications. In the following subsections there will be presented a study of the state of the art of devices that use GaN microLEDs in microscopy and in PoC applications in order to give context and to compare the achievements accomplish during this thesis with previous, contemporaneous and later research.

### 2.3.1. MicroLED based microscopy

The use of microLEDs for microscopy has been seen as a possibility since their research started. The use of GaN microLEDs as light sources for traditional microscopes and lensless microscopes is a logical step to substitute traditional LEDs.

S. Li *et al.* [111] reported the use of microLEDs for a chromatic confocal microscope. Their approach features a microLED-based system with a virtual confocal slit for three-dimensional (3D) profiling, eliminating the need for mechanical scanning or external light sources. Lateral scanning is achieved using a micro-scale light-emitting diode (microLED) panel array, while axial scanning exploits the chromatic aberration of an aspherical objective. Depth reconstruction accuracy and contrast are enhanced through a virtual pinhole technique. Experimental validation on diamond-turned copper and onion epidermis samples verifies the system's efficacy (Figure 25), highlighting microLED panels as a promising solution for portable 3D confocal microscopy. The study also discusses implications and future directions for advancing microLED technologies in confocal imaging.

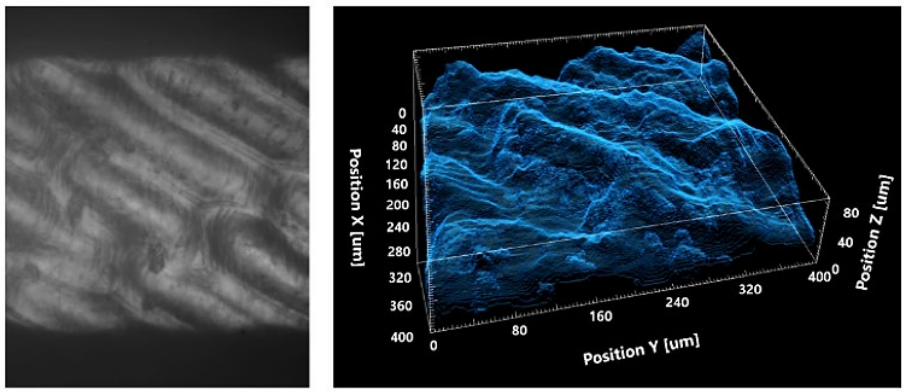


(a) (b)

**Figure 25.** Reconstructed 3D image of an onion epidermis (a) and its volume (b) using the microscope reported by S. Li *et al*. [111].

V. Kumar *et al*. [112] report a microscope that employing microLEDs as a primary light source for optical sectioning structured illumination microscopy (OS-SIM). Traditionally, OS-SIM relies on complex systems like spatial light modulators or digital micromirror devices to generate required illumination patterns, posing challenges in miniaturization for portable systems. MicroLEDs offer a promising alternative due to their inherent brightness and compact size, making them suitable for integrating into compact microscope designs. The study presents a microLED microdisplay featuring a striped configuration with 100 rows. Detailed characterization studies included luminance-current-voltage analysis that confirms the microLEDs' capability to deliver sufficient light output power (up to

3.5 mW at 100 A/cm²) to induce fluorescence in genetically modified brain slice samples. Experimental OS-SIM imaging demonstrated significant enhancements in contrast compared to conventional pseudo-widefield techniques. Specifically, reconstructed optically sectioned images exhibited an 86.92% contrast improvement with OS-SIM, highlighting the microLED array's potential for achieving robust optical sectioning in deep tissue imaging applications. Moreover, the microLEDs emitted at a peak wavelength of 455.56 nm, effectively inducing green fluorescence in PLP-EGFP brain slice samples (Figure 26).

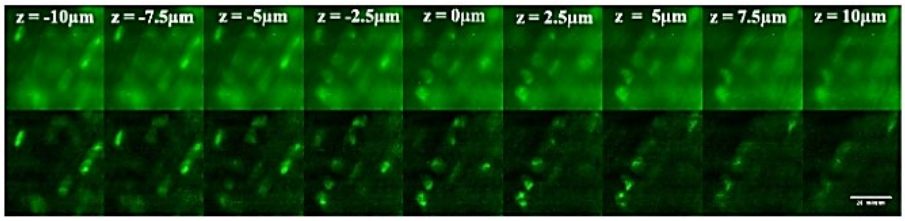


**Figure 26.** Comparison between pseudo-widefield (top) and OS-SIM (bottom) EGFP-PLP brain slice samples. The OS-SIM results were obtained using the microscope reported in [112].

V. Poher *et al.* [165] describe another microscope using a micro-structured stripe-array LED for optical sectioning microscopy (Figure 27 a). The system operates without moving parts and enables the projection of arbitrary line or grid patterns onto specimens. It supports various optical sectioning techniques such as grid-projection structured illumination and line scanning confocal microscopy, facilitating seamless switching between imaging methods without altering the microscope setup. The study provides detailed insights into the design and operation of the micro-structured LED and its driver, along with thorough measurements and calculations of depth discrimination capabilities. These findings underscore the system's efficacy in achieving high-resolution, optically sectioned images with enhanced light efficiency and flexibility in imaging diverse specimens with varying optical properties. Moreover, the micro-structured LED's compact design and intrinsic capability to generate and scan grid or line patterns position it as a promising technology for applications beyond traditional microscopy. Its potential for optically sectioned imaging in endoscopy is highlighted, offering a compact and integrated solution that eliminates the need for external mechanical scanning systems. To support their research, they report images of stained pollen grain with an amplification of 20x (Figure 27 b).

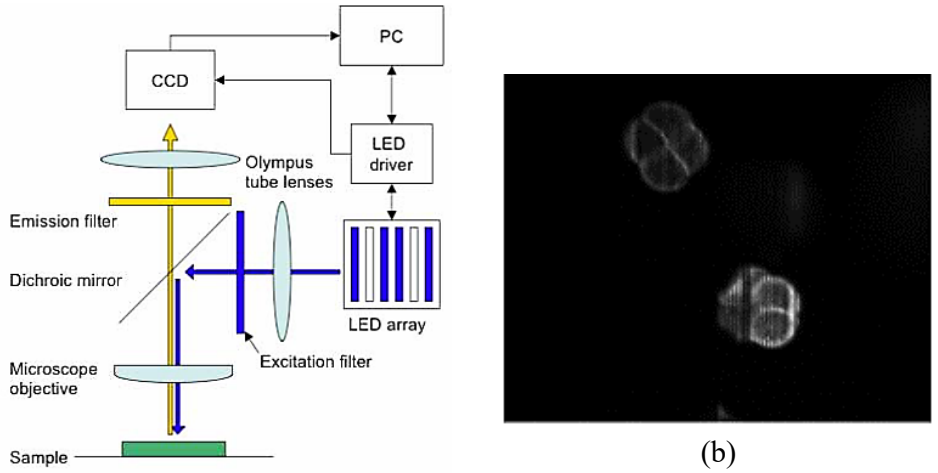


(a) (b)

**Figure 27.** Microscope setup (a) and an image of stained pollen grains acquired with the microscope. Reported by V. Poher *et al.* in [165].

In this thesis we introduce the use of microLEDs for a new type of raster microscope, which is described in Sections 3.2.5 [113] and 3.2.6 [114]. This type of microscope bases their principle in the fact that by decreasing microLEDs size and pitch, one can build a microscope, which special resolution is provided by the light sources size and pitch instead of by the sensor. N. Franch *et al.* [113] developed this pioneer new type of microscopes and reported the technique in February 2020, working with 8 x 8 microLED arrays with 5 µm side size and pitch LEDs. This work accomplished down to 6.4 µm resolution. S. Moreno *et al.* [166] explored the use of lenses and objectives to improve the resolution of this type of microscopes (Figure 28). In this work, a single 200 nm LED was used, which, combined with motors with nanometric precision, simulated a nanoLED array. The use of objectives applied to demagnify the effective spot, and to create an illumination focal point where the sample is allocated, allowed to increase the microscope resolution from 1.6 µm to 790 nm.

# 2. Light sources for biomedical applications

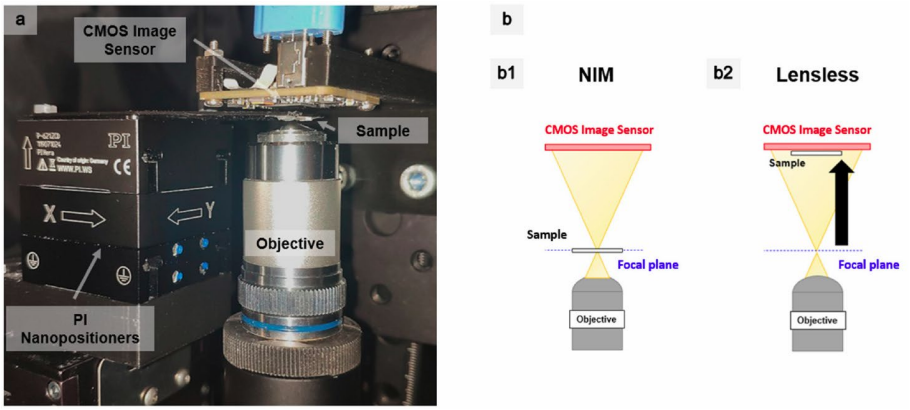


**Figure 28.** Setup of the scanning transmission microscope with demagnification of the LED spot (a) and a comparison between the raster microscope (b1) and a lensless microscope (b2) [166].

Instead of using an array of microLEDs the technology is mature enough to use commercial OLED microdisplays. By using a commercial array of OLED and CMOS camera A. Vilà el al. [167] developed a very compact raster microscope. It was also developed by the same authors a microscope based on a GaN microdisplay with state-of-the-art pixels of 1 μm [168] (Figure 29) demonstrating a resolution of 1.6 μm. Such microscope was demonstrated in raster and holographic modes by A. Vilà in [169]. Almost simultaneously, the interest of chip-sized microscopy motivated another research conducted by E. Prajapati *et al.* [170], where they developed also a lensless holographic microscope using a commercial GaN microdisplay but with lower resolution and FOV (Figure 30). The microscope presented in this work achieves sub-micron half-pitch resolution.

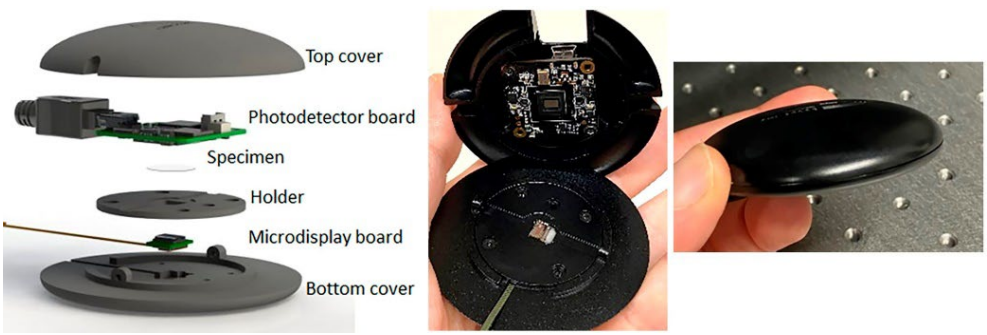


**Figure 29.** Microscope described in [168] and [169]. From left to right, the components of the raster microscope, a photograph of the microscope opened so the components can be seen, and a photograph of the size of the microscope ready to acquire images.

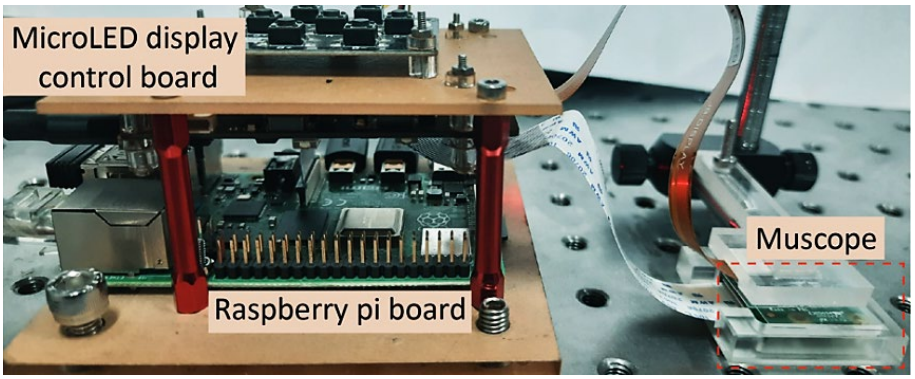


**Figure 30.** Image of the microscope setup reported in [170].

A comparison between existing microscopes is reported in Table 5. Note that this work was published before the others and paved the way for the development of this new microscopic technique.

**Table 5.** Comparison between several microscopes built with microLEDs.

| Reference | [111] | [112] | This work [114] | [166] | [167] | [169] | [170] |
|---|---|---|---|---|---|---|---|
| **Microscope** | Confocal | OS-SIM | Raster | Raster | Raster | Raster Multi-Holographic | Raster |
| **LED array** | microLED | microLED | microLED | microLED | OLED | microLED | microLED |
| **Array type** | DA | DA | DA<br>MA | DA | DA | DA | DA |
| **Array size** | 80 x 72 | 100x1 | 6 x 6<br>32 x 2<br>32 x 32 | 8x8 | 720 x 256 | 1920 x 1080 | 1280 x 720 |
| **LED size** | - | 2mm x 15 µm | 400 nm<br>200 nm<br>20 µm | 5 µm | 5 µm | 1 µm | 2.5 µm |
| **LED pitch** | 25.6 µm | - | 2xLED size | 2xLED size | 5 µm | 2.5 µm | 5 µm |
| **Resolution** | 500 nm | 1.1 µm | 1.6 µm | 790 nm | 1.6 µm | 1.6 µm | 236 nm |
| **FoV** | 31062 $\mu m^2$ | 9225 $\mu m^2$ | 2852 $\mu m^2$ | 10000 $\mu m^2$ | 4.6 $mm^2$ | 12.96 $mm^2$ | 2.5 $mm^2$ |

### 2.3.2. MicroLED based Point-of-Care

Another scope where microLEDs are gaining attention is in PoC devices, thanks to their small size and reduced price. These are key factors that follow what the World Health Organization (WHO) requires for these types of devices. According to WHO, PoC tests considered appropriate for the delivery of healthcare in resource-limited environments should meet the criteria of “ASSURED”, which

stands for Affordable, Sensitive, Specific, User-friendly, Rapid and Robust, Equipment-free, and Deliverable [171,172].

H. Robbins *et al*. [106] developed an integrated fluorescence sensor by coupling a thin film Si fluorescence sensor with a GaN microLED. This compact fluorescence detection module is designed for PoC microfluidic biochemical analysis. The module consists of a SiO2/Ta2O5 multilayer optical interference filter and a hydrogenated amorphous silicon pin photodiode. The integration with a GaN microLED, which features a small size and an asymmetric microlens, enables a focal spot diameter of approximately 200 µm for the excitation light. The sensor demonstrated a high limit of detection (36 nM) for fluorescein solution in a microfluidic channel. Despite the lack of LED light directionality, the system successfully detected fluorescence from a streptavidin R-phycoerythrin conjugate bound to biotinylated antibody-coated microbeads trapped in the microfluidic channel, showcasing its potential for biochemical PoC testing applications.

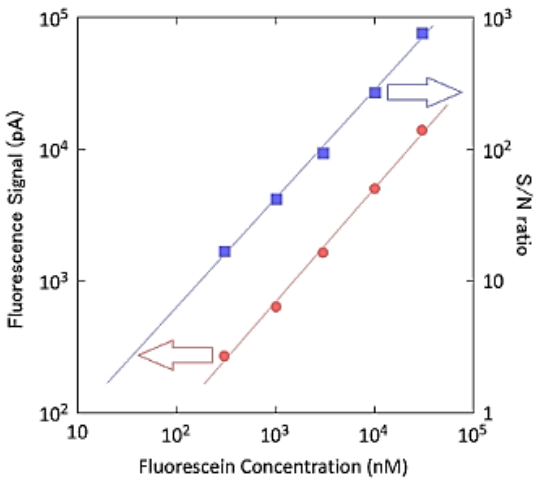


**Figure 31.** Fluorescence signal detected related to the concentration and SNR at a LED power of 100 µW using the PoC device reported in [106].

F. Farrell *et al.* [173] developed a novel micro-LED waveguide for fluorescence applications, presenting a significant advancement in PoC diagnostics. Their work introduces a one-dimensional micro-LED array coupled to a polymeric waveguide for the evanescent excitation of fluorescent analytes on its surface. This innovative setup demonstrated proof-of-concept detection of semiconductor nanocrystals with high sensitivity, reaching concentrations as low as 0.2 pM/cm². The device

leverages the principle of total internal reflection fluorescence to minimize background noise from autofluorescence. The micro-LED array, consisting of ten pixels, each one with a size of 100 x 100 μm². The microLEDs serve as the excitation source, while a PDMS membrane acts as the waveguide due to its high transparency and compatibility with microfluidic structures. Fluorescent measurements were performed using red-emitting colloidal quantum dots deposited on the waveguide. The resulting fluorescence was captured by a CCD sensor, and the data showed a linear relationship between pixel intensity and QD concentration at lower levels.

F. Arshad *et al.* [174] developed another microLED-based total internal reflection fluorescence device (Figure 32 a). This device leverages the properties of micro-LEDs, using them as the excitation source instead of traditional laser diodes. This integration allows for efficient light coupling without the need for intermediate optics, significantly simplifying the design and reducing the overall size of the device. The device employs a glass microscope slide as the waveguiding platform, ensuring high transparency and excellent optical properties necessary for effective detection. The waveguide excites fluorescent analytes on the surface, leveraging the evanescent wave generated by total internal reflection to minimize background noise from autofluorescence and enhance detection sensitivity. By coupling the waveguide with a smartphone camera, the system allows for portable and accessible diagnostic testing. The smartphone detection setup provides a convenient and cost-effective means to capture and analyze fluorescence signals, making the technology highly suitable for PoC applications, where there is a need for rapid, accurate, and portable testing solutions. The platform's high sensitivity, down to a detection limit of 8 nM (Figure 32 b), and specificity enable early detection of diseases, which is critical for timely intervention and treatment (Figure 32 b).

(a)

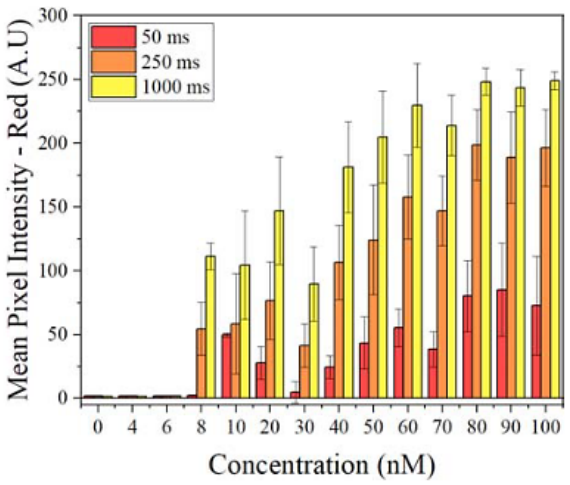


(b)

**Figure 32.** Photograph of the smartphone used to detect fluorescence produced by the quantum dots on the glass surface while being excited by the microLED array (a) and a comparison of the detected intensity by the pixels for different concentrations with 50, 250 and 1000 ms exposure time (b).

A PoC was developed during the development of this thesis, that will be presented in further detail in Section 3.3.4 [148]. This PoC consists of an array of 32x32 matrix addressable microLED array and was tested for both intensity and time-resolved fluorescence measurements. This device is able to detect QD605 (QdotTM 605 ITKTM Streptavidin Conjugate Kit, n.d.) and QD705 (QdotTM 705 ITKTM Amino (PEG) Quantum Dots, n.d.) at

concentrations down to 1/4 µM. As shown in Table 6, the PoC developed in this work is the only capable of performing both intensity and time-resolved fluorescence measurements to our knowledge. It also provides the major number of microLEDs in an array, that are distributed in a 32x32 matrix addressable array.

**Table 6.** Comparison between the different PoC built with microLEDs.

| Reference | [106] | [173] | [174] | This work [148] |
|---|---|---|---|---|
| **LED type** | microLED | microLED | microLED | microLED |
| **Array type** | 1 single LED | 1x10 DA | 1 x 10 DA | 32 x 32 MA |
| **Fluorescence measurements** | Intensity | Intensity | Intensity | Intensity and time-resolved |
| **Concentration** | 0.3 – 3 µM | 0.2 – 100 $pM/cm^2$ | 8-100 nM | 0.25 – 1 µM |

# 3.

# Results

In this section the results that fulfill the objectives of this work are summarized. The first section would describe the microLED drivers developed for each platform, explaining each one in detail. The circuit that controls precisely the bias voltage in a large range (from mA to μA) is described first. Then, the driver that is able to generate fast pulses for Direct Addressing arrays is exposed. The third driver described is the one developed to be used in Matrix Addressable arrays, also with high-speed capabilities. To end, the microdisplay backplane is presented along with the results obtained.

The second section explores the results obtained in microscopy using Direct Addressable microLED arrays. Then, the following section would be about the use of Matrix Addressable microLED platforms for fluorescence PoC devices, using both intensity and time-resolved fluorescence. In the last section, the GaN-on-Si platform developed is presented and characterized.

# 3. Results

## 3.1. MicroLED drivers

### 3.1.1. Precision bias current driver

This driver was designed in order to explore the potential of microLED arrays to develop a new type of raster microscope. Thus, precise control over the driving bias current, with the flexibility to operate across a wide range of currents, was essential. This broad range of current control is crucial for investigating the behavior and capabilities of microLEDs in microscopic applications. The ability to finely adjust the current allows for the optimization of light output, which is vital for high-resolution imaging. Even minor variations in illumination can significantly affect the quality and accuracy of the observed data. This level of precision is particularly important in applications like fluorescence microscopy, where consistent light delivery enhances the detection of subtle biological processes.

The microLEDs are driven by a precise current circuit, implemented using discrete components on a Printed Circuit Board (PCB). Each driver circuit consists of a current source, an eight-channel analog demultiplexer to select the LED to which the current is directed, and a bipolar transistor to enable or disable the selected LED (Figure 33). Each circuit is responsible for driving one row of the LED array, and this setup is replicated eight times to control the entire array. This configuration allows for the simultaneous driving of up to eight LEDs, one per row, if desired.

The current source provides a very stable output current between 27 µA and 3 mA, selected by the value of the variable resistor ($R_{VAR}$) that follows the equation (1).

$$I_{out} = \frac{0.617}{R_{VAR}} + 15\ \mu A \quad \textbf{(1)}$$

The variable resistor is an 8-bit digital potentiometer with 256 possible values from 60 Ω to 50.06 kΩ, allowing to vary the current driven to each LED to, for example, compensate different emission levels.

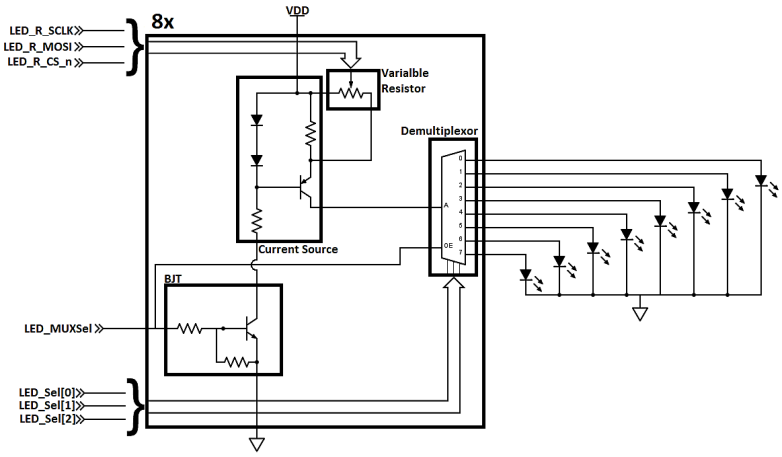


**Figure 33.** The schematic of the driving circuit consists of a current source, an 8-bit variable resistor to select the driving current, an ON/OFF BJT switch and an 8 channel demultiplexor.

The driving circuit was integrated into the PCB shown in Figure 34. In the bottom side (a) are most of the ICs of the circuit, as well as a connector to select the current and which LED is turned on from an FPGA. The top side of the PCB (b) is where the microLED array is connected.

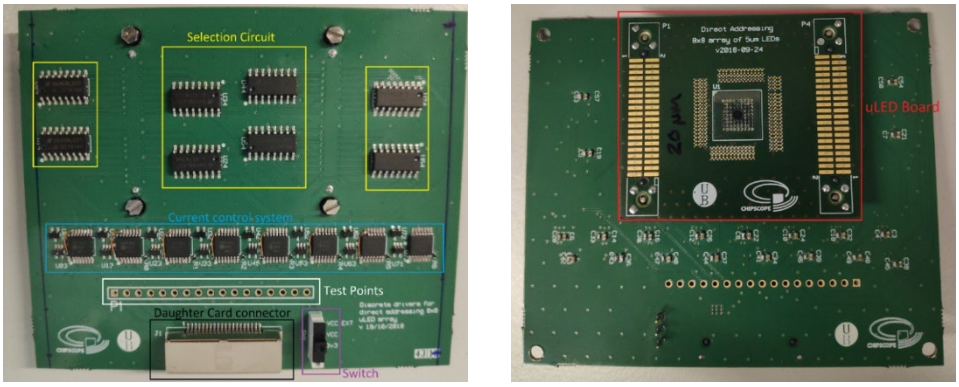


(a) (b)

**Figure 34.** Picture of the implemented PCB with the LED driving circuit for the driving of the 8x8 microLED array. (a) is the bottom side, where the different ICs that drive the LEDs are integrated and (b) is the top side, where the microLEDs are connectedIn Figure 35 examples of the resulting microLED emission can be observed. Three microLED microscopic images are shown, with the microLED A1 driven at a current of 500 µA (a), the same microLED driven at 27 µA (b) and microLED E5 driven at 27 µA (c).

# 3. Results

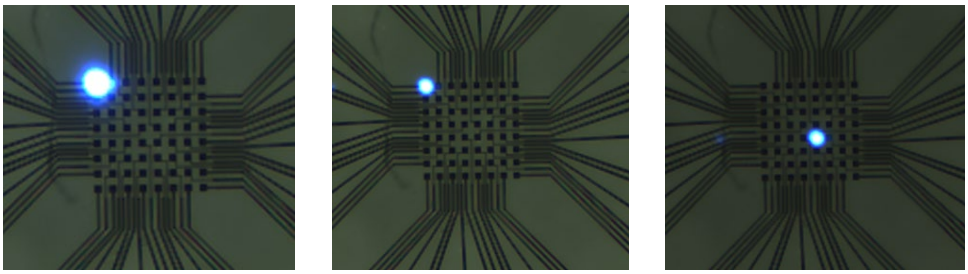

(a) (b) (c)

**Figure 35.** Microscopic picture of the microLEDs being driven by the circuit with different currents. (a) shows the LED driven at 500 µA, (b) shows the same LED driven at 27 µA and (c) shows a different LED driven at the same current, 27 µA.

## 3.1.2. High-speed driver

The driver capable of achieveing high-speed pulses was designed in AMS 0.35 µm CMOS technology. This driver has the capability of driving a Direct Addressed microLED array with up to 64 microLEDs or a 32x32 (1024) Matrix Addressed microLED array.

The anode driver (Figure 36 b, M5-M8) performs electrical pulses in the range of 3.3 V to 10 V amplitude with a FWHM of 1 ns and above. The cathode driver (Figure 36 b, M9-M12) works in reverse way, it performs pulses of amplitude in the range of -3.3 V to -10 V with a FWHM of 5 ns and above. The cathode driver is at the LED bias voltage when the microLED is not selected, so the LEDs are in reverse bias.

Each anode driving pixel measures 572 x 95 µm² and includes a low-voltage short pulse generator (Figure 36 a) and a high-voltage driving circuit (Figure 36 b, M5-M8). The cathode driving pixel measures 175 x 115 µm² and also contains a low-voltage short pulse generator (Figure 36 a) and a high-voltage driving circuit (Figure 36 b, M9-M12). The short pulse generator consists of an AND gate that combines an external input signal (Trig) with its delayed and inverted version. The pulse width (PA for the anode and PC for the cathode) is controlled by a bias voltage (Vbias) that adjusts the resistance of M4. To enable longer pulses, M2 is driven by an enable (En) signal, which disables the circuit, allowing the use of an external signal to drive the LED. The anode driver includes a level shifter (M5 and M6) and a high-voltage inverter (M7 and M8) with a high W/L ratio for fast

charging and discharging of the LEDs. Similarly, the cathode driver comprises a level shifter (M11 and M12) and a high-voltage inverter (M9 and M10).

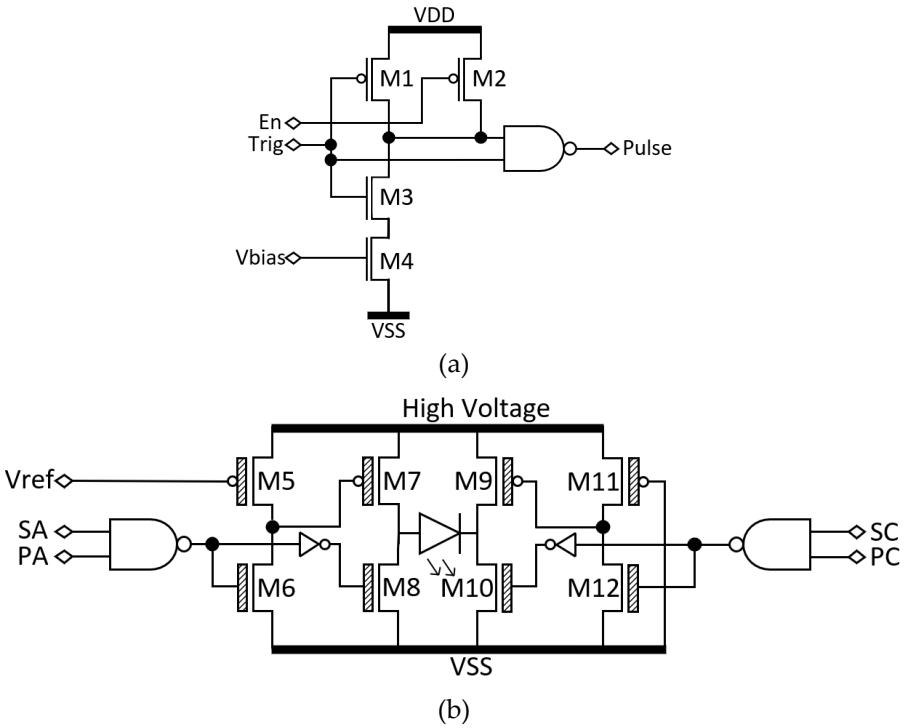


**Figure 36.** Short pulse generation circuit (a) and the anode and cathode driving elements (b). The anode and cathode driving circuits are composed of high voltage output buffers (M7-M8 for the anode driver and M9-M10 for the cathode driver) and level shifters (M5-M6 and M11-M12) with a NAND gate per driver to select the specific LED.

The total chip area is 1.756 mm x 7.318 mm (12.88 $mm^2$). The chip layout is shown in Figure 37, where in the red area are located the anode drivers, which are used for Direct Addressed arrays and Matrix Addressed arrays, and in green the cathode drivers, that combined with one row of anode drivers is used for Matrix Addressed arrays.

# 3. Results

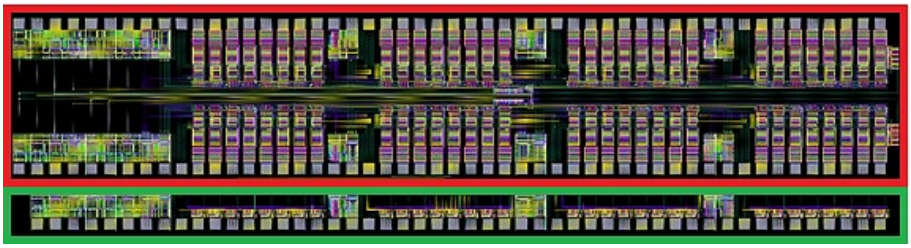

**Figure 37.** Custom CMOS microLED IC driver. In red there are the anode drivers (used for both DA and MA arrays) and in green the cathode drivers (used only for MA arrays).

The anode driver is able to perform pulses with 1 ns FWHM (Figure 38 a) and long pulses with good stability (Figure 38 b). The experiments performed to obtain the graphs shown in Figure 38 were done with the 8 x 8 5 µm LED array driven by the anode circuits. These experiments were performed using a SPAD sensor with the TCSPC method. This method consists of exciting the sample with a pulsed light source. After each excitation pulse, one of the photons emitted by the fluorophore can be detected by the SPAD sensor, which stays inhibited after the detection. The arrival time of the photon is then measured and catalogued in the corresponding histogram bin. By repeating this method several times, the time response of the microLED optical signal is extracted.

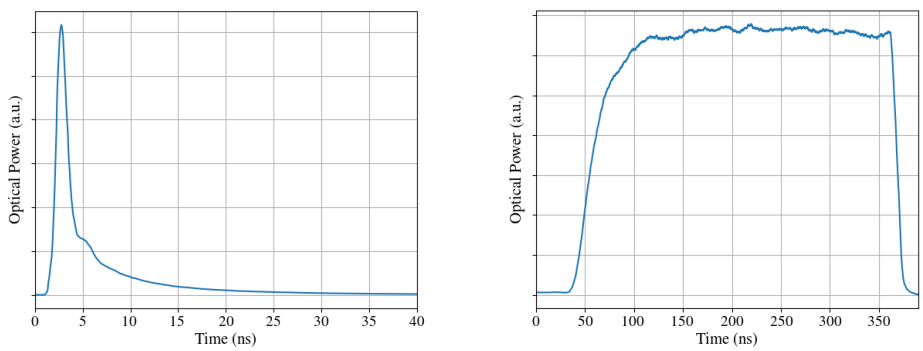


(a) (b)

**Figure 38.** Optical pulses measured with the TCSPC technique of an SPAD camera. (a) shows a 1ns FWHM optical pulse and (b) shows a stable optical pulse with a FWHM higher than 300ns.

In the case of the MA driving circuit, since the capacitance contribution increases because in both the anode and the cathode 32 LEDs contribute, it is not possible to obtain pulses with FWHM in the order of the ns. Nevertheless, the IC is capable of turning off any microLED in the array times smaller than 3 ns (Figure 39). This

enables the possibility of working with time resolved fluorescence for fluorophores with higher decay times than 5 ns. This experiment was performed using an SPAD sensor using the TSCPC method.

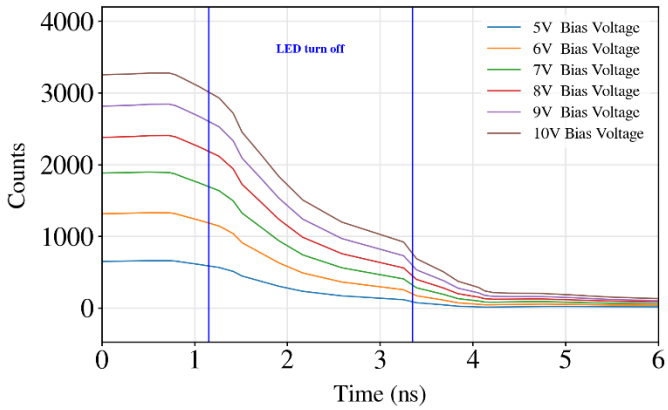


**Figure 39.** MA driving circuit turning off a microLED for different bias voltages. It can be observed that the turn off time is the same for all the bias voltage, therefore making the circuit speed robust to changes in the driving voltage of the LEDs. The y axis (Counts) represents the optical intensity captured by an SPAD sensor.

To sum up, the drivers developed during this thesis for microLED arrays, and their characteristics are listed below in Table 7.

**Table 7.** MicroLED array drivers developed.

| Driver name | Driver type | Current | LEDs Addressing | LEDs Driven | Max bias voltage | Min pulse width | Picture |
|---|---|---|---|---|---|---|---|
| Current driver | Discrete | M24 | Direct | 64 | 5 V | 2 µ |  |
| High-speed driver | CMOS | M26-M27 | Direct | 64 | 10 V | 1 ns | 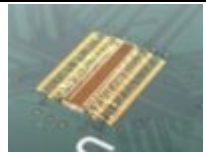 |
| | | | Matrix | 1024 | | | |

# 3. Results

## 3.2. MicroLEDs for microscopy

### 3.2.1. Principle demonstration of raster microscopy using an array of LEDs

A first microscope setup was built in order to test the microLED capabilities to build a raster microscope. In this case, the resolution came from the size and pitch of the microLED array instead of the size and pitch of the sensor array. Furthermore, this microscope was designed to be lensless. In [113] we presented the operation principle of this type of raster microscope with simulations that demonstrate the possibility to use this microscopic technique for super-resolution. The super-resolution capabilities rely on the continuously scaling down of microLEDs.

The first prototype of this new type of microscope consists of an 8 x 8 microLED array with a pixel size of 5 x 5 $\mu m^2$ and a pixel pitch of 10 µm, driven by the Current driver (Table 7), and an optical sensor built with SPADs (Figure 40) placed in front of the LED array. The characterization of the device is done using an Electron-Beam Lithography (EBL) pattern positioned in-between.

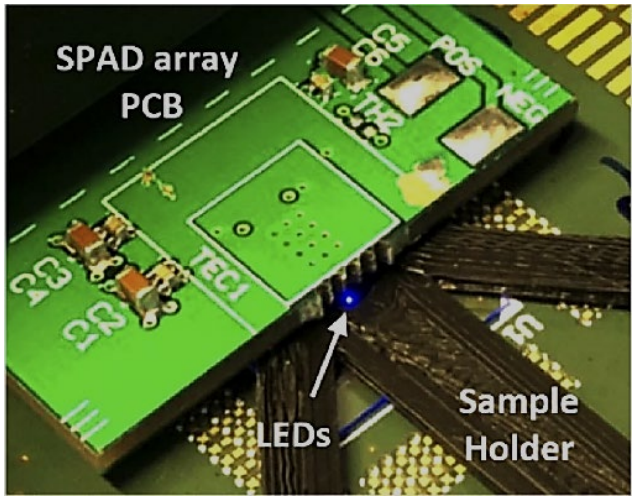


**Figure 40.** Photography of the microscope setup. The microLED array is facing up to the SPAD array sensor (facing down). The sample holder presents an opening where the sample is placed.

# 3. Results

The EBL pattern used as a sample for the characterization of the device has features from 50 µm down to 50 nm in size. This EBL pattern was designed in order to test the resolution of the microscope, since a much higher resolution was expected when the concept of this microscope was conceived, and no commercial patterns were available with structures down to the order of nm. The sample was placed at a distance of around 30 µm from the LED array and from the sensor, and this setup was used to obtain the images shown in Figure 41.

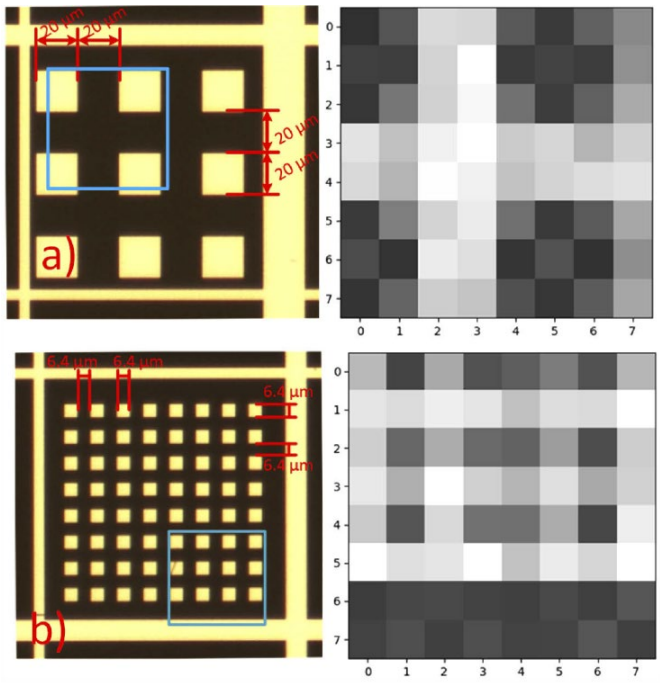


**Figure 41.** EBL patterns, with the focused zone marked by the square (left) and shadow images from nano illumination microscopy method for each (right). 20 µm side squares and separated by 20 µm (a) and 6.4 µm side square separated 6.4 µm (b) are resolved.

This proof-of-concept microscope, using 5 x 5 $\mu m^2$ LEDs was able to resolve down to 6.4 µm squares. However, with this method we expected to achieve a resolution of twice the periodicity of the light source matching the pitch of the LED array used (10 µm), with a field of view matching the size of the LED array used (80 x 80 $\mu m^2$). Nevertheless, the 6.4 µm squares represent a limiting case, as simulations predicted that aliasing would prevent the central squares from being properly resolved, causing them to be sampled as a single object. While features as small as isolated 5 µm separator lines can sometimes be observed, depending

on the relative positioning of the components, resolving two of such lines side by side would not be possible. Nevertheless, this method could still be valuable for detecting the presence or passage of particles down to the size of the LED pitch.

Further research regarding the use of microLEDs for microscopy was performed following two paths. The first path was focused on achieving a higher down-scale of microLEDs to accomplish higher resolution. The second path was to use MA LED arrays to increase the FoV of the microscope.

In the work in [114], three generations of microscopes are described. The first-generation microscope described uses the 8x8 microLED array [114] but using a full custom CMOS IC driver (High-speed driver from Table 7). The second-generation microscope uses an array of 2x32 Direct Addressable nanoLED array with 200 nm side size 400 nm pitch. This microscope was designed to push the resolution limit of nanoLEDs by creating a structure with minimal spacing along one axis. Because of technical reasons, only one LED was used in the microscope as described later in the following section. Finally, the third-generation microscope was built using a completely different structure, consisting in a 32x32 MA microLED array with 20 x 20 $\mu m^2$ LED size and 40 µm pitch. By using the MA microLED array a larger FoV can be achieved. However, at this time, the technological challenges producing a MA array with lower LED size and pitch limits the achievable resolution.

The first and second generation microLED arrays (8x8 and 2x32 arrays) were driven by the same CMOS circuit, the High-speed driver with the Direct Addressable circuits (Table 7), and the third generation is driven by the High-speed driver with the Matrix Addressable configuration (Table 7).

### 3.2.2. Looking for resolution limits: second generation microscopes

For the second-generation microscope we used nanoLEDs of 200 x 200 $nm^2$ [114]. We used only one LED in the array and performed a 2D scan by moving the sample, emulating a larger LED array. Figure 10a presents the reconstructed image of the EBL pattern region with 1.6 µm and 6.4 µm squares, obtained using a step size of 200 nm in both directions. The spatial resolution was determined using the edge spread function (ESF) and line spread function (LSF) methods,

measured between 10–90%. The resolution extracted from one of the 1.6 µm square's edges was 1.56 µm (Figure 42), which is four times the expected resolution (400 nm). The expected resolution relies on the sample being placed directly over the nanoLEDs. Further analysis of the nanoLED array configuration, conducted using finite difference time domain simulations, indicated that the metal structure and the depth of the light emitter region influenced the spot shape and size at the chip surface (where the sample is placed), thereby degrading the resolving power of the setup.

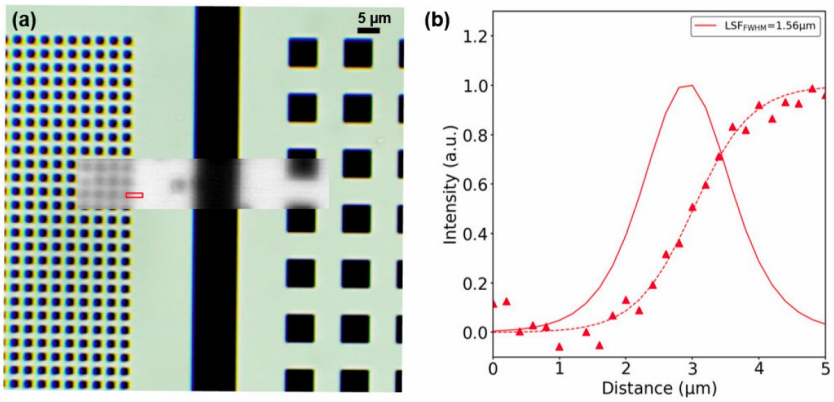


**Figure 42.** Optical image of the 1.6 µm (left) and 6.4 µm (right) squares of the EBL pattern, with the reconstructed image of the same region superposed. (b) The ESF and the LSF calculated on the specified region of the inset image.

### 3.2.3. Acquisition time improvements

In order to improve acquisition times, the focus of our research was directed to the use of custom CMOS sensors, in this case a SPAD camera. According to A. Ingle *et al* [177] it is possible to enhance a SPAD sensor properties, like dynamic range, by using temporal information. So, if instead of acquiring an intensity measure of a continuous light we acquire also the temporal behavior of this light, we have a decay curve that is related to the light intensity. In Section 3.2.7 [178] a study is presented where different statistical methods that could improve both the acquisition time and dynamic range of a SPAD sensor are applied. Furthermore, in this work, we study how to minimize the amount of hardware used in order to accomplish these results. This is possible by applying a statistical technique known as the weighted average, as described in Equation (2). This approach significantly reduces the total number of measurements required by the SPAD

sensor, thus reducing the acquisition time considerably. This method has been proven to optimize the readout of the sensor from 50 ms to 140 µs, thus potentially allowing to decrease acquisition times compared to commercial CMOS cameras that are used in raster technique.

$$average = \frac{\sum_{bins=1}^{n} time_{bin} \cdot counts_{bin}}{\sum_{bins=1}^{n} counts_{bin}} \quad \textbf{(2)}$$

### 3.2.4. Conclusions

To conclude, the use of microLEDs for raster microscopy has been proved. The operational principle was confirmed using three different LED array configurations, revealing that the system's resolution is mainly influenced by the size and pitch of the LEDs when the sample is in direct contact with the emitters. While the prototypes demonstrated had a limited field of view and did not achieve submicron resolution, even with 200 nm LED arrays, there is considerable potential for enhancement. Future improvements could involve strategies such as utilizing transparent conductive oxides for contact lines, reducing the thickness of the insulating layer between the metal pattern and the LED structure, and further minimizing the LED size.

Nevertheless, to accomplish a large field of view proportionally increases scanning time. This is a challenge that must be addressed. LEDs have demonstrated the capability to switch at MHz frequencies, indicating that the limiting factor for scanning speeds lies with the sensor technology. Standard CMOS sensors typically operate at frame rates ranging from 30 fps to 1000 fps, which constrains the scanning speed to a similar range of pixels per second. Thus, it was performed a study in which different statistical methods were applied to the temporal information of the behavior of the light acquired. This has allowed to reduce the number of measurements needed to acquire by the SPAD, thus reducing significantly the acquisition time for each microLED in the array from 50 ms to 140 µs.

### 3.2.5. Publication 1

## Nano illumination microscopy: a technique based on scanning with an array of individually addressable nanoLEDs

by

Nil Franch[1], Joan Canals[1], **Victor Moro[1]**, Ana Vilá[1], Albert Romano-Rodríguez[1], Juan Daniel Prades[1], Jan Gülink[2,3], Daria Bezshlyakh[2,3], Andreas Waag[2,3], Katarzyna Kluczyk-Korch[3], Matthias Auf der Maur[3], Aldo di Carlo[3] and Angel Diéguez[1]

*[1]Department of Electronic and Biomedical Engineering, Universitat de Barcelona, Spain*
*[2]Institute for Semiconductor Technology, University of Technology Braunshweig, Germany*
*[3]Laboratory for Emerging Nanometrology LENA, Braunschweig, Germany*
*[4]Department of Electronic Engineering, University of Rome "Tor Vergata", Italy*

*Published in*
**Optics Express** 28 (2020) 19044–19057

Research Article | Vol. 28, No. 13 / 22 June 2020 / Optics Express 19044
Optics EXPRESS

# Nano illumination microscopy: a technique based on scanning with an array of individually addressable nanoLEDs

NIL FRANCH,[1,*] JOAN CANALS,[1] VICTOR MORO,[1] ANNA VILÁ,[1] ALBERT ROMANO-RODRÍGUEZ,[1] JUAN DANIEL PRADES,[1] JAN GÜLINK,[2,3] DARIA BEZSHLYAKH,[2,3] ANDREAS WAAG,[2,3] KATARZYNA KLUCZYK-KORCH,[4] MATTHIAS AUF DER MAUR,[4] ALDO DI CARLO,[4] AND ÁNGEL DIÉGUEZ[1]

[1]*Department of Electronic and Biomedical Engineering, Universitat de Barcelona, Spain*
[2]*Institute for Semiconductor Technology, University of Technology Braunshweig, Germany*
[3]*Laboratory for Emerging Nanometrology LENA, Braunschweig, Germany*
[4]*Department of Electronic Engineering, University of Rome "Tor Vergata", Italy*
[*]*nfranch@el.ub.edu*

**Abstract:** In lensless microscopy, spatial resolution is usually provided by the pixel density of current digital cameras, which are reaching a hard-to-surpass pixel size / resolution limit over 1 µm. As an alternative, the dependence of the resolving power can be moved from the detector to the light sources, offering a new kind of lensless microscopy setups. The use of continuously scaled-down Light-Emitting Diode (LED) arrays to scan the sample allows resolutions on order of the LED size, giving rise to compact and low-cost microscopes without mechanical scanners or optical accessories. In this paper, we present the operation principle of this new approach to lensless microscopy, with simulations that demonstrate the possibility to use it for super-resolution, as well as a first prototype. This proof-of-concept setup integrates an $8 \times 8$ array of LEDs, each $5 \times 5\ \mu m^2$ pixel size and $10\ \mu m$ pitch, and an optical detector. We characterize the system using Electron-Beam Lithography (EBL) pattern. Our prototype validates the imaging principle and opens the way to improve resolution by further miniaturizing the light sources.



## 1. Introduction

Nowadays, lensless microscopy is a relevant competitor to the classical optical approach. Taking advantage of the electronics downscaling as well as of the increased availability of processing power, lensless arrangements appeared as an effort to reduce the complexity of optical setups. They made available simpler, inexpensive and more flexible microscopes, thanks to the lack of optical elements [1–6], even enabling the integration of microfluidics directly on dedicated microscopes [7]. With these capabilities, lensless microscopes evolved to become widely used for example in disease diagnosis [8], tracking of biological samples [9] or microbial observation [10].

In parallel, conventional microscopy kept improving until it finally met a fundamental limit: the diffraction inherent to all optical systems [11]. The observation of objects with dimensions below this limit remained only accessible to electronic microscopy techniques, but at the price of becoming bulky and expensive, as well as excluding the possibility to observe live samples due to the preparation processes involved [12]. The development of super-resolution techniques (STED [13], STORM [14], PALM [15]) opened up the direct observation of objects at scales where molecular processes are important, and offered the possibility to look inside of the living cells [16,17]. As these techniques kept improving, new uses have been found, moving towards the chemical world for single molecule tracking [18–20] or offering information about chemical

#391497 https://doi.org/10.1364/OE.391497
Journal © 2020 Received 26 Feb 2020; revised 26 Apr 2020; accepted 29 Apr 2020; published 12 Jun 2020

Optics EXPRESS

reactions [21,22]. Nevertheless, these methods did not escape the need for relatively large and expensive setups [23].

One of the problems of trying to apply the lensless microscopy approach to super-resolution in order to simplify the setups is the ultimate resolution achievable. In its standard configuration, the sample is illuminated from a known and controlled light source while a CCD or CMOS camera records the shadow image, which is used to reconstruct the object. In this case, lensless microscopes are limited by the pixel size of the camera, which is restricted by the microelectronic technology used and its noise levels. Currently this size is constrained to around 1 µm [24]. This limitation can be mitigated using additional techniques such as pixel super-resolution, though at the expense of additional mobile parts and complex setups [25] .

Another approach capable of providing resolutions below the diffraction limit are the methods within the Scanning Near-field Optical Microscopy (SNOM) family. These methods consist on scanning the zone of interest with a point light source, which is then scattered by the sample and recovered on a far field regime, providing information about the topology of the illuminated area. Lateral resolutions of 20 nm and vertical resolutions of 2–5 nm have been demonstrated by these means [26–30]. SNOM and its variations are being used in diagnosis [31], nanoscale electro-magnetic field mapping with biosensing or quantum optics applications [32], development of new photonic metamaterials and subwavelength confinement structures [33] or protein structure imaging [34].

As an alternative approach, we propose to use spatially resolved light sources to scan the sample by switching on and off, one after the other, the Light Emitting Diodes (LEDs) on a single chip. As we demonstrate in this work, a microscope can be built by measuring the intensity of light reaching the sensor from every individual LED as it passes through a sample, in what one could call Nano Illumination Microscopy (NIM). At present, high luminosity GaN LEDs arrays can be fabricated with pixel sizes in the micrometer range [35], and research results on even smaller devices are promising [36]. Following the approach proposed here it is thus feasible to use, in the future, arrays of nanoLEDs with a pitch smaller than Abbe's diffraction limit to potentially render super-resolution images. Since no bulky lenses nor mobile parts are involved in such a device and since the components are exclusively based on mass producible microelectronic technologies, these new lensless microscopes have the potential for making super-resolution microscopy on a chip ubiquitous and accessible to everyone. This would open the possibility to integrate microscopes into much smaller devices than the conventional lensless approach and without the expensive scanning setups needed for SNOM measurements [37].

In this context, this work presents the basis of this new operation principle, with simulations that predict its operation in super-resolution conditions for an LED array with a pitch of 100 nm. We also present the first proof-of-concept prototype to investigate the imaging capabilities of this new NIM approach to lensless microscopy, with the corresponding simulations. This microscope is composed of an array of $8 \times 8$ LEDs with 5 µm size and 5 µm spacing, and a CMOS Single Photon Avalanche Photodiode (SPAD) detector. The results obtained thanks to this prototype confirm the abilities of the proposed setup for super-resolution.

## 2. NIM operation principle

The principle behind NIM is similar to that of SNOM, but without the need for mobile parts nor scanning tips. Instead, the sampling is done by switching on and off alternatively the LEDs in an array close to the sample. Figure 1 shows a schema of the image acquisition process for a single line of the LED array. When the same process is repeated for every row of the array, the result is a direct map of the sample according to the light it blocks from each LED. This means that for this method, the microscope sensor only needs to capture the light/shadow cone from every LED in the array to operate properly, hugely relaxing the impact of its fill factor or pixel size.

Optics EXPRESS

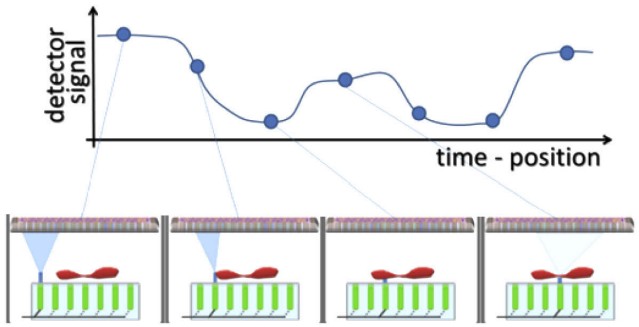


**Fig. 1.** Operation principle of the NIM microscope: the sample is scanned by illuminating alternatively with different LEDs, and the sensor on top records the intensity of light reaching it.

In a general lensless setup, the field of view and the resolution depend on the distances between the light emitter, the sample and the sensor. For a NIM setup this influence has been analyzed by means of calculations. Figure 2 shows the distribution and results of ray tracing simulations comparing three fundamental operating conditions with a single LED row –since the process will be the same for each one. In this case, the sensor is 10 µm in diameter, and the samples are four completely opaque, 12 µm wide objects at different distances from the LEDs and the sensor.

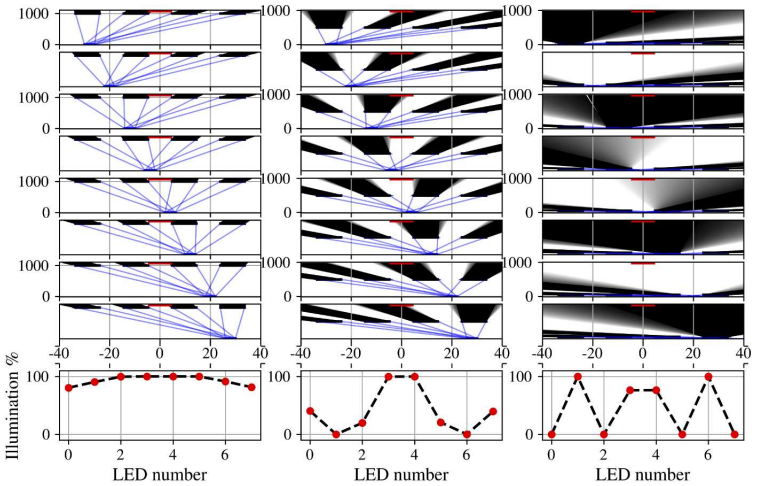


**Fig. 2.** Detail and results for the ray tracing simulation of the microscope operation, for a single LED row. The red surfaces on the top part of each figure are the 10 µm sensor, while the test samples are in black and are 12 µm wide patterns. The LEDs (in blue at the lower part of each figure) switch on and off sequentially, creating shadow patterns on the sensor. The figure at the bottom shows the relative illumination received on the sensor with each LED. (a) Shadow imaging case: the samples are close to the sensor, far from the LED. (b) Intermediate case: the increased distance makes proper sampling more difficult (c) Ideal NIM scan mode: the samples are very close to the LEDs, creating large shadow patterns.

Optics EXPRESS

In Fig. 2 a) the setup would operate in the conventional lensless microscopy approach. Samples are placed far from the light sources, creating the same shadows on the sensor plane when illuminated by different LEDs. This is due to the small pitch of the LEDs in comparison to the distance to the sample (note the difference in scale between the x and y axis). In shadow imaging, it is important to keep the sample as close to the imager as possible, in order to have both maxiμm resolving power and field of view [19], so that the resolution is limited by the sensor pixel pitch. It is the opposite in NIM setups, since the distance, which should be minimized, is between sample and light sources.

The process of creating a NIM image is shown in Figs. 2 b) and c) for a single row of the LED array, and consists on switching on and off a single LED to illuminate a small piece of the sample. The amount of light reaching the sensor gives information about the object geometry, and the closer the object to the light source, the better in order to produce sharper contrasted images. The ultimate resolution of a NIM microscope, i.e. the capability to resolve sample features, is related to the pitch of the LEDs, and objects less spaced than the LEDs cannot be resolved. In the particular case of a pattern of the same periodicity as the LEDs, the same signal would be measured while scanning (i.e. all samples would equally cover the LEDs). Single objects with the same pitch than the LEDs can be detected, although it is a limit case which depends on the relative positions of the samples and the sensor. Nevertheless, to properly resolve two objects their pitch has to be larger than twice the LEDs pitch, in accordance to sampling theory. For objects below that limit, aliasing occurs and information is lost. As visible in the example in Fig. 2 b), the opaque squares with a pitch of 12.8 μm and a length of 6.4 μm are not properly imaged in the central area because they are aliased together. This figure simulates the distances involved in the prototype built and shown later. Besides that, Fig. 2 c) simulates the ideal case with the object very near to the LED array, which creates large shadow areas easily detected by the sensor and whose field of view is the size of the array itself.

Figure 3 shows the evolution of contrast as the system moves from bad operating distances (sample much closer to the sensor than to the LED array) to NIM conditions. It has been obtained from ray tracing simulations, with the intensities measured on the sensor while scanning with the LEDs of a single row from the array, varying the $D$ distances between sample and sensor. The

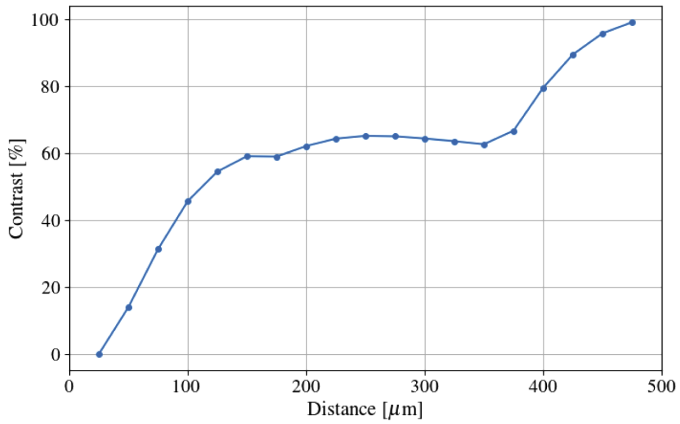


**Fig. 3.** Contrast detected from scanning with a single row of the LED array as a function of the distance D between sample and sensor. Results obtained from ray tracing simulation, with the rest of the parameters fixed and chosen to reproduce the experimental setup.

Optics EXPRESS

rest of the parameters have been selected equal to those of the prototype setup, that is $d$ = 300 µm, $L$ = 5 µm and $x_{\mathrm{det}}$ = 10 µm. For completion, the samples used are 11 µm squares. We see the improvement in contrast as the sensor moves away from the sample, shifting into proper NIM operation conditions. As distance D grows the contrast increases as expected, in agreement also to the design conditions given in following sections.

## 3. Discussion of super-resolution capabilities

In order to demonstrate that this method is viable for super-resolution measurements and depends only on the development of miniaturized LED arrays, full field electromagnetic simulations on the range of the hundreds of nanometers were calculated. These simulations used Finite Difference Time Domain method (FDTD) implemented in software CST studio. A schematic of the simulated array and sample can be seen in Fig. 4. Al bar periodicities ($P_b$ in Figs. 4 and 5) were changed between 100 nm and 300 nm and distances between bars and light spots (D in Figs. 4 and 5) from 50 nm to 400 nm. The pitch of the LED array was kept constant at 100 nm, and the width of the Al bars is $W = P_b/2$ at each simulation. As expected, the simulations result in no contrast when the Al grating pitch is equal to the LED pitch, due to aliasing. Figure 5 presents the intensity of the z component of the Poynting vector integrated over the surface above the Al bars, and normalized to the corresponding intensity without bars present. The dielectric function for Al was taken from [38].

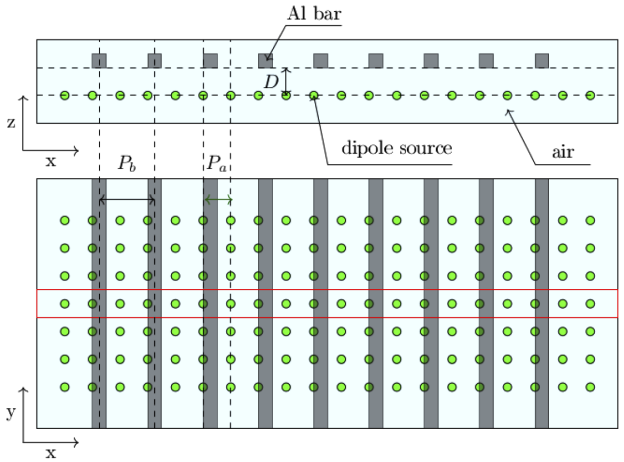


**Fig. 4.** Schema of the near field model for electromagnetic simulations. The rectangle limited by red lines indicates the part of the array presented in the simulations. In all cases the LED array period is $P_a$ = 100 nm, and $P_b$ is the period of the Al bars.

Simulations also show the distance between LEDs and sample to be important for the contrast of the received signal, as expected and demonstrated on the raytracing simulations. In Fig. 5, the simulated far-field intensity from each dipole –simulating a nanoLED as an ensemble of 8 nm dipoles– is drawn over the representation of the aluminum bars. The bars have a periodicity of 210 nm, and are properly sampled as shown by the different responses for polarization perpendicular o parallel to the bar axis. The contrast of the received signal depends on the distance between the light sources and the sample, as shown for the far-field case before. These simulations show that NIM would be able to resolve objects below the Abbe limit, achieving super-resolution. Moreover, this study demonstrates that NIM setups can be more compact than traditional lensless

Optics EXPRESS

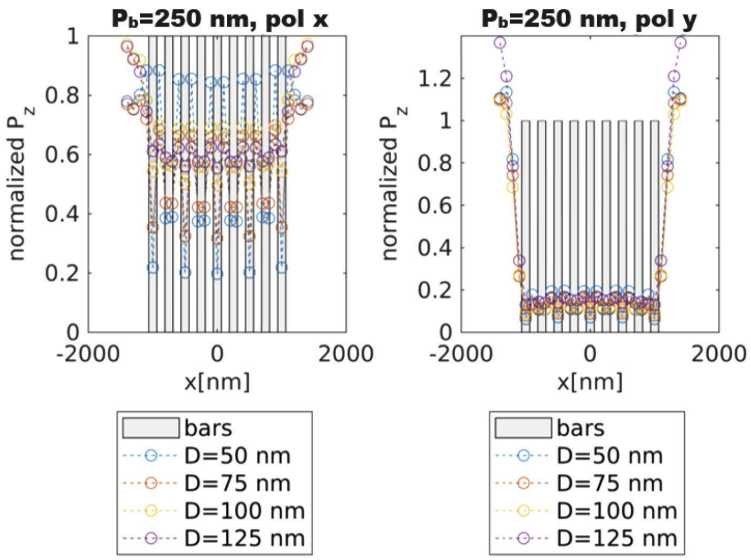


**Fig. 5.** Far-field light intensity outgoing from an Al bar grating for a dipole array spaced 100 nm normalized to the intensity of a single dipole source. Different distances between bars and dipoles (D) are simulated using FDTD, for a periodicity $P_b$ of the Al bars of 210 nm. The dipole source is polarized in x direction (perpendicular to the bar axis) in the left image, and in y direction (along bar axis) on the right side. The gray areas indicate the positions of the Al bars.

microscopes, since the distance of the sample to the LED array is necessarily minimized, and the distance between sample and camera can be kept small as long as it is several times larger than the LED – sample distance.

To better approximate realistic sizes for the future LEDs, simulations where also carried with bigger ensembles of 50 nm dipoles. The simulations in Fig. 6 show how the size of the dipole ensembles (and thus the simulated nanoLEDs) is not a critical influence on the contrast of the NIM setup, with differences only showing up at distances closer than the 100 nm. This supports the idea that for NIM microscopes, the performance is mainly affected by the distances and the LED pitch, more than the actual LED sizes. The contrast is defined by Eq. (1).

$$C = 100 \cdot \frac{I_{max} - I_{min}}{I_{max} + I_{min}} \tag{1}$$

To complete this simulation study, Fig. 7 shows the Fast Fourier Transform (FFT) obtained when bars with different periodicities are sampled with LEDs spaced 100 nm. The FFT should have a peak on the bar periodicity, but it can be seen that it is only properly sampled for $P_b$ larger than 200 nm, as expected from sampling theory. For lower periods, aliasing appears, such as for periodicity $P_b = 150$ nm, which generates a response that is almost the same as for periodicity $P_b = 300$ nm. For $P_b = 100$ nm, there is no way to properly reconstruct the bar distribution.

Optics EXPRESS

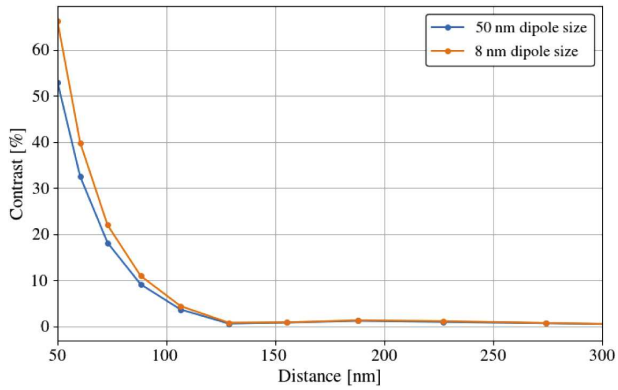


**Fig. 6.** Contrast obtained by the different dipole models, ensemble of 8 and 50 nm dipoles forming square patterns to simulate the nanoLEDs. Results obtained from the FDTD simulations.

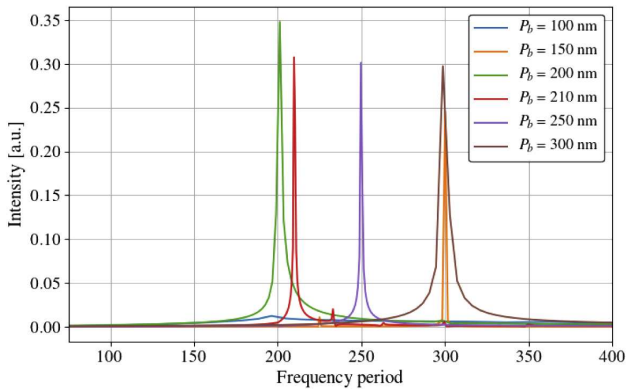


**Fig. 7.** FFT of the far-field intensity signals obtained for different Al bar periods ($P_b$) on the EM simulations for an extended LED array. Results obtained from the FDTD simulations.

## 4. NIM design principles

Discussion about the requirements on the design of a NIM microscope is illustrated with the help of Fig. 8, where d is the distance between LEDs and sample, and D is the distance between sample and sensing area. Figure 8 a) shows the field of view (FOV) of a NIM setup, and how it depends on the LED – sensing area distance , as well as the width of the sensing area itself and the width of the nanoLED array. When the distance D is much larger than the distance d, that is, the microscope operates in ideal NIM conditions, the field of view is the width of the LED array, as long as the effect of the angle of incidence for the light can be compensated (for example, by adjusting the current through the LEDs). A way to remove any dependence on the angle from the FOV could be to make the optical detector as wide as the LED array, but this would result in a reduced contrast for the microscope as illustrated in Figs. 8 b) and 8 c). In Fig. 8 b) it is shown the worst case in which the shadows from different LEDs overlap. That would happen

Optics EXPRESS

if the sensor at a distance D from the sample crossed the dashed red lines. To avoid this, the maxiμm width of the detector, $x_{\mathrm{det}}$ is determined by Eq. (2), in which L is the size of the LEDs.

$$x_{\mathrm{det}} < 2\frac{3D - 2d}{2d}L \tag{2}$$

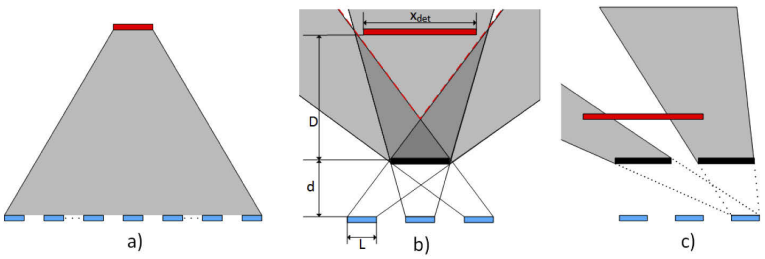


**Fig. 8.** General schematics of the NIM microscope. In blue, LEDs from the array. In red, sensing area or sensor. a) shows the field of view for an arbitrary large LED array and sensor (grey shaded region). b) shows the shadow cones projected by a single sample (in black) from different LEDs and how they may overlap, which would mean the same area of the sample would be sampled by different LEDs, reducing the contrast of the microscope. The dashed red lines show the limits of that overlap zone c) shows the shadow cones projected by different samples while illuminated by the same LED, and how they may be integrated together by a sensor too large.

This relationship confirms that there is a minimal distance between sample and detector. Moreover, to relax the requirements on the sensor the distance D should be kept larger than d as necessary. For the prototype built and presented below (D = 600 μm, d = 300 μm) the maxiμm size for the sensor to avoid the shadow overlapping problem is 20 μm in diameter.

At the same time, Fig. 8 c) illustrates another situation to be considered. In it, the sensor pictured integrates the shadows projected by different regions of the sample being illuminated by the same LED. If we remember that only samples spaced twice the LED pitch can be observed, the condition follows Eq. (3). This relationship is less restrictive than the previous one (for the prototype dimensions, $x_{\mathrm{det}} < 40\mu m$), so the microscope should conform to the condition presented in Eq. (2).

$$x_{\mathrm{det}} < 2\frac{3D + 2d}{2d}L \tag{3}$$

While for small LED arrays such as the integrated in the prototype presented below the dependence of the recovered light on the angle of incidence is corrected by a calibration process, this might be difficult to do for arbitrary large LED arrays. In that case, it would be useful to add additional sensor pixels or take new sensing areas in parallel, each with their own FOV. The spacing between pixels required for this is very low (in the current experimental setup, one pixel each 100 μm is enough), and easily met with any camera. Since trying to sample a large array with a single sensor would get in the way of contrast, this strategy would serve both purposes, keeping contrast as sharp as possible while recovering the maxiμm amount of light, since arbitrarily sized sensing areas placed directly above a group of nanoLEDs can be used for that purpose.

## 5. Microscope components and setup

Nowadays, Gallium nitride (GaN) LED technology is developing beyond solid-state lightning, leading to highly efficient micro- and nanodevices for applications such as point light sources for

Optics EXPRESS

optical communications, imaging and sensing [39]. In particular, the nanoLEDs used in this work were obtained from standard blue LED structure, based on InGaN/GaN quantum wells grown on a sapphire wafer [40]. Their design granted individual access to each one of the pixels of the array by defining individual contacts (top) to the p side of each LED and an n-type contact (bottom) common to all pixels. This is a major factor limiting the number of LEDs in the array, because the driving electronics must access the LEDs through a metallic interconnection. The low number of LEDs sets the field of view of the microscope, which is only as large as the array itself. The entire chip for our prototype, including the LED array and contact pads, is $1 \times 1 cm^2$ in size. The LEDs are distributed in an $8 \times 8$ matrix of 5 μm LEDs (spaced also 5 μm), which makes them smaller than any commercially available GaN LED array (Fig. 9). The metal contacts are produced by deposition of Cr/Au, and light is emitted through the 300 μm thick sapphire substrate. The different illumination levels between LEDs were corrected by adjusting the driving current for each one to equalize the response measured in the optical detector, which removes the dependence with the angle of incidence too. The LED array is driven by a digitally controlled current source, supplying from 27 muA up to 3 mA through $8 \times 8$ channel analog demultiplexers, implemented with discrete components.

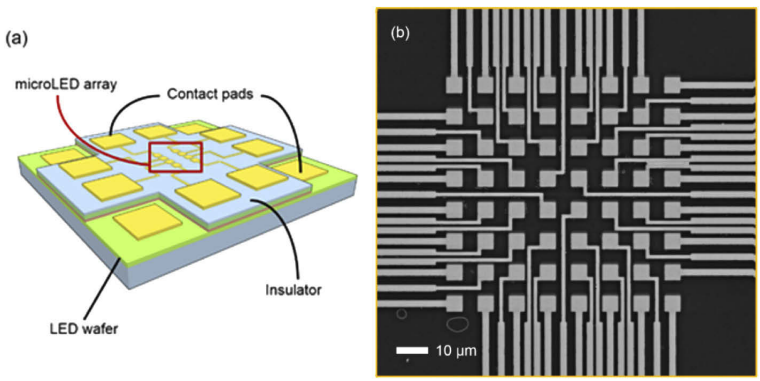


**Fig. 9.** The NIM light source: a GaN nanoLED array chip with 64 ($8 \times 8$) pixels sized 5 μm. (a) 3D sketch of the chip. (b) Image of the microLED array chip.

As commented before, the NIM microscope effectively relaxes any requirements on the optical detector, which could be any conventional CCD or CMOS camera. For the prototype, a custom SPAD camera was implemented because of its adequate form factor (low profile when mounted on the PCB, no additional optical components), as well as to prepare for future fluorescence experiments with the NIM technique. Moreover, the SPAD sensors are useful as a benchmark for the possibility that future miniaturized LEDs present a much lower emission power, which other sensors could have problem detecting, and could help for example confronting shot noise. For all these reasons, the camera consists on a circular SPAD sensor integrated on a 0.35 μm CMOS process and with a 10 μm diameter. The dark noise for this pixel configuration is 200 Hz, while the PDP at 450 nm (dominant wavelength emitted by the LED) is around 10% [41]. In our demonstrator, creating an image frame in the NIM mode requires scanning through the 64 different LEDs, and their switching speed limits the framerate to 20 frames per second.

The LED chip is ball-bonded on the exposed contacts of a PCB containing its driving electronics and control connections. Opposite to the LEDs, the imaging chip is mounted on its own PCB, with its wire bonds protected with spin coated SU-8 [42]. Positioning stagers are used for both the sample and the SPAD sensor, to allow studying the images obtained at different relative positions

Optics EXPRESS

between sample, LEDs and sensor. They provide flexibility for testing different alignments and setups, but they are not an essential part of the microscope. Additionally, a sample holder is used to position and move the sample over the LED array, in direct contact with the surface of the sapphire layer, in order to obtain the maxiμm resolving power. A general schematic of the setup can be seen in Fig. 10, while Fig. 11 shows a close view photography of the actual construction.

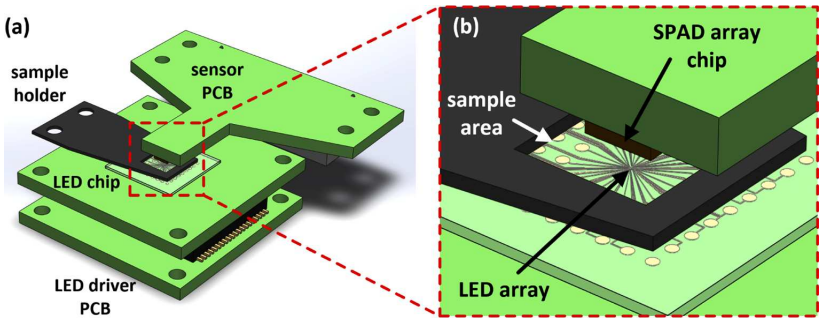


**Fig. 10.** General scheme of the microscope. The LED array is ball-bonded over the driver PCB. The sample is placed over the LEDs as close as allowed by the sapphire layer. The light transmitted through the sample reaches the SPAD sensor, opposite the LEDs.

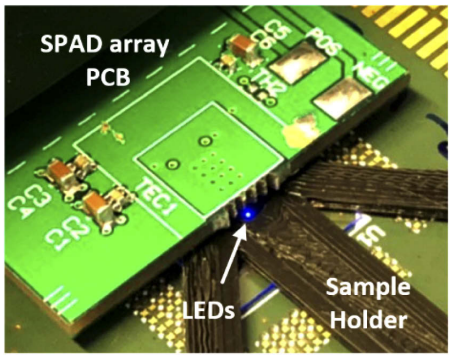


**Fig. 11.** Close up photography of the microscope setup. The sample holder presents an opening where the sample is placed and the SPAD imager is directly above it.

## 6. Experimental results

In order to test the capabilities of the setup, 40 nm of Cr was deposited on a fused silica wafer patterned by Electron-Beam Lithography (EBL) with features from 50 μm down to 50 nm in size. The dies resulting after wafer dicing were used as samples for the system. These were placed over the sapphire layer of the LED chip, with a holder ring around it to allow for positioning, as shown in Figs. 10 and 11. The sample was at a distance of around 300 μm from the LED array and from the sensor, to obtain the images shown in Fig. 12. Note that the colors are inverted between the microscope picture and the NIM image because the picture is taken from a reflection microscope, while the NIM setup operates by transmission. Each pixel from the images in the right part of

Optics EXPRESS

Fig. 12 corresponds to the light intensity measured from turning on the corresponding LED of the array, the sensor being the same in all cases, and each pixel of the image representing the sample (or lack of) right above the corresponding pixel. Before taking the image of the sample, each LED is characterised and calibrated so that for each one the sensor receives the same light intensity.

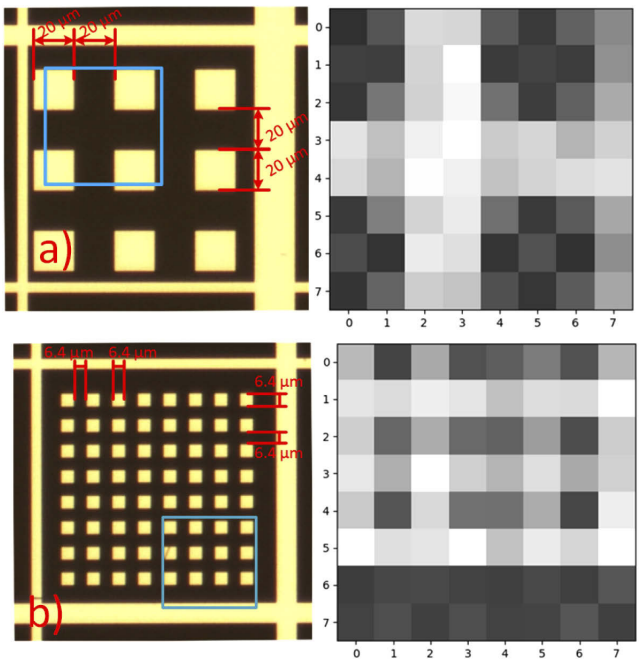


**Fig. 12.** EBL patterns, with the focused zone marked by the square (left) and shadow images from nano illumination microscopy method for each (right). (a) 20 µm side squares, separated 20 µm. (b) 6.4 µm side squares, separated 6.4 µm

With the current LED array, the smallest resolved patterns are the 6.4 µm squares, as can be seen in Fig. 12(b). This can be considered a limit case, because the aliasing predicted by simulations causes that the central squares to not be properly resolved and to be sampled as a single object. Features down to isolated 5 µm separator lines can also be observed, depending on the relative positioning of the parts, but it would not be possible to resolve two side by side. Still, this could be useful for detecting the presence or passage of particles of sizes down to the LED pitch for example.

## 7. Conclusion

In this work, we have demonstrated a new approach to shadow imaging microscopy, Nano Illumination Microscopy (NIM), which bases its resolving power on miniaturized light sources instead of the sensor geometry, while avoiding the use of any moving parts or optics. Simulations in different scales for the imaging process are presented. An experimental demonstrator validates the imaging principle, and opens the way to improve resolution by further miniaturizing the light sources. A key issue for the image formation is the distance between the light sources and the

Optics EXPRESS

sample, which should be kept as low as possible. For future nanometric setups, it can prove difficult to be able to guarantee the planarity of an entire sample over the LED array, although for biological ones such as cells, with their membrane resting just above the insulation layer, this still would be possible.

Together with the low requirements on the distance between sample and optical detector, NIM setups are very compact, which will result in smaller microscopes when compared with optical or conventional lensless shadow imaging setups. As an example, the total height of the experimental prototype is 1 mm. It is worth noting that since the process to build an image requires to scan through all the LEDs in the array, capturing enough photons from each, building an image with this method will be slower than conventional lensless shadow imaging.

The NIM method provides a resolution of two times the periodicity of the light source and a field of view of the same size as the LED array used. Therefore, the resolution will improve with the technological progress of GaN LED emitters, with sizes and pixel to pixel distances moving into the nanoscale. Additionally, a reduction of the distance between illumination source and sample will also allow for higher frequency components to be sampled correctly. The same technological improvements will also increase the number of pixels in an array, directly increasing the field of view available. Additionally, the high brightness of inorganic GaN LEDs makes them a good technological choice for size reduction.

Since the resolving power depends on the light sources, NIM relaxes the requirements on the sensors. As shown in the paper, using a single SPAD detector is enough to obtain images for the small LED array used. Nevertheless, for bigger arrays additional sensors positioned to cover the whole LED array have to be used. This opens the field to play with other CMOS or CCD commercial sensors. Future areas of study could be to use this new microscopy method, NIM, together with other resolution enhancement methods, such as pixel super-resolution. Since the illumination technique consists on using nanoLEDs and each one from the array is individually controllable and addressable, it could also have direct applications for structured illumination microscopy, since it is possible to create a diversity of patterns with them.

## Funding

Horizon 2020 Framework Programme (737089).

## Acknowledgments

This work is being carried out in the European project ChipScope, funded by the European Union's Horizon 2020 research and innovation program under grant agreement no. 737089.

## Disclosures

The authors declare that there are no conflicts of interest related to this article.

## References

1. W. S. Haddad, D. Cullen, J. C. Solem, J. W. Longworth, A. McPherson, K. Boyer, and C. K. Rhodes, "Fourier-transform holographic microscope," *Applied Optics* (2009).
2. W. Xu, M. H. Jericho, I. A. Meinertzhagen, and H. J. Kreuzer, "Digital in-line holography for biological applications," Proc. Natl. Acad. Sci. **41**(25), 5367–5375 (2002).
3. L. Repetto, E. Piano, and C. Pontiggia, "Lensless digital holographic microscope with light-emitting diode illumination," Opt. Lett. **29**(10), 1132–1134 (2004).
4. G. Pedrini and H. J. Tiziani, "Short-coherence digital microscopy by use of a lensless holographic imaging system," *Applied Optics* (2007).
5. A. K. Singh, G. Pedrini, M. Takeda, and W. Osten, "Scatter-plate microscope for lensless microscopy with diffraction limited resolution," Sci. Rep. **7**(1), 10687 (2017).
6. A. Ozcan and E. McLeod, "Lensless Imaging and Sensing," Annu. Rev. Biomed. Eng. **18**(1), 77–102 (2016).

Optics EXPRESS


7. A. C. Sobieranski, F. Inci, H. C. Tekin, M. Yuksekkaya, E. Comunello, D. Cobra, A. Von Wangenheim, and U. Demirci, "Portable lensless wide-field microscopy imaging platform based on digital inline holography and multi-frame pixel super-resolution," Light: Sci. Appl. **4**(10), e346 (2015).
8. C. W. Pirnstill and G. L. Coté, "Malaria Diagnosis Using a Mobile Phone Polarized Microscope," Sci. Rep. **5**(1), 13368 (2015).
9. J. F. Restrepo and J. Garcia-Sucerquia, "Automatic three-dimensional tracking of particles with high-numerical-aperture digital lensless holographic microscopy," Opt. Lett. **37**(4), 752–754 (2012).
10. Y. Wu and A. Ozcan, "Lensless digital holographic microscopy and its applications in biomedicine and environmental monitoring," Methods **136**, 4–16 (2018).
11. M. Born, E. Wolf, A. B. Bhatia, P. C. Clemmow, D. Gabor, A. R. Stokes, A. M. Taylor, P. A. Wayman, and W. L. Wilcock, *Principles of Optics* (Cambridge University, Cambridge, 1999).
12. L. Schermelleh, R. Heintzmann, and H. Leonhardt, "A guide to super-resolution fluorescence microscopy," J. Cell Biol. **190**(2), 165–175 (2010).
13. T. A. Klar and S. W. Hell, "Subdiffraction resolution in far-field fluorescence microscopy," Opt. Lett. **24**(14), 954–956 (1999).
14. M. J. Rust, M. Bates, and X. Zhuang, "Sub-diffraction-limit imaging by stochastic optical reconstruction microscopy (STORM)," Nat. Methods **3**(10), 793–796 (2006).
15. E. Betzig, G. H. Patterson, R. Sougrat, O. W. Lindwasser, S. Olenych, J. S. Bonifacino, M. W. Davidson, J. Lippincott-Schwartz, and H. F. Hess, "Imaging intracellular fluorescent proteins at nanometer resolution," Science **313**(5793), 1642–1645 (2006).
16. A. G. Godin, B. Lounis, and L. Cognet, "Super-resolution microscopy approaches for live cell imaging," Biophys. J. **107**(8), 1777–1784 (2014).
17. Y. Chen, W. Liu, Z. Zhang, C. Zheng, Y. Huang, R. Cao, D. Zhu, L. Xu, M. Zhang, Y.-H. Zhang, J. Fan, L. Jin, Y. Xu, C. Kuang, and X. Liu, "Multi-color live-cell super-resolution volume imaging with multi-angle interference microscopy," Nat. Commun. **9**(1), 4818 (2018).
18. K. I. Mortensen, L. S. Churchman, J. A. Spudich, and H. Flyvbjerg, "Optimized localization analysis for single-molecule tracking and super-resolution microscopy," Nat. Methods **7**(5), 377–381 (2010).
19. A. Von Diezmann, Y. Shechtman, and W. E. Moerner, "Three-Dimensional Localization of Single Molecules for Super-Resolution Imaging and Single-Particle Tracking," Chem. Rev. **117**(11), 7244–7275 (2017).
20. D. Jin, P. Xi, B. Wang, L. Zhang, J. Enderlein, and A. M. van Oijen, "Nanoparticles for super-resolution microscopy and single-molecule tracking," Nat. Methods **15**(6), 415–423 (2018).
21. K. Bermudez-Hernandez, S. Keegan, D. R. Whelan, D. A. Reid, J. Zagelbaum, Y. Yin, S. Ma, E. Rothenberg, and D. Fenyö, "A Method for Quantifying Molecular Interactions Using Stochastic Modelling and Super-Resolution Microscopy," Sci. Rep. **7**(1), 14882 (2017).
22. F. A. Caetano, B. S. Dirk, J. H. Tam, P. C. Cavanagh, M. Goiko, S. S. Ferguson, S. H. Pasternak, J. D. Dikeakos, J. R. de Bruyn, and B. Heit, "MIiSR: Molecular Interactions in Super-Resolution Imaging Enables the Analysis of Protein Interactions, Dynamics and Formation of Multi-protein Structures," PLoS Comput. Biol. **11**(12), e1004634 (2015).
23. H. Ma, R. Fu, J. Xu, and Y. Liu, "A simple and cost-effective setup for super-resolution localization microscopy," Sci. Rep. **7**(1), 1542 (2017).
24. W. G. J. Jerome, *Confocal Digital Image Capture* (Springer International Publishing, Cham, 2018), pp. 155–186.
25. W. Bishara, U. Sikora, O. Mudanyali, T.-W. Su, O. Yaglidere, S. Luckhart, and A. Ozcan, "Handheld, lensless microscope identifies malaria parasites," *SPIE Newsroom* pp. 10–12 (2011).
26. D. W. Pohl, W. Denk, and M. Lanz, "Optical stethoscopy: Image recording with resolution $\lambda/20$," Appl. Phys. Lett. **44**(7), 651–653 (1984).
27. E. Betzig, M. Isaacson, and A. Lewis, "Collection mode near-field scanning optical microscopy," Appl. Phys. Lett. **51**(25), 2088–2090 (1987).
28. L. Novotny, D. W. Pohl, and P. Regli, "Near-field, far-field and imaging properties of the 2D aperture SNOM," Ultramicroscopy **57**(2-3), 180–188 (1995).
29. U. Dürig, D. W. Pohl, and F. Rohner, "Near-field optical-scanning microscopy," J. Appl. Phys. **59**(10), 3318–3327 (1986).
30. P. Bazylewski, S. Ezugwu, and G. Fanchini, "A review of three-dimensional scanning near-field optical microscopy (3D-SNOM) and its applications in nanoscale light management," Appl. Sci. **7**(10), 973 (2017).
31. H. Abramczyk, J. Surmacki, M. Kopeć, A. K. Olejnik, A. Kaufman-Szymczyk, and K. Fabianowska-Majewska, "Epigenetic changes in cancer by Raman imaging, fluorescence imaging, AFM and scanning near-field optical microscopy (SNOM). Acetylation in normal and human cancer breast cells MCF10A, MCF7 and MDA-MB-231," Analyst **141**(19), 5646–5658 (2016).
32. N. Rotenberg and L. Kuipers, "Mapping nanoscale light fields," Nat. Photonics **8**(12), 919–926 (2014).
33. D. Denkova, N. Verellen, A. V. Silhanek, P. Van Dorpe, and V. V. Moshchalkov, "Lateral magnetic near-field imaging of plasmonic nanoantennas with increasing complexity," Small **10**(10), 1959–1966 (2014).
34. F. Huth, M. Schnell, J. Wittborn, N. Ocelic, and R. Hillenbrand, "Infrared-spectroscopic nanoimaging with a thermal source," Nat. Mater. **10**(5), 352–356 (2011).
35. D. Hwang, A. Mughal, C. D. Pynn, S. Nakamura, and S. P. DenBaars, "Sustained high external quantum efficiency in ultrasmall blue III-nitride micro-LEDs," Appl. Phys. Express **10**(3), 032101 (2017).

Optics EXPRESS


36. K. Ogawa, R. Hachiya, T. Mizutani, S. Ishijima, and A. Kikuchi, "Fabrication of InGaN/GaN MQW nano-LEDs by hydrogen-environment anisotropic thermal etching," Phys. Status Solidi A **214**(3), 1600613 (2017).
37. W. Luo, Y. Zhang, A. Feizi, Z. Göröcs, and A. Ozcan, "Pixel super-resolution using wavelength scanning," Light: Sci. Appl. **5**(4), e16060 (2016).
38. A. D. Rakić, "Algorithm for the determination of intrinsic optical constants of metal films: application to aluminum," Appl. Opt. **34**(22), 4755–4767 (1995).
39. H. S. Wasisto, J. D. Prades, J. Gülink, and A. Waag, "Beyond solid-state lighting: Miniaturization, hybrid integration, and applications of GaN nano-and micro-LEDs," Appl. Phys. Rev. **6**(4), 041315 (2019).
40. J. Gülink, S. Bornemann, H. Spende, M. A. der Maur, A. D. Carlo, J. D. Prades, H. S. Wasisto, A. Waag, J. Gülink, S. Bornemann, H. Spende, M. A. der Maur, A. D. Carlo, J. D. Prades, H. S. Wasisto, and A. Waag, "InGaN/GaN nanoLED Arrays as a Novel Illumination Source for Biomedical Imaging and Sensing Applications," Proc. **2**(13), 892 (2018).
41. F. Villa, D. Bronzi, Y. Zou, C. Scarcella, G. Boso, S. Tisa, A. Tosi, F. Zappa, D. Durini, S. Weyers, U. Paschen, and W. Brockherde, "CMOS SPADs with up to 500 μm diameter and 55% detection efficiency at 420 nm," J. Mod. Opt. **61**(2), 102–115 (2014).
42. J. Canals, N. Franch, O. Alonso, A. Vilà, and A. Diéguez, "A Point-of-Care Device for Molecular Diagnosis Based on CMOS SPAD Detectors with Integrated Microfluidics," *Sensors* (Basel, Switzerland) (2019).

### 3.2.6. Publication 2

## A Novel Approach for a Chip-Sized Scanning Optical Microscope

by

Joan Canals[1], Nil Franch[1], **Victor Moro**[1], Sergio Moreno[1], Juan Daniel Prades[1], Albert Romano-Rodríguez[1], Steffen Bornemann[2], Daria D. Bezshlyakh[2], AndreasWaag[2], Florian Vogelbacher[3], Stefan Schrittwieser[3], Katarzyna Kluczyk-Korch[4], Matthias Auf der Maur[4], Aldo Di Carlo[4] and Angel Diéguez[1]

*[1]Department of Electronic and Biomedical Engineering, Universitat de Barcelona, Spain*
*[2]Institute for Semiconductor Technology, University of Technology Braunshweig, Germany*
*[3]Molecular Diagnostics, AIT Austrian Institute of Technology, 1210 Vienna, Austria;*
*[4]Department of Electronic Engineering, University of Rome "Tor Vergata", Italy*

*Published in*
**Micromachines (Basel)** (2021)

micromachines

MDPI

*Article*

# A Novel Approach for a Chip-Sized Scanning Optical Microscope

**Joan Canals [1,*], Nil Franch [1], Victor Moro [1], Sergio Moreno [1], Juan Daniel Prades [1], Albert Romano-Rodríguez [1], Steffen Bornemann [2], Daria D. Bezshlyakh [2], Andreas Waag [2], Florian Vogelbacher [3], Stefan Schrittwieser [3], Katarzyna Kluczyk-Korch [4], Matthias Auf der Maur [4], Aldo Di Carlo [4] and Angel Diéguez [1]**

[1] Department of Electronic and Biomedical Engineering, University of Barcelona, 08028 Barcelona, Spain; nfranch@ub.edu (N.F.); vmoro@ub.edu (V.M.); sergiomoreno@ub.edu (S.M.); dprades@ub.edu (J.D.P.); albert.romano@ub.edu (A.R.-R.); angel.dieguez@ub.edu (A.D.)

[2] Institute of Semiconductor Technology, Technische Universität Braunschweig, 38106 Braunschweig, Germany; steffen.bornemann@tu-bs.de (S.B.); d.bezshlyakh@tu-bs.de (D.D.B.); a.waag@tu-braunschweig.de (A.W.)

[3] Molecular Diagnostics, AIT Austrian Institute of Technology, 1210 Vienna, Austria; vogelbacher@ieee.org (F.V.); stefan.schrittwieser@ait.ac.at (S.S.)

[4] Dipartimento di Ingegneria Elettronica, University of Rome Tor Vergata, 00133 Rome, Italy; katarzyna.kluczyk@uniroma2.it (K.K.-K.); matthias.aufdermaur@uniroma2.eu (M.A.d.M.); aldo.dicarlo@uniroma2.it (A.D.C.)

* Correspondence: canals@ub.edu

**Abstract:** The recent advances in chip-size microscopy based on optical scanning with spatially resolved nano-illumination light sources are presented. This new straightforward technique takes advantage of the currently achieved miniaturization of LEDs in fully addressable arrays. These nano-LEDs are used to scan the sample with a resolution comparable to the LED sizes, giving rise to chip-sized scanning optical microscopes without mechanical parts or optical accessories. The operation principle and the potential of this new kind of microscope are analyzed through three different implementations of decreasing LED dimensions from 20 µm down to 200 nm.

**Keywords:** chip-size microscope; nanoLEDs; scanning optical microscopy; lensless; shadow imaging



**Citation:** Canals, J.; Franch, N.; Moro, V.; Moreno, S.; Prades, J.D.; Romano-Rodríguez, A.; Bornemann, S.; Bezshlyakh, D.D.; Waag, A.; Vogelbacher, F.; et al. A Novel Approach for a Chip-Sized Scanning Optical Microscope. *Micromachines* **2021**, *12*, 527. https://doi.org/10.3390/mi12050527

Academic Editors: Anton Köck and Marco Deluca

Received: 31 March 2021
Accepted: 5 May 2021
Published: 6 May 2021



## 1. Introduction

In the last two decades, on-chip microscopy based on computational imaging has received much attention due to its clear advantages as a low-cost biomedical research and diagnostic tool over conventional optical microscopy by providing high resolution and a large field of view (FOV) simultaneously [1]. Among the different computational microscopy implementations [2], lensless microscopy has been extensively used because of its versatility and flexibility to implement different techniques, from shadow imaging to fluorescence [3–7], while keeping the microscope implementation simpler. Lensless microscopy relies on the traditional microscopy principle, where the analyzed sample area is illuminated homogeneously by a single light source, and the scattered light from each point is collected by an area-selective detector providing the spatial resolution, commonly a high-resolution image sensor. Then, the captured diffracted shadow pattern is used to reconstruct the object image digitally.

The typical lensless scheme requires placing the sample away from the light source (>5 cm) to consider the illumination light as a planar wave and close to the sensor (less than 1mm) to maintain a unit magnification gain to the sensor plane, where the pitch and size of the pixels determine the resolution of the image [8]. However, the spatial resolution of lensless microscopy is reaching its limit. Pixel sizes smaller than 1 µm are challenging to achieve in CMOS technologies [9,10]. To overcome this pixelation limit, several techniques known as pixel-super-resolution have been developed, achieving resolutions below 1 µm by shifting the illumination source [8,11], reaching the diffraction limit by scanning the

illumination angle across a dome surface [12]. Although all these techniques provide a high-resolution image with wide FOV, they require high computational power to reverse-engineer the diffraction patterns into images [13].

A completely new approach to conventional lensless microscopy was presented in [14], where a spatially resolved illumination source provides the microscope resolution instead of the detector system. As depicted in Figure 1, the traditional lensless setup is reversed. A structured light source, composed of homogeneously distributed tiny individually addressable elements, illuminates the sample. Whenever a single emitter is activated, the light propagation depends on the sample morphology directly above it. Therefore, to obtain an image, the light intensity transmitted through the sample region is sensed by an optical detector, activating one light element at a time and thereby scanning across the sample space. If the specimen and the light source are in close contact, the system spatial resolution is mainly determined by the emitter's pitch. Consequently, the constraints in the detector are simplified, and an arbitrary photodetector can be used to collect the transmitted light, since the spatial resolution is given by the illumination source. Thus, the microscope size is reduced to the measurement cavity formed by the key elements: the structured illumination device and the integrated optical detector [15].

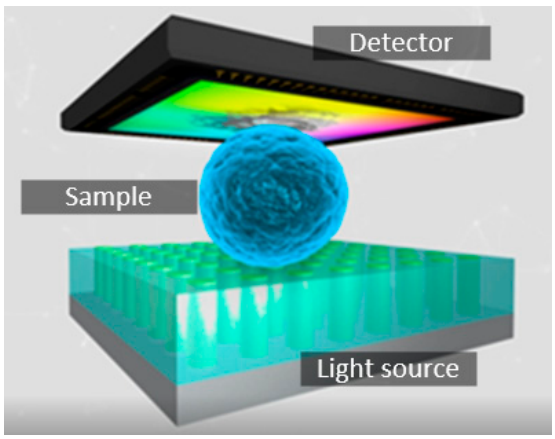


**Figure 1.** Illustration of the spatial resolved illumination-based scanning optical microscope. The specimen lying on the nanoLED chip surface is scanned, while the projected shadow intensity is recorded.

This straightforward technique generates the shadow images without any computational need, since the transmitted light intensity through the sample is mapped directly by the array of light sources. Furthermore, for light element sizes in the nanometer regime, below the diffraction limit, and with the sample in close contact with them, super-resolution imaging may become possible with a chip-based microscope following this approach [16].

In this work, the different components and microscope prototypes built to demonstrate the feasibility of this new type of microscopy are presented. First, the structured light source was achieved by an array of light-emitting diodes (LEDs). Although LEDs have conquered the market for general lighting applications [17] due to their superior characteristics compared to other traditional light systems; e.g., the halogen-based emitters, there are still no structured LED arrays with individually addressable submicron pixels commercially available. Thus, sub-μm LED arrays were developed [18] to build up the first microscope prototypes and validate this new technique. On the other hand, high-sensitive light detectors are required to detect the light emitted by the submicron LEDs. Several CMOS cameras, including CMOS single-photon avalanche diode (SPAD), were used in the prototypes. Although in this work, we present prototypes working in the blue range of the

visible spectrum, this new microscopy method will work independently of the wavelength of the light being emitted, as long as the light source and the sensor are compatible.

In particular, we focused on the implementation of three microscope prototypes, each based on unique LED arrays with different pixel sizes, pitch, and array elements, demonstrating the potential to implement a true chip-sized scanning optical microscope without moving parts. In the following subsections, we describe the implementation and characteristics of the different microscopes' setups and their operation principles to finally present their major results.

## 2. Materials and Methods

### *2.1. Microscope Architecture Overview*

As mentioned above, the three microscope setups were assembled based on three different LED array configurations to explore the technology potential progressively. Through all the microscope versions, the system architecture was maintained, since the microscope principle is the same for all of them. Figure 2 shows the basic microscope stack-up structure implemented, with the sample laying over the LED array chip and the optical sensor on top collecting the transmitted light. The architecture was designed modularly to provide flexibility to test each microscope element independently and allow easy replacement without compromising the rest of the system. To that end, each component of the microscopes was implemented on a separated printed circuit board (PCB) carrier. All the key elements of the setup (LEDs, the drivers, and the CMOS sensor) were connected to an FPGA board. The FPGA controls the microscope operation, with all the routines such as image acquisition, calibration, and test procedures implemented at the hardware level, relegating the computer to displaying images and selecting configuration settings through the graphical user interface.

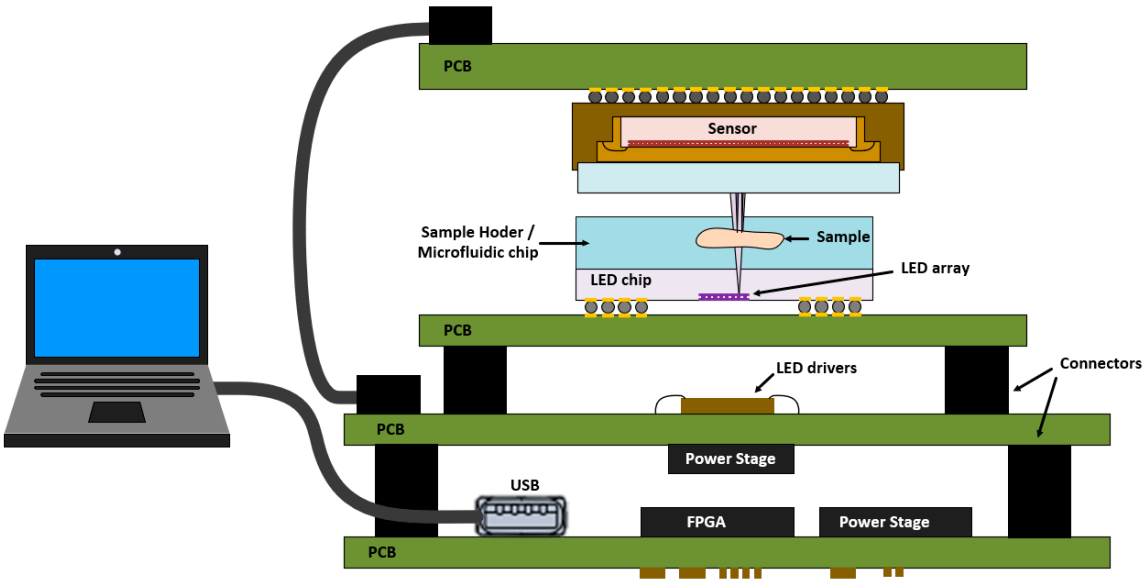


**Figure 2.** Scheme diagram of the basic stack-up structure used in all the microscopes.

#### 2.1.1. LED Chips

Three different planar GaN-based blue LED array architectures using direct and matrix addressing were constructed. With direct addressing, each LED of the array is individually driven through a specific contact line, requiring N × M connections for an N × M size array. In contrast, in matrix addressing, each LED is selected through its row and column

contact lines, reducing the number of control signals to N + M for the same array. The emission peak for all the LED chips was centered at 450 nm.

The first LED array, named Led1, implemented a direct-addressing approach in an 8 × 8 array. The LEDs had a square shape with 5 µm sides, regularly spaced with a 10 µm pitch (Figure 3a). The final chip had 8 n-contact pads running as a common n-GaN contact and 64 p-contacts surrounding the LED array, and presented a cut size of 1 cm × 1 cm. The fabrication process was the metal-oxide-GaN (MOGaN) process reported in [17], which employed an insulating layer of $SiO_2$, which was opened up via photolithography and etching steps to define the p- and n-contact areas. The metal stacks of the n- and p-contacts were optimized to ensure proper ohmic contact. Finally, each gold-terminated pixel was connected to one p-contact pad via a gold lead. Since the Led1 presented a land grid array (LGA) contact pattern, it was assembled to the carrier PCB using a low-temperature bonding process based on standard industry stencil printing [19], but using a silver-based conductive epoxy (CW2400 from Chemtronics Circuit Works, Kennesaw, GA, USA) instead of solder paste. The procedure adopted avoided the stress generated on the contact pads by the different expansion rates of the sapphire and the PCB, produced in a standard flip-chip reflow soldering [20], which may damage the contact pad.

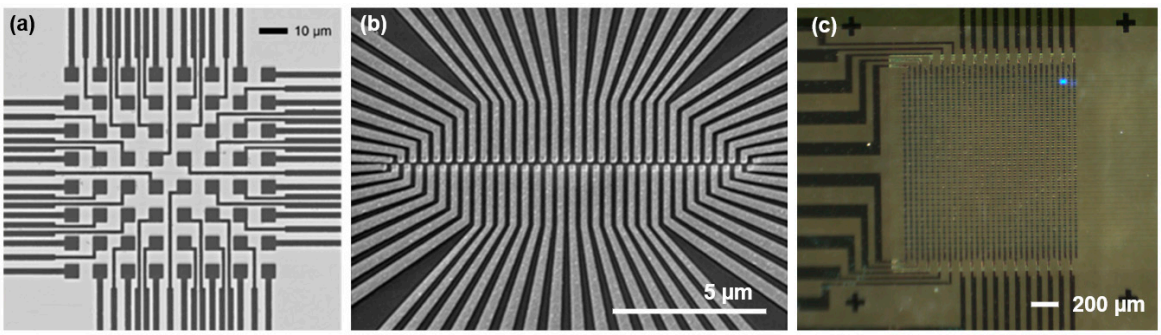


**Figure 3.** (**a**) Led1: direct addressing LED array chip with 8 × 8 5 µm pixels regularly spaced at 5 µm. (**b**) Led2: 2 × 32 direct-addressing linear array LED chip with pixels sized 200 nm. (**c**) Led3: 32 × 32 matrix-addressing LED array of 20 µm pixel size and pitch.

The second LED chip, Led2, consisted of 2 × 32 direct addressable 200 nm nanoLEDs with a 400 nm pitch. The array configuration illustrated in Figure 3b presented a shift of 200 nm in the alignment of the columns of the different rows to give an effective pitch of 200 nm when a sample crossed perpendicular to the array. The final chip size was 7.1 × 8.5 mm with 64 p-pads and 4 n-pads located on the chip's sides, at a distance of 6 mm. The fabrication process was the same as that of Led1, but using electron beam lithography (EBL) instead of photolithography, which was necessary to achieve submicron LED structures as detailed in [21].

The third LED chip (Led3) followed a completely different architecture. It consisted of 32 × 32 matrix-addressable 20 µm LEDs spaced 20 µm. The fabrication process relied on deep-etching parallel fins into a GaN-wafer down to the underlying sapphire, ensuring electrical insulation between the fins, which functioned as n-contact lines [22]. To do so, a Cr hard mask was deposited to define the fin structure. Next, the n-contact openings were defined at the ends of the fins by an additional etching step. Before applying orthogonal metal lines on top of the fins, the space between the fins was filled with benzocyclobutene (BCB), which acted as an insulating polymer. A mechanical polishing was performed down to the Cr mask to ensure good planarity of the surface. After the planarization step, the chip surface was insulated with an SU-8 with openings directly over the array area and at the larger end of the fins, where n-contact pads were subsequently created by etching the BCB down to the n-GaN and applying Ti/Au metal stack. Finally, orthogonally running p-contact lines were done by the usual lift-off process, applying Pd and Au for ohmic

p-contacts (a semitransparent metal stack), and a final insulating SU-8 layer to protect the metal contact lines. The Led3 chip (Figure 3c) was designed to have the same configuration as the Led2 chip, the same dimensions, and pad layout, placing all the p-contacts on the right side and the n-contacts on the left.

#### 2.1.2. LED Array Driver

In order to control the different LED arrays, a specific driver chip (from here on, called the driver) was fabricated in a 0.35 µm HV-CMOS process. The driver consisted of 64 anode and 32 cathode driving circuits arranged in a single chip of 1.76 mm × 7.32 mm (Figure 4). The driving circuits were distributed in three rows across the chip, where the outer ones were the anode drivers and the central row the cathode. Thus, the driver chip could manage up to 64 direct addressable or 32 × 32 pixels with a matrix-addressing scheme. Both drivers could generate pulses (from an external trigger signal) with selectable amplitude from 3.3 V up to 10 V and widths down to 700 ps and 10 ns at full width half maximum (FWHM) for the anode and cathode driver, respectively. The cathode driver was designed to maintain a positive voltage (between 3.3 V to 10 V) to the unselected LEDs, preventing them from turning on while generating a reverse pulse (from bias voltage to 0 V) on the selected LED.

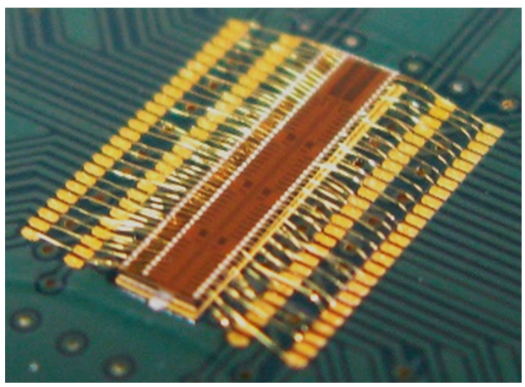

**Figure 4.** Integrated HV-CMOS LED driver chip, wire-bonded in a matrix-addressing configuration.

#### 2.1.3. Optical Detector

As a further component, a CMOS SPAD camera was designed in a 0.35 µm HV-CMOS process. The camera was composed of an array of 16 × 16 pixels, with each pixel including the 10 µm diameter sensor, the readout, and control electronics. Each pixel's output was connected to a dedicated 8-bit counter per pixel and bridged directly to one common output for all the pixels. The designed pixel presented a dark noise of 200 Hz and a photo-detection probability of 10% at 450 nm [23]. The low profile provided by the bare die directly wire-bonded on a custom PCB (Figure 5) allowed us to place the image sensor as close as possible to the sample.

Alternatively, a commercial CMOS image sensor was also used as a light sensor due to the advantages it provided: a bigger FOV for searching the area of interest, relaxation of the system alignment, and the possibility to define the sensing area size and position. The used sensor was the Aptina MT9V024 camera module (from OnSemiconductor®, Phoenix, AZ, USA). The sensor has a monochromatic array of 744 × 488 pixels of 6 µm with an 8-bit dynamic range, resulting in a 4.55 mm × 2.97 mm sensing area. The pixel array implemented a global shutter that could provide 76 fps at full resolution. The sensor was mounted on a commercial board (DMM-22BU, C03-ML, from The Imaging Source Europe GmbH, Bremen, Germany) and was controlled through a USB interface.

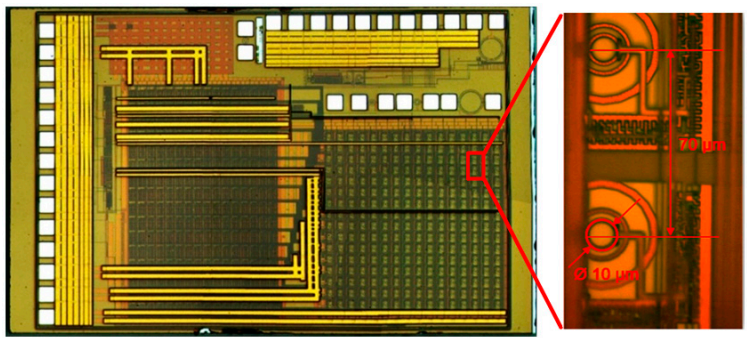


**Figure 5.** CMOS SPAD camera with a detail of the 10 µm circular pixels.

### *2.2. Microscope Operation*

#### 2.2.1. Transmission Image Reconstruction

The transmission images of the sample region directly over the LED array were generated as follows. The LEDs were sequentially switched on and off, scanning the sample. One frame of the image sensor was acquired per each LED. The same sensing area of N × N pixels of each frame was selected to measure the total intensity emitted per LED through the sample. Finally, the measured intensities were arranged to create an N × M (the size of the LED array) transmission image that offered information about the shape of the object under investigation at these particular LEDs-on positions. Figure 6 illustrates the transmission image reconstruction using Led1 and the MT9V024 CMOS image sensor. Figure 6b shows the composition of raw lensless shadow images of the structure (Figure 6a) under study generated by each LED (with the common sensing area highlighted in red), and Figure 6c shows the reconstructed transmission image by integrating the intensity in the sensing area (9 × 9 pixels) for each LED and arranging them according to their position within the LED array.

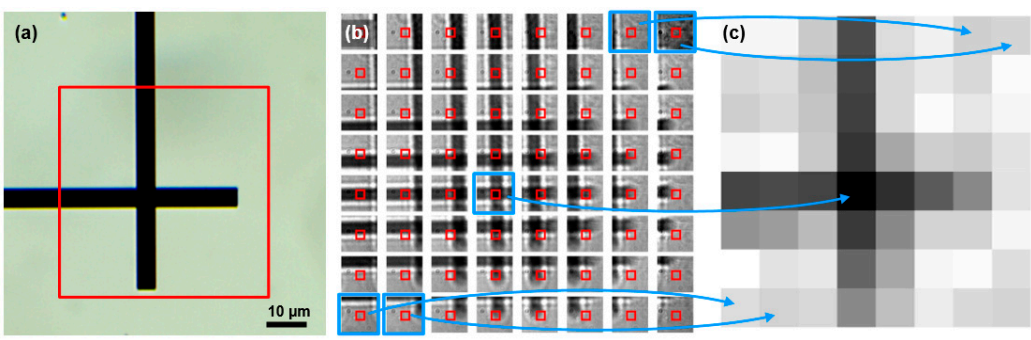


**Figure 6.** Transmission image reconstruction of the intersection of two lines of 5 µm width using the Led1 and MT9V024 image sensor as a light collector. The sensing area used was 9 × 9 pixels. (**a**) Optical image of the intersection of two lines of 5 µm width with the observed area highlighted in red. (**b**) Composition of the different raw shadow images generated by each micro-LED with the sensing area highlighted in red. (**c**) Reconstructed transmission image using the spatially resolved illumination.

The quality of the reconstructed image in terms of contrast is limited by the relationship of the distances between the sensor, the sample, and the light sources, as well as the size of the detection area, as shown in [20], where this technique was reported for the first time. To produce sharper contrasted images, the sample should be placed as close as possible to the light sources, and the size of the observed objects must be larger than twice the LED pitch according to sampling theory. Otherwise, poor contrasted images are obtained, which could present aliasing in a limit case.

#### 2.2.2. LED Array Equalization

Since the emission of the LEDs in a single array can vary by more than 30%, it is essential to equalize them for correct image reconstruction. For this purpose, each LED emission was dimmed by pulse width modulation (PWM) to a user-defined target intensity, reducing the inhomogeneity in the array emission below 2%. The PWM period must be higher than the measurement window of the photodetector used (the exposure time in the CMOS sensors) to avoid detecting light modulation. First, the camera was fixed over the LED array in the distances necessary for the measurement, but without a sample inserted. Next, the sensing area (size and position) and the target intensity were selected, taking care to avoid saturating the sensor and using a small sensing area centered with the LED array, since they had a direct impact on the contrast of the reconstructed image [24]. Once the camera position and all user-defined parameters were set, each LED was individually turned on, and its intensity was measured and equalized by varying the duty cycle of the PWM driving signal until it matched the target intensity. The resulting duty cycles associated with each LED were stored in a look-up-table for later use during image acquisition.

### *2.3. Test Sample*

As is often the case in scanning microscopy techniques, the areas studied were mainly the surfaces of samples. Thick objects can also be partially observed, but with less resolution because the information from thick objects is lost as soon as the light is absorbed within the sample. Given this, and that the structure of the scanning LED array was fixed on the plane, this microscopy method was suited only for samples as flat and thin as possible. To validate the prototypes, a set of patterns (with structures from 50 nm up to 20 µm) fabricated by aluminum EBL was used to characterize the resolution of the microscopes.

The EBL sample fabrication was performed on device-quality 4" fused silica wafers (0.525 mm thick). First, the wafer was dehydrated in an oven at 250 °C for 2 h. Next, a nominally 180 nm-thick CSAR-P6200-09 positive photoresist was spun at 4000 rpm for 1 min and cured at 180 °C for 3 min. Before the exposure with a beam current of 2 nA, a 20 nm-thick aluminum layer was thermally evaporated at 0.3 nm/s to reduce charge build-up in the wafers. The aluminum layer was removed by a 60" single bath in a 2.38% tetramethyl–ammonium hydroxide solution, and the development of the CSAR photoresist was done using the developer AR 600-546 for 1 min. The sample was further covered by a 40 nm-thick electron-beam evaporated chromium layer, deposited at 0.5 nm/s. Finally, the lift-off of the deposited metal was achieved in Remover 1165 at 45 °C for 20 min, followed by rinsing in isopropyl alcohol.

## 3. Results

### *3.1. First Microscope Generation*

The first microscope was based on the Led1 chip and the CMOS SPAD camera. For this implementation, the Led1 chip was fixed at the bottom, whereas the sample rested on the sapphire substrate with two (XY) degrees of freedom. The camera was positioned on top of the stack-up by means of the XYZ microstager. A custom 3D-printed sample holder was designed to move the sample in direct contact with the Led1 chip. The rest of the setup was fabricated, including the two microstages used to align the sample and the camera with the LED chip, by a 3D aluminum computer numeric control (CNC) machining. The setup was enclosed in a dark box measuring $31 \times 21 \times 12$ cm$^3$ (Figure 7).

A complete analysis and characterization of this microscope were reported in [22]. N. Franch et al. validated the technique, demonstrating that the principle of the microscope relied on the close contact of the sample under study with the LED array, providing a spatial resolution (the ability to identify two nearby objects) of two times the LEDs' pitch, and a FOV determined by the size of the LED array used.

As in scanning microscopy techniques, the time to construct an entire image depends on the number of scanning steps (64, total LEDs of the array) and the time each step takes. For this first prototype, the scanning speed was 1000 LED/s (or samples per second).

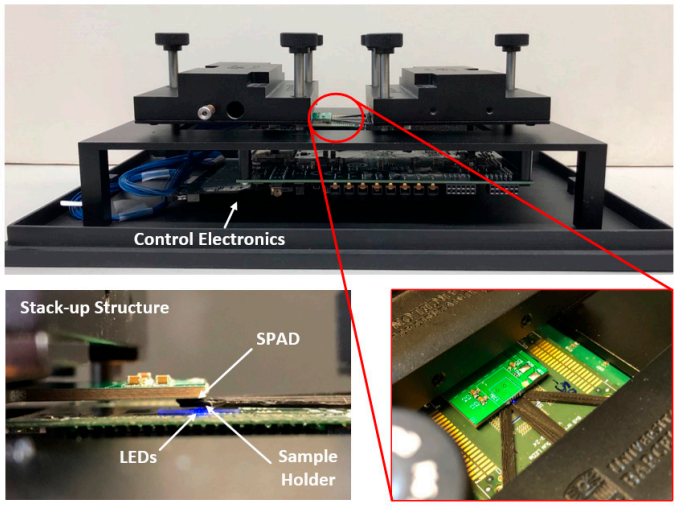


**Figure 7.** Setup of the first-generation microscope with a detail of the stack-up composed by the Led1 chip, sample/sample holder, and CMOS SPAD camera.

Figure 8 shows the smallest resolved patterns observed (an array of 6.4 µm squares) with this microscope setup. The poor quality of the reconstructed image compared to the optical one was, according to sampling theory, because the size and periodicity of the squares were similar to the size and pitch of the LEDs (6.4 µm/12.8 µm and 5 µm/10 µm, respectively). Therefore, the 6.4 µm squares were not imaged correctly in the central area because they were aliased. Additionally, the FOV for this setup was smaller than the LED array size because the microscope was operated in far-field conditions since the emission of the LEDs was through the sapphire substrate. This set a vertical distance between the sample and the LED array of 300 µm, which, conjointly with the sample-sensor distance (~600 µm) and the sensing area used (a single 10-µm SPAD detector), reduced the FOV from $75 \times 75$ µm$^2$ down to $53.4 \times 53.4$ µm$^2$.

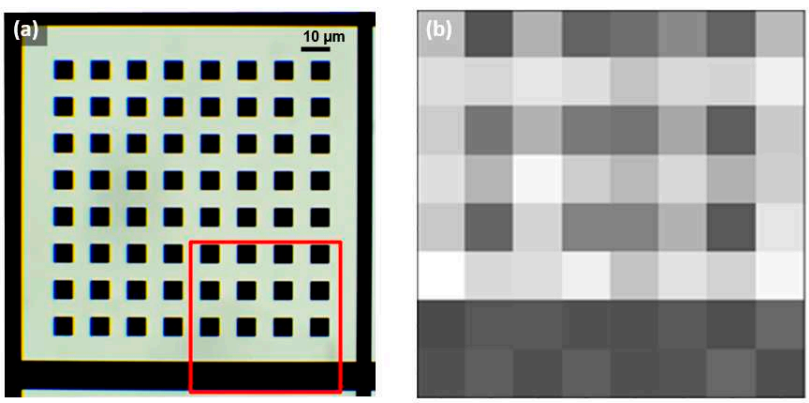


**Figure 8.** (**a**) Optical image of the EBL pattern of 6.4 µm squares regular spaced at 6.4 µm, with the observed region highlighted in red. (**b**) Image reconstructed with the microscope prototype based on the 8 × 8 5 µm LED array chip (Led1), which presented aliasing, indicating the limit to observe periodic objects of sizes comparable to the LED.

### 3.2. Second Microscope Generation

The second microscope generation was based on the Led2 chip. Unlike Led1, the Led2 chip configuration allowed the emission through the p-contact metal lines, reducing the critical distance (emitter-sample) to the minimum. Another problem faced with the first generation was the limited FOV of the array, which in this case was critical due to the smaller pixel size (200 nm) and the array configuration of Led2 (2 rows of 32 elements). However, the Led2 chip was designed as a high-resolution scanning line array, which required moving the sample orthogonally over it, thus extending the FOV. Therefore, a custom sample holder attached to a nanopositioning system was fabricated (by 3D aluminum CNC machining) to move and hold the sample in direct contact with the LEDs inside the observation cavity. The nanopositioning system was formed by a compact XY piezo stage (P-621.2CD, from Physik Instrumente GmbH & Co. KG, Karlsruhe, Germany) stacked on a vertical Z piezo stage (P-621.2ZCD, from Physik Instrumente). Both actuators presented a 0.1 nm resolution and 100 µm travel range, with a positioning accuracy of 0.02%. To extend the movement range for coarse position of the sample, XY micropositioning stages were integrated into the microscope shield (Figure 9a).

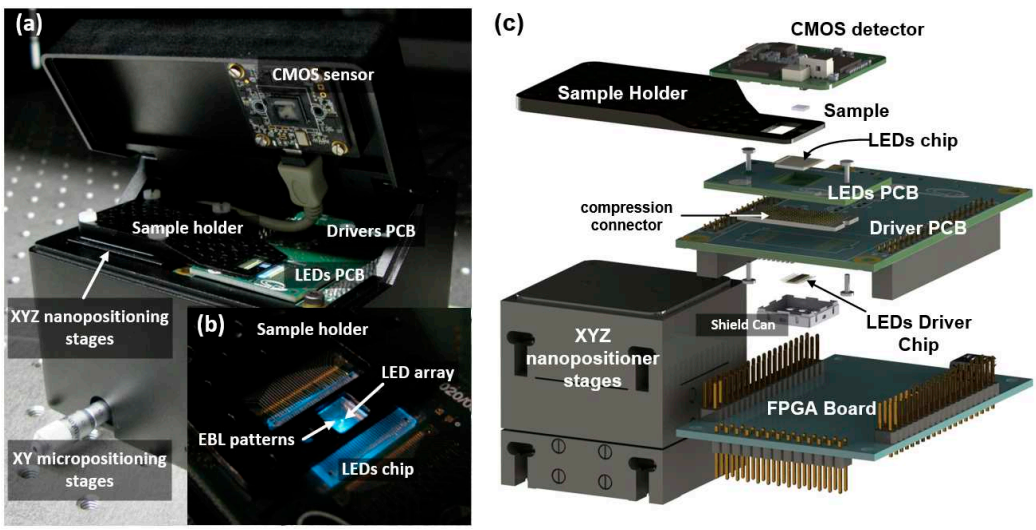


**Figure 9.** (**a**) Image of the microscope configuration with nanopositioner stages to extend the FOV, and (**b**) a detail of the sample over the LED array. (**c**) Exploded view of the second generation microscope stack-up structure with nano-stages.

The speed of this second microscope was only 20 LEDs/s. Nevertheless, this setup was not aimed at maximizing the scanning speed, but to study the resolution improvement using smaller LEDs.

As shown in Figure 9c, the implementation presented the basic stack-up structure of the first generation. However, in this setup, the Led2 chip was placed in a recess on the PCB (providing a flat surface with the PCB for the sample holder) and wire bonded to it (Figure 9b). The connection to the LED driver PCB was made through an ultra-low-profile compression connector (ZA1-20-2-1.00-Z-10 from SAMTEC Inc., New Albany, IN, USA), simplifying the LED carrier board to its bare minimum without any other components (not even a connector). At the bottom, the LED drivers were wire-bonded and protected with a shield cap. The entire setup was enclosed in a custom aluminum CNC-machined case (measuring $11 \times 8.7 \times 7.4$ cm$^3$) that provided the dark environment required for the measurement. The CMOS sensor used (the MT9V024) was attached to the hatch, allowing direct access to the LED chip and the sample when open, and placing the sensor at 1.9 mm from the LED surface when closed.

With this setup, smaller EBL structures were observed (Figure 10a). However, due to the performance of the LED array in which only a few LEDs worked, we decided to use only one LED and perform a 2D scan by moving the sample, emulating a larger LED array. Figure 10a shows the reconstructed image of the EBL pattern region with 1.6 μm and 6.4 μm squares, using a step size of 200 nm in both directions. The spatial resolution was determined by the edge spread function (ESF) and line spread function (LSF) methods [25] measured between 10–90%. The extracted resolution from one of the 1.6 μm square's edges was 1.56 μm (Figure 10b), four times the expected resolution (400 nm), since the sample was placed directly over the nanoLEDs. However, further analysis of the nanoLED array configuration (by finite difference time domain simulations [26]) showed that the metal structure and the depth of the light emitter region affected the spot shape and size at the chip surface, degrading the resolving power of the setup.

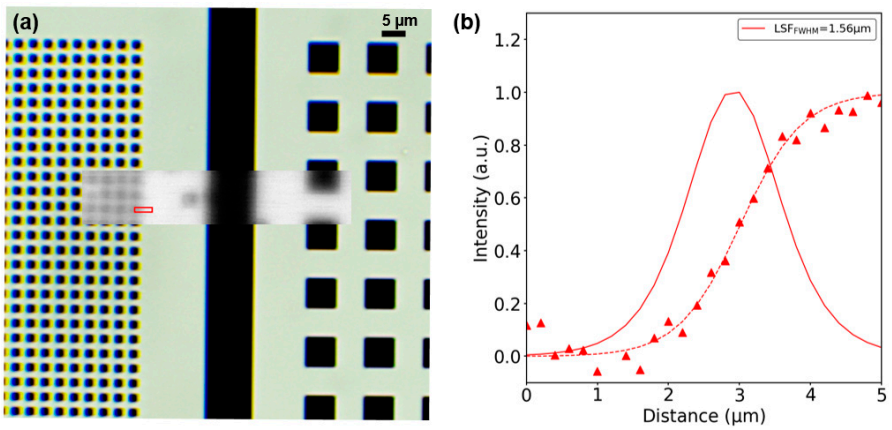


**Figure 10.** (**a**) Optical image of the 1.6 μm (left) and 6.4 μm (right) squares of the EBL pattern, with the reconstructed image of the same region superposed. (**b**) The ESF and the LSF calculated on the specified region of the inset image.

The poor reconstruction of the 1.6 μm squares in Figure 10 was because the size of the light spot was comparable to the observed squares and their periodicity, thus reducing the contrast of the image in this region, even when scanning with a step eight times smaller (200 nm). This showed that the image quality (in terms of contrast and resolution) did not depend only on the LED pitch, but also on the light spot size on the sample plane.

### *3.3. Third Microscope Generation*

The third microscope generation was not designed to improve the resolving power of the microscope. Instead, the intent was to study a matrix-addressing connection, thanks to which the FOV was much larger with the same number of connections, taking aside the size of the pixel, since each pixel was addressed by its column and row contact lines. A total of 1024 pixels arranged in a 32 × 32 array were addressed using only 64 driving circuits. Thus, the control electronics for large arrays were simplified while solving the scalability problem presented by the direct-addressing approach. Furthermore, this implementation shows the simplicity of measurement and easy sample positioning for large arrays.

The microscope was implemented using the matrix-addressing Led3 chip. Since the Led2 and Led3 chips were designed to have compatible configurations (die size and contact pads layout), the Led3 chip was compatible with the second-generation microscope setup, with two minor changes. First, the LED driver connection was changed because the matrix scheme required 32 cathode drivers and 32 anode drivers, and second, a minor upgrade of the FPGA firmware was implemented according to the new driving scheme.

Figure 11 shows a reconstructed image of an EM-Tec TEM support grid (200 mesh with 90 μm holes and 37 μm bars) placed directly over the LED array without any holder.

The scanning speed was 60 LEDs per second, determined by the frame rate of the camera used. The reconstructed image presented some dead pixels (black ones) and vertical artifact lines due to emissions from some p-contact lines (identified by red arrows in Figure 11c), directly affecting the image quality in contrast and reconstruction. This reflected how, in the matrix-addressing approach, a failure in a contact line had a high impact on image reconstruction, since a whole line of the LEDs was affected, as opposed to direct addressing, where only one LED/pixel from the resulting image was affected. Even so, the edge of the grid and the mesh can be identified on the top left side of Figure 11c. However, the TEM grid used was at the limit of the resolution of this microscope (based on Led3: 32 × 32 20 µm LED array with 40 µm pitch) according to the previous results. The spatial resolution extracted by the ESF and LSF methods measured between 10–90% was 42 µm (Figure 11d), showing that in this case, the pitch of the LEDs was the limiting factor instead of the size of the light spot. Therefore, to resolve two objects, they must be spaced at at least twice the pitch of the LEDs. As shown in Figure 11c, the mesh bars were not correctly sampled, and not all spaces between bars were sampled equally, affecting the contrast of the image, which was already poor because of the defective pixels on the LED array.

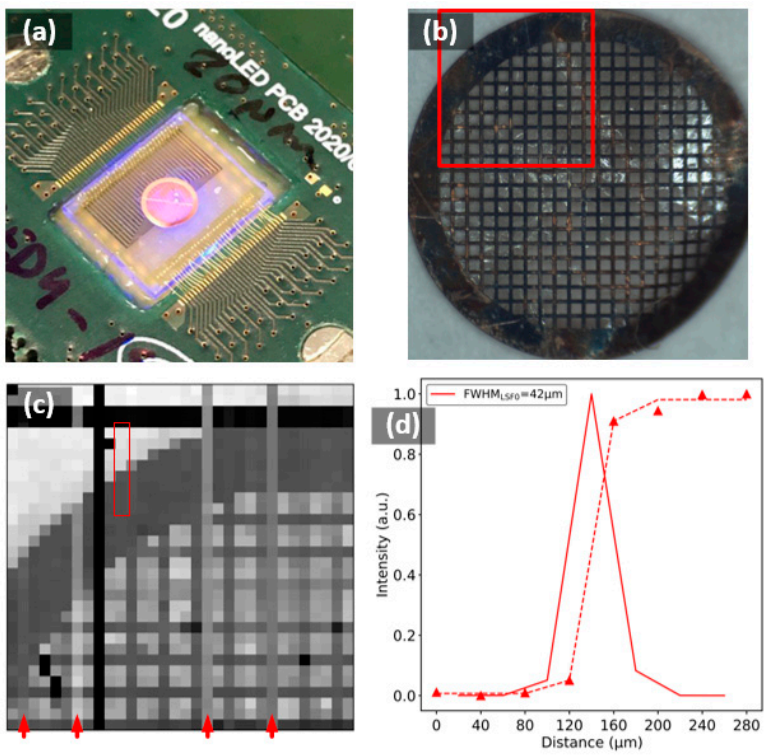


**Figure 11.** (**a**) EM-Tec TEM over the Led3 chip. (**b**) EM-Tec TEM square mesh support grids, 200 mesh, 90 µm hole, 37 µm bar with the observed area highlighted. (**c**) Reconstructed ChipScope image of the highlighted region with 20 µm Led3 version. The red arrows indicated the vertical artifact lines due to emissions coming from some p-contact lines. (**d**) The ESF and the LSF calculated on the specified region of the image in (**c**).

## 4. Discussion

In summary, we have presented a new approach toward on-chip scanning optical microscopy, based on the miniaturization of light sources instead of the sensor geometry. The novelty of this technique relies on the use of individually addressable nanoLEDs to scan the sample in close contact to provide a direct mapping of the sample without

requiring focusing systems or mobile parts, and just measuring the received intensity. The presented devices allow us to observe samples unresolvable by plain human sight, offering information about the structure observed. The resolving power of microscopes constructed using this technique is set, in accordance with sampling theory, by the distribution of the LEDs, and for the microscopes constructed so far, this went from being able to resolve 20 µm objects in the first prototype down to 3.2 µm with the second generation.

Since the resolving power relies on the light sources, the proposed technique relaxes the requirements on the sensor side, where an arbitrary detector can be used. Nevertheless, a multiple pixel sensor provides significant advantages over using a single one as in [22], such as sample previsualization, variable sensing, and multiple sensing areas. Furthermore, the straightforward implementation of this technique without image postprocessing makes it ideal for integration, enabling a true low-cost chip-size microscope, as opposed to other microscope techniques based on the transport of intensity equation [27], such as ptychography [7] or digital holographic microscopy and its variants [28–30], which combine wide FOV with submicron resolution, and even 3D reconstruction, which requires complex optical setups and high computational power to recover the image.

The operation principle was validated using three different LED array configurations, showing that the system resolution was primarily determined by the LEDs' size and pitch, with the sample placed in contact with the emitters. Although the presented prototypes had a small FOV, and the submicron resolution was not achieved even with 200 nm LED arrays, there is still room for improvement by adopting different strategies; i.e., using transparent conductive oxides for the contact lines, thinning the insulating layer between the metal pattern and the LED structure, and of course, reducing the LED size.

However, the future of this new kind of microscope relies on the matrix-addressing approach thanks to its scalable nature. Matrix addressable arrays have the potential to create large arrays of thousands of nanoLEDs. Compared to current microdisplay technology that implements a hybrid interconnection to solve the routing problem of direct addressing [31], matrix addressing performs even better because it leverages the limit of the CMOS backplane circuits as well [25]. With matrix addressing, the number of connections is minimized, simplifying the interconnection scheme and, consequently, driving electronics.

While a large FOV is desirable, it increases scanning time by the same proportion, a problem that should be tackled. Since LEDs have been shown to be able to switch at MHz [32], the limiting factor for scanning speeds is in the sensor used, with standard CMOS sensors showing frame rates usually between 30 fps up to 1000 fps, which bounds the scanning speed to this same number of pixels per second. So far, the prototypes presented are slower compared to other optical-scanning techniques, such as scanning confocal microscopy, which presents a scanning speed of hundreds of kSamples/s, acquiring an image in few seconds [33]. However, the image-acquisition speed was not considered, since the aim was to validate the proposed method and study the resolving power and how to improve the FOV.

**Author Contributions:** Conceptualization, A.D., A.D.C., J.D.P., and A.W.; resources, F.V. and S.S.; LED chip design, S.B. and D.D.B.; LED integrated drivers, V.M.; SPAD CMOS camera, N.F.; EBL sample, designed by N.F. and A.D. and manufactured by A.R.-R.; software, S.M. and J.C.; simulations and formal analysis, K.K.-K., M.A.d.M., and N.F; methodology, N.F. and J.C.; experiments—investigation, N.F., S.M., and J.C.; writing—original draft preparation, J.C.; writing—review and editing, J.C. and A.D.; principal investigator and research supervisor, A.D. All authors have read and agreed to the published version of the manuscript.

**Funding:** This research was funded by the European Union's Horizon 2020 research and innovation program within the project of ChipScope under grant agreement no. 737089, as well as the APC.

**Institutional Review Board Statement:** Not applicable.

**Informed Consent Statement:** Not applicable.

**Data Availability Statement:** Data sharing not applicable.

**Acknowledgments:** This work was supported by the European Union's Horizon 2020 317 research and innovation program under grant agreement no. 737089—ChipScope.

**Conflicts of Interest:** The authors declare no conflict of interest.

## References

1. McLeod, E.; Ozcan, A. Microscopy without Lenses. *Phys. Today* **2017**, *70*, 51–56. [CrossRef]
2. McLeod, E.; Ozcan, A. Unconventional Methods of Imaging: Computational Microscopy and Compact Implementations. *Rep. Prog. Phys.* **2016**, *79*, 076001. [CrossRef]
3. Zhang, X.; Khimji, I.; Gurkan, U.A.; Safaee, H.; Catalano, P.N.; Keles, H.O.; Kayaalp, E.; Demirci, U. Lensless Imaging for Simultaneous Microfluidic Sperm Monitoring and Sorting. *Lab Chip* **2011**, *11*, 2535–2540. [CrossRef]
4. Dolega, M.E.; Allier, C.; Kesavan, S.V.; Gerbaud, S.; Kermarrec, F.; Marcoux, P.; Dinten, J.-M.; Gidrol, X.; Picollet-D'hahan, N. Label-Free Analysis of Prostate Acini-like 3D Structures by Lensfree Imaging. *Biosens. Bioelectron.* **2013**, *49*, 176–183. [CrossRef]
5. Stybayeva, G.; Mudanyali, O.; Seo, S.; Silangcruz, J.; Macal, M.; Ramanculov, E.; Dandekar, S.; Erlinger, A.; Ozcan, A.; Revzin, A. Lensfree Holographic Imaging of Antibody Microarrays for High-Throughput Detection of Leukocyte Numbers and Function. *Anal. Chem.* **2010**, *82*, 3736–3744. [CrossRef]
6. Coskun, A.F.; Sencan, I.; Su, T.-W.; Ozcan, A. Lensless Wide-Field Fluorescent Imaging on a Chip Using Compressive Decoding of Sparse Objects. *Opt. Express* **2010**, *18*, 10510. [CrossRef] [PubMed]
7. Jiang, S.; Zhu, J.; Song, P.; Guo, C.; Bian, Z.; Wang, R.; Huang, Y.; Wang, S.; Zhang, H.; Zheng, G. Wide-Field, High-Resolution Lensless on-Chip Microscopy via near-Field Blind Ptychographic Modulation. *Lab Chip* **2020**. [CrossRef] [PubMed]
8. Bishara, W.; Su, T.-W.; Coskun, A.F.; Ozcan, A. Lensfree On-Chip Microscopy over a Wide Field-of-View Using Pixel Super-Resolution. *Opt. Express* **2010**, *18*, 11181. [CrossRef] [PubMed]
9. Takahashi, S.; Huang, Y.-M.; Sze, J.-J.; Wu, T.-T.; Guo, F.-S.; Hsu, W.-C.; Tseng, T.-H.; Liao, K.; Kuo, C.-C.; Chen, T.-H.; et al. A 45 Nm Stacked CMOS Image Sensor Process Technology for Submicron Pixel. *Sensors* **2017**, *17*, 2816. [CrossRef]
10. Kapusta, P.; Wahl, M.; Erdmann, R. *Advanced Photon. Counting: Applications, Methods, Instrumentation*; Kapusta, P., Wahl, M., Erdmann, R., Eds.; Springer: Berlin/Heidelberg, Germany, 2015; ISBN 978-3-319-35429-3.
11. Barnard, K.J.; Barnard, K.J.; Bognar, J.G.; Armstrong, E.E.; Watson, E.A. High-Resolution Image Reconstruction from a Sequence of Rotated and Translated Frames and Its Application to an Infrared Imaging System. *Opt. Eng.* **1998**, *37*, 247. [CrossRef]
12. Luo, W.; Greenbaum, A.; Zhang, Y.; Ozcan, A. Synthetic Aperture-Based on-Chip Microscopy. *Light Sci. Appl.* **2015**, *4*. [CrossRef]
13. Ozcan, A.; McLeod, E. Lensless Imaging and Sensing. *Annu. Rev. Biomed. Eng.* **2016**. [CrossRef]
14. EU Funded Research Project ChipScope. Overcoming the Limits of Diffractionwith Super-Resolution Lighting on a Chip. 737089. 2020. Available online: www.chipscope.eu (accessed on 31 March 2021).
15. Auf der Maur, M.; Palazzo, D.; Gülink, J.; Bornemann, S.; Wasisto, H.S.; Reale, A.; Prades, J.D.; Waag, A.; di Carlo, A. Towards Super-Resolution Illumination from InGaN/GaN NanoLED Arrays. In *Light-Emitting Devices, Materials, and Applications*; Kim, J.K., Krames, M.R., Strassburg, M., Eds.; SPIE: San Francisco, CA, USA, 2019.
16. Wasisto, H.S.; Prades, J.D.; Gülink, J.; Waag, A. Beyond Solid-State Lighting: Miniaturization, Hybrid Integration, and Applications of GaN Nano-and Micro-LEDs. *Appl. Phys. Rev.* **2019**, *6*, 41315. [CrossRef]
17. Bezshlyakh, D.D.; Spende, H.; Weimann, T.; Hinze, P.; Bornemann, S.; Gülink, J.; Canals, J.; Prades, J.D.; Dieguez, A.; Waag, A. Directly Addressable GaN-Based Nano-LED Arrays: Fabrication and Electro-Optical Characterization. *Microsyst. Nanoeng.* **2020**, *6*, 1–10. [CrossRef]
18. Grist, S.M.; Nasseri, S.S.; Laplatine, L.; Schmok, J.C.; Yao, D.; Hua, J.; Chrostowski, L.; Cheung, K.C. Long-Term Monitoring in a Microfluidic System to Study Tumour Spheroid Response to Chronic and Cycling Hypoxia. *Sci. Rep.* **2019**, *9*, 1–13. [CrossRef] [PubMed]
19. Rodriguez, G.; Rodriguez, D.F. Analysis of Solder Paste Release in Fine Pitch Stencil Printing Processes. *J. Electron. Packag. Trans. ASME* **1999**, *121*, 169–178. [CrossRef]
20. Madenci, E.; Shkarayev, S.; Mahajan, R. Potential Failure Sites in a Flip-Chip Package with and without Underfill. *J. Electron. Packag. Trans. ASME* **1998**, *120*, 336–341. [CrossRef]
21. Gülink, J.; Bornemann, S.; Spende, H.; der Maur, M.A.; di Carlo, A.; Prades, J.D.; Wasisto, H.S.; Waag, A. InGaN/GaN NanoLED Arrays as a Novel Illumination Source for Biomedical Imaging and Sensing Applications. *Proceedings* **2018**, *2*, 892. [CrossRef]
22. Franch, N.; Canals, J.; Moro, V.; Vilá, A.; Romano-Rodríguez, A.; Prades, J.D.; Gülink, J.; Bezshlyakh, D.; Waag, A.; Kluczyk-Korch, K.; et al. Nano Illumination Microscopy: A Technique Based on Scanning with an Array of Individually Addressable NanoLEDs. *Opt. Express* **2020**, *28*, 19044–19057. [CrossRef]
23. Piruska, A.; Nikcevic, I.; Lee, S.H.; Ahn, C.; Heineman, W.R.; Limbach, P.A.; Seliskar, C.J. The Autofluorescence of Plastic Materials and Chips Measured under Laser Irradiation. *Lab Chip* **2005**, *5*, 1348. [CrossRef]
24. Canals, J.; Moro, V.; Franch, N.; Moreno, S.; Alonso, O.; Vilà, A.; Prades, J.D.; Gülink, J.; Bezshlyakh, D.D.; Waag, A.; et al. A Shadow Image Microscope Based on an Array of NanoLEDs. In Proceedings of the Unconventional Optical Imaging II, 6–10 April 2020; Online Event. Fournier, C., Georges, M.P., Popescu, G., Eds.; SPIE: Cardiff, UK, 2020; Volume 11351, p. 11.
25. Ding, K.; Avrutin, V.; Izyumskaya, N.; Özgür, Ü.; Morkoç, H. Micro-LEDs, a Manufacturability Perspective. *Appl. Sci.* **2019**, *9*, 1206. [CrossRef]

26. Kluczyk-Korch, K.; Palazzo, D.; Waag, A.; Diéguez, A.; Prades, J.D.; di Carlo, A.; der Maur, M.A. Optical Design of InGaN/GaN NanoLED Arrays on a Chip: Toward: Highly Resolved Illumination. *Nanotechnology* **2020**, *32*, 105203. [CrossRef] [PubMed]
27. Zuo, C.; Li, J.; Sun, J.; Fan, Y.; Zhang, J.; Lu, L.; Zhang, R.; Wang, B.; Huang, L.; Chen, Q. Transport of Intensity Equation: A Tutorial. *Opt. Lasers Eng.* **2020**, *135*, 106187.
28. Lee, S.-H.; Roichman, Y.; Yi, G.-R.; Kim, S.-H.; Yang, S.-M.; van Blaaderen, A.; van Oostrum, P.; Grier, D.G. Characterizing and Tracking Single Colloidal Particles with Video Holographic Microscopy. *Opt. Express* **2007**, *15*, 18275. [CrossRef] [PubMed]
29. Mann, C.J.; Yu, L.; Lo, C.-M.; Kim, M.K. High-Resolution Quantitative Phase-Contrast Microscopy by Digital Holography. *Opt. Express* **2005**, *13*, 8693. [CrossRef] [PubMed]
30. Sheng, J.; Malkiel, E.; Katz, J. Digital Holographic Microscope for Measuring Three-Dimensional Particle Distributions and Motions. *Appl. Opt.* **2006**, *45*, 3893–3901. [CrossRef]
31. Ou, F.; Chong, W.C.; Xu, Q.; Chen, Y.; Li, Q.; Zhang, L. Monochromatic Active Matrix Micro-LED Micro-displays with >5,000 Dpi Pixel Density Fabricated Using Monolithic Hybrid Integration Process. *Sid Symp. Dig. Tech. Pap.* **2018**, *49*, 1677–1680. [CrossRef]
32. James Singh, K.; Huang, Y.-M.; Ahmed, T.; Liu, A.-C.; Huang Chen, S.-W.; Liou, F.-J.; Wu, T.; Lin, C.-C.; Chow, C.-W.; Lin, G.-R.; et al. Micro-LED as a Promising Candidate for High-Speed Visible Light Communication. *Appl. Sci.* **2020**, *10*, 7384. [CrossRef]
33. Dixon, A.E.; Damaskinos, S.; Atkinson, M.R. A Scanning Confocal Microscope for Transmission and Reflection Imaging. *Nature* **1991**, *351*, 551–553. [CrossRef]

### 3.2.7. Publication 3

## Using Time-Correlated Single-Photon Counting Technique on SPAD Sensors to Enhance Acquisition Time and Dynamic Range

by

**Victor Moro**[1], Sergio Moreno[1], Oscar Alonso[1], Ana Vilà[1], Juan Daniel Prades[1] and Angel Diéguez[1]

[1]*Department of Electronic and Biomedical Engineering, Universitat de Barcelona, Spain*

*Published in*
**Proceedings of SPIE** (2022)
*Presented in*
**SPIE Photonics Asia** (2022), Online

# Using time-correlated single-photon counting technique on SPAD sensors to enhance acquisition time and dynamic range

Victor Moro, Sergio Moreno, Oscar Alonso, Anna Vilà, Juan D. Prades, et al.

Victor Moro, Sergio Moreno, Oscar Alonso, Anna Vilà, Juan D. Prades, Angel Diéguez, "Using time-correlated single-photon counting technique on SPAD sensors to enhance acquisition time and dynamic range," Proc. SPIE 12316, Advanced Optical Imaging Technologies V, 123160K (30 December 2022); doi: 10.1117/12.2641176

SPIE.

Event: SPIE/COS Photonics Asia, 2022, Online Only

# Using time-correlated single-photon counting technique on SPAD sensors to enhance acquisition time and dynamic range

Victor Moro*[a], Sergio Moreno[a], Oscar Alonso[a], Anna Vilà[a], Juan D. Prades[a], Angel Dieguez[a]
[a] Department of Electronic and Biomedical Engineering, Facultat de Fisica, Universitat de Barcelona, Marti i Franques 1, Barcelona, 08028, Spain

## ABSTRACT

In modern single pixel microscopy techniques, like Nano-Illumination Microscopy, long measurement times can become a major issue, especially when imaging biological tissues with large field of view. Usually, light intensity measurements are performed with CMOS pixel cameras, with typical integration times around tens of milliseconds. In this work, we propose to obtain light intensity data indirectly by applying statistical techniques to the photon arrival times measured with a SPAD photodetector. We will present how the different statistical measurements can be used to minimize the total acquisition time and minimize also the hardware required. In this work, with only 256 Single Photon Avalanche Diode (SPAD) measurements, the exposure time is reduced from 50 ms to 140 us. The dynamic range is extended by combining statistical techniques with standard intensity measurements. Standard intensity acquisitions are used to obtain low light intensity data, and, when the SPAD sensor is in saturation range, the time information obtained by the distribution of the photons allows to determine light intensity. This paves the way to practical Nano-Illumination Microscopy and other single pixel microscopy techniques.

**Keywords:** Nano Illumination Microscopy, Acquisition time, Dynamic range, Time Correlated Single Photon Counting, SPAD, single pixel microscopy.

## 1. INTRODUCTION

Thanks to the development of camera sensors with everyday smaller pixel size and pitch, and consequently larger density of pixels (pixels per inch, ppi), lensless microscopy has become a relevant competitor to classical optical microscopy techniques [1–3]. Lensless microscopes made available simple, low-cost and miniaturized microscopes with resolution provided by the CMOS camera pixel pitch and field of view (FoV) limited by the size of the sensor. Due to that, the capabilities of lensless microscopy rely in their majority in the CMOS sensor development. So, these microscopes are limited by the miniaturization of the electronics. Even with a 5nm technological CMOS node and below[4], high resolution CMOS cameras are limited to 0.64µm pixel size[5] and to 200-megapixel (16384x12288).

This limitation has encouraged the research in other directions. One field that has gathered a lot of attention is single pixel imaging[6]. These techniques transfer the resolution limitation and FoV from the sensor or camera to the illumination stage. Pixel arrays of GaN Light Emitting Diodes (LEDs) have achieved sizes of 200nm, with a pitch of 400nm[7], potentially increasing the resolution of lensless techniques. These LED arrays were used to develop Nano-Illumination Microscopy (NIM)[8]. This technique (Figure 1. (a)) is based on a nano or microLED array with the sample on its surface and a single pixel detector. Each LED in the array is turned on and off, scanning the sample, while the sensor receives the light intensity. Then, the light measured by each LED in the array is used to reconstruct the image. On the other hand, these nanoLED arrays are not large, so the FoV of the NIM technology using these arrays is limited. Despite that, there exist microLED arrays (microdisplays) with 2.5µm pixel pitch with a FoV of 51.84cm$^2$ (1920x1080 pixels)[9]. As it can be observed, the research of LED arrays has reached lofty goals in just the last 20 years. It is expected that large FoV LED arrays with smaller pitch are achieved, increasing drastically the value of NIM.

*vmoro@ub.edu; phone 934039146; https://www.ub.edu/portal/web/dp-electronica

Advanced Optical Imaging Technologies V, edited by Xiao-Cong Yuan, P. Scott Carney, Kebin Shi, Proc. of SPIE Vol. 12316, 123160K
 · 0277-786X · doi: 10.1117/12.2641176

Nonetheless, there is a limitation in techniques such as NIM. They depend on the sensor acquisition rate. While in traditional lensless microscopy each pixel of the detector is sensing at the same time, in NIM the light sensor must acquire a measurement of each one of the LEDs in the array. So, using a commercial camera with typically 50ms acquisition time, in lensless microscopy it is possible to have an image every 50ms, while scanning a FoV of 1mm$^2$ with a 2µm LED pitch with NIM, to obtain an image takes 7 hours. This is a handicap, especially when scanning biological tissues or samples that has motion artifacts or are affected by external conditions (such as temperature, humidity…). In this work we study a bunch of possible solutions to overcome this handicap.

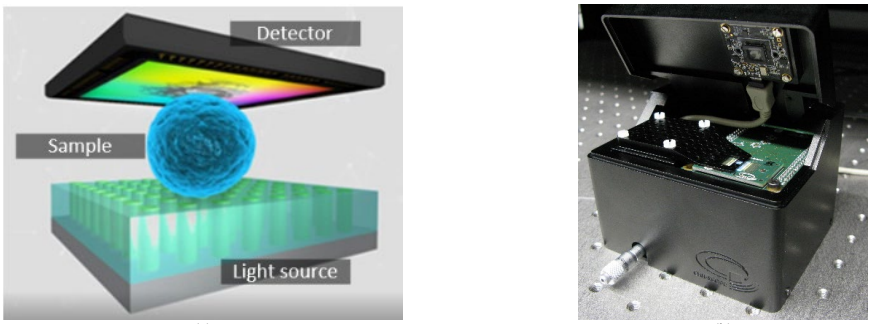


(a) (b)

Figure 1. (a) shows an illustration of the Nano-Illumination microscopy technique, based on a sample lying on a nanoLED array surface being scanned, while the projected shadow intensity is recorded. A prototype of a Nano-Illumination Microscope is shown in (b).

On the other hand, SPAD sensors have much lower acquisition times. They can make single photon measurements well below 1ns. To perform a light intensity measurement, counting of individual photons is usually done (typically $10^4$ or above)[10]. In a SPAD camera several pixels are available and for the method described it is possible to use the best suitable pixel for the detection, i.e., the pixel with highest Signal to Noise Ratio (SNR) and with higher Photon Detection Efficiency (PDE). Another possibility of using a SPAD camera is to consider several pixels jointly as if it was a silicon photomultiplier and sum the measurements acquired[11]. This, if having a 16x16 camera, can potentially reduce the acquisition times from $10^4 \cdot t_{acq}$ to $\frac{10^4 \cdot t_{acq}}{16 \cdot 16}$, although it should be considered that some pixels might need to be removed for having low SNR.

Hence, the use of a SPAD can potentially reduce the number of measurements needed to acquire the light intensity of each pixel. But SPAD sensors have the capability of providing more information when integrated with a Time to Digital Converter (TDC). When these two circuits are integrated together, it is possible to obtain the temporal information corresponding to when the photon was detected. Ingle et al.[12] have proven that it is possible to use this temporal information to enhance the SPAD capabilities, such as increase the dynamic range and SNR. Improving SNR in intensity SPAD measurements is typically achieved by increasing the number of times individual photons are counted. Using these methods, it is possible to improve significantly the SNR with lower number of measurements, thus, decreasing the acquisition times, which improves significantly their use in single pixel microscopy techniques, especially in NIM.

In this work we present results obtained by using a custom a SPAD camera designed in a standard 0.35µm CMOS technology with a TDC, to acquire temporal information of the photon arrival times. Then we investigate different statistical methods on the photon arrival times to decrease the acquisition time and increase the dynamic range of the sensing system. We think that the results of this work can be applied to single pixel microscopy techniques like NIM.

## 2. MATERIALS AND METHODS

This work is developed using a SPAD designed in AMS 0.35µm HV-CMOS technology with a TDC integrated off-chip in a Xilinx Zynq-7000 System on Chip (SoC). As illumination source, a 510 nm LED is used. The measurements obtained by this system are processed with software methods after all the acquisitions are made. Comparisons with intensity measurements were performed for each light intensity in order to characterize the quality of the method. For statistical purposes and to be able to ensure which methods are more optimal, 100 repetitions of the measurements were performed for each light intensity. The raw data used for all the statistical calculations is the same.

### 2.1 SPAD camera

The SPAD array was manufactured by AMS 0.35µm HV-CMOS technology, since this technology granted lower noise than other production lines[13]. The SPAD sensors are biased above their breakdown voltage and operated in gated mode. This reduces the noise detection probability[14].

Figure 1 (a) shows an image of the chip, where the sensing area and readout are on the right part, and the counting electronics and pads are at the left. The sensing area has a 1.6% fill factor. It is composed by a 16x16 SPAD sensors, each of them with a diameter of 10µm and a pitch of 70µm. Since all the I/O pads are at one side of the chip, the SPAD array can be on the chip and PCB edge, as shown in Figure 1 (b), which makes the alignment of the sensing area with the incoming light from the LEDs easier. For the purpose of this work, a single SPAD from the camera was used, selecting among the 16x16 array the one with higher SNR. The acquisition time for one measurement was 350ns and the dead time of the SPAD (the time between measurements to avoid extra noise sources) was 200ns. Thus, the total acquisition time for each measurement was 550ns.

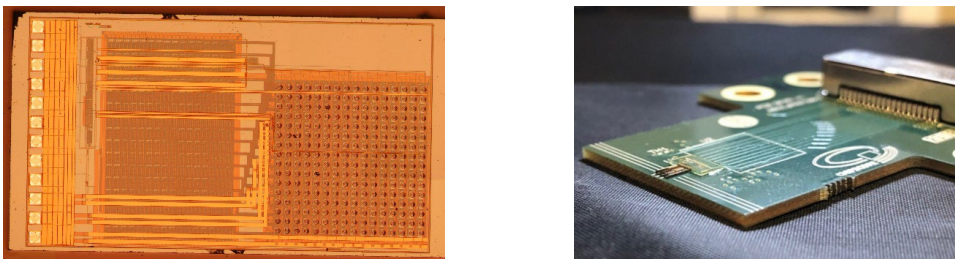

(a) (b)

Figure 2. The SPAD camera chip is shown in (a) with the sensing area at the right of the chip and (b) shows the PCB where the SPAD camera is integrated with the camera bonded to it.

### 2.2 Time to Digital Converter

The Time to Digital Converter used in this work is integrated in a Field Programable Gate Array (FPGA) developed by Xilinx, the Zync-7000 SoC[15]. In the whole acquisition time of 350ns, this TDC has 6400 delay elements of 55 ps each one. When a photon is detected, it is associated to the corresponding time delay. For the purpose of this work, the maximum number of delay elements (6400) are grouped in bins (8, 16, 32, …) in order to study the minimum number of bins required to detect different light intensities with enough resolution.

### 2.3 Light source

The light source used for this work was a 510 nm LED. This light source was selected because the SPAD camera has a good PDE in this wavelength. Also, the smallest nanoLED arrays developed in GaN emit in the green wavelengths[7]. The LED is set at 19mm from the SPAD array. This provides light intensities striking the sensor of 0.2pCd to 100nCd.

### 2.4 Statistical methods

Different statistical methods are applied to the measurements obtained using the optical system described above. Each method is compared with the intensity measurements. Figure 3 shows an example of histogram that was used to apply these statistical methods.

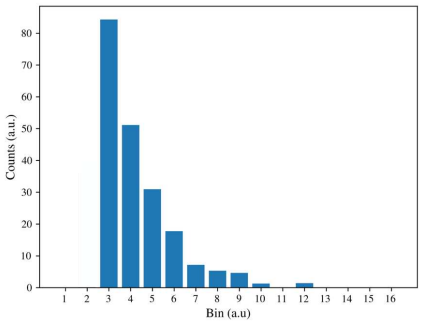


Figure 3. Example of a histogram obtained with the optical setup described above.

### 2.4.1 Difference maximum – minimum arrival times

This method consists of considering the last bin and the first bin where a photon has been detected during the measurement and subtracting the bin values. This technique provides the total time where the detector has received photons. The equation used for this method (1) is simple and easy to implement with not a high computational cost.

$$dif = bin_n - bin_0 \tag{1}$$

### 2.4.2 Median

This method takes the number of photons per bin and then calculates the median from them, i.e., if in the bin 1 there are 5 photons detected, in the bin 2 there are 3 and in the bin 3 there is 1, the median of these measurements is the bin 1. Median is described in equation (2) if the number of photons detected is even, and in (3) if the number of photons is odd.

$$n = \frac{Photons_{detected}}{2} \rightarrow median = bin_n \tag{2}$$

$$n = \frac{Photons_{detected} + 1}{2} \rightarrow median = bin_n \tag{3}$$

### 2.4.3 IQR

This method describes the statistical dispersion of the histogram. It is defined as the difference between the 25$^{th}$ and 75$^{th}$ percentiles of the data. In order to calculate the IQR, the histogram is divided into quartiles. These quartiles are spread into the Q1, or lower quartile, Q2, or the median, and Q3, or the upper quartile. The lower quartile is the 25$^{th}$ percentile and the upper quartile is the 75$^{th}$. Thus, the IQR = Q3 – Q1.

### 2.4.4 Full Width at Half Maximum

The Full Width at Half Maximum (FWHM) is the difference between the two values of the independent variable at which the dependent variable is equal to half of its maximum value. In the case of the histogram, since the maximum is expected to be the first bin, it is implemented in this work as the difference between the first bin and the bin where the counts are half the counts of the first bin. This method is described in equation (4).

$$FWHM = bin_{max\ counts/2} - bin_0 \tag{4}$$

### 2.4.5 Standard deviation from the delay element 0

This method is an extrapolation of the standard deviation, where instead of using the mean to calculate the standard deviation of a gaussian distribution, here is used the delay element 0, or the bin 1. This method provides with a higher value the last bins, where the number of photons detected should be lower. It is described in equation (5). This method has a high computational cost, since it requires square roots, which are complex to integrate in hardware.

$$\sigma = \frac{\sqrt{\sum_{bins=1}^{n} (time_{bin} - 0)^2 \cdot counts_{bin}}}{\sum_{bins=1}^{n} counts_{bin}} \tag{5}$$

#### 2.4.6 Average

This method calculates the typical value in the set of data provided by the SPAD. It is assigned to each bin the number of photon counts detected on it, and they are summed. Then, this data is divided by the total number of photons detected, which is the intensity value. This provides a similar value than the provided by the standard deviation from the delay element 0, but without providing any higher value to any bin specifically. This method is described in equation (6).

$$average = \frac{\sum_{bins=1}^{n} time_{bin} \cdot counts_{bin}}{\sum_{bins=1}^{n} counts_{bin}} \quad (6)$$

#### 2.4.7 Intensity

This method provides the same output of a SPAD camera without TDC. It is calculated to compare the statistical methods using the values of the same measurement, to be able to ensure that the methods improve the acquisition time and dynamic range. This control data is acquired by summing all the counts, without considering the time where they were detected. It is described in equation (7)

$$Intensity = \sum_{bins=1}^{n} counts_{bin} \quad (7)$$

## 3. RESULTS

All the techniques described in section 2 were applied to 256 measurements. The results obtained were compared with measurements of high number of acquisitions ($10^5$), typically used in SPAD measurements, as reference data.

The resolution was obtained by considering the combination of using the intensity measurements for low light intensities and the statistical techniques for high light intensities[12]. To analyze and conclude the better technique to accomplish the objectives of this work the resolution and the dynamic range gain are the values considered.

### 3.1 Difference maximum – minimum arrival times

This is the easiest technique to implement, with the lower computational cost. The resolution provided by this technique is 0.5nCd. The dynamic range provided using this technique is 20nCd. The results extracted from the 256 measurements both applying this technique for 256 and $10^5$ and with intensity raw measurements are shown in Figure 4 (a). As it can be observed, the resolution is not good enough even with an increase of the dynamic range of one magnitude order.

### 3.2 Median

This technique provides a resolution of 0.1nCd. On the other hand, the dynamic range improvement of this technique is only up to 2nCd. Even with improving the resolution and, thus, the SNR, the increment of dynamic range is not optimal. The results obtained by the implementation of this technique are shown in Figure 4 (b).

### 3.3 IQR

IQR show similar results than the median method. The resolution provided by this technique is 0.2nCd, worse than the obtained with the median, and the dynamic range accomplished is 2nCd. Figure 4 (c) illustrates the results obtained by applying this technique.

### 3.4 Full Width at Half Maximum

Full Width at Half Maximum is a technique normally applied to gaussian distributions. Nevertheless, it can be applied to several function types and provide quality information. As it can be seen in Figure 4 (d), this method improves the results provided by the methods above. The resolution provided by this technique is 0.4nCd and the dynamic range is increased up to 50nCd.

### 3.5 Standard deviation from the delay element 0

The Standard deviation from the delay element 0, with the weighted average, are the most promising techniques. The resolution provided by this technique is a great increase compared with the techniques below. It is 0.1nCd. The dynamic range provided using this technique is also a great improvement, being 70nCd. Figure 4 (e) show the results of the use of standard deviation from 0, with a separator where the light would be measured with intensity measurements or with TDC data treated with this method.

### 3.6 Weighted Average

The weighted average method has provided the best results compared with the other techniques studied in this work. The resolution provided by this technique is 0.05nCd and the dynamic range accomplished is 100nCd, increasing by two magnitude orders the dynamic range provided by intensity measurements. Figure 4 (f) show the results obtained when this technique is applied.

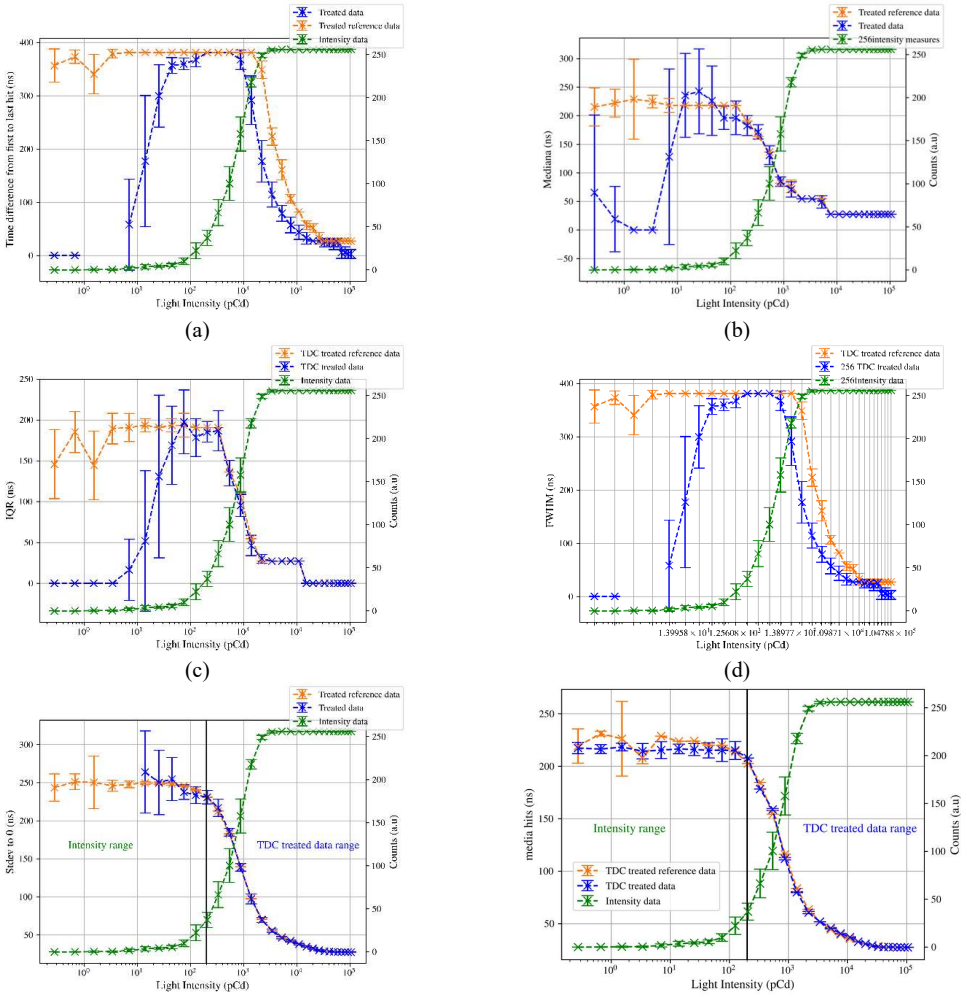


Figure 4. The results of applying diverse statistic techniques described in section 2.4 to the data acquired. The methods are presented in order, being (a) the difference between maximum and minimum arrival photons, (b) the median, (c) the IQR, (d) the FWHM, (e) the standard deviation from the delay element 0 and (f) the weighted average.

Furthermore, seeing that with this technique we obtain the best results, an analysis was done reducing the number of bins and measurements by 1 bit (from 16 to 8 bins and from 256 to 128 measurements).

The dynamic range obtained with 8 bins decreases from 100nCd to 10nCd and the resolution decreases from 0.05nCd to 0.5nCd as it can be observed in Figure 10 (a). In Figure 10 (b), results are shown from using 16 bins and 128 measurements. Here can be observed that the resolution has decreased to 0.25nCd and the dynamic range to 20nCd.

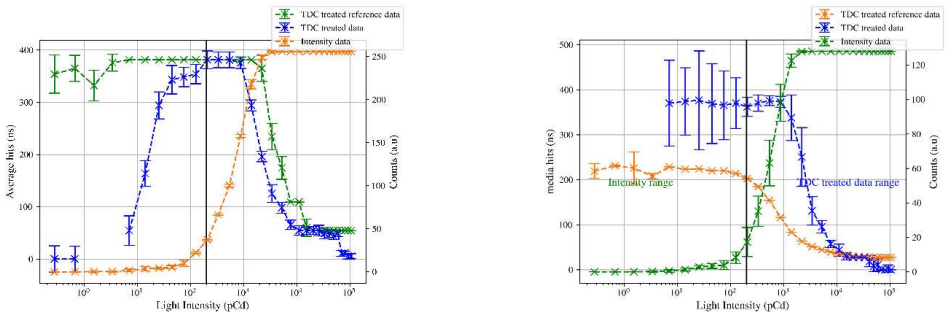


(a) (b)

Figure 5. (a) shows the results obtained when applying the weighted average method to 8 bins and 256 measurements and the weighted average applied to 128 measurements and 16 bins is shown in (b).

## 4. CONCLUSIONS AND DISCUSSION

After analyzing the methods applied to measurement obtained with a SPAD camera and a TDC using Time Correlated Single Photon Counting (TCSPC) technique and applying statistical methods, we are able to ensure the SNR (or resolution) and the dynamic range are increased by applying the weighted average method with 256 repetitions and a TDC of 16 bins. The dynamic range have been increased more than 2 orders of magnitude and the acquisition time has been reduced from $10^4 \cdot 550$ns to $256 \cdot 550$ns, 40 times faster. Furthermore, if we compare with the acquisition times of commercial CMOS cameras used in NIM technique, we reduced the 7 hours that takes to scan 1mm$^2$ to 1.7 minutes. This is a potential breakthrough when implemented in this technique, since it reduces the motion artifacts and the artifacts generated by external variables, like temperature.

We also analyzed the repetitions and bins needed for the implementation of this method and concluded that the optimal result is 256 measurements with 16 bins, providing a resolution of 0.05nCd and a dynamic range of 100nCd.

To conclude, a study of the hardware needed to implement the average method has been done, and its main components would be counters and a shift register, which are not high area consumption components.

## 5. ACKNOWLEDGMENT

The authors would like to acknowledge fundings from the Spanish government under the project AnaSPAD (number PID2019-105714RB-I00).

## REFERENCES

[1] Haddad, W. S., Cullen, D., Solem, J. C., Longworth, J. W., Mcpherson, A., Boyer, K. and Rhodes, C. K., "Fourier-transform holographic microscope" (1992).
[2] Ozcan, A. and McLeod, E., "Lensless Imaging and Sensing," Annu Rev Biomed Eng 18, 77–102 (2016).
[3] Singh, A. K., Pedrini, G., Takeda, M. and Osten, W., "Scatter-plate microscope for lensless microscopy with diffraction limited resolution," Sci Rep 7(1) (2017).
[4] Hiramoto, T., "Five nanometre CMOS technology," Nat Electron 2(12), 557–558 (2019).

[5] “Samsung Breaks New Ground With Mass Production of Industry’s Smallest 0.64µm-Pixel Mobile Image Sensor.”, <https://news.samsung.com/global/samsung-breaks-new-ground-with-mass-production-of-industrys-smallest-0-64micrometer-pixel-mobile-image-sensor> (2 November 2022 ).
[6] Gibson, G. M., Johnson, S. D. and Padgett, M. J., “Single-pixel imaging 12 years on: a review,” Opt Express 28(19), 28190 (2020).
[7] Bezshlyakh, D. D., Spende, H., Weimann, T., Hinze, P., Bornemann, S., Gülink, J., Canals, J., Prades, J. D., Dieguez, A. and Waag, A., “Directly addressable GaN-based nano-LED arrays: fabrication and electro-optical characterization,” Microsyst Nanoeng 6(1) (2020).
[8] Franch, N., Canals, J., Moro, V., Vilá, A., Romano-Rodríguez, A., Prades, J. D., Gülink, J., Bezshlyakh, D., Waag, A., Kluczyk-Korch, K., Auf der Maur, M., di Carlo, A. and Diéguez, Á., “Nano illumination microscopy: a technique based on scanning with an array of individually addressable nanoLEDs,” Opt Express 28(13), 19044 (2020).
[9] “Microled 0.22" Display JBD.”, 2022, <https://www.jb-display.com/weixianshiping/3.html> (2 November 2022 ).
[10] Pancheri, L., Massari, N. and Stoppa, D., “SPAD image sensor with analog counting pixel for time-resolved fluorescence detection,” IEEE Trans Electron Devices 60(10), 3442–3449 (2013).
[11] Alonso, O., Franch, N., Canals, J., Arias-Alpízar, K., de la Serna, E., Baldrich, E. and Diéguez, A., “An internet of things-based intensity and time-resolved fluorescence reader for point-of-care testing,” Biosens Bioelectron 154 (2020).
[12] Ingle, A., Velten, A. and Gupta, M., “High Flux Passive Imaging with Single-Photon Sensors” (2019).
[13] Bronzi, D., Villa, F., Tisa, S., Tosi, A. and Zappa, F., “SPAD Figures of Merit for Photon-Counting, Photon-Timing, and Imaging Applications: A Review,” IEEE Sens J 16(1), 3–12 (2016).
[14] Vilella, E. and Diéguez, A., “A gated single-photon avalanche diode array fabricated in a conventional CMOS process for triggered systems,” Sens Actuators A Phys 186, 163–168 (2012).
[15] Franch, N., Alonso, O., Canals, J., Vila, A. and Dieguez, A., “A low cost fluorescence lifetime measurement system based on SPAD detectors and FPGA processing,” Journal of Instrumentation 12(2), Institute of Physics Publishing (2017).

## 3.3. MicroLEDs for PoC

Another significant area in biomedicine, particularly in recent years, is the development of PoC devices for use in healthcare. In our work described in Section 3.3.4 [148] a multi-detection device using a lensless matrix addressable microLED array is described. The instrument is aimed to be a portable low resolution fluorescence microscope using the matrix addressing array and custom CMOS chips already described. This multi-detection PoC device can perform both intensity and time resolved fluorescence measurements. Furthermore, when performing time resolved fluorescence measurements the device is able to make multi-detection of fluorophores with different decay times. It was developed by using an hybrid micro-structure (Figure 43 a, b) based on the 32 x 32 matrix addressable GaN microLED array (Figure 43 c), consisting on square LEDs of 50 µm edge length and 100 µm pitch, with the matrix addressable CMOS chip presented in Section 3.1.2 (Figure 36) wire bonded underneath (Figure 43 d), and an array of 16 x 16 SPAD CMOS chip [113]. The development of this device not only replaces instrumentation based on lasers, bulky optical components and discrete electronics with a full hybrid micro-system, but also enables the measurement of 32 x 32 spots in the same chip without any mechanical components.

To characterize this device, two different fluorescent particles were used. These particles are QDot® 605 ITK™ Streptavidin (QdotTM 605 ITKTM Streptavidin Conjugate Kit, n.d.) and QDot® 705 ITK™ Amino PEG (QdotTM 705 ITKTM Amino (PEG) Quantum Dots, n.d.) (QD 605 and QD 705), both purchased from Life Technologies, Waltham, MA, USA. The maximum emission peaks for QD 605 and QD 705 are in 605 nm and 705 nm, respectively. Both are excited in the UV but have a reasonable excitation with maximum emission at 450 nm for the LEDs used in this work around 20%. QD 605 has an expected lifetime in the order of 32 ns, reported by J. Canals *et al*. [60]. QD 705 has an expected lifetime of around 80 ns, as reported in [179] by S. Bhuckory *et al.* To place the fluorescent particles, a micromesh with microwell diameters of 250 µm with 500 µm pitch was used. In the experiments a volume of 5 nL QD was loaded in selected microwells of the micromesh. The micromesh was purchased from Tebu-bio Spain S.L., Barcelona, Spain [180].

# 3. Results

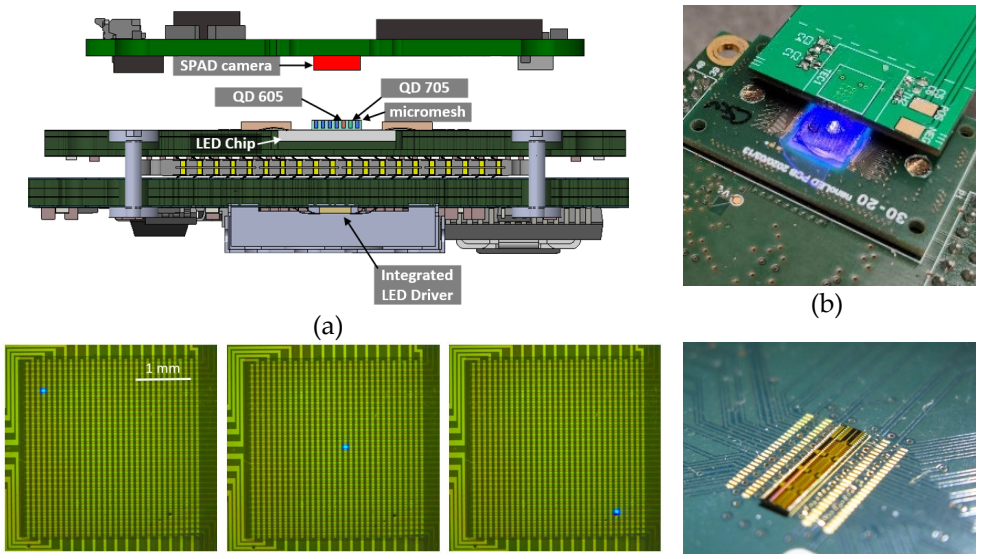


**Figure 43.** The schematic view of the set-up is shown in (a), and a picture of the set-up is in (b). (c) is a microscopic picture of the array of microLEDs with different LEDs turned on and (d) is a picture of the CMOS driver wire bonded to the PCB.

## 3.3.1. Fluorescence intensity measurements

This device was proved capable of detecting fluorescent particles (QD605) in two different microwells performing intensity fluorescence measurements (Figure 44 a). There are 5 LEDs under every microwell. As can be observed, the only place where QD605 is detected is in the orange areas, corresponding to two crosses formed by the LEDs, where the microwells contain samples. The number of counts measured in the areas where QD605 was deposited is in the range from 950 to 1050. On the other areas, the number of counts measured is lower than 150. So, the device is able to discriminate areas with QD605 at concentration of 1 µM at low volumes (5 nL). Furthermore, to test the Limit of Detection (LoD) of the device, both QD605 and QD705 were measured decreasing their concentrations. The LoD of the system is 1/4 µM. As can be observed in Figure 44 b, at 1/8 µM, same number of counts are detected than in the Instrument Response (IR), i.e. the background counts when there is no fluorophore.

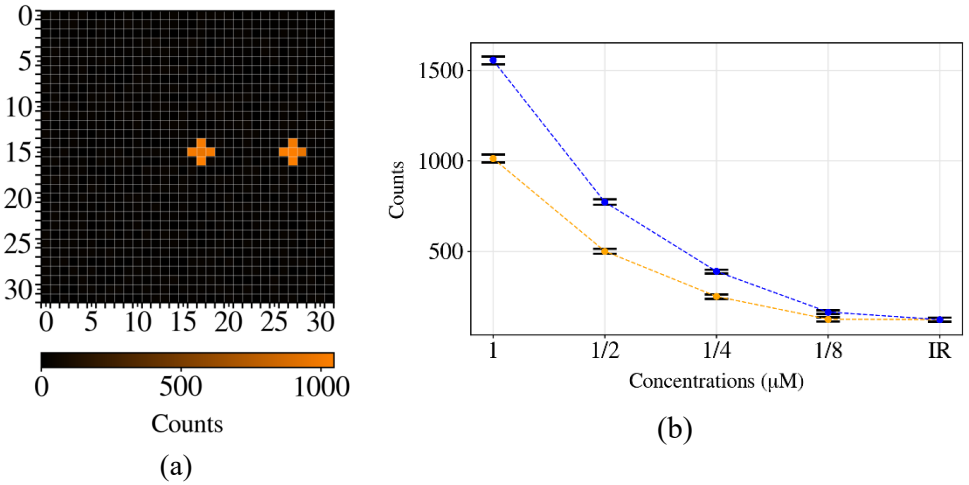


**Figure 44.** Image acquired by the device, where QD605 is detected in the orange areas (above 1000 counts in each one). The other part of the image corresponds to absence of QD605 (a). Intensity obtained in different measurements for different concentrations of QD605 and QD705 (b).

### 3.3.2. Time-resolved fluorescence measurements

For time resoled fluorescence the device is able to discern between different QD. This is possible because each QD has different lifetimes. Figure 45 (a) shows two different QD deposited in two microwells. QD605 is the purple spot and QD705 is the yellow spot. The lifetimes of the two QD are different enough so the device can discern them with no margin of error. QD605 has a lifetime of 31.3 ± 0.4 ns and QD706 has a lifetime of 81.7 ± 0.6 ns (Figure 45 b). The LoD for time resolved fluorescence is the same as for intensity fluorescence, 1/4 μM.

# 3. Results

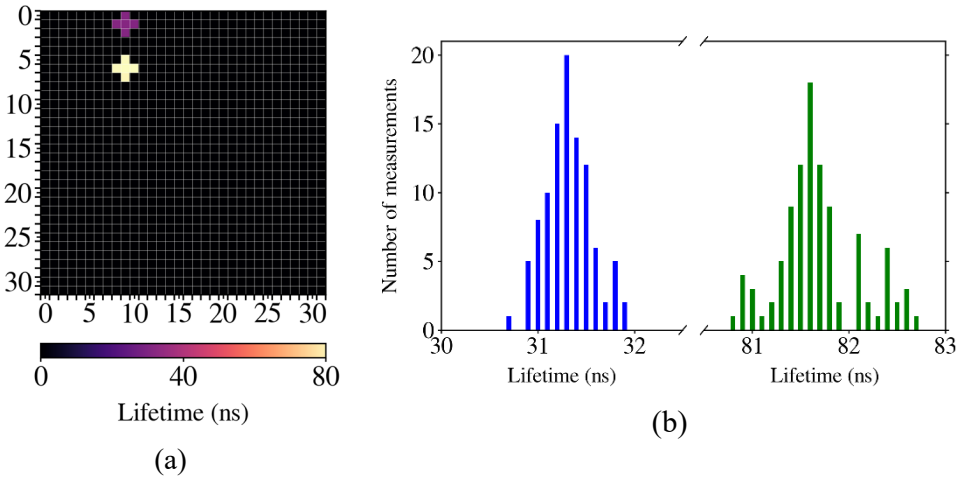


**Figure 45.** Image obtained with the device where the two fluorophores were deposited in microwells (a). Lifetimes of QD605 (blue) and QD705 (green) for 1 µM for 100 sampled measurements to extract statistical values (b).

## 3.3.3. Conclusions

The system's results demonstrate its capability to detect fluorophores in intensity mode at high speed. Furthermore, it can identify different fluorophores in a single measurement using time-resolved fluorescence methods, all while operating with very small sample volumes (5 nL). This device holds significant potential for applications in scanning biological samples, analytical laboratories, and clinical diagnostics.

### 3.3.4. Publication 4

## Fluorescence Multi-Detection Device Using a Lensless Matrix Addressable microLED Array

by

**Victor Moro**[1], Sergio Moreno[1], Oscar Alonso[1], Ana Vilà[1], Juan Daniel Prades[1] and Angel Diéguez[1]

[1]*Department of Electronic and Biomedical Engineering, Universitat de Barcelona, Spain*

*Published in*
**Biosensors (Basel)** 14 (2024) 265

biosensors

MDPI

*Article*

# Fluorescence Multi-Detection Device Using a Lensless Matrix Addressable microLED Array

**Victor Moro [1,*], Joan Canals [1], Sergio Moreno [1], Steffen Higgins-Wood [2], Oscar Alonso [1], Andreas Waag [2], J. Daniel Prades [1,2] and Angel Dieguez [1,*]**

[1] Electronic and Biomedical Engineering Department, University of Barcelona, 08028 Barcelona, Spain; canals@ub.edu (J.C.); sergiomoreno@ub.edu (S.M.); oalonso@ub.edu (O.A.); dprades@ub.edu (J.D.P.)
[2] Institute of Semiconductor Technology, Technical University of Braunschweig, 38106 Braunschweig, Germany; steffen.bornemann@tu-braunschweig.de (S.H.-W.); a.waag@tu-braunschweig.de (A.W.)
* Correspondence: vmoro@ub.edu (V.M.); angel.dieguez@ub.edu (A.D.); Tel.: +34-93-403-9149 (A.D.)

**Abstract:** A Point-of-Care system for molecular diagnosis (PoC-MD) is described, combining GaN and CMOS chips. The device is a micro-system for fluorescence measurements, capable of analyzing both intensity and lifetime. It consists of a hybrid micro-structure based on a 32 × 32 matrix addressable GaN microLED array, with square LEDs of 50 µm edge length and 100 µm pitch, with an underneath wire bonded custom chip integrating their drivers and placed face-to-face to an array of 16 × 16 single-photon avalanche diodes (SPADs) CMOS. This approach replaces instrumentation based on lasers, bulky optical components, and discrete electronics with a full hybrid micro-system, enabling measurements on 32 × 32 spots. The reported system is suitable for long lifetime (>10 ns) fluorophores with a limit of detection ~1/4 µM. Proof-of-concept measurements of streptavidin conjugate Qdot™ 605 and Amino PEG Qdot™ 705 are demonstrated, along with the device ability to detect both fluorophores in the same measurement.

**Keywords:** Point-of-Care; multiplex; microLED array; SPAD; fluorescence; lifetime fluorescence; GaN; CMOS; microLED driver



**Citation:** Moro, V.; Canals, J.; Moreno, S.; Higgins-Wood, S.; Alonso, O.; Waag, A.; Prades, J.D.; Dieguez, A. Fluorescence Multi-Detection Device Using a Lensless Matrix Addressable microLED Array. *Biosensors* **2024**, *14*, 264. https://doi.org/10.3390/bios14060264

Received: 25 March 2024
Revised: 29 April 2024
Accepted: 21 May 2024
Published: 22 May 2024



## 1. Introduction

During the last decades, the increase in life expectancy has led to a global population aging, significantly increasing the demand for healthcare services for elderly individuals. According to the World Health Organization (WHO), this trend of the global population's average age rising is anticipated to continue in the years ahead. It is expected that by 2030, 1 in 6 people worldwide will be over 60 years old (1.4 billion), and by 2050, this number is projected to reach 2.1 billion. Additionally, the number of people over 80 years old is expected to triple from 2020 to 2050. The expectation is that by 2050, 80% of older people will live in low- and middle-income countries [1]. In these environments, access to the health system is difficult due to several factors, including lack of resources, low staff pay, and lack of equipment and infrastructure, including accessibility of health services or low levels of education [2]. One outcome of inadequate access to the health system is the delay in disease diagnosis, which can be critical for saving patients' lives and preventing the spread of infectious diseases [3–6]. Moreover, studies indicate that early detection and analysis of diseases led to a decreased time, cost, and necessity for further diagnostic procedures, for example, early detection of a disease such as influenza in children presenting with fever at emergency rooms [7].

The emergence of technologies that enhance efficiency and reduce diagnosis time has spurred the development of several rapid diagnostic platforms suitable for Point-of-Care (PoC) applications [8]. With the application of fast diagnostic methods such as PoC devices for just four common diseases–syphilis, tuberculosis, malaria, and bacterial pneumonia–it is possible to prevent 1.2 million deaths annually [9,10].

PoC takes special relevance by bringing the clinical laboratory closer to the patient and with reduced cost. This is especially relevant since the majority of the population that would require higher access to healthcare services is located in places with limited access to these services. The key features of PoC include portability, ease of use, and rapid result turnaround times. These features enable diagnosis and monitoring of diseases, and furthermore, management near to the patient, which facilitates personalized therapy and enhances patient outcomes with a reduced overall cost for the National Health Systems [11]. According to WHO, PoC tests considered appropriate for the delivery of healthcare in this resource-limited environment should meet the criteria of "ASSURED", which stands for Affordable, Sensitive, Specific, User-friendly, Rapid and Robust, Equipment-free, and Deliverable [12,13].

A PoC device is usually formed by five components: sensing tool, transducer, target, prove, and signal readout device [14]. PoC devices have been proven to be useful in a wide range of applications, such as diagnosis of immunological [15], cardiovascular [16], infectious [12], neurodegenerative [17], and oncological diseases [18]. Moreover, they can also be used in blood [19], genetic [20], and microbiology testing [21]. All these applications are performed by different transducers, but the most common and inexpensive one is optics, specifically imaging analysis by fluorescence [22–24]. There are several PoC devices that use fluorescence as transduction tools in the literature. The research reports that PoC devices based on fluorescence have good efficiency and performance, and they aim to improve the limit of detection (LoD) and miniaturization. In these devices, the most used light source to produce fluorescence is a laser [25–28]. However, in recent years, the use of Light Emitting Diodes (LEDs) and microLEDs has been introduced in some PoC devices [29–32]. Additional elements of these PoC are lenses to focus light on the sample and to improve the detection of light coming from the fluorophores, emission and excitation filters, and a photodetector.

Fluorescence-based PoCs are typically designed to identify the presence of a specific substance through intensity measurements. The intensity measurements are performed by continuously illuminating the sample that is excited by the light. If the targeted analyte is present, the sample emits fluorescence light red-shifted compared to the original excitation light. The emitted light is tracked and utilized to measure a biochemical reaction or binding occurrence, offering high accuracy, sensitivity (capable of single molecule detection), and precise labeling of biological samples [33]. Nevertheless, fluorescence techniques relying on intensity measurements are susceptible to misinterpretation because they depend on factors such as excitation light intensity and fluorophore concentration. It can be found in the literature that one of the solutions proposed to overcome these limitations is provided by time-resolved techniques, in which the lifetime or the decay of the fluorophores is measured. The lifetime of a fluorophore is an intrinsic characteristic of each molecule, and is therefore independent of the concentration or excitation intensity of the fluorophore [24,34]. In these measurements, the light source is pulsed, exciting the sample for a specified time. Once the light source is turned off, it is possible to measure the lifetime of the fluorophore. A key feature that limits the capability to detect fluorophores lifetimes is the speed at which the device can turn off the light source, limiting the minimum detectable lifetime. Moreover, the possibility of detecting fluorophore lifetimes enhances the specificity of the measurement by time domain discrimination, thus allowing us to discern the light of interest from the background noise [35]. Furthermore, it allows us to discern between different fluorophores with overlapping emission spectra but with different lifetimes in multiplexed assays [36–38].

In recent years, several advances have been made in PoC devices, especially using LEDs, since they are less expensive than lasers. Furthermore, the use of LEDs in arrays allows multiplexing. U. Obahiagbon et al. [39] presented a PoC using an array of 2 × 2 green LEDs to detect antibodies to HPV16 and 18 proteins. In [40], F. B. Myers et al. designed a PoC and performed an assay for the HIV integrase gene, which they were able to detect at a concentration of $10^3$ copies/µL. J. T. Smith et al. [41] used the device presented in [39] to measure a disposable 4-site fluorescent microscope slide reader with high sensitivity for LMIC disease diagnosis. Manzanas et al. [42] developed a rapid and sensitive multiplexed PoC device capable of simultaneous detection of SARS-CoV-2 and influenza A HINI viruses in 50 min with the use of a blue LED. In [43], B. Shu et al. pursued an ultraportable, automated, and multiplexed PoC molecular platform that can provide screening of infectious pathogens rapidly and with high sensitivity. The PoC device reported has the possibility to work with 15-channel performing real-time quantitative detection.

In this work, we present a PoC device that uses a GaN-based microLED array chip, instead of lasers, LEDs, or LED arrays, as an excitation source. By following the trend in LED platform development and making use of the advances in GaN-based microLED arrays, it is possible to develop a device with high multiplexity. Specially, the high brightness capabilities of the GaN-based LEDs [44,45] allow them to be a suitable substitute for the lasers that are typically used in fluorescence PoC devices. Furthermore, their high modulation bandwidth [46,47] (up to 1 GHz) makes them a perfect candidate for time-resolved fluorescence measurements. Therefore, in this work, a PoC device is built with a 32 × 32 matrix addressable (MA) microLED array and a single-photon avalanche photodiodes (SPAD) camera as the main components; that the device is able to perform both intensity and time-correlated fluorescence measurements. Moreover, this device can perform both types of measurements without any optical components.

In the subsequent sections, we describe the instrument and its components, followed by a detailed characterization of the device. This includes measurements of fluorescence intensity and fluorescent lifetimes across varying concentrations of two distinct quantum dot molecules.

## 2. Materials and Methods

### *2.1. Instrument*

A device was constructed that enables the acquisition of fluorescence intensity and facilitates time-resolved experiments to assess fluorescence lifetime (Figure 1a,b). The setup built for both fluorescence methods is the same. To perform the measurements, the LED light is pulsed, and time gating is applied before the failing edge of the excitation [48,49]. For intensity measurements, the light measured after the LED is turned off is measured, thus detecting a fluorophore or background. To perform time-correlated measurements, the arrival time of the photons is measured, and the lifetime is obtained after processing the obtained histogram [50]. Thus, when performing the measurements as described, a filter is not necessary. This allows the setup to increase its miniaturization and reduce its cost, which are both key factors for PoC devices, following the "ASSURED" criteria. The main part of the setup consists of a sandwich with the microLED array (Figure 1c) on one side driven by a custom CMOS chip (Figure 1d) underneath and a custom CMOS SPAD optical sensor on top. The sample is placed in between using a micromesh. Validation of the instrument was conducted with two different quantum dots (QD605 and QD705, described in Section 2.5) with different lifetimes. The quantum dots are deposited in different wells of a micromesh plate (Section 2.6).

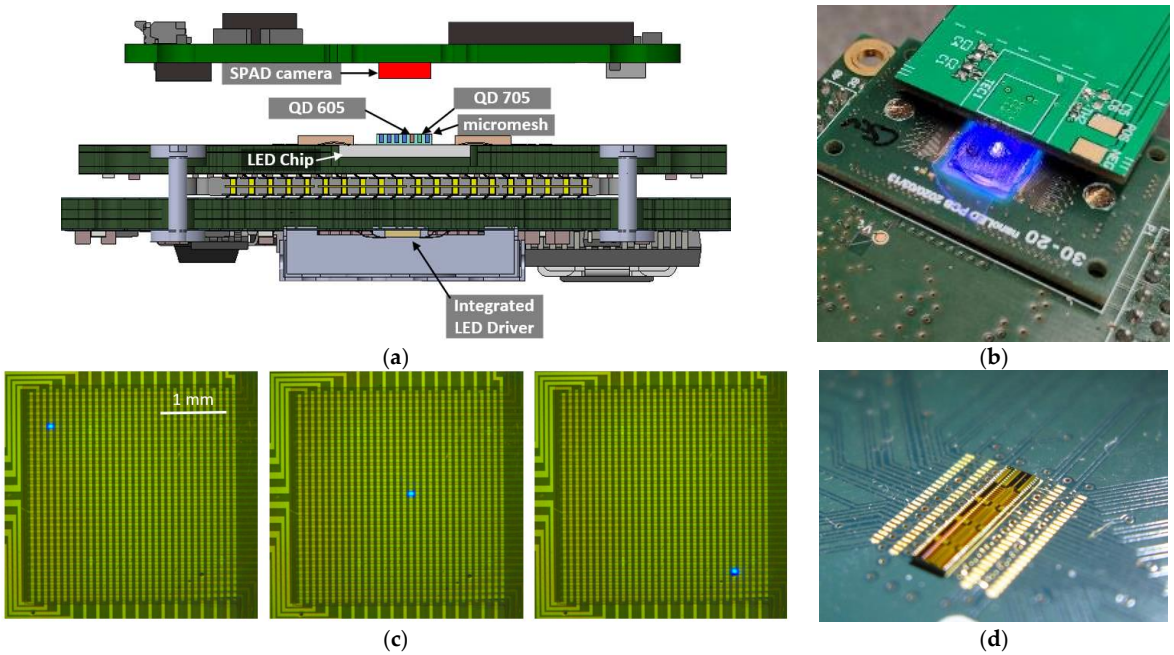


**Figure 1.** The schematic view of the setup is shown in (**a**), and a picture of the setup is in (**b**). (**c**) is a microscopic picture of the array of microLEDs with different LEDs turned on and (**d**) is a picture of the CMOS driver wire bonded to the PCB.

### 2.2. *microLED Array*

The fabrication of the matrix-addressed LED arrays (Figure 1c) is described in detail in a previous publication [51]. It consists of 32 × 32 squared LEDs of 50 µm edge length edge length with 100 µm pitch (Figure 1c). This array is matrix addressable, having all the anodes in the same column connected and all the cathodes in the same row connected (Figure 2). This means the LED chip needs only 32 anode connections and 32 cathode connections to address 1024 LEDs (32 × 32). They were fabricated from standard blue LED wafers on InGaN/GaN basis, emitting at a peak wavelength of approximately 450 nm.

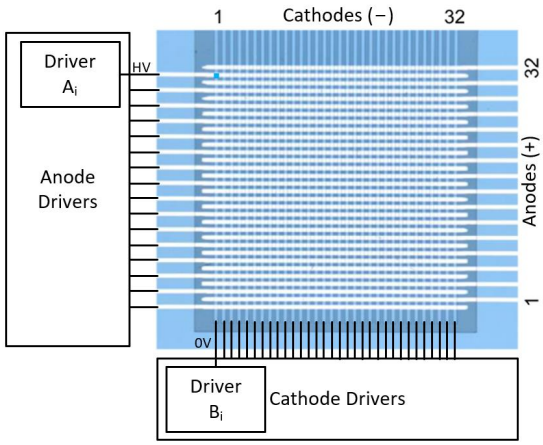


**Figure 2.** Image of the LED chip with the anodes at the right side and the cathodes at the top. As can be observed in the image, only 32 anode connections and 32 cathode connections are needed for an array of 32 × 32 LEDs [51].

The microLED chip was created by etching fin structures into the GaN film. Coupled plasma reactive ion etching (ICP-RIE) was used to etch down to the sapphire substrate. A subsequent wet etch in KOH ensured smoother fin sidewalls and improved passivation. A Ti/Au-based metal pad was provided to each cathode on two opposite edges of the chip as electrical contacts. Subsequently, the trenches in between the array of fins were filled with the polymer benzocyclobuthene (BCB) that was applied by spin-coating. The following hardbake is required to cure the BCB. After this procedure, the resin covers the whole array, and careful mechanical polishing was used for removal and planarization of the BCB, until the fin surfaces were exposed again. Subsequently, an SU-8-based insulation layer was created on the planarized surface, with 32 × 32 openings that define the pixel positions on the fins. Pd/Au contact pads to the p-GaN were then deposited in the opening of the SU-8, and metal lines of Ti/Au were deposited perpendicular to the fins, each connecting a row of pixels and leading to a contact pad at the two remaining chip edges. Another SU-8 layer was then applied as encapsulation of the chip.

From matrix addressable LED chips, it is expected that the larger the number of pixels is, the larger the capacitance to drive is, since the capacitance of every LED per row (or column) is added to the anode (or cathode) node. This would affect the driving rate of the LEDs and, for a large number of pixels, a higher current will be required compared to a smaller number. However, a similar problem affects direct addressable (DA) arrays, since the resistance of the interconnection between each LED with its driver increases considerably, causing a similar RC delay [52,53].

### 2.3. Custom Driver Chip

A chip was produced with the capability of driving the 32 × 32 matrix addressing LED array. The chip contains 32 anodes (p-contacts) and 32 cathodes (n-contacts) drivers. Each driver consists of a combination of these two main circuits (one anode driver $A_i$ and one cathode driver $B_i$), both shown in Figure 3b. In MA, to switch on an LED, the associated row (anode) must be biased positive while the associated column (cathode) is at ground (Figure 2). The rest of the columns must be biased positive too. First, a column of cathodes $B_i$ (Figure 2) is selected by switching the voltage to 0 V, thus allowing us to drive the LEDs in that column. Then, the LEDs in each row are turned on and off by switching the anode drivers $A_i$ (Figure 2). These circuits are designed so the critical node is the anode, which determines the rate at which the LED is charged/discharged.

The driver can operate up to 10 V, thus allowing the LED to provide high optical power (~30 µW at 6 V [51]). The capability of these drivers to generate driving voltages up to 10 V also enables the circuit to be used to drive nanoLEDs [54], which usually work at a higher voltage bias [55] because of the high resistance associated with the interconnection of the LED with the CMOS [54]. In the matrix addressing LED array of this work, the driver can turn off an LED in 2 ns (Figure 4), thus allowing this circuit to be used in time-resolved fluorescence.

Each anode driving pixel measures 572 × 95 µm$^2$ and contains a low-voltage short pulse generator (Figure 3a) and the high-voltage driving circuit (Figure 3b M5–M8). The cathode driving pixel measures 175 × 115 µm$^2$, has the low-voltage short pulse generator (Figure 3a), and the high-voltage driving circuit (Figure 3b M9–M12). The short-pulse generator consists of an AND gate between an external input signal (*Trig*) and its delayed and inverted version. The width of the pulse (*PA* for the anode and *PC* for the cathode) is controlled by a bias voltage ($V_{bias}$) that changes the resistance of M4. To allow longer pulses, M2 is driven by an enable (*En*) signal, which disables the circuit, allowing the use of an external signal to drive the LED. The anode driver consists of a level shifter (M5 and M6) and a high voltage inverter (M7 and M8) with a high W/L ratio that allows fast charge/discharge of the LEDs. The cathode driver consists of a level shifter (M11 and M12) and a high-voltage inverter (M9 and M10).

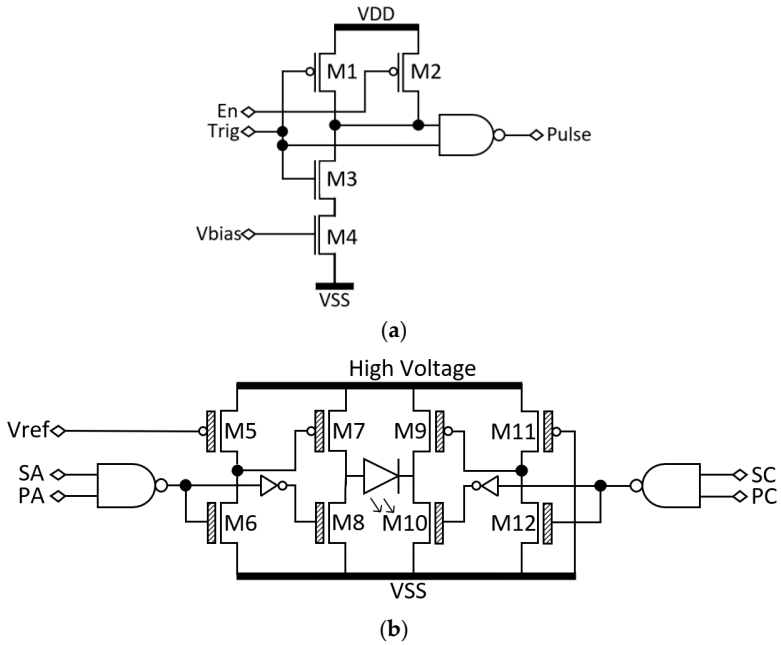


**Figure 3.** Short pulse generation circuit (**a**) and the anode and cathode driving elements (**b**). The anode and cathode driving circuits are composed of high voltage output buffers (M7–M8 for the anode driver and M9–M10 for the cathode driver) and level shifters (M5–M6 and M11–M12) with a NAND gate per driver to select the specific LED.

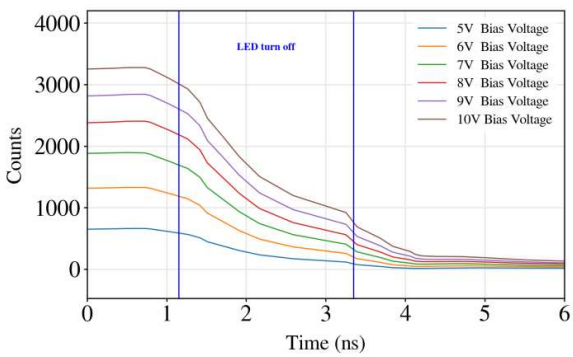


**Figure 4.** Driving circuit turning off a microLED for different bias voltages. It can be observed that the turn off time is the same for all the bias voltage, therefore making the circuit speed robust to changes in the driving voltage of the LEDs. The y axis (Counts) represents the optical intensity captured by the SPAD sensor.

To measure the response time of the fluorophore and to calculate its decay time constant (or lifetime), the sample must be excited with a light source that is able to turn off as fast as possible. The faster the driver can turn off the light source, the shorter the decay times of the fluorophores the device would be able to measure. Figure 4 shows the results of performing time-correlated single photon counting with single LED pulses to observe its rapid response. To conduct such measurements, the SPAD camera described in the following section was used. As can be observed in Figure 4, the CMOS driving circuit is designed to be able to perform fast transitions, thus enabling it to harness the rapid response that GaN LEDs provides. In this case, it is proven that the LED can be turned

off in the 2 ns range for all the bias voltages (calculated from 90% to 10% of the maximum signal), which allows the device to perform detections of fluorophores with lifetimes down to the range of several ns.

### 2.4. SPAD Camera

Details about the custom CMOS SPAD camera, designed in Barcelona, Spain, and manufactured by Austria MicroSystems, Premstaetten, Austria, can be found in a previous publication [56]. It was manufactured in a 0.35 µm High-Voltage (HV) CMOS process. The camera consists of 16 × 16 circular SPAD sensors with 10 µm diameter and a pitch of 70 µm. The camera has low noise, with a Dark Count Rate (DCR) below 1 kHz for 90% of the pixels at the working conditions (19 V breakdown voltage, with an overvoltage of 1.3 V). However, for the experiments performed here, one pixel is selected with a DCR of only 300 Hz. The Photon Detection Probability (PDP) of the chip is 12% centered in 570 nm. For timing measurements, a SPAD sensor provides a time resolution in the order of ps [57,58]. Acquisition in this work is performed with an external FPGA (ZedBoard Zynq.7000, purchased from Digilent, Pullman, WA, USA [59]) with a minimum bin resolution of 68 ps and a maximum number of bins of 6402 [60].

### 2.5. Fluorescent Particles

QDot® 605 ITK™ Streptavidin [61] and QDot® 705 ITK™ Amino PEG [62], referred to as QD605 and QD705, respectively, were both purchased from Life Technologies, Waltham, MA, USA. D705 is equipped with amine-derivatized polyethylene glycol (PEG) ligands covalently bonded to an amphiphilic coating, which enhances their water solubility and facilitates the conjugation of biomolecules. This conjugation is enabled through the reactive amino groups via N-hydroxysuccinimide (NHS) esters. QD605 is comprised of a biotin-binding protein linked to a fluorescent label. Due to its high affinity for biotin, streptavidin in QD605 is typically used with biotinylated conjugates for the targeted detection of various proteins, protein motifs, nucleic acids, and other biomolecules.

The maximum emission peaks for QD605 and QD705 are in 605 nm and 705 nm, respectively. Both are excited in the UV but have a reasonable excitation, with maximum emission at 450 nm for the LEDs used in this work around 20%. QD605 has an expected lifetime in the order of 32 ns, reported by J. Canals et al. [24]. QD705 has an expected lifetime of around 80 ns, as reported in [63] by S. Bhuckory et al.

### 2.6. Micromesh

To distribute the fluorophores in known distance zones, a micromesh was used. The micromesh was purchased from Tebu-bio Spain S.L., Barcelona, Spain [64]. Microwell diameter is 250 µm with 500 µm pitch. In the experiments, a volume of 5 nL QD was loaded in selected microwells of the micromesh.

## 3. Results

### 3.1. Intensity of Fluorescence Measurements

For fluorescence intensity measurements, the LEDs were initially calibrated to provide the same optical output, measured as 150,000 counts in the SPAD. The SPAD sensor measured 255,000 times, with windows of detection of 200 ns for each LED. In Figure 5, we present the map of the intensity the LEDs have at 6 V bias voltage (Figure 5a) and the equalization for 150,000 counts (Figure 5b).

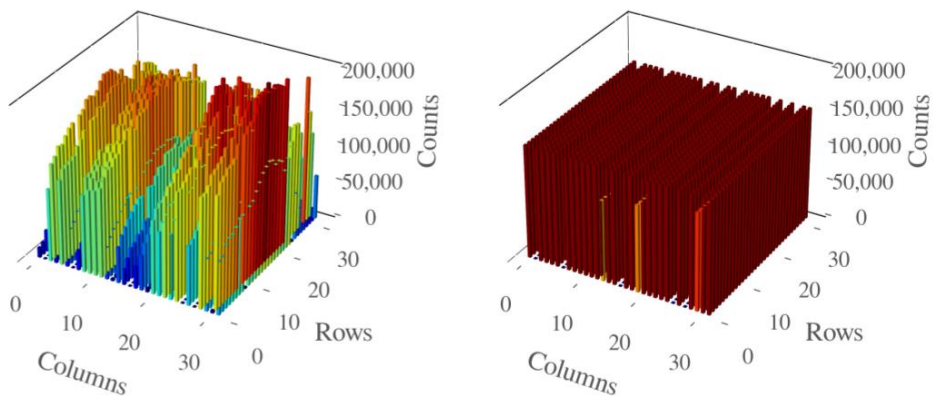


**Figure 5.** LEDs at 6V bias voltage (**a**) without any calibration. Each LED emits different power. In (**b**) all the LEDs were calibrated to 150 kcounts. In (**b**) there are visible non-working LEDs.

With the LEDs calibrated, the experiment was performed. A micromesh with QD605 placed in two microwells was positioned on top of the microLED array. The measurement for each LED was performed for 2 ms. In this period, the LED was pulsed 10,000 times. First, the LED was switched on for 130 ns to excite the fluorophore. Then, the LED was switched off and the SPAD was activated to measure the light emitted by the fluorophore. The SPAD sensor was activated 3 ns after the LED was turned off. Figure 6 shows the intensity emitted by the QD605 after exciting the 32 × 32 LEDs one by one. QD605 was detected in the two microwells as it is shown in Figure 6, such that there are five LEDs under every microwell. As can be observed, the only place where QD605 is detected is in the orange areas, corresponding to two crosses formed by the LEDs, where the microwells contain samples. The number of counts measured in the areas where QD605 was deposited is in the range from 950 to 1050. On the other areas, the number of counts measured is lower than 150. So, the device can discriminate areas with QD605 at concentration of 1 µM at low volumes (5 nL).

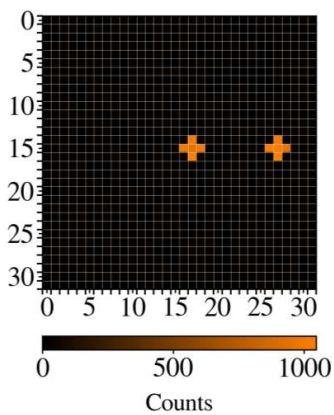


**Figure 6.** Image acquired by the device, where QD605 is detected in the orange areas (above 1000 counts in each one). The other part of the image corresponds to absence of QD605.

Moreover, to test the capabilities of the device, different concentrations were measured for both QD605 and QD705, with the device being able to achieve a LoD of 1/4 µM. As can be observed, at 1/8 µM, the same number of counts are detected as in the Instrument Response (IR), i.e., the background counts when there is no fluorophore (Figure 7).

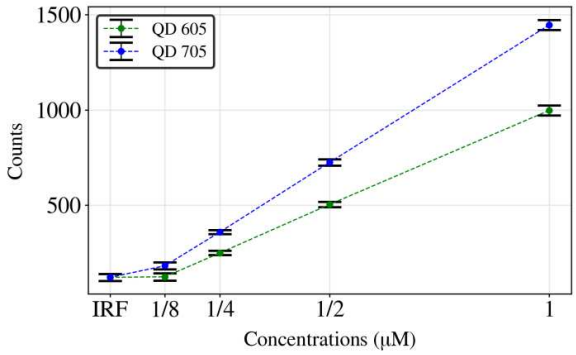


**Figure 7.** Intensity obtained in different measurements for different concentrations of QD605 and QD705.

### *3.2. Time-Correlated Fluorescence Measurements*

Time-Correlated Single Photon Counting (TCSPC) was used to acquire temporal information. This method consists of exciting the sample with a pulsed light source. After each excitation pulse, one of the photons emitted by the fluorophore can be detected by the SPAD sensor, which stays inhibited after the detection. The arrival time of the photon is then measured and catalogued in the corresponding histogram bin. By repeating this method several times, a histogram that represents the decay curve of the fluorophore can be reconstructed. The number of times the measurement was performed is one million, with an exposure time of each measurement of 200 ns, which makes a total exposure time of 200 ms. In this case, the number of photons detected never exceeds 5% of the total number of measurements performed (1 million measurements, maximum of 50,000 counts) in order to avoid pile-up effects [65]. In this work, the maximum counts detected for 1 μM concentration is 15,000 counts, so it can be assured that pile-up effects would not affect the device.

Figure 8 shows different reconstructed histograms corresponding to the two different fluorophores and a measurement of the Instrument Reference Function (IRF). As can be observed, the first 11 ns correspond to the LED source lighting the sample. After that, the LED is turned off and the sum of the fluorophore light and the LED light decays are detected. Then, after 3 ns, the LED is completely off (response < 3 counts). So, the influence of the LED decay is negligible and the QD fluorescence light decay can be measured. The decay of the fluorescence of QDs is described as a multi-exponential curve [66]. However, sometimes it can be approximated as a mono-exponential decay $\left(I_{fluor} = Ae^{(-t\backslash\tau)}\right)$ [24]. Figure 8 presents a linear fit of the logarithmic representation of the decay curve from 30 to 60 ns. Thus, from the inverse of the slope, the extracted lifetimes for QD605 and QD705 are of ~31.3 ns ± 0.6 ns and ~81.7 ns ± 0.9 ns, respectively, which are in good agreement with the reported values (32.7 ± 0.2 ns and 80.0 ± 3 ns, respectively) [24,63]. We also performed the analysis with a mixture of both QDs, as both fluorophores are excited by the same wavelength. Figure 8c,d shows the fit with a bi-exponential model $\left(I_{fluor} = A_1e^{(-t\backslash\tau_1)} + A_2e^{(-t\backslash\tau_2)}\right)$. Two different fluorescence lifetime channels can be selected, and we can estimate the QD605/QD705 ratio on the sample from the amplitude coefficients of both exponentials. Simple linear unmixing of the dyes can be conducted while assuming that there is no modification of the individual lifetimes [67].

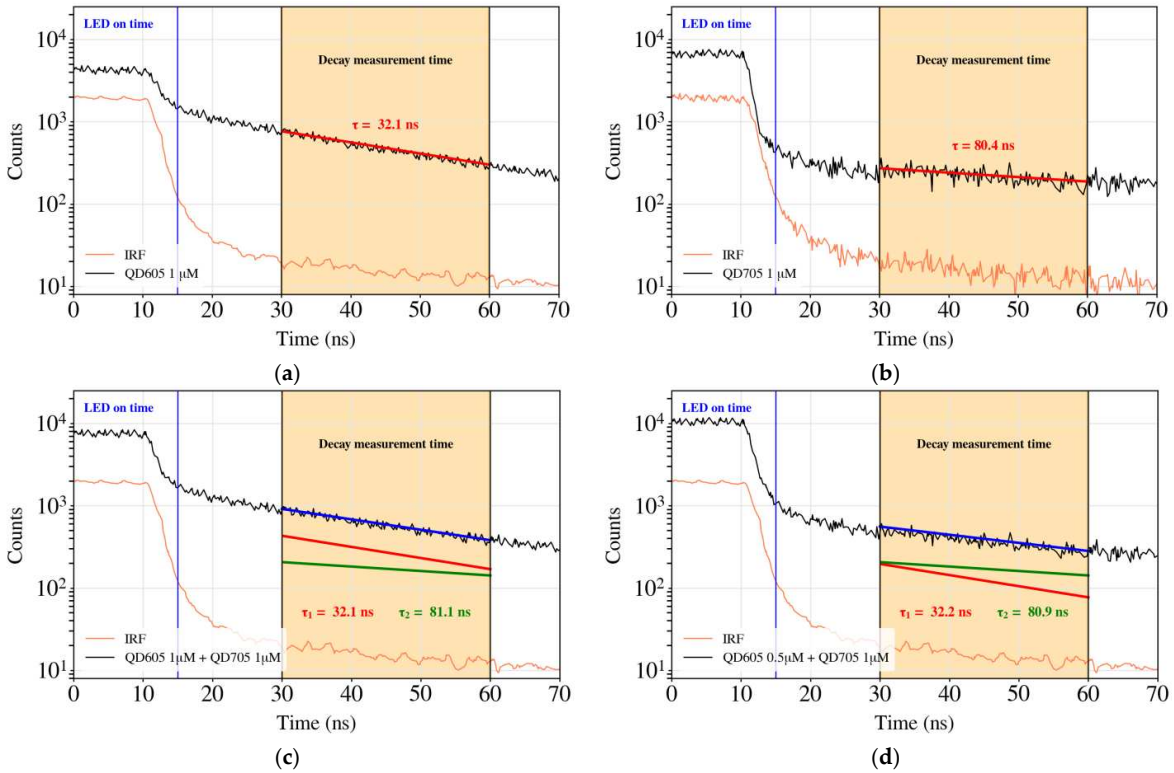


**Figure 8.** Decay time for QD605 at a concentration of 1 μM (**a**) (with A = 1953 and τ = 32.1 ns) and for QD705 also at a concentration of 1 μM (**b**) (with A = 306 and τ = 80.4 ns). In both cases, it is shown the fitted line (in red) where the amplitudes (A) and the lifetimes (τ) are obtained. (**c**,**d**) correspond to a mixture of QD605/QD705 in ratio 1 μM/1 μM and 0.5 μM/1 μM, respectively. Bi-exponential fitting results in $A_1$ = 1915 and $\tau_1$ = 32.1 ns; $A_2$ = 417 and $\tau_2$ = 81.1 ns in (**c**) and $A_1$ = 989 and $\tau_1$ = 32.2 ns; $A_2$ = 397 and $\tau_2$ = 80.9 ns in (**d**).

The LoD of this device using time-correlated fluorescence measurements is the same as that obtained with intensity measurements: 1/4 μM, as expected. Using the measurement method mentioned above, 100 histograms were obtained. From these histograms, the lifetime of each fluorophore was calculated for statistics. They are shown in Figure 9, where QD605 has a mean lifetime of 31.3 ns ± 0.6 ns for concentrations from 1 μM to 1/4 μM and QD705 has a mean lifetime of 81.7 ns ± 0.9 ns for concentrations from 1 μM to 1/4 μM.

Figure 10 shows a representation of the lifetimes measured on top of each LED. As is clear from Figure 8, the slopes of QD705 and the IRF are very similar. To ensure that we could discern the signal from the background, bins were integrated for every LED in the range [30 ns, 60 ns], and a threshold of 5000 counts was established. Then, lifetimes were evaluated, as described previously, for curves with higher counts. In Figure 10, the zones where the fluorophores were detected correspond to the LEDs marked for QD605 and QD705. Pseudocolor was used to identify lifetimes, so that purple corresponds to QD605 and yellow to QD705. Considering the differences observed among the different fluorophores tested, we validated the instrument to develop a PoC based on fluorescence lifetime measurements using microLED arrays operating by matrix addressing.

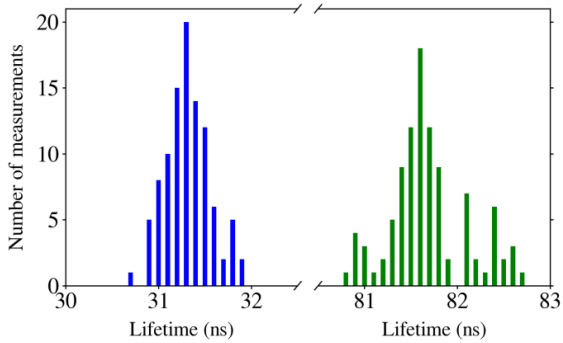


**Figure 9.** Lifetimes of QD605 (blue) and QD705 (green) for 1 μM for 100 sampled measurements to extract statistical values.

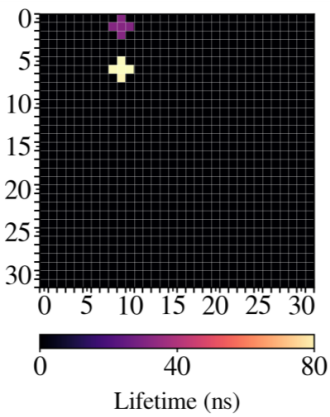


**Figure 10.** Image obtained with the device where the two fluorophores were deposited in microwells.

## 4. Discussion

This research proposes a compact multiplex fluorescence detection system using an array of matrix addressable microLED arrays. The advancements in GaN technology over the past few years indicate that these devices could potentially replace lasers and other illumination sources in the field of fluorescence, particularly in PoC technology [68,69]. GaN-based devices offer simplicity, greater integration capabilities, and cost-effectiveness, making them promising alternatives. The performance of the device was validated through experiments using reference fluorophores. Furthermore, the system was employed to detect two different QD using time-correlated fluorescence measurements in the same assay. Further studies on the proposed PoC device with fluorophores bonded to antibodies and target infections are required to determine applicability. Moreover, the LoD of this setup, with its current characteristics, is 1/4 μM. Nevertheless, this does not invalidate the potential of the technique for detecting even lower concentrations, since the sensitivity depends directly on factors such as the distance between the SPAD and the sample. In this setup, the sample is located at 8 mm of the SPAD sensor, hence the low sensitivity. Some improvement could be obtained by reducing the distance between the sample and the sensors. Additionally, microlenses can be incorporated into the LED array chip to increase the optical power on the fluorophores [70]. Similarly, microlenses can be added to the SPAD array to gather the light being emitted from the fluorophores [71]. The upper LoD of this setup could also be increased from 1 μM until the pile-up effect appears (5% counts over total number of measurements) [65]. Nevertheless, to avoid pileup distortion in case it occurs at higher concentrations, we can decrease the intensity of the excitation light by controlling the bias current of the LEDs [72].

Arrays of microLEDs were used for the first time in [73]. Thus, the use of microLEDs for fluorescence detection has been implemented over and over in the past decades, but typically this has been performed with directly addressable LED arrays, which are limited by their own structure. The LED downscale size, pitch, and density in directly addressable arrays is limited by the size that the connection lines can achieve. Thus, to have drivers capable of providing the necessary speed to perform time-correlated fluorescence measurements, an array with a certain pixel and pitch size is required, or, alternatively, a low LED density on the chip. D. Bezshlyakh et al. [55] reported an array with 400 nm LED size and 400 nm distance between adjacent LEDs with a maximum number of pixels achieved of 6 × 6 due to limitations in space to connect the center pixels to the exterior. Thus, a tradeoff must be made between the size and pitch of the pixels and the size of the array. In [74], a custom chip was used to drive an array of 8 × 8 microLEDs for time-resolved fluorescence measurements. There, the microLED array was bonded by flip-chip onto the custom CMOS driver chip to obtain a direct addressing mode. The state of the art in microLED arrays driven by CMOS circuits is hybrid interconnected arrays [75]. In these devices, the CMOS driver must fit under the pixel; therefore, the smaller the pixel size and pitch is, the smaller the driver is, which limits the switching speed of the circuit. The circuits that achieved the higher speed in the field are reported by J. Canals et al. [76] and N. B. Hassan et al. [77], achieving maximum speeds of 1 MHz, which makes these devices unsuitable for time-resolved fluorescence measurements. Thus, this approach is a tradeoff between driving capabilities, due to the size of the driving circuit that is below the LED, and the density and size of LEDs. Given that the trend of microLED technology for displays is to make smaller microLEDs integrated in higher density arrays, it is a limitation for the use of this addressing mode. On the other hand, there is no limit on the size of the driving circuitry for matrix addressable driving since there is a driver for each column and row of the array that does not need to be under the LED pixel. This allows the driver to provide enough driving current for fluorescence excitation and to be as large as necessary to achieve the driving speeds required for time-resolved fluorescence.

Table 1 summarizes microLED arrays for framerate and array size used for different fields. It can be observed in the tradeoff between array and pixel size, power, and speed. An array with high PPI used for display applications is presented [78] for comparison. Such an array has 1920 × 1080 pixels, but with a limited speed of 125 fps. On the high current side, Poher et al. [79] described a matrix addressable array of 64 × 64 used for neuron stimulation. They achieve high optical power by driving the LEDs up to 10 mA, but with a limited speed of 600 fps.

**Table 1.** Comparison of GaN microLED arrays driven by CMOS circuits.

| **Reference** | [77] | [76] | [78] | [79] | [74] | **This Work** |
|---|---|---|---|---|---|---|
| Driver type | in-pixel | in-pixel | in-pixel | MA | DA | MA |
| Application | display | display | display | neuron stimulation | fluorescence | fluorescence |
| Resolution | 128 × 128 | 512 × 512 | 1920 × 1080 | 64 × 64 | 8 × 8 | 32 × 32 |
| Pixel pitch | 50 µm | 18 µm | 2.5 µm | 40 µm | 200 µm | 100 µm |
| Pixel density | 508 PPI | 1411 PPI | 10,000 PPI | 635 PPI | 127 PPI | 254 PPI |
| Switch speed | 83 kfps | 1 MHz–9.15 kfps | n.a. | 600 fps | 1.28 GHz | 500 MHz |
| Max. LED current | 87 µA | 120 µA | 1.6 µA | 10 mA | n. a. | 20 mA |
| LED bias voltage | 5 V | up to 5V | n.a. V | up to 4V | up to 5V | up to 10 V |
| CMOS Tech. Node | 0.18 µm | 0.18 µm | n.a. | n.a. | 0.35 µm | 0.35 µm |

In this work, we propose the use of microLEDs for multiplexed time-resolved fluorescence in PoC devices. It is centered on matrix addressable arrays that allow for high integration, with the only limit being on the pixel pitch and size, which is determined by the GaN technological limit. Moreover, the driving circuit can be placed outside the

microLED array, which eliminates the limitation of the driver size that appears in hybrid interconnected arrays, thus allowing us to design the driver to achieve the rates required for time-resolved fluorescence measurements.

In addition, the research presented in this work paves the way for the development of miniaturized microscopes [80–84] based on fluorescence, the gold standard tool used in biology. This promising advancement is envisaged through the utilization of large arrays integrating smaller LEDs, complemented by the appropriate driving circuits.

## 5. Conclusions

In this paper, we present a fluorescence detection device that allows for both intensity and lifetime measurements. The device is small and easy to assemble, achieved by joining the advantages of a camera with high SNR CMOS SPAD detectors with an array of microLEDs, which provide high optical power and fast switching speed. Moreover, by using time-gating with the SPAD, the device avoids the use of any optical filter to isolate the fluorescence intensity from the LED light. This is possible thanks to the measurement being taken after the LED is turned off. However, with the auxiliary electronics used to control the device, this approach has some limitations. For lifetime evaluation, it restricts the use of fluorophores to those with decay times longer than ~10 ns. This limits the use of the PoC for organic fluorophores, with lifetimes well below 5 ns. To address such range, new arrays with smaller LED size can be developed to reduce the parasitic capacitance and decrease the switching response. Additionally, more efficient LED drivers with improved switching times can be produced. Nevertheless, addressing such lifetimes could be difficult for a miniaturized microLED-based PoC.

The results obtained by the system endorse that it can detect fluorophores in intensity mode at a high speed, and, moreover, it can detect different fluorophores in the same measurement by using the time-resolved fluorescence method. All of this can be achieved while operating with very small samples volumes (5 nL). This device holds high potential for applications in the scan of biological samples, analytical laboratories, and for clinical diagnosis.

Furthermore, the device enables the possibility of advances in different fields, such as building a fluorescence microscope by using an array of microLEDs [85] or building multi-well detection devices for multiplexed assays.

**Author Contributions:** Conception of the device, A.D. and V.M.; experiments, V.M.; construction of the device, O.A. and V.M.; PCB design, J.C.; software, J.C., S.M. and V.M.; FPGA firmware, J.C., S.M. and V.M.; design of CMOS driving chip, V.M.; data analysis, V.M.; investigation, A.D. and V.M.; microLED design and fabrication, S.H.-W., J.D.P. and A.W.; writing—original draft preparation, V.M.; writing—review and editing, V.M. and A.D.; supervision, A.D.; funding acquisition, A.D. and J.D.P. All authors have read and agreed to the published version of the manuscript.

**Funding:** This work received funding from the European Union's Horizon 2020 research and innovation program under grant agreement No 737089. Grants PID2019-105714RB-I00 and PID2022-136833OB-C21 funded by MICIU/AEI/10.13039/501100011033 and the European Regional Development Fund. Grant PRE2020-093659 funded by MICIU/AEI/10.13039/501100011033 and by ESF invests in your future.

**Data Availability Statement:** The original contributions presented in the study are included in the article, further inquiries can be directed to the corresponding authors.

**Conflicts of Interest:** The authors declare no conflicts of interest.

## References

1. World Health Organization Ageing and Health. Available online: https://www.who.int/news-room/fact-sheets/detail/ageing-and-health (accessed on 8 March 2024).
2. Mills, A. Health Care Systems in Low- and Middle-Income Countries. *N. Engl. J. Med.* **2014**, *370*, 552–557. [CrossRef] [PubMed]
3. Sharma, S.; Zapatero-Rodríguez, J.; Estrela, P.; O'Kennedy, R. Point-of-Care Diagnostics in Low Resource Settings: Present Status and Future Role of Microfluidics. *Biosensors* **2015**, *5*, 577–601. [CrossRef] [PubMed]

4. Boniface, R.; Moshabela, M.; Zulliger, R.; MacPherson, P.; Nyasulu, P. Correlates of Delayed Diagnosis among Human Immunodeficiency Virus-Infected Pulmonary Tuberculosis Suspects in a Rural HIV Clinic, South Africa. *Tuberc. Res. Treat.* **2012**, *2012*, 827148. [CrossRef] [PubMed]
5. Mashamba-Thompson, T.P.; Sartorius, B.; Drain, P.K. Operational Assessment of Point-of-Care Diagnostics in Rural Primary Healthcare Clinics of KwaZulu-Natal, South Africa: A Cross-Sectional Survey. *BMC Health Serv. Res.* **2018**, *18*, 380. [CrossRef] [PubMed]
6. Zhang, H.; Miller, B.L. Immunosensor-Based Label-Free and Multiplex Detection of Influenza Viruses: State of the Art. *Biosens. Bioelectron.* **2019**, *141*, 111476. [CrossRef] [PubMed]
7. Hojat, K.; Duppenthaler, A.; Aebi, C. Impact of the Availability of an Influenza Virus Rapid Antigen Test on Diagnostic Decision Making in a Pediatric Emergency Department. *Pediatr. Emerg. Care* **2013**, *29*, 696–698. [CrossRef] [PubMed]
8. Chin, C.D.; Linder, V.; Sia, S.K. Lab-on-a-Chip Devices for Global Health: Past Studies and Future Opportunities. *Lab. Chip* **2007**, *7*, 41–57. [CrossRef] [PubMed]
9. Hansen, G.T. Point-of-Care Testing in Microbiology: A Mechanism for Improving Patient Outcomes. *Clin. Chem.* **2020**, *66*, 124–137. [CrossRef] [PubMed]
10. Drain, P.K.; Hyle, E.P.; Noubary, F.; Freedberg, K.A.; Wilson, D.; Bishai, W.R.; Rodriguez, W.; Bassett, I.V. Diagnostic Point-of-Care Tests in Resource-Limited Settings. *Lancet Infect. Dis.* **2014**, *14*, 239–249. [CrossRef]
11. Vashist, S.K. Point-of-Care Diagnostics: Recent Advances and Trends. *Biosensors* **2017**, *7*, 62. [CrossRef]
12. Kozel, T.R.; Burnham-Marusich, A.R. Point-of-Care Testing for Infectious Diseases: Past, Present, and Future. *J. Clin. Microbiol.* **2017**, *55*, 2313–2320. [CrossRef] [PubMed]
13. Global HIV Hepatitis and STIs Programmes (HHS); Sexual and Reproductive Health and Research (SRH); World Health Organization. *The Diagnostics Landscape for Sexually Transmitted Infections*; WHO: Geneva, Switzerland, 2023; ISBN 9789240077126.
14. Qin, J.; Wang, W.; Gao, L.; Yao, S.Q. Emerging Biosensing and Transducing Techniques for Potential Applications in Point-of-Care Diagnostics. *Chem. Sci.* **2022**, *13*, 2857–2876. [CrossRef] [PubMed]
15. Pruksaphon, K.; Intaramat, A.; Ratanabanangkoon, K.; Nosanchuk, J.D.; Vanittanakom, N.; Youngchim, S. Diagnostic Laboratory Immunology for Talaromycosis (Penicilliosis): Review from the Bench-Top Techniques to the Point-of-Care Testing. *Diagn. Microbiol. Infect. Dis.* **2020**, *96*, 114959. [CrossRef] [PubMed]
16. Ouyang, M.; Tu, D.; Tong, L.; Sarwar, M.; Bhimaraj, A.; Li, C.; Coté, G.L.; Di Carlo, D. A Review of Biosensor Technologies for Blood Biomarkers toward Monitoring Cardiovascular Diseases at the Point-of-Care. *Biosens. Bioelectron.* **2021**, *171*, 112621. [CrossRef] [PubMed]
17. Wei, T.Y.; Fu, Y.; Chang, K.H.; Lin, K.J.; Lu, Y.J.; Cheng, C.M. Point-of-Care Devices Using Disease Biomarkers to Diagnose Neurodegenerative Disorders. *Trends Biotechnol.* **2018**, *36*, 290–303. [CrossRef] [PubMed]
18. Sandbhor Gaikwad, P.; Banerjee, R. Advances in Point-of-Care Diagnostic Devices in Cancers. *Analyst* **2018**, *143*, 1326–1348. [CrossRef] [PubMed]
19. Diamond, S.L.; Rossi, J.M. Point of Care Whole Blood Microfluidics for Detecting and Managing Thrombotic and Bleeding Risks. *Lab. Chip* **2021**, *21*, 3667–3674. [CrossRef] [PubMed]
20. Stedtfeld, R.D.; Tourlousse, D.M.; Seyrig, G.; Stedtfeld, T.M.; Kronlein, M.; Price, S.; Ahmad, F.; Gulari, E.; Tiedje, J.M.; Hashsham, S.A. Gene-Z: A Device for Point of Care Genetic Testing Using a Smartphone. *Lab. Chip* **2012**, *12*, 1454–1462. [CrossRef]
21. Clerc, O.; Greub, G. Routine Use of Point-of-Care Tests: Usefulness and Application in Clinical Microbiology. *Clin. Microbiol. Infect.* **2010**, *16*, 1054–1061. [CrossRef]
22. Cholkar, K.; Hirani, N.D.; Natarajan, C. Nanotechnology-Based Medical and Biomedical Imaging for Diagnostics. In *Emerging Nanotechnologies for Diagnostics, Drug Delivery and Medical Devices*; Elsevier Inc.: Amsterdam, The Netherlands, 2017; pp. 355–374. ISBN 9780323429979.
23. Pennathur, S.; Fygenson, D.K. Improving Fluorescence Detection in Lab on Chip Devices. *Lab. Chip* **2008**, *8*, 649–652. [PubMed]
24. Canals, J.; Franch, N.; Alonso, O.; Vilà, A.; Diéguez, A. A Point-of-Care Device for Molecular Diagnosis Based on CMOS SPAD Detectors with Integrated Microfluidics. *Sensors* **2019**, *19*, 445. [CrossRef] [PubMed]
25. Hang, Y.; Boryczka, J.; Wu, N. Visible-Light and near-Infrared Fluorescence and Surface-Enhanced Raman Scattering Point-of-Care Sensing and Bio-Imaging: A Review. *Chem. Soc. Rev.* **2022**, *51*, 329–375. [CrossRef]
26. Berner, M.; Hilbig, U.; Schubert, M.B.; Gauglitz, G. Laser-Induced Fluorescence Detection Platform for Point-of-Care Testing. *Meas. Sci. Technol.* **2017**, *28*, 085701. [CrossRef]
27. Jin, B.; Li, Z.; Zhao, G.; Ji, J.; Chen, J.; Yang, Y.; Xu, R. Upconversion Fluorescence-Based Paper Disc for Multiplex Point-of-Care Testing in Water Quality Monitoring. *Anal. Chim. Acta* **2022**, *1192*, 339388. [CrossRef]
28. He, Q.; Yu, D.; Bao, M.; Korensky, G.; Chen, J.; Shin, M.; Kim, J.; Park, M.; Qin, P.; Du, K. High-Throughput and All-Solution Phase African Swine Fever Virus (ASFV) Detection Using CRISPR-Cas12a and Fluorescence Based Point-of-Care System. *Biosens. Bioelectron.* **2020**, *154*, 112068. [CrossRef]
29. Mukunda, D.C.; Joshi, V.K.; Mahato, K.K. Light Emitting Diodes (LEDs) in Fluorescence-Based Analytical Applications: A Review. *Appl. Spectrosc. Rev.* **2022**, *57*, 1–38. [CrossRef]
30. Wang, Y.; Fang, Y.; Liu, H.; Su, X.; Chen, Z.; Li, S.; He, N. A Highly Integrated and Diminutive Fluorescence Detector for Point-of-Care Testing: Dual Negative Feedback Light-Emitting Diode (LED) Drive and Photoelectric Processing Circuits Design and Implementation. *Biosensors* **2022**, *12*, 764. [CrossRef]

31. Mohanan, S.M.P.C.; Russell, K.; Duncan, S.; Kiang, A.; Lochenie, C.; Duffy, E.; Kennedy, S.; Prajna, N.V.; Williams, R.L.; Dhaliwal, K.; et al. FluoroPi Device with SmartProbes: A Frugal Point-of-Care System for Fluorescent Detection of Bacteria from a Pre-Clinical Model of Microbial Keratitis. *Transl. Vis. Sci. Technol.* **2023**, *12*, 1. [CrossRef]
32. Lian, C.; Young, D.; Randall, R.E.; Samuel, I.D.W. Organic Light-Emitting Diode Based Fluorescence-Linked Immunosorbent Assay for SARS-CoV-2 Antibody Detection. *Biosensors* **2022**, *12*, 1125. [CrossRef] [PubMed]
33. He, H.; Wu, C.; Saqib, M.; Hao, R. Single-Molecule Fluorescence Methods for Protein Biomarker Analysis. *Anal. Bioanal. Chem.* **2023**, *415*, 3655–3669. [CrossRef]
34. Berezin, M.Y.; Achilefu, S. Fluorescence Lifetime Measurements and Biological Imaging. *Chem. Rev.* **2010**, *110*, 2641–2684. [CrossRef] [PubMed]
35. Kobayashi, H.; Ogawa, M.; Alford, R.; Choyke, P.L.; Urano, Y. New Strategies for Fluorescent Probe Design in Medical Diagnostic Imaging. *Chem. Rev.* **2010**, *110*, 2620–2640. [CrossRef] [PubMed]
36. Kanani, S.S.; Tsai, H.Y.; Algar, W.R. Quantitative and Multiplexed Chopper-Based Time-Gated Imaging for Bioanalysis on a Smartphone. *Anal. Chem.* **2023**, *95*, 13258–13265. [CrossRef] [PubMed]
37. Qiu, X.; Xu, J.; Cardoso Dos Santos, M.; Hildebrandt, N. Multiplexed Biosensing and Bioimaging Using Lanthanide-Based Time-Gated Förster Resonance Energy Transfer. *Acc. Chem. Res.* **2022**, *55*, 551–564. [CrossRef] [PubMed]
38. Fan, Y.; Wang, P.; Lu, Y.; Wang, R.; Zhou, L.; Zheng, X.; Li, X.; Piper, J.A.; Zhang, F. Lifetime-Engineered NIR-II Nanoparticles Unlock Multiplexed In Vivo Imaging. *Nat. Nanotechnol.* **2018**, *13*, 941–946. [CrossRef] [PubMed]
39. Obahiagbon, U.; Smith, J.T.; Zhu, M.; Katchman, B.A.; Arafa, H.; Anderson, K.S.; Blain Christen, J.M. A Compact, Low-Cost, Quantitative and Multiplexed Fluorescence Detection Platform for Point-of-Care Applications. *Biosens. Bioelectron.* **2018**, *117*, 153–160. [CrossRef] [PubMed]
40. Myers, F.B.; Henrikson, R.H.; Xu, L.; Lee, L.P. A Point-of-Care Instrument for Rapid Multiplexed Pathogen Genotyping. In Proceedings of the 2011 Annual International Conference of the IEEE Engineering in Medicine and Biology Society, Boston, MA, USA, 30 August–3 September 2011; IEEE: New York, NY, USA, 2011. ISBN 9781424441228.
41. Smith, J.T.; Obahiagbon, U.; Ewaisha, R.; Katchman, B.A.; Kaftanoglu, K.; Arafa, H.M.; Kullman, D.E.; Anderson, K.S. Low-Cost, Disposable Fluorescence-Based Biorecognition System for Multiplexed Point-of-Care Molecular Diagnostics. In Proceedings of the 2016 IEEE Healthcare Innovation Point-Of-Care Technologies Conference (HI-POCT), Cancun, Mexico, 9–11 November 2016.
42. Manzanas, C.; Alam, M.M.; Loeb, J.C.; Lednicky, J.A.; Wu, C.Y.; Fan, Z.H. A Valve-Enabled Sample Preparation Device with Isothermal Amplification for Multiplexed Virus Detection at the Point-of-Care. *ACS Sens.* **2021**, *6*, 4176–4184. [CrossRef] [PubMed]
43. Shu, B.; Lin, L.; Wu, B.; Huang, E.; Wang, Y.; Li, Z.; He, H.; Lei, X.; Xu, B.; Liu, D. A Pocket-Sized Device Automates Multiplexed Point-of-Care RNA Testing for Rapid Screening of Infectious Pathogens. *Biosens. Bioelectron.* **2021**, *181*, 113145. [CrossRef] [PubMed]
44. Wasisto, H.S.; Prades, J.D.; Gülink, J.; Waag, A. Beyond Solid-State Lighting: Miniaturization, Hybrid Integration, and Applications of GaN Nano-and Micro-LEDs. *Appl. Phys. Rev.* **2019**, *6*, 041315. [CrossRef]
45. Tian, P.; McKendry, J.J.D.; Gong, Z.; Zhang, S.; Watson, S.; Zhu, D.; Watson, I.M.; Gu, E.; Kelly, A.E.; Humphreys, C.J.; et al. Characteristics and Applications of Micro-Pixelated GaN-Based Light Emitting Diodes on Si Substrates. *J. Appl. Phys.* **2014**, *115*, 033112. [CrossRef]
46. Rae, B.R.; Yang, J.B.; McKendry, J.; Gong, Z.; Renshaw, D.; Girkin, J.M.; Gu, E.; Dawson, M.D.; Henderson, R.K. A Vertically Integrated CMOS Microsystem for Time-Resolved Fluorescence Analysis. *IEEE Trans. Biomed. Circuits Syst.* **2010**, *4*, 437–444. [CrossRef]
47. Xie, E.; Bian, R.; He, X.; Islim, M.S.; Chen, C.; Mckendry, J.J.D.; Gu, E.; Haas, H.; Dawson, M.D. Over 10 Gbps VLC for Long-Distance Applications Using a GaN-Based Series-Biased Micro-LED Array. *IEEE Photonics Technol. Lett.* **2020**, *32*, 499–502. [CrossRef]
48. Vilella, E.; Diéguez, A. A Gated Single-Photon Avalanche Diode Array Fabricated in a Conventional CMOS Process for Triggered Systems. *Sens. Actuators A Phys.* **2012**, *186*, 163–168. [CrossRef]
49. Vilella, E.; Diéguez, A. Dynamic Range Extension of SiPM Detectors with the Time-Gated Operation. *Opt. Express* **2014**, *22*, 12007. [CrossRef]
50. Wang, Y.; Rae, B.R.; Henderson, R.K.; Gong, Z.; McKendry, J.; Gu, E.; Dawson, M.D.; Turnbull, G.A.; Samuel, I.D.W. Ultra-Portable Explosives Sensor Based on a CMOS Fluorescence Lifetime Analysis Micro-System. *AIP Adv.* **2011**, *1*, 032115. [CrossRef]
51. Bornemann, S.; Gulink, J.; Moro, V.; Canals, J.; Wolter, S.; Schottler, G.; Bezshlyakh, D.; Prades, J.; Dieguez, A.; Waag, A. Processing and Characterization of Monolithic Passive-Matrix GaN-Based MicroLED Arrays with Pixel Sizes from 5 to 50 Mm. *IEEE Photonics J.* **2021**, *13*, 8200209. [CrossRef]
52. Lim, S.G.; Lee, K.; Kim, Y.J. Mobile AMOLED Display Power Model Considering I-R Drop in Smartphones. *IEEE Trans. Ind. Electron.* **2021**, *68*, 2694–2702. [CrossRef]
53. Seong, J.; Jang, J.; Lee, J.; Lee, M. CMOS Backplane Pixel Circuit with Leakage and Voltage Drop Compensation for an Micro-LED Display Achieving 5000 PPI or Higher. *IEEE Access* **2020**, *8*, 49467–49476. [CrossRef]
54. Canals, J.; Franch, N.; Moro, V.; Moreno, S.; Prades, J.D.; Romano-Rodríguez, A.; Bornemann, S.; Bezshlyakh, D.D.; Waag, A.; Vogelbacher, F.; et al. A Novel Approach for a Chip-Sized Scanning Optical Microscope. *Micromachines* **2021**, *12*, 527. [CrossRef]

55. Bezshlyakh, D.D.; Spende, H.; Weimann, T.; Hinze, P.; Bornemann, S.; Gülink, J.; Canals, J.; Prades, J.D.; Dieguez, A.; Waag, A. Directly Addressable GaN-Based Nano-LED Arrays: Fabrication and Electro-Optical Characterization. *Microsyst. Nanoeng.* **2020**, *6*, 1–10. [CrossRef]
56. Franch Masdeu, N. *Development of a Nano-Illumination Microscope*; University of Barcelona: Barcelona, Spain, 2022; Available online: http://hdl.handle.net/2445/189889 (accessed on 15 March 2024).
57. Gulinatti, A.; Maccagnani, P.; Rech, I.; Ghioni, M.; Cova, S. 35 Ps Time Resolution at Room Temperature with Large Area Single Photon Avalanche Diodes. *Electron. Lett.* **2005**, *41*, 272–274. [CrossRef]
58. Acerbi, F.; Ferri, A.; Gola, A.; Cazzanelli, M.; Pavesi, L.; Zorzi, N.; Piemonte, C. Characterization of Single-Photon Time Resolution: From Single SPAD to Silicon Photomultiplier. *IEEE Trans. Nucl. Sci.* **2014**, *61*, 2678–2686. [CrossRef]
59. ZedBoard Zynq-7000 ARM/FPGA SoC Development Board. Available online: https://digilent.com/shop/zedboard-zynq-7000-arm-fpga-soc-development-board/ (accessed on 21 March 2024).
60. Franch, N.; Alonso, O.; Canals, J.; Vila, A.; Dieguez, A. A Low Cost Fluorescence Lifetime Measurement System Based on SPAD Detectors and FPGA Processing. *J. Instrum.* **2017**, *12*, C02070. [CrossRef]
61. QdotTM 605 ITKTM Streptavidin Conjugate Kit. Available online: https://www.thermofisher.com/order/catalog/product/Q10001MP?SID=srch-srp-Q10001MP (accessed on 8 March 2024).
62. QdotTM 705 ITKTM Amino (PEG) Quantum Dots. Available online: https://www.thermofisher.com/order/catalog/product/Q21561MP?SID=srch-srp-Q21561MP (accessed on 8 March 2024).
63. Bhuckory, S.; Lefebvre, O.; Qiu, X.; Wegner, K.D.; Hildebrandt, N. Evaluating Quantum Dot Performance in Homogeneous FRET Immunoassays for Prostate Specific Antigen. *Sensors* **2016**, *16*, 197. [CrossRef]
64. tebu-bio Micromesh Array, Well Size 250 um, 8 mm Array. Available online: https://www.tebubio.com/es-eur/micromesh-array-well-size-250um-8mm-array-10-arrays-per-p/5637365732.p (accessed on 8 March 2024).
65. The Principle of Time-Correlated Single Photon Counting. Available online: https://www.picoquant.com/images/uploads/page/files/7253/technote_tcspc.pdf (accessed on 10 May 2024).
66. Giraud, G.; Schulze, H.; Bachmann, T.T.; Campbell, C.J.; Mount, A.R.; Ghazal, P.; Khondoker, M.R.; Ember, S.W.J.; Ciani, I.; Tlili, C.; et al. Solution State Hybridization Detection Using Time-Resolved Fluorescence Anisotropy of Quantum Dot-DNA Bioconjugates. *Chem. Phys. Lett.* **2010**, *484*, 309–314. [CrossRef]
67. Bückers, J.; Wildanger, D.; Vicidomini, G.; Kastrup, L.; Hell, S.W. Simultaneous Multi-Lifetime Multi-Color STED Imaging for Colocalization Analyses. *Opt. Express* **2011**, *19*, 3130–3143. [CrossRef]
68. Sipior, J.; Carter, G.M.; Lakowicz, J.R.; Rao, G. Blue Light-Emitting Diode Demonstrated as an Ultraviolet Excitation Source for Nanosecond Phase-Modulation Fluorescence Lifetime Measurements. *Rev. Sci. Instrum.* **1997**, *68*, 2666–2670. [CrossRef]
69. Araki, T.; Misawa, H. Light Emitting Diode-Based Nanosecond Ultraviolet Light Source for Fluorescence Lifetime Measurements. *Rev. Sci. Instrum.* **1995**, *66*, 5469–5472. [CrossRef]
70. Kim, D.; Lee, H.; Cho, N.; Sung, Y.; Yeom, G. Effect of GaN Microlens Array on Efficiency of GaN-Based Blue-Light-Emitting Diodes. *Jpn. J. Appl. Phys. Part 2 Lett.* **2005**, *44*, L18. [CrossRef]
71. Burri, S.; Maruyama, Y.; Michalet, X.; Regazzoni, F.; Bruschini, C.; Charbon, E. Architecture and Applications of a High Resolution Gated SPAD Image Sensor. *Opt. Express* **2014**, *22*, 17573. [CrossRef]
72. Léonard, J.; Dumas, N.; Caussé, J.P.; Maillot, S.; Giannakopoulou, N.; Barre, S.; Uhring, W. High-Throughput Time-Correlated Single Photon Counting. *Lab. A Chip—Miniaturisation Chem. Biol.* **2014**, *14*, 4338–4343. [CrossRef]
73. Griffin, C.; Gu, E.; Choi, H.W.; Jeon, C.W.; Rolinski, O.J.; Birch, D.J.S.; Girkin, J.M.; Dawson, M.D. Fluorescence Excitation and Lifetime Measurements Using GaN/InGaN Micro LED Arrays. In Proceedings of the The 17th Annual Meeting of the IEEELasers and Electro-Optics Society, 2004. LEOS 2004, Rio Grande, PR, USA, 11 November 2004.
74. Rae, B.R.; Muir, K.R.; Gong, Z.; McKendry, J.; Girkin, J.M.; Gu, E.; Renshaw, D.; Dawson, M.D.; Henderson, R.K. A CMOS Time-Resolved Fluorescence Lifetime Analysis Micro-System. *Sensors* **2009**, *9*, 9255–9274. [CrossRef]
75. Ou, F.; Chong, W.C.; Xu, Q.; Chen, Y.; Li, Q.; Zhang, L. Monochromatic Active Matrix Micro-LED Micro-Displays with >5,000 Dpi Pixel Density Fabricated Using Monolithic Hybrid Integration Process. *Dig. Tech. Pap.* **2018**, *49*, 1677–1680. [CrossRef]
76. Canals, J.; Moro, V.; Schöttler, G.; Bornemann, S.; Waag, A.; Prades, J.D.; Diéguez, A. A 9 Kfps 1411 PPI GaN-Based MLED Display CMOS Backplane. *Dig. Tech. Pap.* **2023**, *54*, 125–128. [CrossRef]
77. Bani Hassan, N.; Dehkhoda, F.; Xie, E.; Herrnsdorf, J.; Strain, M.J.; Henderson, R.; Dawson, M.D. Ultrahigh Frame Rate Digital Light Projector Using Chip-Scale LED-on-CMOS Technology. *Photonics Res.* **2022**, *10*, 2434. [CrossRef]
78. Jade Bird Display, "0.22" MicroLED | JBD | 10000PPI MicroLED". Available online: https://www.jb-display.com/weixianshiping/3.html (accessed on 10 May 2024).
79. Poher, V.; Grossman, N.; Kennedy, G.T.; Nikolic, K.; Zhang, H.X.; Gong, Z.; Drakakis, E.M.; Gu, E.; Dawson, M.D.; French, P.M.W.; et al. Micro-LED Arrays: A Tool for Two-Dimensional Neuron Stimulation. *J. Phys. D Appl. Phys.* **2008**, *41*, 094014. [CrossRef]
80. Moreno, S.; Canals, J.; Moro, V.; Franch, N.; Vilà, A.; Romano, A.; Prades, J.D.; Bezshlyakh, D.D.; Waag, A.; Diéguez, A. Nano-Illumination Microscopy as a Fast Low-Cost Chip-Sized Technique to Face Pandemics. In Proceedings of the Biosensors for Pandemics, online, 6 May 2020.
81. Canals, J.; Moro, V.; Franch, N.; Moreno, S.; Alonso, O.; Vilà, A.; Prades, J.D.; Gülink, J.; Bezshlyakh, D.D.; Waag, A.; et al. A Shadow Image Microscope Based on an Array of NanoLEDs. *Proc. SPIE* **2020**, *11351*, 113510D.

82. Vilà, A.; Moreno, S.; Canals, J.; Diéguez, A. A Compact Raster Lensless Microscope Based on a Microdisplay. *Sensors* **2021**, *21*, 5941. [CrossRef]
83. Vila, A.; Moreno, S.; Canals, J.; Moro, V.; Franch, N.; Wartenberg, P.; Dieguez, A. Ultra-Compact and Large Field-of-View Nano-Illumination Light Microscope Based on an Array of Organic Light-Emitting Diodes. *Proc. SPIE* **2021**, *11693*, 1169308.
84. Prajapati, E.; Kumar, S.; Kumar, S. Muscope: A Miniature on-Chip Lensless Microscope. *Lab. Chip* **2021**, *21*, 4357–4363. [CrossRef]
85. Franch, N.; Canals, J.; Moro, V.; Vilà, A.; Romano-Rodríguez, A.; Prades, J.D.; Guelink, J.; Bezshlyakh, D.; Waag, A.; Kluczyk, K.; et al. Nano-Illumination Microscopy: A Technique Based on Scanning with an Array of Individually Addressable NanoLEDs. *Opt. Express* **2020**, *28*, 19044–19057. [CrossRef] [PubMed]

## 3.4. GaN-on-Si hybrid interconnected devices for microdisplays

As GaN technology keeps improving, it is clear that in the future, the most promising integration path to create platforms of microLEDs that can be used for several biomedical applications is by the use of GaN-on-Si devices. In the work presented in Sections 3.4.5 and 3.4.6, we reported a CMOS backplane manufactured in the 0.18 µm OnSemi technology. The backplane was designed to drive an array of 512 x 512 square microLEDs with edge size of 10 µm and a pitch of 18 µm. Thus, this limits the in-pixel CMOS driver area to an 18 x 18 $\mu m^2$ size. The in-pixel driver developed for this work consist of 4 internal digital storage memories (6T SRAMs), 4 driving transistors with different W/L ratios that form a current source that provides 16 different grey levels, which are programed by the SRAMs, a pulsing transistor that allows the array to have a 5V LED bias voltage and to achieve switching rates up to 1MHz, and a calibration feedback circuit, that provides information of the bias current driven by the current source to the LED in order to compare and compensate any mismatch either form the CMOS driver or the GaN LED array (Figure 46). The circuit was designed to operate at a maximum bias voltage of 1.8V for the LED anode node, allowing to design the driver circuit using a majority of low voltage 1.8V transistors, reducing the area needed to implement them. To achieve high driving currents and a bias voltage up to 5V, the circuit was designed to allow a -3.2V cathode voltage.

# 3. Results

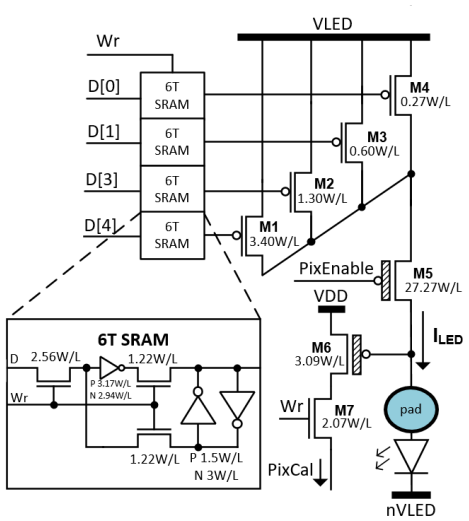


**Figure 46.** Schematic of the driver based on 6T SRAMs.

## 3.4.1. In-pixel driver

The pixel driver purposed is a high-density integrated circuit that fills all the 18 x 18 $\mu m^2$ area available for the design. In Figure 47 it can be observed that the design is filled with transistors and connection lines, so little improvement can be performed for this size of pixel and this technological CMOS node.

The in-pixel circuit is capable of providing constant currents up to 120 µA. Furthermore, by having the possibility of modifying the driving voltage from 1.8V to 5V, the driver is not limited to a range of 0 to 120 µA with 8 steps, but it can achieve a larger number of possible bias currents. To test the electrical characteristics of the driver, a setup was made with a probe station connecting the CMOS backplane output to an external 10 x 10 $\mu m^2$ microLED (Figure 48).

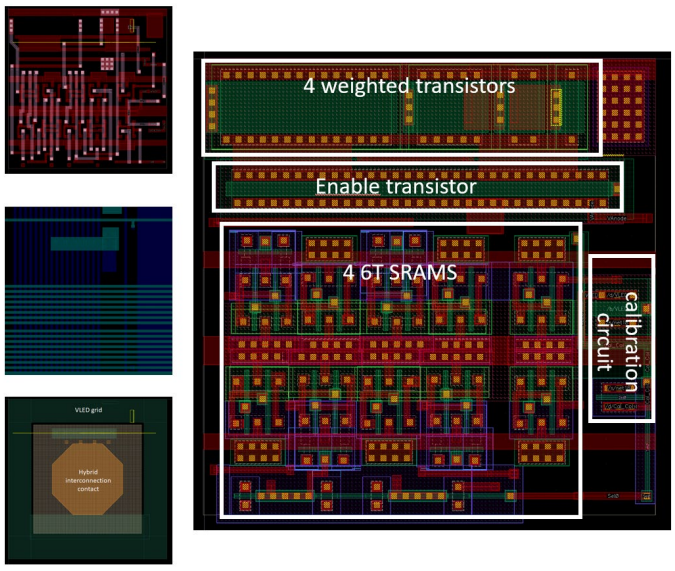


**Figure 47.** Layout of the driving circuit. In the left it can be observed metal 1 and 2 layers, metal 3 and 4 layers and metal 5 and 6 layers in that order. In the right it can be observed the transistor level layout.

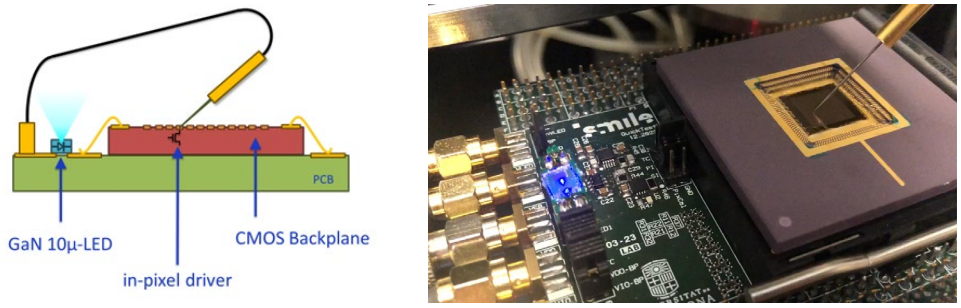


**Figure 48.** Setup made to test the electrical characteristics of the backplane. In (a) an schematic view is shown and in (b) a photograph of the setup.

### 3.4.2. In-pixel driver results

The first characteristic to be tested is the bias current that the driver is able to deliver. Figure 49 shows a comparison between simulated and experimental currents for the in-pixel circuit driving a square microLED with edge size of 10 µm for different bias voltages. As it is observed, the measured currents match with the ones observed in the simulations.

# 3. Results

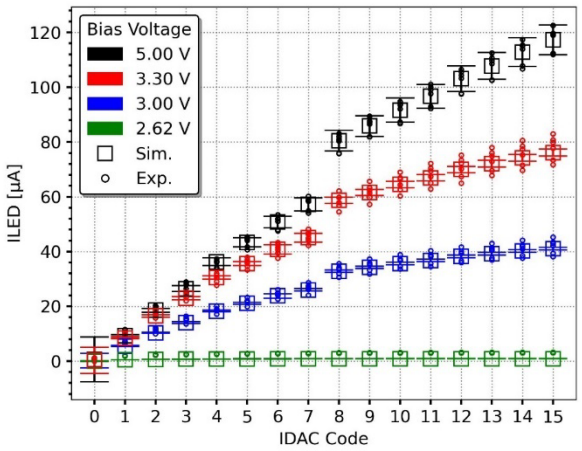


**Figure 49.** Bias currents provided by the in-pixel circuit driving a 10 x 10 µm$^2$ microLED, both simulated and measured, for different bias voltages.

The next test performed was to ensure that the calibration circuit was able to provide good measurements of what current was passing through the LED. A resistance of 3.7 kΩ needs to be added connected between the PixCal node in the schematic presented in Figure 46 and GND in order to make lectures of the PixCal node. As it is observed in Figure 50, the calibration signal provides a different measurement in the order of mV for each current value the LED is biased at 5V bias voltage.

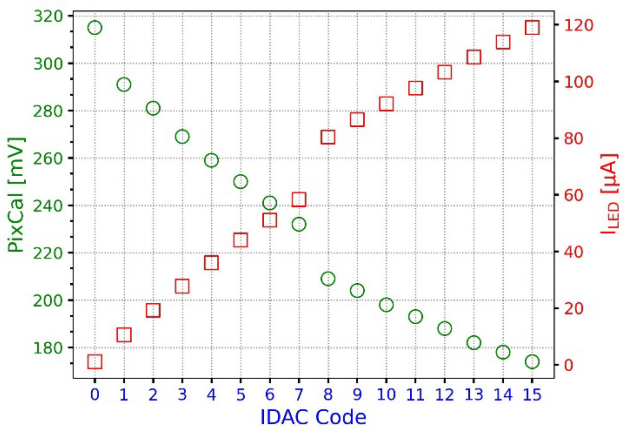


**Figure 50.** Intensity driven to the microLED compared to the DAC code and the voltage red at PixCal terminal.

The last electrical characteristic that was tested to fully characterize the capabilities of the microdisplay is the switching ON/OFF speed up to 1 MHz.

Figure 51 show captures of the oscilloscope of the PixEnable signal and the microLED driving signal that demonstrates that the circuit can operate at a switching speed of 1 MHz as intended. Due to the setup used for this test, when the circuit operates at 1 MHz, a slight delay is observed between the Pixel Enable signal and the output signal (PixOutput), as well as a minor attenuation in the LED control signal (PixelOutput). This may be attributed to parasitic components present in the test setup, which will not be present in the final device (since the LED will be directly connected to the controller), and to the input capacitance of the oscilloscope (800 pF).

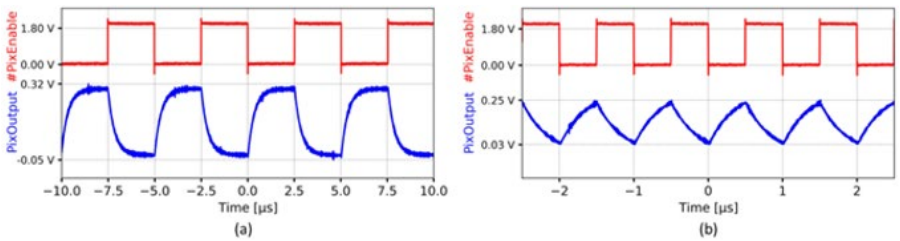


**Figure 51.** Oscilloscope captures of the PixEnable signal (Figure 46) and the microLED driving signal (PixOutput). The speeds at which the LED is being driven are 200 KHz (a) and 1 MHz (b).

Moreover, this backplane was designed so it could operate at fps rates up to 10kHz, which is the state of the art of microdisplays up to our knowledge. To achieve these high fps rates, the array is programed as four arrays of 256 x 256 pixels, thus increasing the programming speed four times.

### 3.4.3. Microdisplay results

To test the capabilities of the display to operate at such fps rates, tests with the transmission interface were performed. The writing time for each row is calculated as the time all the bits for one row are written, and then multiplying by the number of rows in the microdisplay (256 rows). The time it takes to a row to be programmed is showed in Equation (3) and the fps are calculated in Equation(4). Furthermore, an oscilloscope capture of a transmitted row is shown in Figure 52.

$$t_{Row} = \frac{PixelBits}{BitRate} \cdot RowPixels \; = 426\, ns \tag{3}$$

$$T_{Frame} = T_{Row} \cdot N_{Row} = \; 109.056\, \mu s \rightarrow 9.15\, kfps \tag{4}$$

# 3. Results

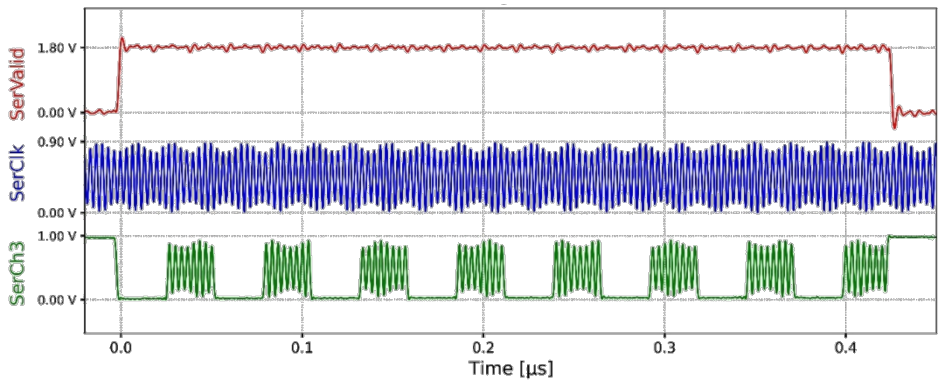


**Figure 52.** Transmission of a single row to the array. As can be observed, the transmission time for one row is 426 ns. SerValid indicates the backplane that a valid data is being sent, SerClk is the clock used to transmit and SerCh3 is the data transmitted.

The backplane is in state of improving the microLEDs yield, and last versions have had several short circuits. Further research of different bonding methods is being explored by a team of Technische Universität Braunschweig, with whom we collaborated to develop this microdisplay. Nevertheless, some preliminary results were obtained with these preliminary versions. Figure 54 shows an image of a tree being displayed by the microdisplay designed in this work. Figure 53 show a quarter of the display (256 x 256 pixels) with all the different gray levels that the backplane can drive to the microdisplay with a bias voltage of 5V. The reason because there are only 256 x 256 pixels shown in the images is because the quantity of bondings to operate the whole display is not functional, and because the microdisplay was designed to be programmed by quarters, by testing one fourth of the microdisplay the functionality of the whole microdisplay can be validated. Nevertheless, one synchronization signal is shared by one half of the array, which is making the down left part of the quarter does not get programmed properly. In order to fix it, one half of the array should be bonded. Unfortunately, the hybrid interconnection problems mentioned above make it impossible to verify this, since there are no more microdisplays available up to this date to be tested.

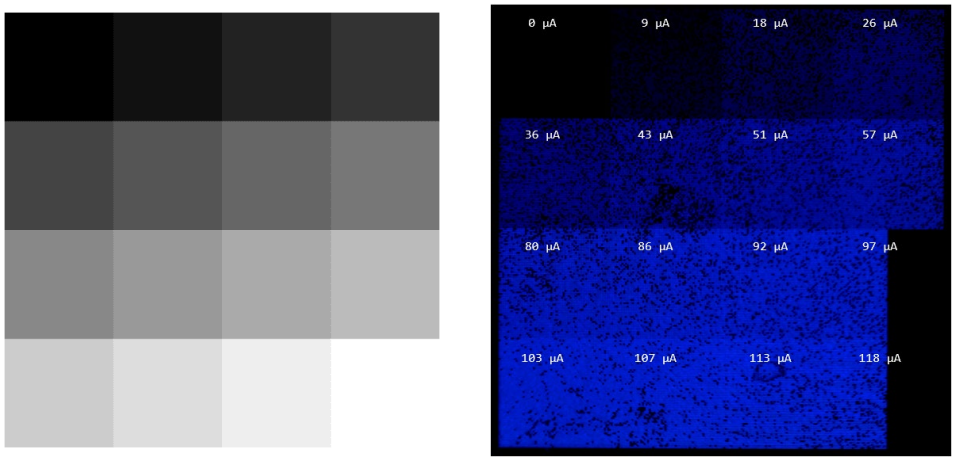


(a) (b)

**Figure 53.** An image of the microdisplay divided into 16 parts where all the possible currents delivered by the backplane are shown. (a) shows a black and white image of 16 different gray levels and (b) shows the same image in the microdisplay with a bias voltage of 5V.

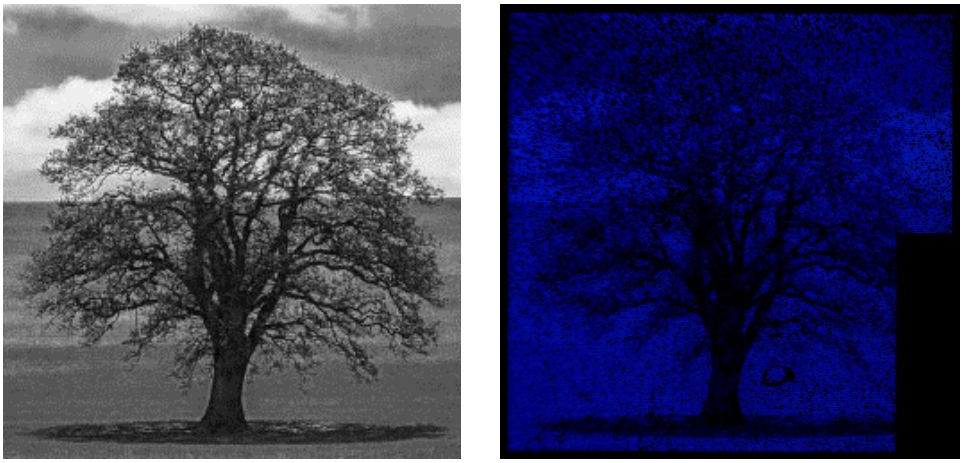

(a) (b)

Figure 54. (a) shows a black and white image of a tree and (b) shows the same image in the microdisplay presented in this work.

### 3.4.4. Conclusions

This device has the potential to serve as a microdisplay that could improve the development of raster microscopes, both for transmission and fluorescence, with a very large FoV (up to 1 $cm^2$), despite being limited in resolution (pixel pitches of 18 µm). However, the microdisplay has not yet been fully tested due to technical

challenges in establishing the hybrid interconnection between the microLED array and the CMOS backplane. Once these technical issues are resolved, the application of the microdisplay to the platforms presented earlier in this thesis is expected to be immediate, owing to their versatility.

### 3.4.5. Publication 5

## SRAM-Based LED CMOS Driver Circuit for a 512x512 GaN Microdisplay

by

**Victor Moro[1]***, Joan Canals[1], Georg Schöttler[2], Steffen Bornemann[2], Andreas Waag[2], Juan Daniel Prades[1] and Angel Diéguez[1]

*[1]Department of Electronic and Biomedical Engineering, Universitat de Barcelona, Spain*
*[2]Institute of Semiconductor Technology, Technical University of Braunschweig, 38106 Braunschweig, Germany*
**Presenter*

*Published in*
**Proceedings of the Digest of Technical Papers -SID International symposium** 54 (2023) 135-139
*Presented in*
**International Conference on Display Technology** (2023) Hifei, China

International Conference on Display Technology 2023 (Volume 54, Issue S1)

# SRAM-based LED CMOS driver circuit for a 512x512 GaN microdisplay

*Victor Moro*, Joan Canals*, Georg Schöttler**, Steffen Bornemann**, Andreas Waag**, Juan Daniel Prades*, Angel Diéguez**

*** Department of Electronic and Biomedical Engineering, Universitat de Barcelona, Barcelona, Spain**
**** Institute of Semiconductor Technology, Technische Universität Braunschweig, Braunschweig, Germany**

## Abstract

***GaN microLED technology has the potential to offer displays with high brightness, bandwidth, and long lifetime with a very low energy consumption. Moreover, GaN-on-Si hybrid interconnection technology allows the development of displays with a very high pixel density integration. In this work we present an in-pixel driving circuit designed in a 0.18µm CMOS technology to be integrated on a 512x512 microLED array by using the KlettWelding hybrid interconnection technique forming a microLED display of 1411 ppi with 10kfps working speed. The pixel driver is able to achieve switching times of 1MHz and can be operated at high bias currents of 120µA. The individual driver consists of 4 SRAMs that apply a weighted current and allows to avoid the current stability problems associated to CMOS backplanes in hybridly interconnected displays.***

## Author Keywords

Microdisplay; GaN-on-Si; CMOS; in-pixel driver; high brightness; high bandwidth; high ppi; hybrid interconnection.; SRAM based; 6T SRAM; current source; calibration circuit.

## 1. Introduction

Nowadays there are two main competitive technologies for microdisplay productions. Organic Ligth Emitting Diodes (OLED) and GaN LEDs technologies have achieved pixel sizes below 10µm and high integration densities that has made them the most promising technologies for the development of microdisplays [1, 2]. Despite their self-emission capabilities, OLED technology suffers from stability, lifetime, and brightness issues, especially when they are driven at high current densities. [3].

MicroLED technology has emerged and gained significant attention in the last two decades due to its high modulation bandwidth and high brightness. MicroLEDs are based on GaN/InGaN, which is an inorganic semiconductor material that shows higher robustness and longer lifespan providing higher brightness than OLED devices. They are self-emitting devices that can provide high contrast and efficiency, which lowers the power consumption compared to other technologies, such as Liquid Crystal Displays (LCD) and OLED. The most promising field of application for microLEDs are all kind of microdisplay implementations, such as projectors and near-to-eye (NTE) displays, including augmented reality (AR) [4, 5] wearable devices [6, 7] and virtual reality (VR) [8]. Nevertheless, it has also enabled promising applications in a high number of technological fields. To name a few, it has revitalized the field of visible light communication (VLC) [9–11], and boosted neuron stimulation and optogenetic sources [12–14].

One of the last advances in inorganic microdisplay design is the GaN-on-Si hybrid integration [15]. This is still a technology under development with great potential to be used for emerging applications [16, 17]. The use of GaN-on-Si provides microdisplays with huge density of pixels, accomplished due to the miniaturization of GaN microLEDs, including even microLEDs in the nanometric scales developed recently [18].

To achieve devices with high pixels per inch (PPI), the area for the CMOS driver is limited to the LED pitch in direct addressing hybrid interconnected displays. Several in-pixel drivers have been developed in recent years. Most of them are based on a 2 transistor 1 capacitor (2T1C) circuit [19]. The major advantage of the use of the 2T1C circuit is its simplicity (Figure 1a). This circuit forms a current sink with a DRAM memory. They allow a high PPI because of the small area of the circuit. However, this type of circuits lacks voltage stability over time, leading to a deterioration of the LED current in the microsecond scale [19]. This deterioration is produced in pixel due to the leakage current of the switch transistor.

Several modifications of the basic driver circuit were presented in the literature. In order to increase the grey levels of a display, a transistor is added to the typical 2T1C circuit (Figure 1b) to allow PWM dimming [20]. Also, to achieve higher stability times, two extra transistors (4T1C) are added (Figure 1c), leading to a current degradation in the LED current around 25% of the programmed current in 16 ms [19]. A modification of this circuit that includes the 4T1C structure where the transistor that fixes the LED current is bulk-driven (Figure 1d), extends the input data voltage range and improves the performance of the greyscale accuracy [22]. However, in spite of these efforts, the use of a capacitance as an analog storage unit always has leakage over time, making the microLED optical power to have poor stability over time. Thus, it has been always necessary a frame refresh in the range of microseconds (≥10kHz).

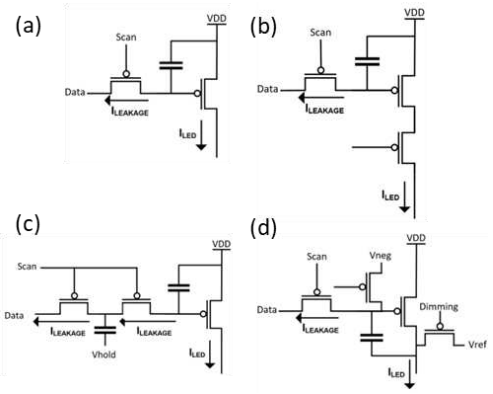


**Figure 1.** The different circuits described are shown. (a) shows the 2T1C standard circuit, (b) shows the circuit described in [20]. (c) is a 4T1C circuit to reduce the leakage current [19] and (d) is a 4T1C circuit with PHM capabilities

[21].

In this work we present an in-pixel driver based on four 6T SRAM and four transistors to deliver a weighted current to the LED, as a part of a whole CMOS backplane to drive a 512x512 microdisplay at high luminosities and high frame rates. The driver can provide currents from 0µA to 120µA with 16 different grey levels. Furthermore, the usage of SRAMs storing the current digital value, instead of a capacitor storing an analogic value, avoids the current degradation during driving time.

## 2. GaN microLED model

A SPICE model was generated in order to design an accurate driver that fits the GaN LEDs requirements. For this purpose, we used the LED model described in [25]. The parameters used were extracted from manufactured 10µm-side GaN LEDs in our GaN-based microLED array.

The microLED model (**Error! Reference source not found.**) is composed by a 3kΩ serial resistor, a 33MΩ and a 0.1pF parallel capacitor. To simulate the threshold voltage of the microLED, a diode and a voltage source were used. When the LED is not emitting, the parallel resistor limits the current biasing the LED, and when it starts emitting, the voltage source and the diode reduce the resistance of the branch, thus a realistic current through the LED is achieved (**Error! Reference source not found.**).

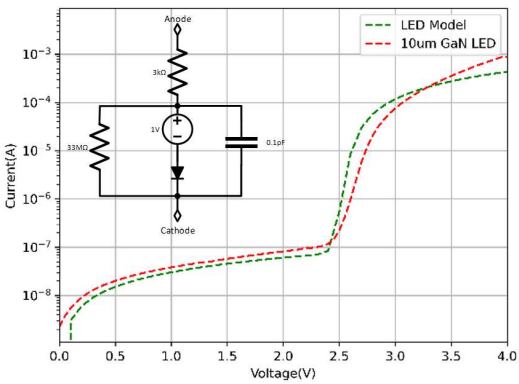


**Figure 2.** MicroLED SPICE model and the comparison between the simulation of the microLED model used for this work and the experimental data measurements.

## 3. In Pixel Driver

The in-pixel circuit design uses 4 internal digital storage memories (6T SRAMs), a current source that provides 16 different grey levels, which are programed by the SRAMs, a pulsing transistor that allows the array to have a 5V LED bias voltage and to achieve switching rates up to 1MHz, and a calibration circuit, that provides information of the bias current driven by the current source to the LED in order to compare and compensate any mismatch either form the CMOS driver or the GaN LED array. The driver with the modules described in this section is detailed in Figure 3 and 4.

The circuit is designed to operate at a maximum bias voltage of 1.8V for the LED anode node, allowing to design the driver circuit using a majority of low voltage 1.8V transistors, reducing the size of the pixel. To achieve high driving currents and a bias voltage up to 5V, the circuit was designed to allow a -3.2V cathode voltage.

### A. 6T SRAM

The pixel design is based on 4 6T memories which store a digital value of 4 bits, providing 16 possible LED bias current values. Each of the standard SRAM cells [26] have a leakage current of ~18pA, but since they are digital memories, they are capable to maintain the value and allow a constant light emission for any on LED time.

### B. Current source and pulsing transistor

Each LED is driven by a current source obtained by a 4 bits DAC composed by 1.8 PMOS weighted transistors. Each one of these transistors is driven by one of the 4 SRAMs, setting it on or off.

The current source was designed to operate at a current range between 80$\mu$A and 120$\mu$A motivated by the high current required for the applications of this microdisplay. Nevertheless, since one bit is needed to turn off the LED, an additional operation region appears from turning off the MSB SRAM. This current range can be used for applications requiring lower optical power.

The enable transistor is designed with a large W/L to allow 1MHz On/Off switch of the microLED. This is a 5V transistor acting as a cascode, thus, allowing the LED to have a bias voltage up to 5V (-3.2V at the LED cathode node) without having greater drain-source voltages than the 1.8V supported by the current source PMOS transistors. This allows the driver to provide up to 120$\mu$A bias current. Furthermore, the Enable transistor allows also a PWM diming of the LED, which leads to have a greater amount of grey values, but has to be operated for the whole array.

### C. Calibration circuit

Two additional transistors (M6 and M7 on Figure 3) were added to each pixel for calibration purposes. The gate of M6 measures the current and M7 enables the output of the calibration signal. The signal that enables the output of the calibration signal is the same as used to program the SRAMs. This makes that the calibration of the circuit must be performed during the pixel programming cycle.

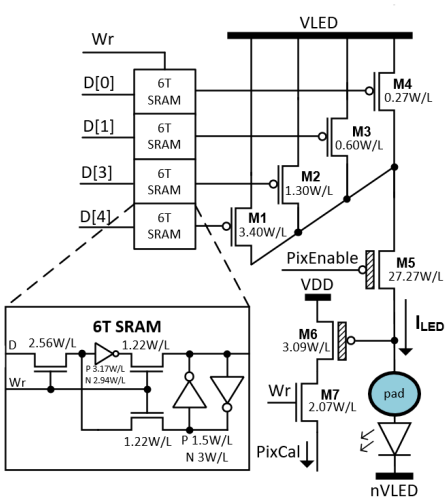


**Figure 3.** Schematic of the 4-bit SRAM based driver.

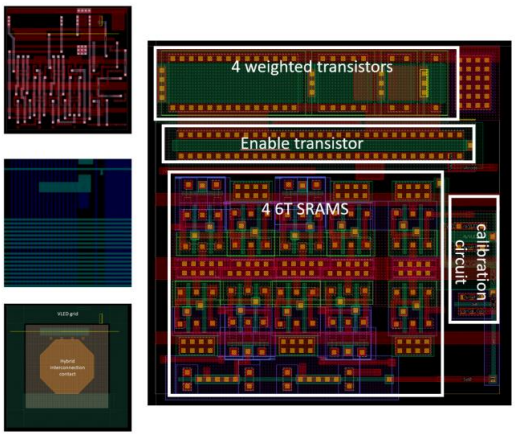


**Figure 4.** Layout of the 4-bit SRAM based driver.

This circuit allows to calibrate possible mismatches that would appear during the manufacturing process of the CMOS backplane, the microLED array and the hybrid interconnection. The idea is that I can be used also to calibrate and compensate the IR drop that could appear in such a large array due to supply paths resistance [27, 28]. Mismatches as well as bias drops are expected as the microdisplay would be quite large (512x512 LEDs on a 12.1x13.6mm$^2$ chip).

## 4. Results

The in-pixel circuit designed in this work provides a constant current up to 120$\mu$A. By having the possibility of modifying the cathode voltage from 0V to -3.2V, it can achieve a high number of possible variations in the driving bias voltage of the LED.

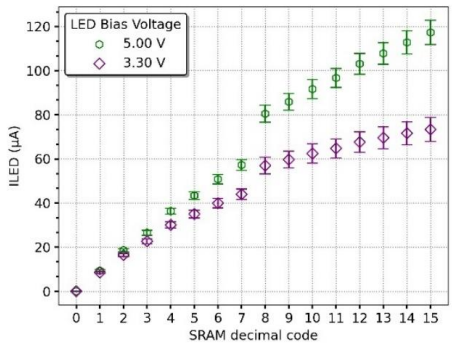


**Figure 5.** Post-layout simulation results of the in-pixel driver currents for different LED bias voltages.

Figure 5 shows the 16 driving currents for 5V and 3.3V LED bias voltage provided by a post-layout simulation with all the parasitic devices considered and using the LED model described in Section 2. Monte Carlo simulations were performed which are shown as error bars, representing the only variations taking place on the CMOS backplane. As expected, the error increases as the current increases, presenting a maximum deviation of 6$\mu$A at maximum driving current.

As Figure 5 shows, the current source provides the desired bias currents from 80$\mu$A to 120$\mu$A. Furthermore, as mentioned in Section 3 B, there is another current operating range from 0$\mu$A to 60$\mu$A.

Table 1 presents a comparison with the in-pixel drivers of some GaN microLED displays with similar pixel pitch and size than the display presented on this work. As it is shown, this work provides a much higher frame rate and current than other similar devices.

**Table 1.** Comparison of CMOS backplanes for GaN based microdisplays.

| Reference | [19] | [29] | This work |
|---|---|---|---|
| **Resolution** | 1280x768 | 1640×103 | 512x512 |
| **Pixel type** | 4T1C | 11T1C | SRAM based |
| **Pixel pitch** | 5µm | 9.5 µm | 18µm |
| **Pixel density** | 5094 PPI | 2677 PPI | 1411 PPI |
| **Frame rate** | 60 fps | n.a. | 10 kfps. |
| **Grayscale** | 10-bit | 5-bit | 4-bit |
| **Max. LED current** | 5 to 50µA | 5µA to 20µA | up to 120µA |
| **LED bias voltage** | 3.3V | 5.5V | up to 5V |

## 5. Conclusions

In this work, we report a CMOS in-pixel driver designed in a standard 0.18µm technology. The driver is designed for a GaN microdisplays based on SRAM cells to make the current stable over time. The driver is able to deliver up to 16 current values and is designed to be integrated in a 512x512 microdisplay with 10$\mu$m side size squared LEDs with 18$\mu m$ pitch. The resulting pixel

density is 1411 PPI. The operation range of the pixel is between 0$\mu$A and 120$\mu$A, which makes the pixel viable to be integrated in microdisplays that are suitable for a wide range of applications, i. e. maskless photolithography [30], chip-based microscopy [31, 32], or optogenetics [33].

## 6. Acknowledgements

The authors would like to acknowledge fundings from the SMILE European project (under FETPROACT-EIC-06-2019, Project ID: 952135).

## 7. References

1. Motoyama Y, Sugiyama K, Tanaka H, Tsuchioka H, Matsusaki K, Fukumoto H (2019) High-efficiency OLED microdisplay with microlens array. J Soc Inf Disp 27:354–360
2. Steudel S, Vertommen J, Boulbar E, et al (2022) MircoLED Display Integration on 300mm Advanced CMOS Platform. In: Dig Tech Pap. John Wiley and Sons Inc, pp 748–751
3. Huang Y, Hsiang EL, Deng MY, Wu ST (2020) Mini-LED, Micro-LED and OLED displays: present status and future perspectives. Light Sci Appl. https://doi.org/10.1038/s41377-020-0341-9
4. El-Ghoroury HS, Chuang C-L, Alpaslan ZY (2015) Quantum Photonic Imager (QPI): A Novel Display Technology that Enables more than 3D Applications.
5. Park J, Choi JH, Kong K, et al (2021) Electrically driven mid-submicron pixelation of InGaN micro-LED displays for AR glasses. Res Sq. https://doi.org/10.21203/rs.3.rs-101057/v1
6. Soh MY, Ng WX, Teo TH, Selvaraj SL, Peng L, Disney D, Zou Q, Yeo KS (2019) Design and Characterization of Micro-LED Matrix Display with Heterogeneous Integration of GaN and BCD Technologies. IEEE Trans Electron Devices 66:4221–4227
7. Zhang K, Peng D, Chong WC, Lau KM, Liu Z (2016) Investigation of Photon-Generated Leakage Current for High-Performance Active Matrix Micro-LED Displays. IEEE Trans Electron Devices 63:4832–4838
8. Xiong J, Hsiang EL, He Z, Zhan T, Wu ST (2021) Augmented reality and virtual reality displays: emerging technologies and future perspectives. Light Sci Appl. https://doi.org/10.1038/s41377-021-00658-8
9. Xie E, He X, Islim MS, Purwita AA, McKendry JJD, Gu E, Haas H, Dawson MD (2019) High-Speed Visible Light Communication Based on a III-Nitride Series-Biased Micro-LED Array. Journal of Lightwave Technology 37:1180–1186
10. Lan H-Y, Tseng I-C, Lin Y-H, Lin G-R, Huang D-W, Wu C-H (2020) High-speed integrated micro-LED array for visible light communication. Opt Lett 45:2203
11. Singh KJ, Huang YM, Ahmed T, et al (2020) Micro-LED as a promising candidate for high-speed visible light communication. Applied Sciences (Switzerland) 10:1–32
12. Poher V, Grossman N, Kennedy GT, et al (2008) Micro-LED arrays: A tool for two-dimensional neuron stimulation. J Phys D Appl Phys. https://doi.org/10.1088/0022-3727/41/9/094014
13. Grossman N, Poher V, Grubb MS, et al (2010) Multi-site optical excitation using ChR2 and micro-LED array. J Neural Eng. https://doi.org/10.1088/1741-2560/7/1/016004
14. McGovern B, Palmini RB, Grossman N, Drakakis EM, Poher V, Neil MAA, Degenaar P (2010) A new individually addressable micro-LED array for photogenetic neural stimulation. In: IEEE Trans Biomed Circuits Syst. pp 469–476
15. Zhang X, Li P, Zou X, Jiang J, Yuen SH, Tang CW, Lau KM (2019) Active Matrix Monolithic LED Micro-Display Using GaN-on-Si Epilayers. IEEE Photonics Technology Letters 31:865–868
16. Wasisto HS, Prades JD, Gülink J, Waag A (2019) Beyond solid-state lighting: Miniaturization, hybrid integration, and applications of GaN nano-and micro-LEDs. Appl Phys Rev. https://doi.org/10.1063/1.5096322
17. Templier F (2016) GaN-based emissive microdisplays: A very promising technology for compact, ultra-high brightness display systems. J Soc Inf Disp 24:669–675
18. Bezshlyakh DD, Spende H, Weimann T, Hinze P, Bornemann S, Gülink J, Canals J, Prades JD, Dieguez A, Waag A (2020) Directly addressable GaN-based nano-LED arrays: fabrication and electro-optical characterization. Microsyst Nanoeng. https://doi.org/10.1038/s41378-020-00198-y
19. Seong J, Jang J, Lee J, Lee M (2020) CMOS Backplane Pixel Circuit with Leakage and Voltage Drop Compensation for an Micro-LED Display Achieving 5000 PPI or Higher. IEEE Access 8:49467–49476
20. Li X (2017) Visible Light Communication System-on-Chip Design.
21. Wang L, Liu A, Zhang Y, Zhang M, Liu L, Zhang X, Hwang J, Yao J, Wang Z (2022) A Novel Hybrid Driving Method for Mini/Micro LED Display. SID Symposium Digest of Technical Papers 53:314–317
22. Li HG, Guo XY, Lu HY, Shao X, Yang D, Wang X (2019) Novel 4T1C pixel circuit for high image quality OLEDoS microdisplays. J Soc Inf Disp 27:529–535
23. Kwak B-C, Kim H, Lim H-S, Kwon O-K (2009) A Pixel Structure for OLED-on-Silicon Microdisplays.
24. Liu B, Ding D, Zhou T, Zhang M (2017) A Novel Pixel Circuit Providing Expanded Input Voltage Range for OLEDoS Microdisplays. In: Dig Tech Pap. John Wiley and Sons Inc, pp 1438–1441
25. Mai H, Underwood I Novel dual-branch SPICE model for tandem structure OLED †.
26. Tehranipoor MH, Ahmad Nisar (2008) Nanometer technology designs : high-quality delay tests. Springer
27. Jiang J, Liu X, Ki WH, Mok PKT, Lu Y (2020) A Multiphase Switched-Capacitor Converter for Fully Integrated AMLED Microdisplay System. IEEE Trans Power Electron 35:6001–6011
28. Seong J, Jang J, Lee J, Lee M (2020) CMOS Backplane Pixel Circuit with Leakage and Voltage Drop Compensation for an Micro-LED Display Achieving

5000 PPI or Higher. IEEE Access 8:49467–49476

29. Vigier M, Pilloix T, Dupont B, Moritz G, Moritz Very High Brightness G, Margaux VIGIER A (2020) Very High Brightness, High Resolution CMOS Driving Circuit for Microdisplay in Augmented Reality. 876–879

30. Jeon CW, Gu E, Dawson MD (2005) Mask-free photolithographic exposure using a matrix-addressable micropixellated AlInGaN ultraviolet light-emitting diode. Appl Phys Lett 86:1–3

31. Franch N, Canals J, Moro V, et al (2020) Nano illumination microscopy: a technique based on scanning with an array of individually addressable nanoLEDs. Opt Express 28:19044

32. Moreno S, Canals J, Moro V, et al (2021) Pursuing the diffraction limit with nano-led scanning transmission optical microscopy. Sensors 21:1–14

33. Weber W, Fussenegger M (2012) Emerging biomedical applications of synthetic biology. Nat Rev Genet 13:21–35

### 3.4.6. Publication 6

## A 9 kfps 1411 PPI GaN-based µLED Display CMOS Backplane

by

Joan Canals[1], **Victor Moro[1]***, Georg Schöttler[2], Steffen Bornemann[2], Andreas Waag[2], Juan Daniel Prades[1] and Angel Diéguez[1]

*[1]Department of Electronic and Biomedical Engineering, Universitat de Barcelona, Spain*
*[2]Institute of Semiconductor Technology, Technical University of Braunschweig, 38106 Braunschweig, Germany*
**Presenter*

*Published in*
**Proceedings of the Digest of Technical Papers -SID International symposium** 54 (2023) 125-128
*Presented in*
**Display Week** (2023) Los Angeles, CA, USA

# A 9 kfps 1411 PPI GaN-based µLED Display CMOS Backplane

*Joan Canals*, Victor Moro*, Georg Schöttler**, Steffen Bornemann**, Andreas Waag**, Juan Daniel Prades*, Angel Diéguez**

*** Department of Electronic and Biomedical Engineering of the Universitat de Barcelona, Barcelona, Spain**
**** Institute of Semiconductor Technology Technische Universität Braunschweig, Braunschweig, Germany**

## Abstract

***The revolution of the GaN-on-Si hybrid integration has redefined microdisplay as a point-light source for scientific, communication and visualization applications, thanks to their superior capabilities in terms of resolution, brightness and switching speed. In this work, we present a CMOS (Complementary Metal-Oxide Semiconductor) backplane able to exploit the GaN microarrays capabilities, producing high-speed patterns (up to 9.15 kfps) at high optical intensities (up to 120 uA per pixel and 16 grey levels) at an unprecedented resolution of 1411 PPI (512×512 pixel with 18um pitch). In addition, the backplane can be operated in pulsed mode, allowing the entire array to be toggled between the stored frame and off state at 1 MHz. Its unique characteristics expand the range of possible applications, from fluorescence-based performance assays to the manufacturing of DNA chips.***

## Author Keywords

microdisplay; microLEDs; CMOS backplane; smart pixel; in-pixel; high-throughput.

## 1. Introduction

MicroLEDs displays with hybrid technology based on GaN-on-Si have gained much attention in recent years due to the high performance of the GaN micro-LED devices and the possibility of creating smart pixels (1). Furthermore, with the evolution of technology, a new generation of applications has emerged, from visual light communications to optogenetic stimulation, fluorescence-based assays, and chip-based microscopy (2). These new applications take advantage of the high pixel counts at small pitches but require pixel modulation rates and brightness beyond what the microdisplays used in visualization applications can provide.

Many demonstrations have been made of GaN micro-LED arrays integrated with CMOS backplanes for applications that require high resolution at a slow frame rate and small driving currents. An example of 0.18 µm CMOS backplane for the typical microdisplay application is reported in (3), featuring a 2560×1536 RGB array with 5080 PPI (5 µm pitch) with 256 grey levels and a regular driving current up to 2 µA per pixel. Another example is (4), where a CMOS backplane for augmented reality is presented, with higher driving capacity per pixel (up to 20 µA) while maintaining high-resolution (1640×1033 pixels at 2677 PPI). Furthermore, GaN-based microdisplays are becoming commercially available such as the JBD25UMFHDB (from JBD, Pudong, Shanghai, China), a monochromatic GaN-based microLED display with 10000 PPI (2.5 µm pitch) at 1080P resolution, which delivers 1.6 µA per pixel with 256 grey levels through PWM (Pulse Width Modulation) driving (5).

Nevertheless, many new microdisplay applications are still at the proof-of-concept stage, as they have only been achieved on tiny arrays with low pixel densities (6). An example is a work presented in (7), where an 8×8 100 µm pitch micro-LED array bonded on a CMOS driving pixel array capable of generating optical pulses of 300 ps FWHM with optical power 2.21 W/cm$^2$ was used in fluorescence lifetime measurements. Also, microLED arrays bonded to CMOS backplanes as maskless photolithography tools have been demonstrated (8).

The first device to achieve high-frame rates (kfps) at high optical intensities was presented in (9). The CMOS backplane was optimized for high-speed spatiotemporal pattern projection, operating a 128×128-pixel array of 100 µm pitch at 83 kfps with a 5-bit grayscale pixel intensity resolution, achieving 22 µW optical power at 87 µA. It also implements three complementary modes of operation switching patterns using on-chip memory. However, despite its high performance in terms of speed and power, it remains with a small form factor and low pixel densities. Therefore, combining high resolution, high speed and high brightness at low pixel pitch still remains challenging.

This paper presents a step forward to develop a new structured light platform for scientific applications, from DNA chip fabrication to high-tech microscopy. Where not only high integration is essential but also the ability to produce high-speed patterns at high optical intensities. The proposed CMOS backplane features a 512×512 array of SRAM-based in-pixel current drivers with a pitch of 18 µm. The in-pixel driver offers a stable bias current of up to 120 µA per pixel with 16 intensity levels. The entire array can be updated at up to 9.15 kfps. Furthermore, the backplane can be operated in pulsed mode, toggling the entire array between the stored frame and off-state at 1 MHz, which is especially useful in applications such as high-throughput fluorescence-based assays.

The following sections present the CMOS backplane design and its performance.

## 2. Backplane Design

***In-Pixel driver:*** Figure 1-a shows the schematic of the proposed current driver in-pixel circuit. The in-pixel driver stores the 4 bits of pixel data in the 6T SRAM (Static Random-Access Memory) cells. This information is converted into power by driving four weighted transistors of increasing width (M1-M4). The four transistors, conjointly with the SRAM cells, form a current DAC (Digital-to-Analog Converter) of 16 levels that sets a stable current through the LED, overcoming the bias current degradation of the typical driving circuits (3). Additionally, to mitigate the differences in emission between LEDs through the microLED array at high currents, the driving transistors were designed to operate linearly within the high-current range from 80 µA up to 120 µA with a resolution of 5 µA.

The driving branch also includes a thick-oxide transistor (M5) for global enabling purposes, which cuts off the output current and allows PWM-based dimming. Additionally, the M5 transistor allows cathode voltages (nVLED) down to −3.2 V. This increases the LED bias voltage range from 1.8 V to 5 V, thereby extending the current range from 20 nA to 120 µA for the typical LEDs of the GaN technology (10).

Finally, to calibrate the current, two more transistors are added (M6 and M7). The M6 transistor is used to evaluate the voltage variation at the LED anode, thus monitoring the current flowing through the LED. The M7 transistor activates the output of the calibration signal during the SRAMs writing period. Figure 1-b shows the timing diagram of the in-pixel driver.

Figure 1-c shows that all the driving circuit elements are embedded in 18×18 μm$^2$ (including the 8 μm contact for LED anode). In addition, VLED power mesh is located around the LED contact pad opening to ensure proper bias through the pixel array.

***Architecture:*** Figure 2-a shows the overall functional block diagram of the CMOS backplane with the proposed in-pixel driver. This structure is repeated four times, controlling up to 512×512 GaN-based microLED array with a common n-contact ring surrounding the p-contacts array. It contains the peripheral circuitry that drives the 256×256-pixel array, including four 600 Mbps DDR (Double Data Rate) SLVS (Scalable Low-Voltage Signaling) input data channels, a row scan driver, a

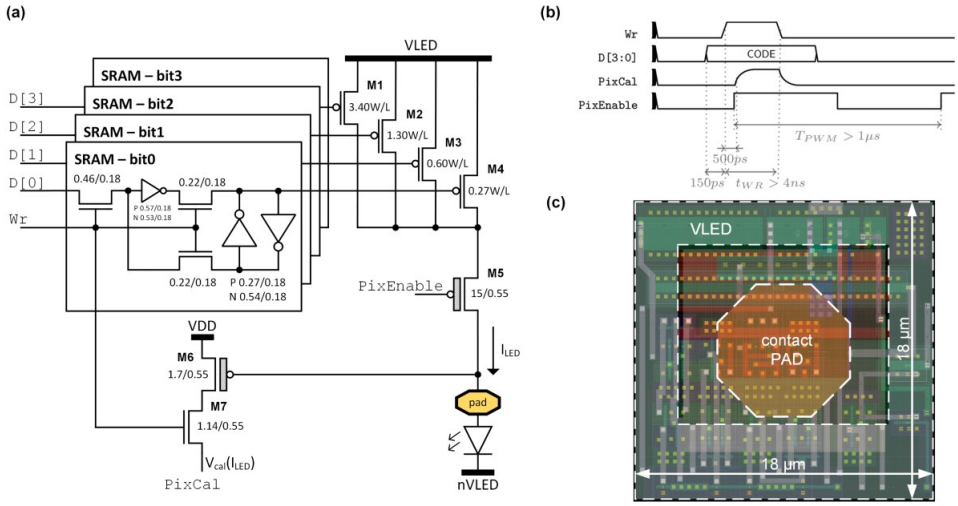


**Figure 1.** (a) Schematic, (b) timing diagram, and (c) layout of the 4-bit SRAM-based in-pixel driver implemented.

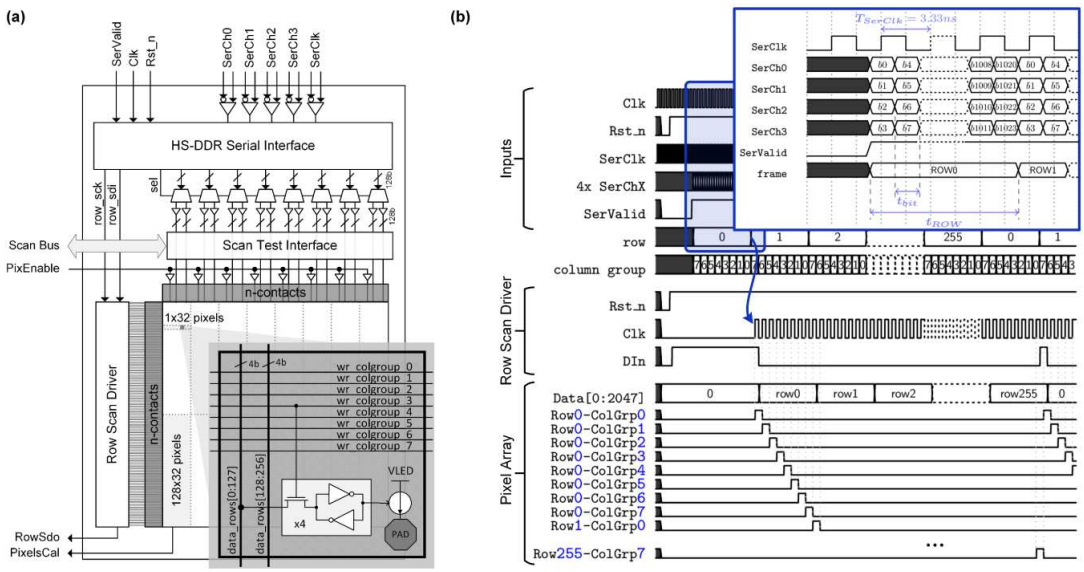


**Figure 2.** (a) Architecture of the proposed CMOS backplane CMOS, with a simplified scheme of the in-pixel driver showing the pixels data and write-enable lines across the pixel, and (b) time diagram of one frame transmission with a detail of the bit alignment and the SerValid timing to start data reception.

column selector, and a high-speed DDR serial interface. The latter is responsible for deserializing the data stream, interleaving it and controlling the writing procedure.

Each set of 256×256 pixels is controlled independently, including a pixel enable signal for global dimming of the array. Additionally, each set was arranged into 2×8 subsets of 128×32 pixels, with the minimum write unit being one row of these subarrays (i.e., 32 pixels). Each subset of pixels has its column data path and row selection signals. Although each quarter of the pixel array is controlled independently, the power rails are shared. The pixel calibration output is also shared by sets of 256×256 pixels.

The power planning consists of two independent power domains, one for the LED array bias voltage (VLED, nVLED) and another for the digital circuitry (VDD, GND). Both power supplies are distributed along the chip within a mesh structure, reducing the IR drop effects and homogenizing the voltage throughout the array.

***Operation:*** The display data is uploaded in parallel through the four HS-DDR serial interfaces (one per array quarter) row by row, as depicted in Figure 2-b. The transmission starts when the SerValid is set high during a low state of the serial clock (SerClk). Each data stream received through the four data channels (one pixel bit per channel) is then captured and deserialized simultaneously by the DDR interface with a 256 factor. Once a complete row (256 pixels) is received, their bits are interlaced to form a 1024-bit pixels data word ready to be uploaded into the pixel array. The pixel data is sequentially written into the array by column groups of 32 pixels. The write-enable signals of each column group are generated internally by the row scan driver. The reception of data and the subsequent writing in the pixel matrix are pipelined so that while the last received row is written, the next is received. In addition, the writing process is independent of the SerValid signal, which only disables data reception, thus ensuring the writing of data already received.

## 3. Results

We used a SPICE microLED model based on (11) with parameters extracted from the target GaN microLED array to validate the in-pixel driver. Figure 3 shows the post-layout simulation results of the in-pixel driver currents through the modelled LED under different bias voltages. The error bars represent the variability of the current through the LED, extracted from a Monte Carlo process simulation. As expected, the error increases with the current, presenting a maximum deviation of 6 µA for 120 µA at 5 V of bias. The figure shows that the DAC transfer function satisfies the linearity in the 80 µA to 120 µA range. Nevertheless, the lower region is still operational for applications that require lower current levels.

The final dimensions of the designed backplane are 12.1×13.6 mm$^2$ by using the 180 nm CMOS technology. The average power consumption of the electronic circuitry for writing into the pixel array at the maximum frame rate (9.15 kfps) is 448.5 mW. Thus, writing to the whole array with the four sequential interfaces at full speed will take 1.8 W. These power estimations are only for the backplane (without LEDs).

Table 1 compares the performance of the CMOS backplane presented in this work with those of the other backplanes for GaN-based microdisplays reported in the literature. To our knowledge, the circuit presented in this work is currently the only one that performs high-frame rates at high pixel density

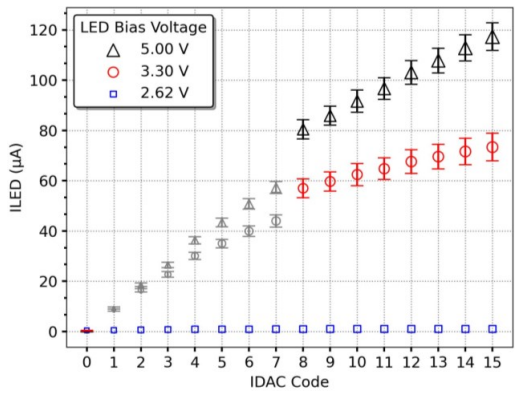


**Figure 3.** Post-layout simulation of the driver current through the modeled LED under different bias voltages.

(1411 PPI) with a reasonable grayscale resolution (4-bit) and the highest driving current (120 µA) per pixel.

## 4. Future Work

The presented 1 cm$^2$-backplane design has been sent to manufacture in 0.18 µm CMOS process within a Multi-Layer Mask run. Furthermore, the resulting wafers will be processed with the KlettWelding technique (12) to transfer the microLED array to the CMOS backplane (Figure 4). Moreover, the future microdisplay will be combined with a microlens array (13) to exchange its versatility as a multipoint light source for scientific applications.

Finally, we expect to present the assembled microdisplay and its characterization at the conference.

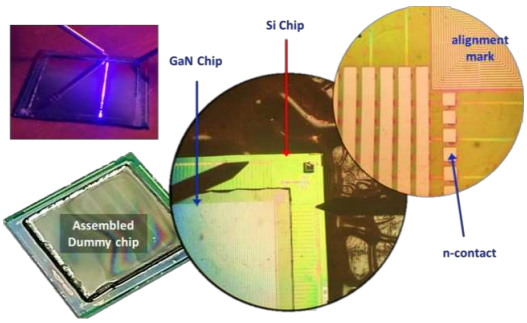


**Figure 4.** GaN microLED array assembled on Si dummy chip using the KlettWelding technique.

## 5. Acknowledgements

The authors want to acknowledge funding from the SMILE European project (under FETPROACT-EIC-06-2019, Project ID: 952135).

## 6. References

1. Templier F. GaN-based emissive microdisplays: A very promising technology for compact, ultra-high brightness display systems. J Soc Inf Disp [Internet]. 2016 Nov 1

**Table 1.** Comparison of CMOS Backplanes for GaN-based Microdisplays.

| Reference | (3) | (4) | (5) | (6) | (7) | (9) | This work |
|---|---|---|---|---|---|---|---|
| **Driver type** | in-pixel | by column | in-pixel | in-pixel | in-pixel | in-pixel | in-pixel |
| **Resolution** | 2560×1536 | 1640×1033 | 1920×1080 | 10×40 | 8×8 | 128×128 | 512×512 |
| **Pixel pitch** | 5 µm | 9.5 µm | 2.5 µm | 100 µm | 200 µm | 50 µm | 18 µm |
| **Pixel density** | 5080 PPI | 2677 PPI | 10000 PPI | n.a. | n.a. | 508 PPI | 1411 PPI |
| **Frame rate** | n.a. | n.a. | n.a. | n.a. | n.a. | 83 kfps | 9.15 kfps |
| **Max. LED current** | up to 2 µA | 5 µA to 20 µA | 1.6 µA. | up to 400 mA | up to 100 mA | up to 87 µA | up to 120 µA |
| **LED bias voltage** | 5 V | 5.5 V | n.a. | up to 8.3 V | > 5 V | 5 V | up to 5 V |
| **Color** | RGB | Mono/RGB | Mono | Mono | Mono | Mono | Mono |
| **Grayscale** | 8-bit | 5-bit | 8-bit | n.a. | n.a. | 5-bit | 4-bit |
| **CMOS Tech. Node** | 0.18 µm | 0.18 µm | n.a. | 0.35 µm | 0.35 µm | 0.18 µm | 0.18 µm |

[cited 2021 Jan 7];24(11):669–75. Available from: http://doi.wiley.com/10.1002/jsid.516

2. Wasisto HS, Prades JD, Gülink J, Waag A. Beyond solid-state lighting: Miniaturization, hybrid integration, and applications of GaN nano-and micro-LEDs [Internet]. Vol. 6, Applied Physics Reviews. American Institute of Physics Inc.; 2019 [cited 2021 Mar 15]. p. 41315. Available from: https://doi.org/10.1063/1.5096322
3. Seong J, Jang J, Lee J, Lee M. CMOS Backplane Pixel Circuit with Leakage and Voltage Drop Compensation for an Micro-LED Display Achieving 5000 PPI or Higher. IEEE Access. 2020;8:49467–76.
4. Vigier M, Pilloix T, Dupont B, Moritz G. Very High Brightness, High Resolution CMOS Driving Circuit for Microdisplay in Augmented Reality. In: Midwest Symposium on Circuits and Systems [Internet]. Institute of Electrical and Electronics Engineers Inc.; 2020 [cited 2021 Jan 7]. p. 876–9. Available from: https://ieeexplore.ieee.org/document/9184480/
5. Jade Bird Display. 0.22" MicroLED | JBD | 10000PPI microLED [Internet]. [cited 2021 Apr 14]. Available from: https://www.jb-display.com/0-22
6. Herrnsdorf J, McKendry JJD, Zhang S, Xie E, Ferreira R, Massoubre D, et al. Active-matrix GaN micro light-emitting diode display with unprecedented brightness. IEEE Trans Electron Devices. 2015 Jun 1;62(6):1918–25.
7. McKendry J, Rae BR, Zheng Gong, Muir KR, Guilhabert B, Massoubre D, et al. Individually Addressable AlInGaN Micro-LED Arrays With CMOS Control and Subnanosecond Output Pulses. IEEE Photonics Technology Letters [Internet]. 2009;21(12):811–3. Available from: http://ieeexplore.ieee.org/document/4814576/
8. Guilhabert B, Massoubre D, Richardson E, McKendry JJD, Valentine G, Henderson RK, et al. Sub-micron lithography using InGaN micro-LEDs: Mask-free fabrication of LED arrays. IEEE Photonics Technology Letters. 2012;24(24):2221–4.
9. Henderson R, Xie E, Dawson MD, Hassan NB, Strain MJ, Herrnsdorf J, et al. Ultrahigh frame rate digital light projector using chip-scale LED-on-CMOS technology. Photonics Research, Vol 10, Issue 10, pp 2434-2446 [Internet]. 2022 Oct 1 [cited 2022 Nov 22];10(10):2434–46. Available from: https://opg.optica.org/viewmedia.cfm?uri=prj-10-10-2434&seq=0&html=true
10. Bezshlyakh DD, Spende H, Weimann T, Hinze P, Bornemann S, Gülink J, et al. Directly addressable GaN-based nano-LED arrays: fabrication and electro-optical characterization. Microsyst Nanoeng [Internet]. 2020 Oct 19 [cited 2021 Mar 15];6(88):1–10. Available from: www.nature.com/micronano
11. Mai H, Underwood I. Novel dual-branch SPICE model for tandem structure OLED. SID Symposium Digest of Technical Papers [Internet]. 2021 [cited 2022 Apr 1];52(S1):369–75. Available from: https://onlinelibrary.wiley.com/doi/full/10.1002/sdtp.14490
12. Roustaie F, Quednau S, Dassinger F, Birlem O. Room Temperature Interconnection Technology for Bonding Fine Pitch Bumps Using NanoWiring, KlettWelding, KlettSintering and KlettGlueing. Proceedings of Technical Papers - International Microsystems, Packaging, Assembly, and Circuits Technology Conference, IMPACT. 2020 Oct 21;2020-October:168–71.
13. Kim D, Lee H, Cho N, Sung Y, Yeom G. Effect of GaN microlens array on efficiency of GaN-based blue-light-emitting diodes. Japanese Journal of Applied Physics, Part 2: Letters [Internet]. 2005 Dec 10 [cited 2022 Nov 22];44(1–7):L18. Available from: https://iopscience.iop.org/article/10.1143/JJAP.44.L18

# 4.

# Conclusions

In this chapter the main conclusions obtained after all the research performed in the frame of this doctoral thesis along with an evaluation of the possible uses and future of microLEDs in biomedicine are discussed.

First, general conclusions are provided to give an overall perspective on the research. Next, specific conclusions are drawn for each study outlined in this thesis. Finally, potential future steps for the development of microLED platforms to be used on biomedical applications, and furthermore, other scientifical applications are discussed.

## 4.1. General Conclusions

- A driver circuit that allows a very precise and stable control over the current biased to the microLED was designed. This platform allowed us to test the capabilities of microLEDs in microscopy and to develop a new microscopy technique.

# 4. Conclusions

- Another driver full custom CMOS IC was designed that is able to drive both DA and MA microLED arrays. It was integrated with different microLED arrays that were applied to build microscopes and PoC devices. The techniques developed include raster lensless brightfield and fluorescence microscopies.
- The integration of GaN microLEDs along with the CMOS drivers designed in this work make suitable the integration of low cost and miniaturized microscopes with high resolution. The work reported up to the date allows to have miniaturized inexpensive devices with a resolution down to 6.4 μm and 1.6 μm. This would be improved as the research in GaN microLEDs develops in the future years, since the current trend is to create smaller LEDs with smaller pitch and higher array density.
- The use of microLED arrays for PoC devices enables the possibility of multiplexed experiments without the need of mechanical components, just performing one experiment per LED. Moreover, by using time correlated fluorescence measurements, different fluorophores can be used prepared for different immunoassays, which allows the detection of one or several diseases in the same microLED.
- In this work we present a new type of microdisplay focused on scientifical applications. The high pixel density along with the high rate allows to perform faster raster microscope measurements. It could set the stage for fast or in vivo inexpensive imaging microscopes.
- The integration of high-current drivers in this microdisplay, combined with the ability to activate multiple LEDs simultaneously to function as a single light source, enables its use in fluorescence applications. Although the microdisplay has a speed limit of 1 MHz, making it unsuitable for time-resolved fluorescence applications, it remains viable for intensity-based fluorescence measurements.

## 4.2. MicroLEDs in microscopy

MicroLEDs are produced with nitride technology. However, when combined with CMOS microelectronics it represents a major breakthrough, as it opens the door to innovative and transformative applications. In this sense, several microscopes have been developed in this PhD.

# 4. Conclusions

It has been possible to develop a new microscope technique, raster microscopy. This is a novel approach to shadow imaging microscopy that relies on miniaturized light sources rather than sensor geometry to achieve high resolution. This technique not only allows to achieve high resolution with inexpensive and miniaturized components, but also eliminates the need for moving parts or optics. Several simulations at various scales demonstrate the capabilities of this type of microscope. An experimental demonstrator validates the imaging principle, suggesting that further miniaturization of the light sources could enhance resolution. Raster microscopy setups are highly compact, owing to the minimal distance requirements between the sample and the optical detector, leading to smaller microscopes compared to traditional optical or conventional lensless shadow imaging systems. For instance, the total height of the experimental prototypes presented in this thesis is merely 1 mm. This opens the possibility to use these microscopes in setups where currently microscopes are not used, like for example inside incubators.

The high brightness of inorganic GaN LEDs, combined with high power CMOS drivers that allows us to extract their optimal performance, makes them an excellent choice for miniaturization. However, since image formation necessitates scanning through all the LEDs in the array and capturing sufficient photons from each, this method is slower than conventional lensless shadow imaging. Moreover, as the number of pixels in the used array increases, the time required to scan the FoV of the microscope also increases. Nevertheless, this technique is based on a single pixel method. There exist techniques that can be implemented, like compressive sensing [179], that could increase acquisition times.

Following this premise, several statistical methods applied to a measurement taken using a SPAD camera and a TDC with the Time Correlated Single Photon Counting (TCSPC) technique have been analyzed. The application of statistical methods has demonstrated that the Signal-to-Noise Ratio (SNR) and dynamic range can be significantly enhanced for intensity measurements. By employing the weighted average method with 256 repetitions and a TDC of 16 bins, we achieved an increase in dynamic range by more than two orders of magnitude. The acquisition time was drastically reduced from $10^4 \cdot 550$ns to $256 \cdot 550$ns, making the process 40 times faster. Nevertheless, this method is useful only for high light intensity cases. The temporal information with the application of the statistical

method (for high light situations) or the standard intensity measures (for low light situations) must be applied depending on the amount of light that the sensor is receiving. In this case, the acquisition time for each measurement goes from 5.5 ms with normal intensity measurements to 140 µs when applying this technique. When it is multiplied by a large number of pixels (needed to accomplish a large FoV), it represents a significant breakthrough for the raster technique.

## 4.3. MicroLEDs in PoC

We also developed a fluorescence detection device capable of both intensity and lifetime measurements. The device is compact and easy to assemble, combining the advantages of high SNR CMOS SPAD detectors with an array of microLEDs that provide high optical power and fast switching speed. By employing time-gating with the SPAD, the device eliminates the need for optical filters to isolate fluorescence intensity from LED light. This is achieved by taking measurements after the LED is turned off. However, the auxiliary hardware used to control the device limits its application to fluorophores with decay times longer than 10 ns, such as QD 605 and QD 705. The results demonstrate that the system can rapidly detect fluorophores in intensity mode and distinguish between different fluorophores in the same measurement using the time-resolved fluorescence method. Additionally, it operates with very small sample volumes (5 nL). This device holds significant potential for applications in biological sample scanning, analytical laboratories, and clinical diagnostics.

The ability to detect fluorophores positioned directly above each microLED effectively transforms this device into a raster fluorescence microscope, with resolution determined by the display's specifications. Consequently, integrating the proof-of-concept technology presented here with advancements in raster microscopy offers significant potential for enhancing fluorescence microscopy. Additionally, this approach could enable the development of multi-well detection systems for multiplexed assays.

In the frame of this thesis, it was demonstrated that the use of large microLED arrays is of high interest for PoC devices using fluorescence techniques. The fact that in MA the driver is not necessarily under the LED, makes MA excellent to

develop further microscopes based on lifetime measurements, as it requires larger drivers not integrable in state-of-the-art microdisplays.

## 4.4. GaN-on-Si devices

As it was already commented, the integration of GaN with CMOS provides flexibility to new functionalities and applications. Beyond its use for augmented and virtual realities, the design of a backplane with high driving currents allows to operate the display at high switching rates and opens the possibility for new applications. The last part of this doctoral thesis was focused on providing such microdisplay that could be of use to enhance both microscopy and PoC platforms presented above.

The development of a device that can maintain a stable current for as long as needed is an improvement compared to traditional displays, that need their frames to be refreshed every microsecond to maintain an acceptable stability. Even with such refreshing rates, the pixel in traditional driving methods does not remain completely stable because of leakage currents in the dynamic memories. Moreover, the in-pixel driver allows for high power driving of the microLED array, providing up to 120 µA to a single LED, thus, providing a current density up to 37 A/cm$^2$.

## 4.5. Future work

Future work relies on improving the characteristics of the developed microscopes. FoV is dependent on array size and resolution on LED size. On the other hand, fluorescence microscopes are dependent also on LED intensity and LED switching off speed. To improve such characteristics both GaN chips and CMOS chips need to be further developed.

We count on our 512x512 microdisplay to improve FoV for brightfield and fluorescence intensity microscopes. With its use, the increase of FoV could be increase up to 1cm$^2$. Nevertheless, the use of this microdisplay in a microscope would decrease its resolution to 18 µm. Nevertheless, it is possible to enhance resolution using lenses.

# 4. Conclusions

Regarding the development of new drivers, using deep submicron processes (<22 nm) would be prohibitively expensive. However, an alternative approach to further enhance microscopes is to utilize a MA approach. To avoid excessive increases in driving capacitance, the microscope could be designed using tiled arrays, with each tile driven by CMOS drivers located underneath. This method would allow for improvements in both resolution and FoV, while also enabling fast enough switching speeds to be suitable for lifetime fluorescence microscopy applications.

In regard to the PoC platform developed in this thesis, there is still work that needs to be done. To determine the applicability of the PoC device presented, further studies with fluorophores bonded to antibodies and target infections are required. Moreover, the current LoD of this setup is 1/4 μM. However, this does not negate the technique's potential for detecting even lower concentrations, as sensitivity depends directly on factors such as the distance between the SPAD and the sample. In this setup, the sample is positioned 8 mm from the SPAD sensor, resulting in low sensitivity. Improvements could be made by reducing the distance between the sample and the sensors. Additionally, incorporating microlenses into the LED array chip could increase the optical power on the fluorophores. Similarly, microlenses could be added to the SPAD array to enhance the collection of light emitted from the fluorophores.

# 5.

## Bibliography


1. Bardell, D. The Invention of the Microscope. *Bios* **2004**, *75*, 78–84.
2. Hooke, R. *Extracts from Micrographia (1665)*; Clay, W.F., Ed.; Reprinted.; The Alembic Club: Edinburgh, 1902;
3. Gest, H. The Discovery of Microorganisms by Robert Hooke and Antoni van Leeuwenhoek, Fellows of the Royal Society. *Notes and Records of the Royal Society* 2004, *58*, 187–201.
4. Linder, T.E.; Simmen, D.; Stool, S.E.; Hopkins, H.H. *Revolutionary Inventions in the 20th Century The History of Endoscopy*; 1997; Vol. 123;.
5. Herschel, J. On a Case of Superficial Colour Presented by a Homogeneous Liquid Internally Colourless. *Philos Trans R Soc London* **1845**, *135*, 143–145.
6. Stokes, G.G. On the Change of Refrangibility of Light. No. II. *Philosofical Transactions of the Royal Society of London* **1853**, *143*, 385–396.

# 5. Bibliography


7. Abbe, E. Beitra ̈ge Zur Theorie Des Mikroskops Und Der Mikroskopischen Wahrneh-Mung. *Archiv f. mikrosk. Anatomie* **1873**, *9*, 413–418.

8. Helmholtz, H. Die Theoretischen Grenzen Für Die Leistungsfähigkeit Der Mikroskope. *Ann Phys* **1874**, 557–584.

9. Baum, E. Fluoreszenz-Mikroskopie. *Die Umschau* **1932**, *36*, 418.

10. Sharma, S.; Sharma, A. Robert Williams Wood: Pioneer of Invisible Light. *Photodermatol Photoimmunol Photomed* **2016**, *32*, 60–65, doi:10.1111/phpp.12235.

11. Whoriskey, G. LEDs in Microscopy: An Emerging Research Tool. *Photonics Spectra* **2017**, 10–12, doi:10.1371/journal.pone.0162419.

12. Khan, N.; Abas, N. Comparative Study of Energy Saving Light Sources. *Renewable and Sustainable Energy Reviews* **2011**, *15*, 296–309, doi:10.1016/J.RSER.2010.07.072.

13. Pawley, J. *Handbook of Biological Confocal Microscopy*; Springer Science & Business Media, 2006; Vol. 236;.

14. Denk, W.; Strickler, J.H.; Webb, W.W. Two-Photon Laser Scanning Fluorescence Microscopy. *Science (1979)* **1990**, *248*, 73–76.

15. Crawford, M.H. LEDs for Solid-State Lighting: Performance Challenges and Recent Advances. *IEEE Journal on Selected Topics in Quantum Electronics* **2009**, *15*, 1028–1040, doi:10.1109/JSTQE.2009.2013476.

16. McKendry, J.J.D.; Gu, E.; McAlinden, N.; Laurand, N.; Mathieson, K.; Dawson, M.D. Micro-LEDs for Biomedical Applications. *Semiconductors and Semimetals* **2021**, *106*, 57–94, doi:10.1016/BS.SEMSEM.2020.12.004.

17. Zhang, K.; Student, S.; Deng, M.); Kei, P.; Lau, M.; Liu, Z. Fully-Integrated Active Matrix Programmable UV and Blue Micro-LED Display System-on-Panel (SoP). **1071**, doi:10.1002/jsid.550.

18. Kim, K.; Wu, F.; Wise, K.D.; Yoon, E. GaN-on-Silicon MicroLEDs for Neural Interfaces. In *Semiconductors and Semimetals*; Academic Press Inc., 2021; Vol. 106, pp. 123–172 ISBN 9780128230411.

19. Chen, J.; Ding, H.; Sheng, X. Advanced Manufacturing of Microscale Light-Emitting Diodes and Their Use in Displays and Biomedicine. *Journal of Information Display* **2024**, *25*, 1–12, doi:10.1080/15980316.2023.2248403.

20. Davy, H. Davy's First Carbon Arc Lamp. *Journal of the A.I.E.E.* **1924**, *43*, 466–466.

21. Hewitt, P.C. U.S. Pat. 682-699, Method of Manufacturing Vapor or Gas Lamps 1901, 682–699.

22. Fundamentals of Mercury Arc Lamps Available online: https://zeiss-campus.magnet.fsu.edu/articles/lightsources/mercuryarc.html (accessed on 12 July 2024).

23. Alexa Fluor 546 Dye Available online: https://www.thermofisher.com/es/es/home/life-science/cell-analysis/fluorophores/alexa-fluor-546.html (accessed on 26 August 2024).

24. 1,2-Dihexadecanoil-Sn-Glicero-3-Fosfoetanolamina Marina Blue™ (DHPE Marina Blue™) Available online: https://www.thermofisher.com/order/catalog/product/M12652?SID=srch-srp-M12652 (accessed on 26 August 2024).

25. Apparatus for Fluorescence Microscopy. *Journal of Scientific Instruments* **1933**, *10*, doi:10.1088/0950-7671/10/3/405.

26. Saito, K.; Kobayashi, K.; Tani, T.; Nagai, T. *A Mercury Arc Lamp-Based Multi-Color Confocal Real Time Imaging System for Cellular Structure and Function*; 2008; Vol. 33;.

27. Thomson, L.A.; Hageage1, G.J. *Evaluation of Excitation Light Sources for Incident Immunofluorescence Microscopy*; 1975;

28. Enerback, L.; Johansson, K.-A. Fluorescence Fading in Quantitative Fluorescence Microscopy: A Cytofluorometerfor the Automatic Recording of Fluorescence Peaks of Very Short Duration. *HistochemicalJournal* **1973**, *5*, 351–362.

# 5. Bibliography


29. Puchtler, H.; Meloan, S.N.; Paschal, L.D. *Histochemistry Infrared Fluorescence Microscopy of Stained Tissues: Principles and Technic*; 1980; Vol. 68;.

30. Fundamentals of Xenon Arc Lamps Available online: https://zeiss-campus.magnet.fsu.edu/articles/lightsources/xenonarc.html (accessed on 16 May 2024).

31. Taatjes, D.J.; Roth, J. *Cell Imaging Techniques Methods and Protocols*; Taatjes, D.J., Roth, J., Eds.; Second Edition.; Springer, 2013;

32. Fundamentals of Metal Halide Arc Lamps Available online: https://zeiss-campus.magnet.fsu.edu/articles/lightsources/metalhalide.html (accessed on 17 May 2024).

33. Brighton, W.D.; Grulicht, R. *An Alternative Lamp for Fluorescence Microscopy*; BRIEF COMMUNICATION, 1972; Vol. 22;.

34. Einstein, A. The Quantum Theory of Radiation. *Laser theory* **1917**.

35. Ladenburg, R. Research on the Anomalous Dispersion of Gases. *Z. Phys.* **1928**, *48*, 15–25.

36. Maiman, T.H. Stimulated Optical Radiation in Ruby. *Nature* **1960**, *187*, 493.

37. Sorokin, P.P.; Stevenson, M.J. Stimulated Infrared emission from Trivalent Uranium. *Pyisical review letters* **1960**, *5*, 557–559.

38. von Neumann, J. Notes on the Photon-Disequilibrium-Amplifier Scheme, September 16, 1953. *IEEE J. Quantum Electronics* **1987**, 658–673.

39. Wolfe, : P; Re, W.; Keyes, J.; Quist, T.M. Recombination Radiation Emitted by gallium Arsenide. *IRE Transactions on Electron Devices* **1962**, *9*, 503–503.

40. Hall, R.N.; Fenner, G.E.; Kingsley, J.D.; Soltys, T.J.; Carlson, R.O. Coherent Light Emission from GaAs Junctions. *Phys Rev Lett* **1962**, *9*, 366–368.

41. Alferov, Zh.I.; Andreev, V.M.; Garbuzov, D.Z.; Zhilyaev, Yu. V.; Morozov, E.P.; Portnoi, E.L.; Trofim, V.G. Effect of the Heterostructure Parameters on the Laser Threshold Current and the Realization of Continuous Generation at Room Temperature. *Fiz. Tekh. Poluprovodn* **1970**, *4*, 1826–1829.

42. Ippen, E.P.; Shank, C.V.; Dienes, A. Passive Mode Locking of the Cw Dye Laser. *Appl Phys Lett* **1972**, *21*, 348–350.

43. Shank, C.V.; Ippen, E.P. Subpicosecond Kilowatt Pulses from a Mode-Locked Cw Dye Laser. *Appl Phys Lett* **1864**, *24*, 373–375.

44. Fork, R.L.; Brito Cruz, C.H.; Becker, P.C.; Shank, C.V. Compression of Optical Pulses to Six Femtoseconds by Using Cubic Phase Compensation. *Optical Letters* **1987**, *12*, 483–485.

45. Elliott, A.D. Confocal Microscopy: Principles and Modern Practices. *Curr Protoc Cytom* **2020**, *92*, doi:10.1002/cpcy.68.

46. Bayguinov, P.O.; Oakley, D.M.; Shih, C.C.; Geanon, D.J.; Joens, M.S.; Fitzpatrick, J.A.J. Modern Laser Scanning Confocal Microscopy. *Curr Protoc Cytom* 2018, *85*.

47. Bohn, S.; Sperlich, K.; Stahnke, T.; Schünemann, M.; Stolz, H.; Guthoff, R.F.; Stachs, O. Multiwavelength Confocal Laser Scanning Microscopy of the Cornea. *Biomed Opt Express* **2020**, *11*, 5689, doi:10.1364/boe.397615.

48. Mitchell, K.R.; Esene, J.E.; Woolley, A.T. Advances in Multiplex Electrical and Optical Detection of Biomarkers Using Microfluidic Devices. *Analytical and Bioanalytical Chemistry* **2021**, *414*, 167–180, doi:0.1007/s00216-021-03553-8.

49. Chu, J.; Ejaz, A.; Lin, K.M.; Joseph, M.R.; Coraor, A.E.; Drummond, D.A.; Squires, A.H. Single-Molecule Fluorescence Multiplexing by Multi-Parameter Spectroscopic Detection of Nanostructured FRET Labels. *Nat Nanotechnol* **2024**, doi:10.1038/s41565-024-01672-8.

50. Sharma, R.; Singh, M.; Sharma, R. Recent Advances in STED and RESOLFT Super-Resolution Imaging Techniques. *Spectrochim Acta A Mol Biomol Spectrosc* 2020, *231*.

# 5. Bibliography


51. Lee, D.R. Progresses in Implementation of STED Microscopy. *Meas Sci Technol* 2023, *34*.

52. Wang, J.; Zhang, J.; Wang, L.; Gao, X.; Shao, Y.; Liu, L.; Yang, Z.; Yan, W.; Qu, J. Dual-Color STED Super-Resolution Microscope Using a Single Laser Source. *J Biophotonics* **2020**, *13*, doi:10.1002/jbio.202000057.

53. Mehra, D.; Puchner, E.M. Correlative Conventional and Super-Resolution Photoactivated Localization Microscopy (PALM) Imaging to Characterize Chromatin Structure and Dynamics in Live Mammalian Cells. *Bio Protoc* **2023**, *13*, doi:10.21769/BIOPROTOC.4850.

54. Rodenberg, M.; Münker, L.J.; Tutsch, R.; Walla, P.J.; Weimann, T. Using a Photo-Activated Localization Micrscopy (PALM) for Imaging Fluorophore-Doped Photoresists. **2023**, doi:10.22032/dbt.58726.

55. Codron, P.; Letournel, F.; Marty, S.; Renaud, L.; Bodin, A.; Duchesne, M.; Verny, C.; Lenaers, G.; Duyckaerts, C.; Julien, J.P.; et al. STochastic Optical Reconstruction Microscopy (STORM) Reveals the Nanoscale Organization of Pathological Aggregates in Human Brain. *Neuropathol Appl Neurobiol* **2021**, *47*, 127–142, doi:10.1111/nan.12646.

56. Badawi, Y.; Nishimune, H. Super-Resolution Microscopy for Analyzing Neuromuscular Junctions and Synapses. *Neurosci Lett* 2020, *715*.

57. Chung, J.; Jeong, U.; Jeong, D.; Go, S.; Kim, D. Development of a New Approach for Low-Laser-Power Super-Resolution Fluorescence Imaging. *Anal Chem* **2022**, *94*, 618–627, doi:10.1021/acs.analchem.1c01047.

58. Hirvonen, L.M.; Suhling, K. Fast Timing Techniques in FLIM Applications. *Front Phys* 2020, *8*.

59. König, K. Review: Clinical in Vivo Multiphoton FLIM Tomography. *Methods Appl Fluoresc* **2020**, *8*, doi:10.1088/2050-6120/ab8808.

60. Canals, J.; Franch, N.; Alonso, O.; Vilà, A.; Diéguez, A. A Point-of-Care Device for Molecular Diagnosis Based on CMOS SPAD Detectors with Integrated Microfluidics. *Sensors (Switzerland)* **2019**, *19*, doi:10.3390/s19030445.

61. Round, H.J. A Note on Carborundum. *Electrical World* **1907**, *49*, 308.

62. Losev, O.V. Soviet Patent 12191 1929.

63. Holonyak, N.; Bevacqua, S.F. Coherent (Visible) Light Emission from Ga(As1-XPx) Junctions. *Appl Phys Lett* **1962**, *1*, 82–83, doi:10.1063/1.1753706.

64. Moser, K.; Wahl, S.; Eisfeld, W.; Prettl, W. Infrared Spectral Distribution of Photoconductivity and Up-Conversion in GaP Light Emitting Diodes. *J Appl Phys* **1985**, *57*, 5438–5442, doi:10.1063/1.334819.

65. Dimiduk, K.C.; Ness, C.Q.; K'evin Foley, J. Electron Irradiation of GaAsP LEDs. *IEEE Trans Nucl Sci* **1985**, *32*.

66. Nakamura, S.; Mukai, T.; Senoh, M. High-Power GaN P-N Junction Blue-Light-Emitting. *Jpn J Appl Phys* **1991**, *30*, 1998–2001.

67. Taguchi, T. Present Status of Energy Saving Technologies and Future Prospect in White LED Lighting. *IEEJ Transactions on Electrical and Electronic Engineering* **2008**, *3*, 21–26, doi:10.1002/tee.20228.

68. Narukawa, Y.; Narita, J.; Sakamoto, T.; Yamada, T.; Narimatsu, H.; Sano, M.; Mukai, T. Recent Progress of High Efficiency White LEDs. In Proceedings of the Physica Status Solidi (A) Applications and Materials Science; June 2007; Vol. 204, pp. 2087–2093.

69. Bando, K.; Sakano, K.; Noguchi, Y.; Shimizu, Y. Development of High-Bright and Pure-White LED Lamps. *Journal of Light & Visual Environment* **1998**, *22*.

70. Wu, B. Sen; Hitti, Y.; MacPherson, S.; Orsat, V.; Lefsrud, M.G. Comparison and Perspective of Conventional and LED Lighting for Photobiology and Industry Applications. *Environ Exp Bot* 2020, *171*.

71. Nardelli, A.; Deuschle, E.; de Azevedo, L.D.; Pessoa, J.L.N.; Ghisi, E. Assessment of Light Emitting Diodes Technology for General Lighting: A Critical Review. *Renewable and Sustainable Energy Reviews* 2017, *75*, 368–379.

# 5. Bibliography


72. Prost, S.; Kishen, R.E.B.; Kluth, D.C.; Bellamy, C.O.C. Choice of Illumination System & Fluorophore for Multiplex Immunofluorescenceon FFPE Tissue Sections. *PLoS One* **2016**, *11*, doi:10.1371/journal.pone.0162419.

73. Shaner, N.C.; Campbell, R.E.; Steinbach, P.A.; Giepmans, B.N.G.; Palmer, A.E.; Tsien, R.Y. Improved Monomeric Red, Orange and Yellow Fluorescent Proteins Derived from Discosoma Sp. Red Fluorescent Protein. *Nat Biotechnol* **2004**, *22*, 1567–1572, doi:10.1038/nbt1037.

74. Ladouceur, A.M.; Brown, C.M. Fluorescence Microscopy Light Source Review. *Curr Protoc* **2021**, *1*, doi:10.1002/cpz1.243.

75. Zheludev, N. The Life and Times of the LED — a 100-Year History. *Nat Photonics* **2007**, *1*, 189–192.

76. RÖsner, J.; Liotta, A.; Angamo, E.A.; Spies, C.; Heinemann, U.; KovÁcs, R. Minimizing Photodecomposition of Flavin Adenine Dinucleotide Fluorescence by the Use of Pulsed LEDs. *J Microsc* **2016**, *264*, 215–223, doi:10.1111/jmi.12436.

77. Moe, A.E.; Marx, S.; Banani, N.; Liu, M.; Marquardt, B.; Wilson, D.M. Improvements in LED-Based Fluorescence Analysis Systems. In Proceedings of the Sensors and Actuators, B: Chemical; November 11 2005; Vol. 111–112, pp. 230–241.

78. Fundamentals of Light-Emitting Diodes (LEDs) Available online: https://zeiss-campus.magnet.fsu.edu/articles/lightsources/leds.html (accessed on 29 May 2024).

79. Dan, D.; Lei, M.; Yao, B.; Wang, W.; Winterhalder, M.; Zumbusch, A.; Qi, Y.; Xia, L.; Yan, S.; Yang, Y.; et al. DMD-Based LED-Illumination Super-Resolution and Optical Sectioning Microscopy. *Sci Rep* **2013**, *3*, doi:10.1038/srep01116.

80. Rajalingham, R.; Sorenson, M.; Azadi, R.; Bohn, S.; DiCarlo, J.J.; Afraz, A. Chronically Implantable LED Arrays for Behavioral Optogenetics in Primates. *Nat Methods* **2021**, *18*, 1112–1116, doi:10.1038/s41592-021-01238-9.

81. Goncalves, S.B.; Palha, J.M.; Fernandes, H.C.; Souto, M.R.; Pimenta, S.; Dong, T.; Yang, Z.; Ribeiro, J.F.; Correia, J.H. LED Optrode with Integrated Temperature Sensing for Optogenetics. *Micromachines (Basel)* **2018**, *9*, doi:10.3390/mi9090473.

82. Forrest, S.R. The Road to High Efficiency Organic Light Emitting Devices. *Org Electron* **2003**, *4*, 45–48, doi:10.1016/j.orgel.2003.08.014.

83. Tang, C.W.; Vanslyke, S.A. Organic Electroluminescent Diodes. *Appl Phys Lett* **1987**, *51*, 913–915, doi:10.1063/1.98799.

84. Organic Light Emitting Diodes (OLEDs) Available online: https://oled.com/oleds/ (accessed on 5 September 2024).

85. Sun, Y.; Giebink, N.C.; Kanno, H.; Ma, B.; Thompson, M.E.; Forrest, S.R. Management of Singlet and Triplet Excitons for Efficient White Organic Light-Emitting Devices. *Nature* **2006**, *440*, 908–912, doi:10.1038/nature04645.

86. Aziz, H.; Popovic, Z.D.; Hu, N.-X.; Hor, A.-M. Degradation Mechanism of Small Molecule-Based Organic-Emitting Devices. *Science (1979)* **1999**, *283*, 1900–1902, doi:10.1126/science.283.5409.190.

87. Isamu Akasaki; Hiroshi Amano; Masahiro Kito; Kazumasa Hiramatsu Photoluminescence of Mg-Doped p-Type GaN and Electroluminescence of GaN p-n Junction LED. *J Lumin* **1991**, *48–49*, 666–670, doi:10.1016/0022-2313(91)90215-H.

88. Nakamura, S. The Roles of Structural Imperfections in InGaN-Based Blue Light-Emitting Diodes and Laser Diodes. *Science (1979)* **1998**, *281*, 956–961, doi:10.1126/science.281.5379.956.

89. Nakamura, S.; Senoh, M.; Iwasa, N.; Nagahama, S. High-Brightness InGaN Blue, Green and Yellow Light-Emitting Diodes with Quantum Well Structures. *Jpn J Appl Phys* **1995**, *34*, 797.

90. Wasisto, H.S.; Prades, J.D.; Gülink, J.; Waag, A. Beyond Solid-State Lighting: Miniaturization, Hybrid Integration, and Applications of GaN Nano-and Micro-LEDs. *Appl Phys Rev* 2019, *6*.

# 5. Bibliography


91. Chen, F.; Bian, J.; Hu, J.; Sun, N.; Yang, B.; Ling, H.; Yu, H.; Wang, K.; Gai, M.; Ma, Y.; et al. Mass Transfer Techniques for Large-Scale and High-Density MicroLED Arrays. *International Journal of Extreme Manufacturing* **2022**, *4*, doi:10.1088/2631-7990/ac92ee.

92. Chen, Z.; Yan, S.; Danesh, C. MicroLED Technologies and Applications: Characteristics, Fabrication, Progress, and Challenges. *J Phys D Appl Phys* 2021, *54*.

93. Peng, D.; Zhang, K.; Liu, Z. Design and Fabrication of Fine-Pitch Pixelated-Addressed Micro-LED Arrays on Printed Circuit Board for Display and Communication Applications. *IEEE Journal of the Electron Devices Society* **2017**, *5*, 90–94, doi:10.1109/JEDS.2016.2631220.

94. Huang, Y.; Hsiang, E.L.; Deng, M.Y.; Wu, S.T. Mini-LED, Micro-LED and OLED Displays: Present Status and Future Perspectives. *Light Sci Appl* 2020, *9*.

95. Zhou, X.; Tian, P.; Sher, C.W.; Wu, J.; Liu, H.; Liu, R.; Kuo, H.C. Growth, Transfer Printing and Colour Conversion Techniques towards Full-Colour Micro-LED Display. *Prog Quantum Electron* **2020**, *71*, 100263, doi:10.1016/J.PQUANTELEC.2020.100263.

96. Lee, V.W.; Twu, N.; Kymissis, I. Micro-LEd Technologies and Applications. *Inf Disp (1975)* **2016**, *32*, 16–23, doi:10.1002/j.2637-496X.2016.tb00949.x.

97. Kim, T.H.; Cho, K.S.; Lee, E.K.; Lee, S.J.; Chae, J.; Kim, J.W.; Kim, D.H.; Kwon, J.Y.; Amaratunga, G.; Lee, S.Y.; et al. Full-Colour Quantum Dot Displays Fabricated by Transfer Printing. *Nat Photonics* **2011**, *5*, 176–182, doi:10.1038/nphoton.2011.12.

98. Bezshlyakh, D.D.; Spende, H.; Weimann, T.; Hinze, P.; Bornemann, S.; Gülink, J.; Canals, J.; Prades, J.D.; Dieguez, A.; Waag, A. Directly Addressable GaN-Based Nano-LED Arrays: Fabrication and Electro-Optical Characterization. *Microsyst Nanoeng* **2020**, *6*, doi:10.1038/s41378-020-00198-y.

99. Jade Bird Display 0.22" MicroLED | JBD | 10000PPI MicroLED Available online: https://www.jb-display.com/weixianshiping/3.html (accessed on 5 June 2024).

100. El-Ghoroury, H.S.; Chuang, C.-L.; Alpaslan, Z.Y. *Quantum Photonic Imager (QPI): A Novel Display Technology That Enables More than 3D Applications*; 2015;

101. Xiong, J.; Hsiang, E.L.; He, Z.; Zhan, T.; Wu, S.T. Augmented Reality and Virtual Reality Displays: Emerging Technologies and Future Perspectives. *Light Sci Appl* 2021, *10*.

102. Soh, M.Y.; Ng, W.X.; Teo, T.H.; Selvaraj, S.L.; Peng, L.; Disney, D.; Zou, Q.; Yeo, K.S. Design and Characterization of Micro-LED Matrix Display with Heterogeneous Integration of GaN and BCD Technologies. *IEEE Trans Electron Devices* **2019**, *66*, 4221–4227, doi:10.1109/TED.2019.2933552.

103. Ding, K.; Avrutin, V.; Izyumskaya, N.; Morkoç, H. Micro-LEDs, a Manufacturability Perspective. **2019**, doi:10.3390/app9061206.

104. Yasunaga, H.; Takagi, T.; Shinko, D.; Nakayama, Y.; Takeuchi, Y.; Nishikawa, A.; Loesing, A.; Ohsawa, M.; Sekiguchi, H. Development of a Neural Probe Integrated with High-Efficiency MicroLEDs for in Vivo Application. *Jpn J Appl Phys* **2020**, *60*, doi:10.35848/1347-4065/abcffa.

105. Ko, E.; Roberto Lopez, J.; 1+, R.; Vöröslakos, M.; Hsieh, M.-L.; Buzsáki, G.; Yoon, E. FlexLiTE: Flexible Micro-LED Integrated Optoelectrodes for Long-Term Chronic Deep-Brain Studies., doi:10.1101/2022.08.05.503006.

106. Robbins, H.; Sumitomo, K.; Tsujimura, N.; Kamei, T. Integrated Thin Film Si Fluorescence Sensor Coupled with a GaN MicroLED for Microfluidic Point-of-Care Testing. *Journal of Micromechanics and Microengineering* **2018**, *28*, doi:10.1088/1361-6439/aa9e6d.

107. Meng, W.; Xu, F.; Yu, Z.; Tao, T.; Shao, L.; Liu, L.; Li, T.; Wen, K.; Wang, J.; He, L.; et al. Three-Dimensional Monolithic Micro-LED Display Driven

by Atomically Thin Transistor Matrix. *Nat Nanotechnol* **2021**, *16*, 1231–1236, doi:10.1038/s41565-021-00966-5.

108. Zhang, Z.; Nie, J.; Chen, K.; Jiang, B.; He, S.; Yang, T.; Sun, J.; Su, A.; Chen, N.; Zhou, J.; et al. Process Optimization of Passive Matrix GaN Micro-LED Displays. In Proceedings of the Digest of Technical Papers - SID International Symposium; John Wiley and Sons Inc, 2022; Vol. 53, pp. 515–519.

109. Choi, H.W.; Jeon, C.W.; Dawson, M.D. Fabrication of Matrix-Addressable Micro-LED Arrays Based on a Novel Etch Technique. *J Cryst Growth* **2004**, *268*, 527–530, doi:10.1016/j.jcrysgro.2004.04.085.

110. Modir, N.; Shahedi, M.; Dormer, J.; Fei, B. Development of a Real-Time Spectral Imaging System Using in-Site Micro-LED-Based Illumination and High-Speed Micro-Camera for Endoscopic Applications. *High-Speed Biomedical Imaging and Spectroscopy VI, SPIE* **2021**, *11654*, 37–44.

111. Li, S.; Song, B.; Peterson, T.; Hsu, J.; Liang, R. MicroLED Chromatic Confocal Microscope. *Opt Lett* **2021**, *46*, 2722, doi:10.1364/ol.427477.

112. Kumar, V.; Behrman, K.; Speed, F.; Saladrigas, C.A.; Supekar, O.; Huang, Z.; Bright, V.M.; Welle, C.G.; Restrepo, D.; Gopinath, J.T.; et al. MicroLED Light Source for Optical Sectioning Structured Illumination Microscopy. *Opt Express* **2023**, *31*, 16709, doi:10.1364/oe.486754.

113. Franch, N.; Canals, J.; Moro, V.; Vilà, A.; Romano-Rodríguez, A.; Prades, J.D.; Guelink, J.; Bezshlyakh, D.; Waag, A.; Kluczyk, K.; et al. Nano-Illumination Microscopy: A Technique Based on Scanning with an Array of Individually Addressable NanoLEDs. *Opt Express* **2020**, *28*, 19044–19057.

114. Canals, J.; Franch, N.; Moro, V.; Moreno, S.; Prades, J.D.; Romano-Rodríguez, A.; Bornemann, S.; Bezshlyakh, D.D.; Waag, A.; Vogelbacher, F.; et al. A Novel Approach for a Chip-Sized Scanning Optical Microscope. *Micromachines (Basel)* **2021**, *12*, doi:10.3390/mi12050527.

115. Zhang, X.; Li, P.; Zou, X.; Jiang, J.; Yuen, S.H.; Tang, C.W.; Lau, K.M. Active Matrix Monolithic LED Micro-Display Using GaN-on-Si

Epilayers. *IEEE Photonics Technology Letters* **2019**, *31*, 865–868, doi:10.1109/LPT.2019.2910729.

116. Templier, F. GaN-Based Emissive Microdisplays: A Very Promising Technology for Compact, Ultra-High Brightness Display Systems. *J Soc Inf Disp* **2016**, *24*, 669–675, doi:10.1002/jsid.516.

117. Quesnel, E.; Lagrange, A.; Vigier, M.; Consonni, M.; Tournaire, M.; Le Marchand, V.; Suhm, | Aurélien; Demars, | Patrick; Pillet, J.-C.; Badhise, |; et al. Dimensioning a Full Color LED Microdisplay for Augmented Reality Headset in a Very Bright Environment. **2020**, doi:10.1002/jsid.884.

118. Wu, M.C.; Chung, M.C.; Wu, C.Y. 3200 Ppi Matrix-Addressable Blue MicroLED Display. *Micromachines (Basel)* **2022**, *13*, doi:10.3390/mi13081350.

119. Jarndal, A.; Arivazhagan, | L; Nirmal, | D On the Performance of GaN-on-Silicon, Silicon-Carbide, and Diamond Substrates. **2020**, doi:10.1002/mmce.22196.

120. Liu, Z.; Chong, W.C.; Wong, K.M.; Lau, K.M. GaN-Based LED Micro-Displays for Wearable Applications. *Microelectron Eng* **2015**, *148*, 98–103, doi:10.1016/j.mee.2015.09.007.

121. Li, l.; Tang, G.; Shi, Z.; Ding, H.; Liu, C.; Cheng, D.; Zhang, Q.; Yin, L.; Yao, Z.; Duan, L.; et al. Transfer-Printed, Tandem Microscale Light-Emitting Diodes for Full-Color Displays. *Proceedings of the National Academy of Sciences* **2021**, *118*, doi:10.1073/pnas.2023436118/-/DCSupplemental.

122. Luo, H.; Wang, C.; Zhang, S.; Song, J. Laser-Driven Transfer Printing Techniques for Micro-LED Display. *Transfer Printing Technologies and Applications* **2024**, 325–351, doi:10.1016/B978-0-443-18845-9.00013-2.

123. Qi, L.; Zhang, X.; Chong, W.C.; Lau, K.M. Monolithically Integrated High-Resolution Full-Color GaN-on-Si Micro-LED Microdisplay. *Photonics Res* **2023**, *11*, 109, doi:10.1364/prj.465489.

124. Bezshlyakh, D.D.; Spende, H.; Weimann, T.; Hinze, P.; Bornemann, S.; Gülink, J.; Canals, J.; Prades, J.D.; Dieguez, A.; Waag, A. Directly

# 5. Bibliography

Addressable GaN-Based Nano-LED Arrays: Fabrication and Electro-Optical Characterization. *Microsyst Nanoeng* **2020**, *6*, doi:10.1038/s41378-020-00198-y.

125. Li, C.; Pan, Z.; Guo, C.; Li, Y.; Zhou, Y.; Wang, J.; Zou, S.; Gong, Z. Transfer Printed, Vertical GaN-on-Silicon Micro-LED Arrays With Individually Addressable Cathodes. *IEEE Trans Electron Devices* **2022**, *69*, 5630–5636, doi:10.1109/TED.2022.3202152.

126. Jeon, C.W.; Choi, H.W.; Gu, E.; Dawson, M.D. High-Density Matrix-Addressable AlInGaN-Based 368-Nm Microarray Light-Emitting Diodes. *IEEE Photonics Technology Letters* **2004**, *16*, 2421–2423, doi:10.1109/LPT.2004.835626.

127. Zhang, H.X.; Gu, E.; Jeon, C.W.; Gong, Z.; Dawson, M.D.; Neil, M.A.A.; French, P.M.W. Microstripe-Array InGaN Light-Emitting Diodes with Individually Addressable Elements. *IEEE Photonics Technology Letters* **2006**, *18*, 1681–1683, doi:10.1109/LPT.2006.879926.

128. Jeon, C.; Choi, H.; Dawson, andMD *Fabrication and Performance of High-Density, Matrix-Addressable Green and Ultraviolet Micro-LED Arrays*;

129. Griffin, C.; Zhang, H.X.; Guilhabert, B.; Massoubre, D.; Gu, E.; Dawson, M.D. Micro-Pixellated Flip-Chip InGaN and AlInGaN Light-Emitting Diodes. In Proceedings of the Conference on Lasers and Electro-Optics (CLEO) Baltimore, M.D.; IEEE, 2007.

130. Zhang, L.; Ou, F.; Chong, W.C.; Chen, Y.; Li, Q. Wafer-Scale Monolithic Hybrid Integration of Si-Based IC and III–V Epi-Layers—A Mass Manufacturable Approach for Active Matrix Micro-LED Micro-Displays. *J Soc Inf Disp* **2018**, *26*, 137–145, doi:10.1002/jsid.649.

131. Ou, F.; Chong, W.C.; Xu, Q.; Chen, Y.; Li, Q.; Zhang, L. Monochromatic Active Matrix Micro-LED Micro-Displays with >5,000 Dpi Pixel Density Fabricated Using Monolithic Hybrid Integration Process. In Proceedings of the Digest of Technical Papers - SID International Symposium; Blackwell Publishing Ltd, 2018; Vol. 49, pp. 1677–1680.

132. Peng, D.; Zhang, K.; Liu, Z. Design and Fabrication of Fine-Pitch Pixelated-Addressed Micro-LED Arrays on Printed Circuit Board for Display and Communication Applications. *IEEE Journal of the Electron Devices Society* **2017**, *5*, 90–94, doi:10.1109/JEDS.2016.2631220.

133. Wei, Z.; Chen, C.-J.; Wang, L.; Zhang, L.; Liu, X.; Pepe, A.; Chen, K.-C.; Wu, M.-C.; Wang, L.; Luo, Y.; et al. *Gbps Real-Time NRZ-OOK Visible Light Communication System Based on a Packaged Single Layer Quantum Dot Blue Micro-LED: First Fabrication and Demonstration*;

134. McGovern, B.; Palmini, R.B.; Grossman, N.; Drakakis, E.M.; Poher, V.; Neil, M.A.A.; Degenaar, P. A New Individually Addressable Micro-LED Array for Photogenetic Neural Stimulation. In Proceedings of the IEEE Transactions on Biomedical Circuits and Systems; December 2010; Vol. 4, pp. 469–476.

135. Poher, V.; Grossman, N.; Kennedy, G.T.; Nikolic, K.; Zhang, H.X.; Gong, Z.; Drakakis, E.M.; Gu, E.; Dawson, M.D.; French, P.M.W.; et al. Micro-LED Arrays: A Tool for Two-Dimensional Neuron Stimulation. *J Phys D Appl Phys* **2008**, *41*, doi:10.1088/0022-3727/41/9/094014.

136. Wang, M.; Ji, Y.; Wang, W. Optogenetics Micro LED Light Source Driver Circuit Design. In Proceedings of the 2022 16th ICME International Conference on Complex Medical Engineering, CME 2022; Institute of Electrical and Electronics Engineers Inc., 2022; pp. 356–361.

137. Dehkhoda, F.; Soltan, A.; Ramezani, R.; Degenaar, P. *Biphasic Micro-LED Driver for Optogenetics*;

138. Rae, B.R.; Yang, J.B.; McKendry, J.; Gong, Z.; Renshaw, D.; Girkin, J.M.; Gu, E.; Dawson, M.D.; Henderson, R.K. A Vertically Integrated CMOS Microsystem for Time-Resolved Fluorescence Analysis. *IEEE Trans Biomed Circuits Syst* **2010**, *4*, 437–444, doi:10.1109/tbcas.2010.2077290.

139. Xie, E.; Stonehouse, M.; Ferreira, R.; McKendry, J.J.D.; Herrnsdorf, J.; He, X.; Rajbhandari, S.; Chun, H.; Jalajakumari, A.V.N.; Almer, O.; et al. Design, Fabrication, and Application of GaN-Based Micro-LED Arrays with Individual Addressing by N-Electrodes. *IEEE Photonics J* **2017**, *9*, doi:10.1109/JPHOT.2017.2768478.

# 5. Bibliography


140. Introduction to Fluorescence Microscopy Available online: https://zeiss-campus.magnet.fsu.edu/articles/basics/fluorescence.html (accessed on 17 June 2024).

141. Wafi, A.; Zuhdi, M. High Performance Drive Circuits for Integrated MicroLED/CMOS Arrays for Visible Light Communication (VLC), Edinburgh Research Archive, 2015.

142. Wei, Z.; Zhang, S.; Mao, S.; Wang, L.; Zhang, L.; Chen, C.-J.; Wu, M.-C.; Dong, Y.; Wang, L.; Luo, Y.; et al. Full-Duplex High-Speed Indoor Optical Wireless Communication System Based on a Micro-LED and VCSEL Array. *Opt Express* **2021**, *29*, 3891, doi:10.1364/oe.412348.

143. Tian, P.; Liu, X.; Yi, S.; Huang, Y.; Zhang, S.; Zhou, X.; Hu, L.; Zheng, L.; Liu, R. High-Speed Underwater Optical Wireless Communication Using a Blue GaN-Based Micro-LED. *Opt Express* **2017**, *25*, 1193, doi:10.1364/oe.25.001193.

144. Rae, B.R. Micro-Systems for Time-Resolved Fluorescence Analysis Using CMOS Single-Photon Avalanche Diodes and Micro-LEDs. **2009**.

145. Chun, H.; Manousiadis, P.; Rajbhandari, S.; Vithanage, D.A.; Faulkner, G.; Tsonev, D.; McKendry, J.J.D.; Videv, S.; Xie, E.; Gu, E.; et al. Visible Light Communication Using a Blue GaN μ LED and Fluorescent Polymer Color Converter. *IEEE Photonics Technology Letters* **2014**, *26*, 2035–2038, doi:10.1109/LPT.2014.2345256.

146. Wang, L.; Wei, Z.; Chen, C.-J.; Wang, L.; Fu, H.Y.; Zhang, L.; Chen, K.-C.; Wu, M.-C.; Dong, Y.; Hao, Z.; et al. 1.3 GHz E-O Bandwidth GaN-Based Micro-LED for Multi-Gigabit Visible Light Communication. *Photonics Res* **2021**, *9*, 792, doi:10.1364/prj.411863.

147. Wei, Z.; Zhang, L.; Wang, L.; Chen, C.-J.; Pepe, A.; Liu, X.; Chen, K.-C.; Wu, M.-C.; Dong, Y.; Wang, L.; et al. 2 Gbps/3 m Air–Underwater Optical Wireless Communication Based on a Single-Layer Quantum Dot Blue Micro-LED. *Opt Lett* **2020**, *45*, 2616, doi:10.1364/ol.393664.

148. Moro, V.; Canals, J.; Moreno, S.; Bornemann, S.; Alonso, O.; Waag, A.; Prades, J.D.; Dieguez, A. Fluorescence Multi-Detection Device Using a

Lensless Matrix Addressable MicroLED Array. *Biosensors (Basel)* **2024**, *14*, 264, doi:10.3390/bios14060264.

149. Chen, K.J.; Haberlen, O.; Lidow, A.; Tsai, C.L.; Ueda, T.; Uemoto, Y.; Wu, Y. GaN-on-Si Power Technology: Devices and Applications. *IEEE Trans Electron Devices* **2017**, *64*, 779–795, doi:10.1109/TED.2017.2657579.

150. Seong, J.; Jang, J.; Lee, J.; Lee, M. CMOS Backplane Pixel Circuit with Leakage and Voltage Drop Compensation for an Micro-LED Display Achieving 5000 PPI or Higher. *IEEE Access* **2020**, *8*, 49467–49476, doi:10.1109/ACCESS.2020.2979883.

151. Li, X. *Visible Light Communication System-on-Chip Design*; 2017;

152. Li, H.G.; Guo, X.Y.; Lu, H.Y.; Shao, X.; Yang, D.; Wang, X. Novel 4T1C Pixel Circuit for High Image Quality OLEDoS Microdisplays. *J Soc Inf Disp* **2019**, *27*, 529–535, doi:10.1002/jsid.763.

153. Wang, L.; Liu, A.; Zhang, Y.; Zhang, M.; Liu, L.; Zhang, X.; Hwang, J.; Yao, J.; Wang, Z. A Novel Hybrid Driving Method for Mini/Micro LED Display. *SID Symposium Digest of Technical Papers* **2022**, *53*, 314–317, doi:10.1002/sdtp.15928.

154. Vigier, M.; Pilloix, T.; Dupont, B.; Moritz, G.; Moritz Very High Brightness, G.; Margaux VIGIER, A. Very High Brightness, High Resolution CMOS Driving Circuit for Microdisplay in Augmented Reality. **2020**, 876–879, doi:10.1109/MWSCAS48704.2020.9184480ï.

155. Victor Moro Joan Canals, G.S.S.B.A.W.J.D.P.A.D. SRAM-Based LED CMOS Driver Circuit for a 512x512 GaN Microdisplay. In Proceedings of the International Conference on Display Technology; 2023.

156. Canals, J.; Moro, V.; Schöttler, G.; Bornemann, S.; Waag, A.; Prades, J.D.; Diéguez, A. A 9 Kfps 1411 PPI GaN-Based MLED Display CMOS Backplane. In Proceedings of the Digest of Technical Papers - SID International Symposium; John Wiley and Sons Inc, 2023; Vol. 54, pp. 125–128.

# 5. Bibliography


157. Bani Hassan, N.; Dehkhoda, F.; Xie, E.; Herrnsdorf, J.; Strain, M.J.; Henderson, R.; Dawson, M.D. Ultrahigh Frame Rate Digital Light Projector Using Chip-Scale LED-on-CMOS Technology. *Photonics Res* **2022**, *10*, 2434, doi:10.1364/prj.455574.

158. Seong, J.; Jang, J.; Lee, J.; Lee, M. CMOS Backplane Pixel Circuit with Leakage and Voltage Drop Compensation for an Micro-LED Display Achieving 5000 PPI or Higher. *IEEE Access* **2020**, *8*, 49467–49476, doi:10.1109/ACCESS.2020.2979883.

159. Herrnsdorf, J.; McKendry, J.J.D.; Shuailong Zhang; Enyuan Xie; Ferreira, R.; Massoubre, D.; Zuhdi, A.M.; Henderson, R.K.; Underwood, I.; Watson, S.; et al. Active-Matrix GaN Micro Light-Emitting Diode Display With Unprecedented Brightness. *IEEE Trans Electron Devices* **2015**, *62*, 1918–1925, doi:10.1109/TED.2015.2416915.

160. McKendry, J.J.D.; Rae, B.R.; Gong, Z.; Muir, K.R.; Guilhabert, B.; Massoubre, D.; Gu, E.; Renshaw, D.; Dawson, M.D.; Henderson, R.K. Individually Addressable AlInGaN Micro-LED Arrays with CMOS Control and Subnanosecond Output Pulses. *IEEE Photonics Technology Letters* **2009**, *21*, 811–813, doi:10.1109/LPT.2009.2019114.

161. Kim, K.; Vöröslakos, M.; Seymour, J.P.; Wise, K.D.; Buzsáki, G.; Yoon, E. Artifact-Free and High-Temporal-Resolution in Vivo Opto-Electrophysiology with MicroLED Optoelectrodes. *Nat Commun* **2020**, *11*, doi:10.1038/s41467-020-15769-w.

162. Grossman, N.; Poher, V.; Grubb, M.S.; Kennedy, G.T.; Nikolic, K.; McGovern, B.; Palmini, R.B.; Gong, Z.; Drakakis, E.M.; Neil, M.A.A.; et al. Multi-Site Optical Excitation Using ChR2 and Micro-LED Array. *J Neural Eng* **2010**, *7*, doi:10.1088/1741-2560/7/1/016004.

163. Hee Lee, J.; Lee, S.; Kim, D.; Jae Lee, K. Implantable Micro-Light-Emitting Diode (MLED)-Based Optogenetic Interfaces toward Human Applications. *Adv Drug Deliv Rev* 2022, *187*.

164. Zhanghu, M.; Wang, Y.; Liu, Z. Compound Semiconductor Micro-Led Array and Its Novel Applications in Phototherapy. In Proceedings of the

Digest of Technical Papers - SID International Symposium; John Wiley and Sons Inc, 2020; Vol. 51, pp. 121–124.

165. Poher, V.; Zhang, H.X.; Kennedy, G.T.; Griffin, C.; Oddos, S.; Gu, E.; Elson, D.S.; Girkin, J.M.; French, P.M.W.; Dawson, M.D.; et al. Optical Sectioning Microscopes with No Moving Parts Using a Micro-Stripe Array Light Emitting Diode. *Optical Society of America* **2007**, *15*, 11196–11206.

166. Moreno, S.; Canals, J.; Moro, V.; Franch, N.; Vilà, A.; Romano-Rodriguez, A.; Prades, J.D.; Bezshlyakh, D.D.; Waag, A.; Kluczyk-Korch, K.; et al. Pursuing the Diffraction Limit with Nano-LED Scanning Transmission Optical Microscopy. *Sensors* **2021**, *21*, 3305.

167. Vilà, A.; Moreno, S.; Canals, J.; Moro, V.; Franch, N.; Wartenberg, P.; Dieguez, A. Ultra-Compact and Large Field-of-View Nano-Illumination Light Microscope Based on an Array of Organic Light-Emitting Diodes. In Proceedings of the Proc. SPIE 11693, Photonic Instrumentation Engineering VIII, 1169308; 2021.

168. Vilà, A.; Moreno, S.; Canals, J.; Diéguez, A. A Compact Raster Lensless Microscope Based on a Microdisplay. *Sensors* **2021**, *21*, doi:10.3390/s21175941.

169. Vilà, A.; Moreno, S.; Diéguez, A. Can Light Microscopes Really Be Chip-Sized? In Proceedings of the Digest of Technical Papers - SID International Symposium; John Wiley and Sons Inc, 2022; Vol. 53, pp. 271–274.

170. Prajapati, E.; Kumar, S.; Kumar, S. Muscope: A Miniature on-Chip Lensless Microscope. *Lab Chip* **2021**, *21*, 4357–4363, doi:10.1039/d1lc00792k.

171. Kozel, T.R.; Burnham-Marusich, A.R. *Point-of-Care Testing for Infectious Diseases: Past, Present, and Future*; 2017;

172. Global HIV Hepatitis and STIs Programmes (HHS); Sexual and Reproductive Health and Research (SRH); World Health Organization *The Diagnostics Landscape for Sexually Transmitted Infections*; 2023; ISBN 9789240077126.

# 5. Bibliography


173. Farrel, F.; Xie, E.; Guilhabert, B.; Haughey, A.M.; Dawson, M.D.; Laurand, N. Micro-LED Waveguide for Fluorescence Applications. In Proceedings of the 2019 IEEE Photonics Conference (IPC); San Antonio, TX, USA, 2019; pp. 1–2.

174. Bruce, N.; Farrell, F.; Xie, E.; Scullion, M.G.; Haughey, A.-M.; Gu, E.; Dawson, M.D.; Laurand, N. MicroLED Biosensor with Colloidal Quantum Dots and Smartphone Detection. *Biomed Opt Express* **2023**, *14*, 1107, doi:10.1364/boe.478276.

175. Qdot™ 605 ITK™ Streptavidin Conjugate Kit Available online: https://www.thermofisher.com/order/catalog/product/Q10001MP?SID=srch-srp-Q10001MP (accessed on 8 March 2024).

176. Qdot™ 705 ITK™ Amino (PEG) Quantum Dots Available online: https://www.thermofisher.com/order/catalog/product/Q21561MP?SID=srch-srp-Q21561MP (accessed on 8 March 2024).

177. Ingle, A.; Velten, A.; Gupta, M. High Flux Passive Imaging with Single-Photon Sensors. **2019**.

178. Moro, V.; Moreno, S.; Alonso, O.; Vilà, A.; Prades, J.D.; Diéguez, A. Using Time-Correlated Single-Photon Counting Technique on SPAD Sensors to Enhance Acquisition Time and Dynamic Range. *Proceedings of SPIE* **2022**.

179. Wu, D.; Luo, J.; Huang, G.; Feng, Y.; Feng, X.; Zhang, R.; Shen, Y.; Li, Z. Imaging Biological Tissue with High-Throughput Single-Pixel Compressive Holography. *Nat Commun* **2021**, *12*, doi:10.1038/s41467-021-24990-0.